Optimal Control Applications in Space Situational Awareness

by

Marcus J. Holzinger

M.S., Aeronautics & Astronautics, University of Washington, 2005

B.S., Aeronautics & Astronautics, University of Washington, 2003

A thesis submitted to the

Faculty of the Graduate School of the

University of Colorado in partial fulfillment

of the requirements for the degree of

Doctor of Philosophy

Department of Aerospace Engineering Sciences

2011

This thesis entitled:
Optimal Control Applications in Space Situational Awareness
written by Marcus J. Holzinger
has been approved for the Department of Aerospace Engineering Sciences

_____

Prof. Daniel Scheeres

_____

Prof. Hanspeter Schaub

Date _____

The final copy of this thesis has been examined by the signatories, and we find that both the content and the form meet acceptable presentation standards of scholarly work in the above mentioned discipline.

Holzinger, Marcus J. (Ph.D., Aerospace Engineering Sciences)

Optimal Control Applications in Space Situational Awareness

Thesis directed by Prof. Daniel Scheeres

There are currently more than 19,000 trackable objects in Earth orbit, 1,300 of which are active. With so many objects populating the space object catalog and new objects being added at an ever increasing rate, ensuring continued access to space is quickly becoming a cornerstone of national security policies. Space Situational Awareness (SSA) supports space operations, space flight safety, implementing international treaties and agreements, protecting of space capabilities, and protecting of national interests. With respect to objects in orbit, this entails determining their location, orientation, size, shape, status, purpose, current tasking, and future tasking. For active spacecraft capable of propulsion, the problem of determining these characteristics becomes significantly more difficult. Optimal control techniques can be applied to object correlation, maneuver detection, maneuver/spacecraft characterization, fuel usage estimation, operator priority inference, intercept capability characterization, and fuel-constrained range set determination. A detailed mapping between optimal control applications and SSA object characterization support is reviewed and related literature visited. Each SSA application will be addressed starting from first-principles using optimal control techniques. For each application, several examples of potential utility are given and discussed.

Dedication

In honest moments we understand that every successful endeavor has been accomplished with the aid, support, and encouragement of other people. Now, at the conclusion of my formal education, I look back on earlier times and realize how greatly I've benefited from selfless actions of those I know.

No dedication in a dissertation would be complete without first recognizing the outstanding efforts of professional educators. Specifically, I would like to thank Mrs. Charles, who always pushed me despite my ambivalent attitude towards homework, Mr. Minton, who helped me realize my fascination with math and engineering, and Mr. Sparks, who piqued my interest in writing.

As my family has known me the longest and put up with the most, they deserve special mention. I dedicate this dissertation to my grandparents, Ralph and Marlene, for giving me the chance to know and appreciate them and for providing room and board during my first years in university. I thank my sister, Mercedes, whose positive attitude has always brought a smile to my face. I dedicate this to my parents, Heinz and Nancy, for putting up with my antics, encouraging me to pursue higher education, and telling me to to my best.

Lastly, I would like to dedicate this dissertation to my wife, Kathryn, for her unbounded love, support, and cheerful manner, as well as her assistance in maintaining my extensive supply of coffee.

Acknowledgements

First and foremost, I would like to acknowledge my advisor, Dan Scheeres. Dan's humble, honest, and friendly manner played no small part in aiding my decision to return to graduate school. I will count my career spectacularly successful if I have half the positive impact Dan does on both the people he works with and the research topics he studies.

One of the great benefits and joys of graduate school is having sharp, fun-loving lab-mates with whom to share camaraderie, bounce ideas off of, ask innumerable questions, and rant with. Jay McMahon is particularly responsible for much stress relief, strategic thinking, sanity checks, and time wasting. Seth Jacobson, Kohei Fujimoto, and Christine Hartzell are similarly guilty of great (though sometimes off-topic) conversations and occasional equation verification.

Through the course of my dissertation research I have had the distinct pleasure of writing papers with several members of the research community. I would like to thank Terry Alfriend for his suggestions and feedback regarding hypothesis testing and his insights into operational realities. I thank John Hauser for his relentless inquisitions and significant patience regarding my abuses of notation. I would also like to thank Scott Erwin for posing the orbit range problem, supporting my work on it as a Space Scholar at Kirtland AFB, and providing excellent career advice.

Many thanks to Hanspeter Schaub, who in addition to always providing outstanding advice and insight into the research community, gave me the chance to help teach his outstanding formation flight course. Lastly, for enriching and productive discussions I would like to thank Moriba Jah, Fred Leve, and Richard Linares.

Contents

Chapter

Tables

Table

Figures

Figure

Chapter 1

Problems in Space Situational Awareness

1.1 Space Situational Awareness Definition and Scope

As of April, 2009, there are approximately 19,000 objects in Earth orbit with a nominal diameter greater than 10cm, 1,300 of which are active spacecraft [1]. These numbers are expected to grow by an order of magnitude in the next decade due to increased tracking capabilities and additional launches [2]. With so many objects currently in the Space Object Catalog (SOC) and with new objects being added at an increasing rate, ensuring continued access to space is quickly becoming a critical component of the United States' and other entities' security policies. For the United States,

> "The need for increased space protection of our space assets is paramount, and requires enhanced Space Situational Awareness (SSA) capabilities ... [3]."

The current Department of Defense (DoD) Joint Publication 3-14 dictating roles and responsibilities for Space Operations defines SSA as

> "... a key component for space control because it is the enabler, or foundation, for accomplishing all other space control tasks. SSA involves characterizing, as completely as necessary, the space capabilities operating within the terrestrial environment and the space domain [4]."

Joint Publication 3-14 further emphasizes that SSA supports key objectives such as ensuring space operations and space flight safety, implementing international treaties and agreements, protecting space capabilities, and protecting military operations and national interests [4].

For each of the 19,000 and growing trackable objects in space, characterization may be further described as

> "... knowing the location of every object orbiting the Earth, active or inactive, big or small; and knowing why it is there, what it is doing now, and what we think it will be doing in the future [5]."

Additional attributes whose determination supports SSA efforts include "shape, motion, and orientation data" [6].

In short, high level space object chacteristics whose determination supports SSA efforts are:

- Location. Where is the object? What is its attitude? How well are these states known?
- Active. Is the object debris, dormant, active, etc.?
- Size. What size is the object?
- Shape. What shape is the object? Does the shape suggest specific capabilities?
- Motion. Is the spacecraft motion homogeneous or is it actively maneuvering?
- Purpose. Why is the object in its current orbit? What capabilities does it possess?
- Current Disposition. What task(s) is the object currently executing?
- Future Disposition. What task(s) could the object potentially do? What task(s) will the object likely do?

Achieving SSA with respect to active spacecraft is both quite difficult and imperative, particularly when active spacecraft are operated by uncooperative or noncooperative parties.

Of particular interest to this research effort are active spacecraft capable of propulsive maneuvers. Such spacecraft, conducting maneuvers in carefully planned sequences, can deeply confound all SSA support efforts listed above. This motivates the following Thesis Statement for this dissertation.

Thesis Statement:

> Optimal Control methods can enable and improve critical Space Situational Awareness activities, specifically track correlation, maneuver detection, fuel usage estimation, operator priority inference, efficient intercept set computation, range set theory, and range set generation for maneuvering space vehicles.

Based on inference only, determining the purpose, current disposition, and future disposition of active, potentially maneuvering spacecraft is effectively an infinite-dimensional problem. To reduce the scope for this research effort, the following guiding principles governing active, uncooperative / noncooperative, and possibly maneuvering spacecraft are assumed:

[P1] The spacecraft available thrust, current fuel, and total fuel capacity are unknown

[P2] Fuel is a scarce on-orbit commodity. When an object maneuvers, all else being equal, it will do so in a fuel-optimal maneuver (with or without time constraints)

[P3] When appropriate, system, boundary condition, and measurement uncertainty should be directly considered

Together, guiding principles [P1], [P2], and [P2] suggest a rigorous application of optimal controls to efforts supporting SSA. A short description on how the application of optimal control techniques can support SSA efforts is given in the following section.

1.2 Optimal Control Problems in SSA

Problems in which careful application of optimal control techniques can support SSA efforts are discussed in the following subsections. In order of discussion, they are object catalog support, object attribute inference, and strategic / tactical planning.

1.2.1 Space Object Catalog Support

The Space Object Catalog (SOC) contains the current ephemerides, uncertainties, and status of all trackable objects in Earth orbit. The herculean task of maintaining the SOC and incorporating new objects is carried out by the Joint Space Operations Center (JSpOC) [4]. Maintaining orbit estimates and uncertainties on potentially active satellites is a tremendously difficult task, particularly when objects are operated by third parties and subject to unknown maneuvers. Also, due to limited tracking resources, some maneuvering objects may be observed irregularly, generating large numbers of Uncorrelated Tracks (UCTs). In view of

principles [P1], [P2], and [P3], maneuver detection and UCT correlation may benefit from optimal controls methods in particular.

1.2.1.1 Object and Track Correlation

Correlating UCTs with specific objects is a persistent and critical endeavor in maintaining the SOC. Fundamentally, object and track correlation is concerned with associating observations or sequences of observations with specific objects. This problem is made quite difficult due to limited tracking resources and unknown, possibly unobserved maneuvers.

Range gating, where the new UCT is correlated with the object if the new measurements are within a certain region of their expected values, is a common method currently in use. Other approaches that directly incorporate uncertainty are the Mahalonobis Distance (M-D) [12], the Kullback-Leibler Distance (KL-D) [7], the Bhattacharyya Distance (B-D) [8], and the Maximum a Posteriori Distance (MaP-D) (also known as Bayesean). Unfortunately, none of these approaches to correlating UCTs with objects (or other UCTs) account for maneuvering spacecraft.

Several approaches to object correlation accounting for maneuvers exist. In traditional tracking approaches, maneuvers are modeled as random processes, often as white noise [13]. As intuition would suggest, on-orbit maneuvers are not random and are often as close to fuel optimal as operations allow. To account for this, batch and sequential estimation methods can use force models that assume fuel-optimal maneuvers [18]. Unfortunately, this approach has only been applied to continuous optimal thrust trajectories where the thrust magnitude is known.

It remains, however, that significant room for application involving optimal control approaches remains. Given two sets of UCTs generated from two distinct sequences of observations, control distance metrics may be used to determine whether the UCTs likely belong to the same (possibly maneuvering) space object. As is shown in Chapter 2, under specific conditions optimal control performance indices also posses the properties of distance metrics, namely positivity, strict positivity, symmetry, and the triangle inequality. A carefully constructed performance index can represent fuel cost (or a fuel cost analog) and may be considered a 'control distance.' Combined with enforcing boundary conditions consistent with UCTs or new

measurements, the control distance of the connecting trajectory can be determined.

Given UCTs generated at different times belonging to the same object, if no maneuver has occurred, the control distance metric will necessarily be zero as the fuel-optimal trajectory connecting the UCTs will be homogeneous. However, if the object has executed a maneuver or experienced un-modeled accelerations, the trajectory connecting the UCTs will have a strictly positive control distance and, further, the control distance will quantify the required fuel to execute the maneuver(s). Also, if multiple objects are in close proximity and it is known that each spacecraft is attempting to minimize fuel usage, the control distance metric may be used to test all UCT association combinations and generate the combinations with the smallest fuel usage.

Because UCTs and existing SOC state knowledge never precisely reflects truth, systemic uncertainty must also be incorporated into the control distance formulation. For control distance calculations, this uncertainty manifests as boundary condition uncertainty. In this instance optimal control methodologies can be used to compute the distribution of control distances given distributions in the initial and final boundary conditions or measurements.

1.2.1.2 Maneuver Detection

Detecting the time and magnitude of unknown maneuvers between measurements is a significant problem in maintaining the SOC for active spacecraft. Traditional optimal variance batch and sequential estimation methods require some modeling of accelerations acting on the spacecraft to accurately estimate its state. If maneuver time, direction, and magnitude are known, this information can be directly given to the optimal estimator and an excellent state estimate may be generated. However, if the maneuvers are unknown, the quantity, timing, direction, and magnitude must be either estimated in additional to other state variables or modeled as a sufficiently large model uncertainty.

Real-time maneuver detection often involves examining the Mahalonobis distance of the new measurement. The nominal state and measurement uncertainties are projected into the measurement space, the new measurement residual is computed, and it is determined whether that measurement residual is the result of systemic uncertainty or the artifact of a maneuver. It remains, however, that even if a good estimate of the

maneuver time is generated, the magnitudes and direction must still be estimated. Further, real-time maneuver detection by definition requires that measurements are taken while the object maneuvers - something that given existing tracking resources may not be guaranteed.

Maneuvers may also be detected by examining subsets of tracking data and examining changes in orbit energy. If the orbit energy estimated from the new data is sufficiently different from the expected energy (as measured by the Mahalanobis Distance), an event can be declared [19]. This method requires that a maneuver change the orbit energy, but it can be imagined that changes in any constant of motion could be examined in a similar fashion. Alternate methods use binary search algorithms to partition tracks or sequences of tracks into segments where no maneuvers occur, then attempt to estimate maneuver timing, magnitudes, and directions [20]. Various metrics of data fit goodness are used in these cases to determine when the maneuver profile estimate is correct. Other methods propagate partial tracks forwards and/or backwards in time and search for close approaches in position space. In situations where position differentials are small, a maneuver time, size, and direction may be estimated [21]. This method implicitly assumes that only a single maneuver has occurred between observations.

Again, if it is assumed that operators are maneuvering their spacecraft in an optimal manner, a control distance metric approach may be used. Because boundary condition uncertainty is directly accounted for in the control distance problem formulation and solution, a control distance distribution resulting from connecting two UCTs or measurements can be divided into deterministic and uncertain components. By treating the deterministic portion of the control distance as an instantiation of the uncertain component, a probability that the measured control distance is the artifact of a maneuver (or some other anomaly). As with real-time maenuver detection using the Mahalanobis-Distance, an anomaly / maneuver probability threshold may be defined and, when exceeded, used to alert operators that a maneuver is likely to have occurred. This approach has the additional advantage that the likely time, direction(s) and total effort of the maneuver(s) can be reconstructed from the control distance calculations, seeding batch maneuver / state estimators with better initial guesses.

1.2.2 Object Attribute Inference

For the purposes of this research, object attribute inference is taken to mean determining the size, shape, motion, and current disposition of an orbiting object. Characterizing these attributes for active spacecraft is of particular interest. The following two subsections discuss particular ways in which the application of optimal control techniques assists in object attribute inference.

1.2.2.1 Fuel Usage

Knowledge of uncooperative / noncooperative spacecraft fuel capacity and current fuel levels can facilitate strategic and tactical decision making. Estimating fuel capacity and current reserves is quite difficult and is intrinsically linked to spacecracft mass estimates and propulsion system characterization. If it is known that a spacecraft is nearing the end of its operational life, maneuvers to de-orbit or place it in a graveyard orbit can be anticipated. Also, as discussed in §1.2.3, estimates of a spacecraft fuel reserves can aid planning and contingency exercises on both the tactical and strategic levels.

A fuel metric commonly used to quantify how much a spacecraft may modify its orbit is characteristic velocity (often called 'ΔV'). Characteristic velocity is a useful metric as it incorporates changes in spacecraft mass due to fuel consumption as well as propulsion system efficiencies. This makes characteristic velocity a platform-independent metric with which to measure trajectory fuel costs or distances. All trajectories 'cost' a specific quantity of ΔV, either zero for homogeneous trajectories or some positive value for trajectories involving maneuvers.

Accurate estimates of cumulative fuel usage depend greatly on correctly estimating the size of every maneuver. As such, cumulative fuel usage estimates can suffer from errors in maneuver detection and characterization. Thus, fuel usage characterization is largely a function of the maneuver characterization method used.

Control distance computations between observations or tracks can directly aid in this characterization problem. If an object is observed sufficiently often, control distances may be computed and a running total of ΔV expenditures may be kept. Combined with a-priori total ΔV capability estimates, these two numbers can be used to estimate remaining fuel reserves in terms of ΔV, potentially providing insight into what

maneuvers are within the spacecraft's remaining capability to perform.

1.2.2.2 Inferences on Operator Priorities

As intuition suggests, minimization of trajectory ΔV usage is not necessarily the sole objective of spacecraft operators. In many cases, operators may execute maneuvers or series of maneuvers that are not fuel-optimal, but serve other operational priorities.

Outside of educated guesswork and inference, past work has leveraged the strong classification capabilities of Bayesan belief networks [21]. In such networks, experts blend Bayes rule, contextual knowledge, and known causal relationships to probabilistically classify events or operator intentions.

By measuring the control distances between previous state estimates and tracks or new observations, valuable insight into operator priorities may be inferred. Specifically, if the maneuvers are consistently fuel sub-optimal, then operator goals may not be limited to preserving fuel and extending spacecraft operational life. Computing control distance distributions to include in analyses related to spacecraft operator priorities can greatly increase the accuracy of such analyses, and in particular may be good inputs for Bayesan belief networks.

1.2.3 Strategic and Tactical Planning

In land, air, and sea operations, concepts such as minimum-time intercept envelopes and vehicle range sets are critical to strategic and tactical planning. The capability to compute and determine such sets directly supports quantification of spacecraft future dispositions, an SSA cornerstone. Currently, there are no rigorously defined analogs for spacecraft. Optimal control methodologies are uniquely suited to generating such analogs, as there are a variety of methods available to generate sets of minimum time and minimum fuel trajectories.

1.2.3.1 Intercept Reachability

In controls literature the full set of reachable states given an initial set of reachable states is called the reachability set. Here the term intercept reachability is meant as the position subspace of the full reachability

set. Position reachability subsets are of specific interest in intercept problems because when conjunctions occur relative velocities are likely so large that their differences are irrelevant. Problematically, full state-space reachability computations suffer from the curse of dimensionality; their computation time and memory scale at an exponential rate dependent on the dimension of the state space. For 3-Degree of Freedom (DoF) motion, which requires 6 states to fully specify, full minimum-time reachability set computation becomes quite cumbersome and in general computationally intractable. Thus, methods to efficiently compute intercept reachability sets (position reachability subspaces) can directly support SSA scenario evaluation.

Full-state, minimum time reachability has largely been the focus of optimal controls literature and has been extensively studied. Reachability computation using zero-level sets of the value function in the Hamilton Jacobi Bellman (HJB) PDE has been rigorously established [60, 62]. Some relationships between minimum time reachability and maximum distance reachability sets are also explored [35] in this framework. Reachability solutions found using the HJB PDE and zero-level set methods benefit tremendously from existing numerical toolboxes [64]. Alternately, rather than propagating the HJB PDE and computing zero level sets, the reachability set surface may be sampled and propagated as individual trajectories [66, 67].

Existing applications of minimum time reachability in aerospace center around collision avoidance and safety-related computations. Collision avoidance may be treated as a differential game and used to compute 'safe' sets [39]. Similarly, for safety-related applications, safe sets for aerial refuling may be computed by treating disturbances as worst-case adversarial inputs [40].

Intercept reachability has been examined using parametric optimization outside of a HJB PDE setting [75]. This particular approach imposes a ΔV constraint and computes linearized changes in the positional reachability over small time intervals assuming Keplerian motion. While this approach to computing position reachability sets does not explicitly minimize time and assumes impulsive maneuvers, it highlights the utility of intercept reachability set computation.

To circumvent this dimensionality-driven intercept set computation limitation, optimal control techniques may again be leveraged. As intercept problems related to SSA are concerned with position conjunctions, it is often unnecessary to compute relative velocities. In particular, by viewing the surface of the intercept sets as a set of final states of individual optimal trajectories, necessary conditions of optimality

governing boundary conditions may be applied to reduce the overall computational burden. By carefully constructing the problem in view of these insights, the overall dimensionality of the minimum time *position* intercept problem is reduced, making the problem computationally tractable. Though the approach given in this dissertation uses minimum time as the implicit performance index, the approach can be modified to accommodate minimum fuel computations as well.

1.2.3.2 Range Set Theory

The term 'range' has may possible interpretations. One can easily imagine defining range as how far an object may travel with a fixed amount of time, fuel, money, etc. As discussed in the previous section, minimum time reachability sets satisfy one potential definition of range. In SSA applications, useful types of range could be minimum time, minimum fuel, minimum energy, or combinations between these. Unfortunately, there does not exist any rigorously defined framework to compute reachability sets given arbitrary constraints on independent parameters.

The aircraft range equation was first derived by Louis Breguet in the early 20^{th} century using a direct change of independent parameter from time to fuel mass [72]. Reachability given both time and fuel constraints has also been preliminarily addressed in an optimal control setting by adding the cumulative fuel usage as an auxilliary state and imposing boundary conditions [79]. More recently, spacecraft range was preliminarily addressed in a parametric optimization setting under Keplerian motion for a single impulsive maneuver with ΔV constraints and no time constraints [78]. While all of these approaches address range in one manner or another, none do so under a unified optimal controls framework.

By carefully defining a new general independent parameter and its mapping function with respect to time a General Independent Parameter (GIP) HJB PDE may be derived. Under the GIP HJB PDE framework, reachability sets using arbitrary constraints on general independent parameters can be computed. Further, as discussed in §1.2.1, performance indices with positive semi-definite Lagrangians are metrics. If such a performance metric is used as the new independent parameter, the resulting GIP HJB PDE solution is defined as a Generalized Metric Range Set. Such sets encompass all types of range discussed above (e.g. minimum time, fuel, energy, combinations thereof). A Generalized Metric Range Set may be computed using

methods found in controls literature for minimum time reachability sets.

1.2.3.3 Orbit Range Computation

Computing minimum fuel range sets for spacecraft directly supports strategic planning efforts related to SSA, as having such information allows space assets, capabilities, and interactions to be expressed in an intuitive geometric manner. Contrary to traditional range computations for air, land, and sea vehicles, space vehicle range computations are confounded by two unique and fundamental hurdles. First, spacecraft in orbit are, by definition, always moving, making range measures difficult to define. Second, spacecraft are not always expending fuel and often experience long periods of quiescence.

Past free-time, fuel-optimal reachability has been addressed in the neighborhood of reference orbit using linearization techniques [76, 77]. Due to the linearization process, these methods are only approximate and only appilcable in the vicinity of these reference orbits. Much more recently, Xue et al. applied direct parametric optimzation to determine range sets by choosing the timing and direction of a single fixed magnitude impulsive maneuver [78].

Both persistent motion and itermittent maneuvers may be addressed directly using the Generalized Metric Range Set framework introduced in §1.2.3.2. First, the problem of consistent motion may be circumvented by using constants of motion as state-space coordinates, rather than traditional Earth Centered Inertial (ECI) or Earth Centered Earth Fixed (ECEF) coordinates. Second, by changing the independent parameter from time to ΔV and ensuring that important characteristics of the problem are preserved, sets of reachable states given ΔV constraints may be computed using existing minimum time software. This approach has the benefit of being time-independent and usable with any set of constants of motion, avoiding coordinate singularities, and it can be shown to reproduce all known fuel optimal orbit transfers.

1.2.4 SSA Object Characterization Support Summary

Table 1.1 reviews which object characteristics listed in §1.1 are supported by optimal control applications. Mappings between object attributes and optimal control applications are not necessarily one-to-one, and in many cases exhibit significant overlap. Also, because SSA activities such as determining object at-

tributes in Table 1.1 are inherently very complicated and deeply interconnected, support of an activity does not suggest that the activity in question is considered 'solved.' Of the attributes listed in §1.1, neither Size nor Shape were directly supported by research included in this dissertation; future research may produce approaches in which optimal control supports determination of Size and Shape, however such research is not considered within the scope of this dissertation.

Table 1.1: SSA object characterization support by optimal control application. A check mark indicates that an optimal control application supports a particular SSA activity outlined in §1.1. The subsections in which each individual optimal control application are introduced and chapters in which the topics are discussed in depth are given on the bottom row.

	Space Object Catalog		Object Attribute Inference		Strategic & Tactical Planning		
Object Attribute	Object Correlation	Maneuver Det. / Char.	Fuel Usage	Priority Inference	Intercept Computation	Range Set Theory	Orbit Range Computation
Location	✓	✓			✓	✓	✓
Active	✓	✓					
Size							
Shape							
Motion	✓	✓					
Purpose	✓	✓	✓	✓	✓	✓	✓
Current Disposition	✓	✓	✓	✓	✓	✓	
Future Disposition			✓	✓	✓	✓	✓
Introduced	§1.2.1.1	§1.2.1.2	§1.2.2.1	§1.2.2.2	§1.2.3.1	§1.2.3.2	§1.2.3.3
Applicable Chapter	Chapter 2	Chapter 2	Chapter 2	Chapter 2	Chapter 3	Chapter 4	Chapter 4

1.3 Organization and Contributions

The organization of this dissertation and highlights of contributions in each chapter are summarized here. Chapter 2 addresses problems introduced in §1.2.1. Optimal control problem distance metrics are introduced and their metric properties on the space of optimal trajectories are demonstrated. This distance metric property is applied to fuel usage metrics and used to define control distance metrics. Both full- and partial-state boundary condition constraints are examined and control distance relationships are generated for each. Uncertain boundary conditions are also considered, generating distributions of control distances. Finally, maneuver detection and stochastic dominance are introduced before several examples are used to illustrate the approach.

Traditional formulations for minimum time reachability are introduced and derived in Chapter 3. The problem of computationally tractable, minimum time position intercept problems discussed in §1.2.3.1 are directly addressed. Several important concepts such as optimal control policies and switching times are reviewed. The primary theorems and corollaries involved in reducing the dimensionality of the problem are introduced, followed by an overview on potential solution procedures and several examples.

Chapter 4 elaborates on approaches to solve the free-time, minimum-fuel range set computation discussed in §1.2.3.3. A mapping function between time and a new independent parameter coordinate is first discussed, followed by a detailed derivation of the Hamilton Jacobi Bellman (HJB) PDE using the new independent parameter coordinate. Implications of left-, right-, and full-invertibility of the mapping function are discussed, and the methodology by which orbit range sets may be computed is outlined. The Generalized Metric Range Set is defined and discussed. Several short illustrates and simple examples are given. Finally, the approach is applied to Gauss' Variational Equations (GVEs) and several range sets are computed using semi-major axis, eccentricity, and inclination. The optimal control policy derived using this first principles is found to generate all orbit maneuvers found in classical astrodynamics orbit transfers.

Finally, Chapter 5 reviews the successful application of optimal control techniques to the problems discussed in §1.2 and enumerates several avenues for future research.

Table 1.3 summarizes how contributions contained within this dissertation relate to SSA applications

as well as enumerates which existing literature is most applicable. Relevant author journal publications for each application are also listed. Lastly, the chapter in which the material is addressed in this dissertation is identified.

Table 1.2: Contribution and Existing Research Summary

	Space Object Catalog		Object Attribute Inference		Strategic & Tactical Planning		
Reference	Object Correlation	Maneuver Det. / Char.	Fuel Usage	Priority Inference	Intercept Computation	Range Set Theory	Orbit Range Computation
Hill [12]	✓						
Poore [13]	✓	✓		✓			
Folcik [18]		✓	✓				
Patera [19]		✓					
Abbot [21]				✓			
Crandall [60]					✓		
Sethian [62]					✓		
Kurzhanski [35]					✓		
Vihn [75]					✓		
Breguet [72]						✓	
Kats [79]						✓	
Xue [78]						✓	✓
Marec [76]							✓
Breakwell [77]							✓
Holzinger [HSA]	✓	✓	✓	✓			
Holzinger [HS]					✓		✓
Holzinger [HSH]						✓	✓
Holzinger [HSE]							✓
	Chapter 2	Chapter 2	Chapter 2	Chapter 2	Chapter 3	Chapter 4	Chapter 4

Table 1.3: Contribution and Existing Research Summary

	Space Object Catalog		Object Attribute Inference		Strategic & Tactical Planning		
Reference	Object Correlation	Maneuver Det. / Char.	Fuel Usage	Priority Inference	Intercept Computation	Range Set Theory	Orbit Range Computation
Hill [12]	Mahalanobis						
Poore [13]	Survey	Markov Aprx.		Mult. Hyp.			
Folcik [18]	Cont. Thrust						
Patera [19]		Δa Det.					
Aaron [21]		Sliding Wind.	Batch/Sum				
Abbot [21]				Bayes. Belief			
Crandall [60]					Viscosity Sol.		
Sethian [62]					V.S. & L. Sets		
Kurzhanski [35]					Linear Results		
Vinh [75]					Const. ΔV		
Breguet [72]						Aircraft	
Kats [79]						Time vs. Fuel	
Xue [78]						Geom. Desc.	Single Impusle
Marec [76]							Linearized
Breakwell [77]							Lin. w/ Restr.
Holzinger [HSA]	✓	✓	✓	✓			
Holzinger [HS]					✓		✓
Holzinger [HSH]						✓	✓
Holzinger [HSE]							✓
Approach	Control Distance	Hypothesis Testing	Sum	Provide Inputs	Subspace Methods	GIP and GIP HJB	GIP HJB and GVEs
	Chapter 2	Chapter 2	Chapter 2	Chapter 2	Chapter 3	Chapter 4	Chapter 4

For reference purposes, journal and conference papers forming the basis for this dissertation are listed below in chronological order (newest to oldest).

Journals

[HSH] M. J. Holzinger, D. J. Scheeres, J. Hauser, "Generalized Range Definition, Computation, and Special Cases," Submitted to IEEE Transactions on Automatic Control in February 2011.

[HSE] M. J. Holzinger, D. J. Scheeres, R. S. Erwin, "On-Orbit Range Computation using Gauss' Variational Equations with J_2 Perturbations," Submitted to AIAA Journal of Guidance, Control, and Dynamics in January 2011.

[HSA] M. J. Holzinger, D. J. Scheeres, K. T. Alfriend, "Object Correlation, Maneuver Detection, and Characterization using Control Distance Metrics," Submitted to AIAA Journal of Guidance, Control, and Dynamics in November 2010.

[HS] M. J. Holzinger, D. J. Scheeres, "Reachability Results for Nonlinear Systems with Ellipsoidal Initial Sets," IEEE Transactions on Aerospace and Electronic Systems, In Press.

Conferences and Workshops

- M. J. Holzinger, D. J. Scheeres, J. Hauser, "Optimal Reachability Sets Using Generalized Independent Parameters," AIAA/IEEE American Control Conference, San Francisco, June 2011.
- M. J. Holzinger, D. J. Scheeres, "LQR Performance Index Distribution with Uncertain Boundary Conditions," AIAA/IEEE American Control Conference, San Francisco, June 2011.
- M. J. Holzinger, D. J. Scheeres, R. S. Erwin, "On-Orbit Range Computation Using Gauss' Variational Equations for Mean Orbit Elements with J_2 Perturbations," 21^{st} AAS/AIAA Space Flight Mechanics Meeting, New Orleans, Louisiana, February 2011.
- M. J. Holzinger, D. J. Scheeres, "Object Correlation and Maneuver Detection Using Optimal Control Performance Metrics," Advanced Maui Optical and Space Surveillance Technologies Conference, Wailea, September, 2010.

- M. J. Holzinger, D. J. Scheeres, "Object Correlation, Maneuver Detection, and Maneuver Characterization using Control Effort Metrics with Uncertain Boundary Conditions and Measurements," AIAA Conference on Guidance, Navigation, and Control, Toronto, August 2010.

- M. J. Holzinger, D. J. Scheeres, "Object Correlation Using Control Effort Metrics with Boundary Condition Uncertainties," 8^{th} US/Russian Space Surveillance Worksop, Wailea, April 2010.

- M. J. Holzinger, D. J. Scheeres, "Analytical Reachability Results for a Class of Nonlinear Systems with Ellipsoidal Initial Sets," IEEE Conference on Decision and Control, Shanghai, December 2009.

- M. J. Holzinger, D. J. Scheeres, "Reachability Analysis Applied to Space Situational Awareness," AMOS 2009, September 2009.

- M. J. Holzinger, D. J. Scheeres, "Applied Reachability for Space Situational Awareness and Safety in Spacecraft Proximity Operations," AIAA Conference on Guidance, Navigation, and Control, Chicago, August 2009.

Chapter 2

Object Correlation, Maneuver Detection, and Fuel Usage Characterization

The problem of properly correlating on-orbit object observations and characterizing object maneuvers is a challenging and persistent endeavor. There are currently at least 19,000 trackable on-orbit objects, 1,300 of which are active [1], and these numbers are expected to grow significantly due to increasing tracking capabilities and new launches [2]. Predicting conjunction events is a difficult task [10], however recent events highlight the mutual interest national and private operators share in accurate object correlation and maneuver detection capability [11].

Fuel usage is directly related to object correlation and maneuver detection, as maneuvers must be correctly detected and attributed to the object in question. Similarly, fuel usage is convolved with operator priority inference, as fuel-optimal maneuvers indicate that the operator is concerned with fuel usage, while sub-optimal maneuvers suggest alternate priorities. Intuitively, under the assumption that maneuvers have been both correctly detected and attributed to a specific object in the Space Object Catalog, fuel usage can be as simple as a direct summation of estimated maneuver fuel costs. Operator priority, however, is for obvious reasons much more difficult to quantify. Bayesean belief networks, in which a directed, acyclic graph is tuned to represent conditional probabilities and observation correlations, has been proposed to identify potential operator priorities [21].

Radar and visible sensor systems, archetypical sensors used in on-orbit applications, have an extensive body of literature with respect to tracking and target association. Poore [13] gives an excellent overview of the approaches and computational implications of the mutli-target / multi-sensor tracking problem. Examples of tracking approaches in literature are Probabilistic Multi-Hypothesis Tracking (PMHT), Probabilistic Data

Association Filter (PDAF), and Modified Gain Extended Kalman Filter (MGEKF) methods, which deal with tracking faults, clutter, and dense target environments [14, 15, 16]. In many of these methods, target maneuvers are partially modeled as Markov processes, with or without mode switching. Also, an integral strength of these methods is that they maintain the state covariance of each track as a function of time and actively blend new observations to minimize the state uncertainty of a given object.

Common metrics used to determine whether a new object should be correlated with a previously tracked object include, amongst others, the Mahalonobis Distance (M-D) [12], the Kullback-Leibler Distance (KL-D) [7], the Bhattacharyya Distance (B-D) [8], and the Maximum a Posteriori Distance (MaP-D) (also known as Bayesean). The Mahalanobis Distance in particular is often used to determine whether a measurement residual is too large to be completely explained by initial state uncertainty, process noise, and measurement noise [17]. All of these measures quantify a distance- or pseudo-distance metric in the presence of uncertainty, and are typically applied to the state difference between a predicted object state and the best estimate of the newly observed object state.

Problematically, it remains that none of the M-, KL-, B-, or MaP-distance metrics, when applied to state distributions, directly quantifies the level of propulsive effort required to effect the state change given a gap in observation. This difference is critical as very small fuel expenditures at specific points in an orbit can produce outsized state discrepancies.

Approaches that account for the intrinsic uncertainties of the problem that also assume some form of active optimal control are needed. There are two fundamental cases under consideration in this paper: 1) full state distributions from separate, Uncorrelated Tracks (UCTs) that serve as boundary conditions for the Two Point Boundary Value Problem (TPBVP), and 2) full or partial state distributions that act as boundary conditions in cases where full state knowledge is not available (such as when a new measurement is taken after a long observation gap).

The first case is largely applicable to associating multiple UCTs with one another. An underlying assumption is that, all else being equal, the UCT combinations with minimum control distance are most likely [P2]. This problem is called the Uncertain Two Point Boundary Value Problem (UTPBVP). This proposed method is fundamentally different from computing the statistical distance from the objects' expected state

distribution as it directly accounts for optimal control usage.

The second case may be used not only to detect maneuvers as they occur, but also generate the distribution of the optimal control profile used in the maneuver. Again there is an assumption that the spacecraft is executing a maneuver that minimizes control usage [P2]. This approach, called the Measurement Residual Boundary Value Problem (MRBVP), is intrinsically different from measuring the Mahalanobis distance of the measured residual. The MRBVP approach directly converts the residual and uncertainties into a control distance metric, allowing not only maneuver detection but also maneuver characterization.

As discussed in §1.3 and summarized in Table 1.3, both cases discussed in this chapter support Space Object Catalog and Object Characterization activities, specifically object correlation, maneuver detection, fuel usage estimation, and inference of operator priorities. Object correlation is addressed using control effort distance metrics to measure how close an object is from an expected homogeneous orbit. Maneuver detection is done by comparing how much of the control distance the cause of systemic uncertainty and how much is attributable to a possible maneuver. As a natural consequence of the choice of control distance metrics, fuel usage estimation (and associated uncertainty) is directly supported by keeping track of maneuver sequences and adding individual control distance estimates. Inferences on operator priority can be made by examining how suboptimal maneuvers are; if maneuvers are not fuel-optimal, it can be inferred that the operators have priorities other than strict fuel minimization, and educated analysis or Bayesan belief network can then be applied.

The contributions of this chapter are a) the use of trajectory optimality as a distance metric to quantify object track association control distance, b) the statistical treatment of boundary condition deviations for tracking problems with large gaps in observations, c) the use of optimal control distance as a metric for operational maneuver detection and characterization based on measurement residuals, d) the use of stochastic dominance to rank individual and/or sums of performance function distributions, and e) hypothesis testing to detect possible object maneuvers probabilities.

2.1 Optimal Control Theory and Boundary Value Problems

This section has five primary constituents. The first discusses the objective function to be optimized and its relation to optimal maneuvers and distance metrics, the second is a short derivation of the optimal control policy, the third portion examines the control distance induced by nonlinear two-point boundary value problems with boundary value uncertainty, the fourth constituent discusses how measurement residuals may be interpreted in terms of control effort distance metrics, the penultimate portion introduces a sensible approach to ranking control distance distributions, and the final section introduces hypothesis testing to determine whether it is likely that a maneuver may have occurred.

2.1.1 Control Performance as a Metric

Before introducing the specific performance function used in this paper it is first necessary to demonstrate that performance functions for Optimal Control Problems (OCPs) are metrics under certain conditions (metric properties are fully defined in Naylor [23]).

Theorem 2.1.1. ***Optimal Control Problem Distance***

The function

$$\begin{aligned} d_{OCP}(a,b) = \inf_{\boldsymbol{u}\in U}\left[\int_{t_a}^{t_b} \mathcal{L}(\boldsymbol{x}(\tau),\boldsymbol{u}(\tau),\tau)d\tau\right] \\ s.t.\ \ \dot{\boldsymbol{x}} = \boldsymbol{f}(\boldsymbol{x},\boldsymbol{u},t) \\ \boldsymbol{h}(\boldsymbol{x}) \leq \boldsymbol{0} \\ \boldsymbol{g}(\boldsymbol{x}_a,t_a,\boldsymbol{x}_b,t_b) = \boldsymbol{0} \end{aligned} \tag{2.1}$$

is a distance metric defined over the arguments a and b, where $\boldsymbol{x} \in \mathbb{R}^n$, $\boldsymbol{u} \in \mathbb{R}^m$, $t \in [t_0, t_f]$, $\mathcal{L} : \mathbb{R}^n \times \mathbb{R}^m \times \mathbb{R} \to \mathbb{R}$, $\mathcal{L}(\cdot,\cdot,\cdot) \geq 0 \ \forall \boldsymbol{x},\boldsymbol{u},t$ is the trajectory cost, $\boldsymbol{f} : \mathbb{R}^n \times \mathbb{R}^m \times \mathbb{R} \to \mathbb{R}^n$ describes the system dynamics, and $\boldsymbol{g} : \mathbb{R}^n \times \mathbb{R} \times \mathbb{R}^n \times \mathbb{R} \to \mathbb{R}^r$ is a function defining boundary conditions. The arguments $a = (\boldsymbol{x}_a, t_a)$ and $b = (\boldsymbol{x}_b, t_b)$, each defined on the cartesian product of the state space and time coordinates $(\mathbb{R}^n \times \mathbb{R})$ must be members of the set of boundary values that satisfy the boundary condition equation $\boldsymbol{g}(\boldsymbol{x}_a, t_a, \boldsymbol{x}_b, t_b) = \boldsymbol{0}$, defined as

$$(a,b) \in \mathcal{G} \equiv \{(\boldsymbol{\alpha},\boldsymbol{\beta}) \mid \boldsymbol{g}(\boldsymbol{x}_\alpha, t_\alpha, \boldsymbol{x}_\beta, t_\beta) = \boldsymbol{0}\}$$

with $\boldsymbol{\alpha} = (\boldsymbol{x}_\alpha, t_\alpha)$ *and* $\boldsymbol{\beta} = (\boldsymbol{x}_\beta, t_\beta)$. *The boundary values* a *and* b *must also be members one another's reachability sets, defined as*

$$b \in \mathcal{R}(U, \boldsymbol{h}, a) \equiv \{b = (\boldsymbol{x}_b, t_b) | (\boldsymbol{x}_b, t_b) \text{ is reachable given } U, \boldsymbol{h}, \text{ and } a\} \tag{2.2}$$

and

$$a \in \mathcal{R}(U, \boldsymbol{h}, b) \equiv \{a = (\boldsymbol{x}_a, t_a) | (\boldsymbol{x}_a, t_a) \text{ is reachable given } U, \boldsymbol{h}, \text{ and } b\} \tag{2.3}$$

The set $\mathcal{R}(U, \boldsymbol{h}, a)$ *is the reachability set relative to* a, *and is a function of the allowable control set* U *and trajectory inequality constraints* $\boldsymbol{h}$ *(see Chapter 3 for a brief optimal controls reachability introduction). Using this definition, given* $(a, b) \in \mathcal{G}$, *it is required that* $b \in \mathcal{R}(U, \boldsymbol{h}, a)$ *or* $a \in \mathcal{R}(U, \boldsymbol{h}, b)$. *A shorthand notation* $a, b \in \mathcal{G}, \mathcal{R}$ *is used to represent both of these cases.*

Proof:

To demonstrate that $d_{OCP}(a, b)$ *is a metric four properties must be demonstrated: positive, strictly positive, symmetry, and the triangle inequality. Each are now proven individually.*

Positivity: $d_{OCP}(a, b) \geq 0 \ \forall a, b \in \mathcal{G}, \mathcal{R}$. *This property is guaranteed by construction, as* $\mathcal{L}(\cdot, \cdot, \cdot) \geq 0$ $\forall \boldsymbol{x}, \boldsymbol{u}, t$.

Strictly Positive: $d_{OCP}(a, b) = 0$ *if and only if* $a \cong b \ \forall a, b \in \mathcal{G}, \mathcal{R}$. *Here, '*$\cong$*' is taken to mean that* $a \cong b$ *if and only if* a *and* b *are in an equivalency class, meaning that there is precisely zero trajectory cost along the entire connecting trajectory. For example, points along a ballistic trajectory in an equivalency class when the Lagrangian measures fuel usage. Given* $a = (\boldsymbol{x}_a, t_a)$ *and* $b = (\boldsymbol{x}_b, t_b)$ *and observing that if* $\boldsymbol{x}_b$ *lies along an optimal zero-cost trajectory with* $\boldsymbol{x}_a$ *(*$\boldsymbol{x}_b = \phi_x(t_b; \boldsymbol{x}_a, \boldsymbol{p}_a, t_a)$*), such that* $\mathcal{L}(\boldsymbol{x}^*(t), \boldsymbol{u}^*(t), t) = 0$ *over* $t \in [t_a, t_b]$, *then* $d_{OCP}(a, b) = 0$. *The converse is true by inspection.*

Symmetry: $d_{OCP}(a, b) = d_{OCP}(b, a) \ \forall a, b \in \mathcal{G}, \mathcal{R}$. *The distance metric value for* $d_{OCP}(a, b)$ *may be written as*

$$d_{OCP}(a, b) = \int_{t_a}^{t_b} \mathcal{L}(\boldsymbol{x}(\tau), \boldsymbol{u}^*(\tau), \tau) d\tau$$

where $\boldsymbol{u}^*(t)$ *is the global optimal control. Then the distance metric* $d_{OCP}(b, a)$ *may be written as*

$$\begin{aligned} d_{OCP}(b, a) &= \int_{t_b}^{t_a} \mathcal{L}(\boldsymbol{x}(\tau), \boldsymbol{u}^*(\tau), \tau) d\tau \\ &= -\int_{t_a}^{t_b} \mathcal{L}(\boldsymbol{x}(\tau), \boldsymbol{u}^*(\tau), \tau) d\tau \end{aligned}$$

Defining $s = -\tau + t_b$ and making a change of integration variables yields

$$d_{OCP}(b,a) = -\int_{t_a}^{t_b} \mathcal{L}(\boldsymbol{x}(\tau), \boldsymbol{u}^*(\tau), \tau) d\tau$$
$$= \int_{t_a}^{t_b} \mathcal{L}(\boldsymbol{x}(-s), \boldsymbol{u}^*(-s), -s) ds$$

which is identical to $d_{OCP}(a,b)$, demonstrating that $d_{OCP}(a,b) = d_{OCP}(b,a)$.

Triangle Inequality: $d_{OCP}(a,b) \leq d_{OCP}(a,c) + d_{OCP}(c,b)\ \forall a,b,c \in \mathcal{G},\mathcal{R}$. This property is guaranteed by the Principle of Optimality. Given $a = (\boldsymbol{x}_a, t_a)$, $b = (\boldsymbol{x}_b, t_b)$, and $c = (\delta\boldsymbol{x}_i, t_i)$, where $\delta\boldsymbol{x}_i$ is an arbitrary intermediate variation in the optimal trajectory defined by $d_{OCP}(a,b)$. If $\delta\boldsymbol{x}_i = \boldsymbol{0}$ then the variation in the optimal control problem cost ($\delta d_{OCP}(a,b)$) is precisely zero. If $\delta\boldsymbol{x}_i \neq \boldsymbol{0}$, then because the trajectory is now sub-optimal (or equally optimal) the cost variation is either zero or positive; $\delta d_{OCP}(a,b) \geq 0$. Then,

$$d_{OCP}(a,c) + d_{OCP}(c,b) = d_{OCP}(a,b) + \delta d_{OCP}(a,b)$$
$$\Rightarrow d_{OCP}(a,c) + d_{OCP}(c,b) \geq d_{OCP}(a,b)$$

□

Corollary 2.1.1. ***Unconstrained Optimal Control Problem Distance***

If the set U spans all of $\mathbb{R}^m$, the system $\dot{\boldsymbol{x}} = \boldsymbol{f}(\boldsymbol{x}, \boldsymbol{u}, t)$ is controllable, and $\boldsymbol{h}(\boldsymbol{x}(t)) \equiv \boldsymbol{0}\ \forall t \in [t_a, t_b]$, then the reachable set starting from either a or b spans the cartesian product between the state space $\mathbb{R}^n$ and epochs $\mathbb{R}$.

$$\mathcal{R}(U, \boldsymbol{h}, a) = \mathcal{R}(U, \boldsymbol{h}, b) \equiv \{\boldsymbol{\alpha} = (\boldsymbol{x}_\alpha, t_\alpha) | \boldsymbol{x}_\alpha \in \mathbb{R}^n, t_\alpha \in \mathbb{R}\}$$

and the boundary values a and b are only required to be members of $\mathcal{G}$.

Proof:

This is seen to be true by realizing that if all control and trajectory constraints are removed and the system is controllable, then given any boundary value $a = (\boldsymbol{x}_a, t_a)$ a feasible optimal trajectory connecting any $b = (\boldsymbol{x}_b, t_b)$ may be constructed. The same is true if b is first specified.

□

The metric $d_{OCP}(a,b)$ defined in (2.1) on the space $a,b \in \mathcal{G},\mathcal{R}$ is valid for a very large class of OCPs.

Given the results demonstrated in Theorem 2.1.1 and Corollary 2.1.1 it is straightforward to argue that

$$P = d_C(a,b) = \int_{t_0}^{t_f} \frac{1}{2}\mathbf{u}(\tau)^T\mathbf{u}(\tau)d\tau \tag{2.4}$$

given boundary conditions $a = (\mathbf{x}_0, t_0)$ and $b = (\mathbf{x}_f, t_f)$, $a, b \in \mathbb{R}^n \times \mathbb{R}$, subject to dynamics $\dot{\mathbf{x}} = \mathbf{f}(\mathbf{x}, \mathbf{u}, t)$ with $\mathbf{x} \in \mathbb{R}^n$, $\mathbf{u} \in \mathbb{R}^m$, and $t \in [t_0, t_f]$ is a metric. This control distance metric is similar to an energy measure. Ultimately, the metric of interest will measure the total change in velocity ΔV:

$$\Delta V_{thrust} = d_{\Delta V}(a,b) = \int_{t_0}^{t_f} \|\mathbf{u}(\tau)\|_2 d\tau \tag{2.5}$$

Minimum ΔV_{thrust} (fuel) problems are much more difficult to solve than minimum energy analogs such as P [25]. ΔV_{thrust} metrics require both that a maximum possible thrust constraint be enforced (often $\|\mathbf{u}\|_2 \leq u_m$, $0 < u_m < \infty$), requiring $U \subset \mathbb{R}^m$, and also result in optimal control policies that involve on-off switching. In the interest of progressing the theory presented in the next sections this chapter simply uses P. It can be shown using the Cauchy-Schwartz inequality [26] that the performance function P bounds ΔV_{thrust} from above:

$$\Delta V_{impulsive} \leq \Delta V_{thrust} \leq \Delta V_C = \sqrt{2(t_f - t_0)P} \tag{2.6}$$

The minimum possible fuel cost $\Delta V_{impulsive}$ is found using purely impulsive optimal maneuvers, and is bounded above by the minimum possible thrusting fuel cost ΔV_{thrust}. This is necessarily true, as impulsive control laws have $U \to \mathbb{R}^m$ because $u_m \to \infty$, guaranteeing that $\Delta V_{impulsive} \leq \Delta V_{thrust}$. This value is further bounded above by ΔV_C, which is enforced by the Cauchy-Schwartz inequality. Thus, the performance function P, an energy cost analog, can produce an upper conservative bound on the possible fuel cost distribution. Written in terms of OCP distance metrics, $d_{\Delta V}(a,b) \leq d_C(a,b)$, which is in many ways analogous to the Euclidean Distance and Manhattan Distance. Using P defined in (2.4) as the performance function metric rather than (2.5) has the additional benefit that the control authority, the maximum possible thrust u_m, need not be known, and that the optimal control is "always on." Note also that in general, along an arbitrary trajectory the following inequalities hold

$$\|\mathbf{u}_n(t) + \delta\mathbf{u}(t)\|_2 \leq \|\mathbf{u}_n(t)\|_2 + \delta\mathbf{u}(t)^T\delta\mathbf{u}(t) \leq (\mathbf{u}_n(t) + \delta\mathbf{u}(t))^T(\mathbf{u}_n(t) + \delta\mathbf{u}(t))$$

meaning that while in this chapter variations in optimal control using the quadratic performance function P are used, an analogous approach using

$$\tilde{P} = \int_{t_0}^{t_f} \frac{1}{2} \left(\|\mathbf{u}_n(\tau)\|_2 + \delta\mathbf{u}(\tau)^T \delta\mathbf{u}(\tau) \right) d\tau$$

will necessarily generate a less conservative control distance metric. An approach leveraging $\tilde{P}$ is considered future work for the purposes of the current effort.

For the remainder of the chapter d_C will be used as a shorthand notation to describe the deterministic component of P given mean boundary conditions $a = (\mathbf{x}_0, t_0)$ and $b = (\mathbf{x}_f, t_f)$.

2.1.2 Optimal Control Policy

To compute the optimal control policy $\mathbf{u}^*$ Hamiltonian-based optimal control methods are used [27, 28, 29]. Given general dynamics defined by $\dot{\mathbf{x}} = \mathbf{f}(\mathbf{x}, \mathbf{u}, t)$, with $\mathbf{x} \in \mathbb{R}^n$, $\mathbf{u} \in \mathbb{R}^m$, and $t \in [t_0, t_f]$, the Hamiltonian is defined as

$$\mathcal{H} = \inf_{\mathbf{u}} \left[\mathcal{L}(\mathbf{x}, \mathbf{u}, t) + \mathbf{p}^T \mathbf{f}(\mathbf{x}, \mathbf{u}, t) \right] \tag{2.7}$$

with $\mathbf{p} \in \mathbb{R}^n$ called the adjoint or co-state. From the definition of the performance function (2.4), the Hamiltonian becomes

$$\mathcal{H} = \inf_{\mathbf{u}} \left[\frac{1}{2} \mathbf{u}^T \mathbf{u} + \mathbf{p}^T \mathbf{f}(\mathbf{x}, \mathbf{u}, t) \right]$$

The optimal control policy $\mathbf{u}^*$ that minimizes (4.35) is then

$$\mathbf{u}^* = -\frac{\partial \mathbf{f}}{\partial \mathbf{u}}^T \mathbf{p} \tag{2.8}$$

The state and adjoint dynamics along the optimal trajectory may be written as

$$\frac{\partial \mathcal{H}}{\partial \mathbf{p}} = \dot{\mathbf{x}} = \mathbf{f}(\mathbf{x}, \mathbf{u}^*, t) \tag{2.9}$$

$$-\frac{\partial \mathcal{H}}{\partial \mathbf{x}} = \dot{\mathbf{p}} = -\frac{\partial \mathbf{f}}{\partial \mathbf{x}}^T \mathbf{p} \tag{2.10}$$

Given boundary values $a = (\mathbf{x}_0, t_0)$ and $b = (\mathbf{x}_f, t_f)$, the optimal connecting trajectories for the state $\mathbf{x}(t)$ and adjoint $\mathbf{p}(t)$ are written as

$$\mathbf{x}^*(t) = \phi_x(t; \mathbf{x}_0, \mathbf{p}_0^*, t_0)$$

$$\mathbf{p}^*(t) = \phi_p(t; \mathbf{x}_0, \mathbf{p}_0^*, t_0)$$

and, as required in Theorem 2.1.1 and Corollary 2.1.1, it is still required that $(a, b) \in \mathcal{G}$, meaning that it is required that

$$((\mathbf{x}_0, t_0), (\phi_x(t_f; \mathbf{x}_0, \mathbf{p}_0^*, t_0))) \in \mathcal{G}$$

or

$$((\phi_x(t_0; \mathbf{x}_f, \mathbf{p}_f^*, t_f)), (\mathbf{x}_f, t_f)) \in \mathcal{G}$$

To ensure that the boundary conditions are satisfied, either $\mathbf{p}_0^*$ or $\mathbf{p}_f^*$ must be found. The initial or final adjoints of an optimal trajectory $(\mathbf{x}(t)^*, \mathbf{p}^*(t))$ must also satisfy the transversality conditions

$$\begin{aligned} \mathbf{p}_0^* &= -\frac{\partial V}{\partial \mathbf{x}_0}^T - \frac{\partial \mathbf{g}}{\partial \mathbf{x}_0}^T \boldsymbol{\lambda} \\ \mathcal{H}_0 &= \frac{\partial \mathcal{H}}{\partial t_0} + \frac{\partial \mathbf{g}}{\partial t_0} \boldsymbol{\lambda} \\ \mathbf{p}_f^* &= \frac{\partial V}{\partial \mathbf{x}_f}^T + \frac{\partial \mathbf{g}}{\partial \mathbf{x}_f}^T \boldsymbol{\lambda} \\ \mathcal{H}_f &= -\frac{\partial \mathcal{H}}{\partial t_f} - \frac{\partial \mathbf{g}}{\partial t_f} \boldsymbol{\lambda} \end{aligned} \tag{2.11}$$

where $V(\mathbf{x}_0, t_0, \mathbf{x}_f, t_f)$ is an initial / final cost term and has been assumed to be incorporated into the Lagrangian, forcing $\partial V / \partial(\mathbf{x}_0, t_0, \mathbf{x}_f, t_f) = 0$. The variables $\boldsymbol{\lambda} \in \mathbb{R}^r$ are Lagrange multipliers associated with enforcing the boundary conditions $\mathbf{g}(\mathbf{x}_0, t_0, \mathbf{x}_f, t_f) = \mathbf{0}$. The transversality conditions are necessary conditions of optimality on $\mathbf{p}_0^*$ or $\mathbf{p}_f^*$ given boundary conditions and costs on the state. If both $\mathbf{x}_0$ and $\mathbf{x}_f$ are fully constrained by $\mathbf{g}$, then $\mathbf{p}_0^*$ and $\mathbf{p}_f^*$ are completely undetermined and the transversality conditions can not help determine $\mathbf{p}_0^*$ and $\mathbf{p}_f^*$. Alternately, if the boundary conditions on the state are not fully specified (some of the initial or final state elements have positive degrees of freedom), then due to the transversality conditions some elements of $\mathbf{p}_0^*$ and/or $\mathbf{p}_f^*$ will be identically zero. H. Yan et. al. [30] have also examined the optimal control policies in the state and adjoint for LQR-type performance functions, of which the control distance Lagrangian in (2.4) is a special case. Both the UTPBVP and the MRBVP solution approaches presented in following subsections use the optimal control policy (2.8) as well as the dynamics along optimal trajectories shown in (2.9) and (2.10). The UTPBVP and MRBVP approaches are now discussed sequentially.

2.1.3 Uncertain Two-Point Boundary Value Problem (UTPBVP)

2.1.3.1 Problem Definition

The problem under consideration is illustrated in Figure 2.1. In this scenario, an initial object track consisting of a sequence of observations ultimately produces a state estimate $\mathbf{x}_0$ and an associated estimate covariance $\mathbf{P}_0$ (corresponding to some arbitrary time t_0). We define this track UCT_0 as the triplet $(t_0, \mathbf{x}_0, \mathbf{P}_0)$. At some later time t_f, a new object track is initiated based on new observations. After all of the new observations are collected an estimate of the state and covariance from when the new track was first started (at time t_f) can be generated, creating the new UCT_f triplet $(t_f, \mathbf{x}_f, \mathbf{P}_f)$.

Supposing now that multiple initial and final UCTs exist, the problem of determining which UCTs should be associated (or 'paired') with one another must be addressed, potentially requiring propulsive thrusts. One way to do this is do compute a measure of how 'expensive' a maneuver between UCTs would be. A logical assumption would be that UCTs with the smallest required connecting control effort should be paired to one another, as on-orbit fuel is a scarce commodity [P2]. This concept is very similar to comparing differences in propagated homogeneous states $\mathbf{x}_{f,p}$ to new UCT states $\mathbf{x}_f$, as if $\mathbf{x}_{f,p} \approx \mathbf{x}_f$, the minimum optimal control is necessarily $\mathbf{u}^*(t) \approx \mathbf{0}$, yielding a control distance of $d_C = 0$ (the Strictly Positive metric property).

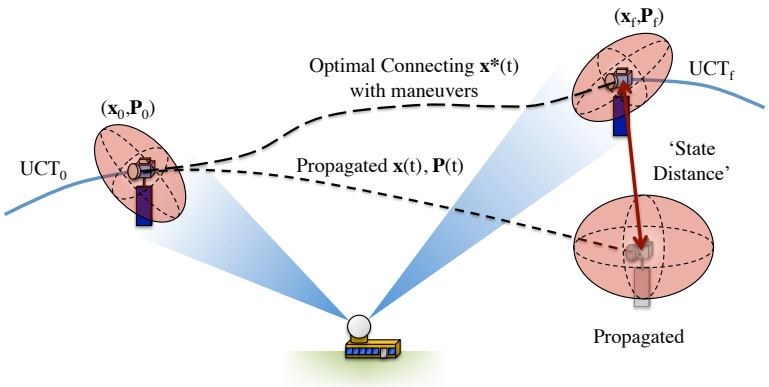

Figure 2.1: UTPBVP Illustration

Since operational boundary conditions are estimates with uncertainty distributions, the resulting distribution of the performance metric P must be determined.

2.1.3.2 Optimal Control Distance Metric Distribution

Now a nominal optimal trajectory $(\mathbf{x}_n(t), \mathbf{u}_n(t))$ connecting the nominal boundary conditions $\mathbf{x}_0$ and $\mathbf{x}_f$ is assumed (which may be numerical), and is expressed as

$$\mathbf{x}_n(t) = \boldsymbol{\phi}_x(t; \mathbf{x}_0, \mathbf{p}_0, t_0)$$

$$\mathbf{p}_n(t) = \boldsymbol{\phi}_p(t; \mathbf{x}_0, \mathbf{p}_0, t_0)$$

for times up to and including t_f. In a manner similar to that of linear systems, the effect of random initial and final states $\mathbf{X}_0$ and $\mathbf{X}_f$ are considered. If the trajectory space surrounding the nominal optimal trajectory $(\mathbf{x}_n(t), \mathbf{p}_n(t))$ is linearized, then linear variations in the boundary conditions may be examined algebraically. Taking the Taylor series expansion of $\mathbf{x}_n(t)$ and $\mathbf{p}_n(t)$ with respect to variations in $\mathbf{x}_0$ and $\mathbf{p}_0$:

$$\mathbf{x}_n(t) + \delta\mathbf{x}(t) = \boldsymbol{\phi}_x(t; \mathbf{x}_0, \mathbf{p}_0, t_0) + \frac{\partial \boldsymbol{\phi}_x}{\partial \mathbf{x}_0}\delta\mathbf{x}_0 + \frac{\partial \boldsymbol{\phi}_x}{\partial \mathbf{p}_0}\delta\mathbf{p}_0 + O(\delta^2)$$

$$\mathbf{p}_n(t) + \delta\mathbf{p}(t) = \boldsymbol{\phi}_p(t; \mathbf{x}_0, \mathbf{p}_0, t_0) + \frac{\partial \boldsymbol{\phi}_p}{\partial \mathbf{x}_0}\delta\mathbf{x}_0 + \frac{\partial \boldsymbol{\phi}_p}{\partial \mathbf{p}_0}\delta\mathbf{p}_0 + O(\delta^2)$$

Keeping only first order variations and realizing that $\mathbf{x}(t) - \boldsymbol{\phi}_x(t; \mathbf{x}_0, \mathbf{p}_0, t_0) = \mathbf{0}$ and $\mathbf{p}(t) - \boldsymbol{\phi}_p(t; \mathbf{x}_0, \mathbf{p}_0, t_0) = \mathbf{0}$, the state transition matrix is produced:

$$\begin{bmatrix} \delta\mathbf{x}(t) \\ \delta\mathbf{p}(t) \end{bmatrix} = \begin{bmatrix} \boldsymbol{\Phi}_{xx}(t, t_0) & \boldsymbol{\Phi}_{xp}(t, t_0) \\ \boldsymbol{\Phi}_{px}(t, t_0) & \boldsymbol{\Phi}_{pp}(t, t_0) \end{bmatrix} \begin{bmatrix} \delta\mathbf{x}_0 \\ \delta\mathbf{p}_0 \end{bmatrix} \tag{2.12}$$

For this local linear approximation it is assumed that both $\delta\mathbf{x}_0$ and $\delta\mathbf{x}_f$ are given, requiring $\delta\mathbf{p}_0$ and $\delta\mathbf{p}_f$ to be determined fully, as the transversality conditions (2.11) do not provide further information. Evaluating (2.12) at $t = t_f$ the following solutions for $\delta\mathbf{p}_0$ and $\delta\mathbf{p}_f$ are found:

$$\delta\mathbf{p}_0 = \begin{bmatrix} -\boldsymbol{\Phi}_{xp}(t_f, t_0)^\dagger \boldsymbol{\Phi}_{xx}(t_f, t_0) & \boldsymbol{\Phi}_{xp}(t_f, t_0)^\dagger \end{bmatrix} \begin{bmatrix} \delta\mathbf{x}_0 \\ \delta\mathbf{x}_f \end{bmatrix}$$

$$\delta\mathbf{p}_f = \begin{bmatrix} \boldsymbol{\Phi}_{px}(t_f, t_0) - \boldsymbol{\Phi}_{pp}(t_f, t_0)\boldsymbol{\Phi}_{xp}(t_f, t_0)^\dagger \boldsymbol{\Phi}_{xx}(t_f, t_0) & \boldsymbol{\Phi}_{pp}(t_f, t_0)\boldsymbol{\Phi}_{xp}(t_f, t_0)^\dagger \end{bmatrix} \begin{bmatrix} \delta\mathbf{x}_0 \\ \delta\mathbf{x}_f \end{bmatrix}$$

The symbol † is defined as the pseudo-inverse operation. Also, for $t_0 \le t \le t_f$, the adjoint variation $\delta\mathbf{p}(t)$ may be found by solving

$$\delta\mathbf{p}(t) = \left[\boldsymbol{\Phi}_{px}(t,t_0) - \boldsymbol{\Phi}_{pp}(t,t_0)\boldsymbol{\Phi}_{xp}(t_f,t_0)^{\dagger}\boldsymbol{\Phi}_{xx}(t_f,t_0)\ \boldsymbol{\Phi}_{pp}(t,t_0)\boldsymbol{\Phi}_{xp}(t_f,t_0)^{\dagger}\right]\begin{bmatrix}\delta\mathbf{x}_0\\ \\ \delta\mathbf{x}_f\end{bmatrix}$$
$$= \boldsymbol{\Lambda}(t,t_0)\begin{bmatrix}\delta\mathbf{x}_0\\ \\ \delta\mathbf{x}_f\end{bmatrix}$$

Note that some of the state transition matrix portions are computed over the interval $[t_0, t]$ while others are computed over $[t_0, t_f]$. After this computation, there now exists a function $\boldsymbol{\Lambda}(t,t_0)$ that maps variations in the initial and final states to variations in the adjoint $\delta\mathbf{p}(t)$ at time t. Since the optimal control is defined in terms of the adjoint, linear variations in the control are written as

$$\mathbf{u}^*(t) = \mathbf{u}_n(t) + \delta\mathbf{u}(t) \approx -\frac{\partial\mathbf{f}}{\partial\mathbf{u}}^T(\mathbf{p}_n(t) + \delta\mathbf{p}(t))$$

Because $\mathbf{u}_n(t) = -\frac{\partial\mathbf{f}}{\partial\mathbf{u}}^T\mathbf{p}_n(t)$, the linear variation in the control is:

$$\delta\mathbf{u}(t) = -\frac{\partial\mathbf{f}}{\partial\mathbf{u}}^T\boldsymbol{\Lambda}(t,t_0)\begin{bmatrix}\delta\mathbf{x}_0\\ \\ \delta\mathbf{x}_f\end{bmatrix}$$

Recall that $\partial\mathbf{f}/\partial\mathbf{u}$ is evaluated along the nominal optimal trajectory $(\mathbf{x}_n(t), \mathbf{u}_n(t))$. Returning now to the performance function P defined in (2.4),

$$P = \frac{1}{2}\int_{t_0}^{t_f}\mathbf{u}^*(\tau)^T\mathbf{u}^*(\tau)d\tau,$$

and substituting $\mathbf{u}^*(\tau) = \mathbf{u}_n(\tau) + \delta\mathbf{u}(\tau)$, the performance function becomes

$$P = \frac{1}{2}\int_{t_0}^{t_f}\mathbf{u}_n(\tau)^T\mathbf{u}_n(\tau)d\tau$$
$$+\int_{t_0}^{t_f}\mathbf{u}_n(\tau)^T\frac{\partial\mathbf{f}}{\partial\mathbf{u}}^T\boldsymbol{\Lambda}(\tau,0)\delta\mathbf{z}d\tau$$
$$+\frac{1}{2}\int_{t_0}^{t_f}\delta\mathbf{z}^T\boldsymbol{\Lambda}(\tau,0)^T\frac{\partial\mathbf{f}}{\partial\mathbf{u}}\frac{\partial\mathbf{f}}{\partial\mathbf{u}}^T\boldsymbol{\Lambda}(\tau,0)\delta\mathbf{z}d\tau$$

where $\delta\mathbf{z}^T = \left[\delta\mathbf{x}_0^T\ \delta\mathbf{x}_f^T\right] \in \mathbb{R}^{2n}$. The variable $\delta\mathbf{z}$ does not depend on τ, so the following definitions are made:

$$d_C = \frac{1}{2}\int_{t_0}^{t_f}\mathbf{u}_n(\tau)^T\mathbf{u}_n(\tau)d\tau, \tag{2.13}$$

$$\boldsymbol{\omega}(t_f, t_0) = \int_{t_0}^{t_f} \boldsymbol{\Lambda}(\tau, 0)^T \frac{\partial \mathbf{f}}{\partial \mathbf{u}} \mathbf{u}_n(\tau) d\tau, \tag{2.14}$$

and

$$\boldsymbol{\Omega}(t_f, t_0) = \frac{1}{2} \int_{t_0}^{t_f} \boldsymbol{\Lambda}(\tau, 0)^T \frac{\partial \mathbf{f}}{\partial \mathbf{u}} \frac{\partial \mathbf{f}}{\partial \mathbf{u}}^T \boldsymbol{\Lambda}(\tau, 0) d\tau, \tag{2.15}$$

Note that d_C is the control distance metric of the nominal optimal trajectory $(\mathbf{x}_n(t), \mathbf{p}_n(t))$ without boundary condition variations. The performance index P is

$$P = d_C + \boldsymbol{\omega}(t_f, t_0)^T \delta\mathbf{z} + \delta\mathbf{z}^T \boldsymbol{\Omega}(t_f, t_0) \delta\mathbf{z}$$

The approximation of P in the linear space about $(\mathbf{x}_n(t), \mathbf{p}_n(t))$ is a quadratic form in terms of the boundary condition variations, $\delta\mathbf{z}$.

2.1.3.3 Uncertain Boundary Conditions

From §2.1.3.1, $\delta\mathbf{z}$ may be treated as the realization of a Gaussian random vector $\delta\mathbf{Z} \in N(\mathbf{0}, \mathbf{P}_z)$, where

$$\mathbb{E}\left[\delta\mathbf{Z}\delta\mathbf{Z}^T\right] = \mathbf{P}_z = \begin{bmatrix} \mathbf{P}_0 & \mathbf{0} \\ \mathbf{0} & \mathbf{P}_f \end{bmatrix}$$

Note that if different distributions for the boundary conditions are used, the preceding results are still valid. Rewriting the performance function as a scalar random variable the following form is obtained:

$$P = d_C + \boldsymbol{\omega}(t_f, t_0)^T \delta\mathbf{Z} + \delta\mathbf{Z}^T \boldsymbol{\Omega}(t_f, t_0) \delta\mathbf{Z} \tag{2.16}$$

The quadratic form shown in (2.16) is an intuitive result, as if the variations in the boundary conditions are reduced to zero, $P = d_C$. Similarly, if the uncertainty in the boundary conditions is large, one would expect the distribution of P to diffuse. From Appendix A.2, the exact expected value $\mathbb{E}[P]$ may be written in a more intuitive form as

$$\mu_P = d_C + \mathrm{Tr}\left[\boldsymbol{\Omega}\mathbf{P}_z\right] \tag{2.17}$$

Similarly, the second moment may be written as

$$\sigma_P^2 = \boldsymbol{\omega}^T \mathbf{P}_z \boldsymbol{\omega} + 2\mathrm{Tr}\left[\boldsymbol{\Omega}\mathbf{P}_z\boldsymbol{\Omega}\mathbf{P}_z\right] \tag{2.18}$$

If third and higher moments are ignored, then the distribution of P may be modeled as a Gaussian distribution P_G with $P_G \in N(\mu_P, \sigma_P^2)$. Now, the question of computing the distribution of P using higher moments arises.

Because (2.16) has a quadratic form, existing theory involving quadratic forms of normal random variables may be applied. To apply existing results (see Appendix A.1) P must be transformed into a standard non-central quadratic form, after which Pearson's Approximation [31] may be used to capture the first three moments of the true distribution of P. Note that in the special case that $\boldsymbol{\omega} = \mathbf{0}$ and the eigenvalues of $\boldsymbol{\Omega}$ are all 0 or 1, the control distance is exactly a χ^2_v distribution with degree v equal to the number of unity eigenvalues [31].

2.1.4 Measurement Residual Boundary Value Problem (MRBVP)

2.1.4.1 Measurement Model

Figure 2.2 describes elements composing the MRBVP approach. At time t_0 the previous observation ends and an observation gap begins. The nominal state $\mathbf{x}_0 = \mathbf{x}(t_0)$ and uncertainty $\mathbf{P}_0 = \mathbf{P}(t_0)$ is propagated over the interval $t \in [t_0, t_f]$ to time t_f, generating the homogeneous state $\mathbf{x}_h$ and uncertainty $\mathbf{P}_h$. The expected measurement is computed using the sensor measurement model to be $\mathbf{y} = \mathbf{h}(\mathbf{x}_h)$, where $\mathbf{y} \in \mathbb{R}^s$. The sensor measurement $\mathbf{y}_m$ is taken, and the measurement residual is defined as $\delta\mathbf{y} = \mathbf{y}_m - \mathbf{y} = \mathbf{y}_m - \mathbf{h}(\mathbf{x}_h)$. The space surrounding the homogeneous trajectory $\mathbf{x}_h(t)$ is linearized, and the measurement residual is decomposed into three constituent residuals due to 1) state uncertainty in $\delta\mathbf{x}_h$, 2) sensor uncertainty η_m, and 3) state deviations due to active control $\delta\mathbf{x}_{u,f}$. The linearization is written as

$$\mathbf{y}_m \approx \mathbf{y} + \delta\mathbf{y} = \mathbf{h}(\mathbf{x}_h) + \frac{\partial \mathbf{h}}{\partial \mathbf{x}_h}\delta\mathbf{x}_h + \frac{\partial \mathbf{h}}{\partial \mathbf{x}_h}\delta\mathbf{x}_{u,f} + \eta_m$$

For homogeneous trajectories about the linearized trajectory without process noise the final state deviation $\delta\mathbf{x}_h$ may be written in terms of the initial state deviation as $\delta\mathbf{x}_h = \boldsymbol{\Phi}_{xx}(t_f, t_0)\delta\mathbf{x}_{h,0}$. Defining $\partial\mathbf{h}/\partial\mathbf{x}_h = \mathbf{H} \in \mathbb{R}^{s\times n}$ and observing that $\mathbf{y} = \mathbf{h}(\mathbf{x}_h)$, the residual is defined in the local linearization about $\mathbf{x}_h$ as

$$\delta\mathbf{y} = \mathbf{H}\boldsymbol{\Phi}_{xx}(t_f, t_0)\delta\mathbf{x}_{h,0} + \mathbf{H}\delta\mathbf{x}_{u,f} + \eta_m \tag{2.19}$$

It is important to understand that there is no model uncertainty under this formulation; any modeling errors will contribute to the total observable control distance. Note that in traditional applications without

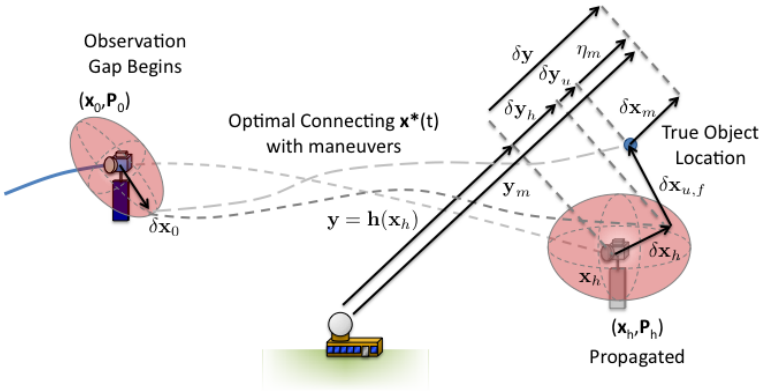

Figure 2.2: MRBVP Definition and Measurement Model

a state deviation due to control ($\delta\mathbf{x}_{u,f} = \mathbf{0}$), the expected variance of the measurement residual is

$$\begin{aligned}\mathrm{Var}[\delta\mathbf{y}_h] = \mathbf{P}_{y,h} &= \mathbb{E}\left[\delta\mathbf{y}_h\delta\mathbf{y}_h^T - \mathbb{E}\left[\delta\mathbf{y}_h\right]\mathbb{E}\left[\delta\mathbf{y}_h\right]^T\right] \\ &= \mathbb{E}\big[\mathbf{H}\boldsymbol{\Phi}_{xx}(t_f,t_0)\delta\mathbf{x}_{h,0}\delta\mathbf{x}_{h,0}^T\boldsymbol{\Phi}_{xx}(t_f,t_0)^T\mathbf{H}^T \\ &\quad + \mathbf{H}\boldsymbol{\Phi}_{xx}(t_f,t_0)\delta\mathbf{x}_{h,0}\eta_m^T + \eta_m\eta_m^T\big] \\ &= \mathbf{H}\boldsymbol{\Phi}_{xx}(t_f,t_0)\mathbf{P}_0\boldsymbol{\Phi}_{xx}(t_f,t_0)^T\mathbf{H}^T + \mathbf{R}\end{aligned}$$

where $\mathbb{E}\left[\delta\mathbf{x}_{h,0}\delta\mathbf{x}_{h,0}^T\right] = \mathbf{P}_0$ and $\mathbb{E}\left[\eta_m\eta_m^T\right] = \mathbf{R}$. $\mathbf{P}_{y,h}$ is the Kalman filter pre-update measurement residual covariance, and is often used in conjunction with the Mahalanobis distance to determine whether a new measurement is statistically probable given the modeled systemic uncertainty.

2.1.4.2 Incorporation of the Measurement Model

The homogeneous solution $\mathbf{x}_h(t)$ is now assumed to be integrated. Also, the adjoint for the homogeneous solution is guaranteed to be $\mathbf{0}$ over $t \in [t_0, t_f]$. Both $\mathbf{x}_h(t)$ and $\mathbf{p}_h(t)$ are written as

$$\mathbf{x}_h(t) = \boldsymbol{\phi}_x(t; \mathbf{x}_0, \mathbf{p}_0 = \mathbf{0}, t_0)$$

$$\mathbf{p}_h(t) = \mathbf{0} = \boldsymbol{\phi}_p(t; \mathbf{x}_0, \mathbf{p}_0 = \mathbf{0}, t_0)$$

To account for deviations due to active control in the state and adjoint, a Taylor expansion about the homogeneous trajectory is again examined. The expansion becomes

$$\mathbf{x}_u(t) \approx \mathbf{x}_h(t) + \delta\mathbf{x}_u(t) = \boldsymbol{\phi}_x(t; \mathbf{x}_0, \mathbf{p}_0 = \mathbf{0}, t_0) + \frac{\partial\boldsymbol{\phi}_x}{\partial\mathbf{x}_0}\delta\mathbf{x}_{u,0} + \frac{\partial\boldsymbol{\phi}_x}{\partial\mathbf{p}_0}\delta\mathbf{p}_{u,0} + O(\delta^2)$$

$$\mathbf{p}_u(t) \approx \mathbf{p}_h(t) + \delta\mathbf{p}_u(t) = \boldsymbol{\phi}_p(t; \mathbf{x}_0, \mathbf{p}_0 = \mathbf{0}, t_0) + \frac{\partial \boldsymbol{\phi}_p}{\partial \mathbf{x}_0}\delta\mathbf{x}_{u,0} + \frac{\partial \boldsymbol{\phi}_p}{\partial \mathbf{p}_0}\delta\mathbf{p}_{u,0} + O(\delta^2)$$

Keeping only first order variations and realizing that $\mathbf{x}_h(t) - \boldsymbol{\phi}_x(t; \mathbf{x}_0, \mathbf{p}_0 = \mathbf{0}, t_0) = \mathbf{0}$ and $\mathbf{p}_h(t) - \boldsymbol{\phi}_p(t; \mathbf{x}_0, \mathbf{p}_0 = \mathbf{0}, t_0) = \mathbf{0}$, the state transition matrix is produced:

$$\begin{bmatrix} \delta\mathbf{x}_u(t) \\ \delta\mathbf{p}_u(t) \end{bmatrix} = \begin{bmatrix} \boldsymbol{\Phi}_{xx}(t, t_0) & \boldsymbol{\Phi}_{xp}(t, t_0) \\ \boldsymbol{\Phi}_{px}(t, t_0) & \boldsymbol{\Phi}_{pp}(t, t_0) \end{bmatrix} \begin{bmatrix} \delta\mathbf{x}_{u,0} \\ \delta\mathbf{p}_{u,0} \end{bmatrix}$$

The measurement equation (2.19) is now considered a final state constraint on the local linear problem in $\delta\mathbf{x}_u(t_f) = \delta\mathbf{x}_{u,f}$ of the form

$$\mathbf{g}_f(\delta\mathbf{x}_{u,f}, t_f) = \mathbf{H}\delta\mathbf{x}_{u,f} + \mathbf{H}\boldsymbol{\Phi}_{xx}(t_f, t_0)\delta\mathbf{x}_{h,0} + \eta_m - \delta\mathbf{y} = \mathbf{0}$$

where $\mathbf{g}_f \in \mathbb{R}^s$, and $\delta\mathbf{x}_{h,0}$, η_m, and $\delta\mathbf{y}$ are considered given. Applying the transversality conditions (2.11) generates

$$\delta\mathbf{p}_{u,f} = \frac{\partial \mathbf{g}_f}{\partial \delta\mathbf{x}_{u,f}}^T \boldsymbol{\lambda} = \mathbf{H}^T\boldsymbol{\lambda}$$

with $\boldsymbol{\lambda} \in \mathbb{R}^s$ being the Lagrange multiplier associated with enforcing the final state constraint described by the measurement equation (2.19). As with the UTPBVP the goal here is to determine the local optimal control policy $\delta\mathbf{u}(t)$ over the interval $t \in [t_0, t_f]$. To do so, the variation in the adjoint $\delta\mathbf{p}_u(t)$ must first be determined. Because the initial state deviation due to active control is $\delta\mathbf{x}_{u,0} = \mathbf{0}$ by construction, the initial adjoint may be written as

$$\delta\mathbf{p}_{u,0} = \boldsymbol{\Phi}_{pp}(t_f, t_0)^{-1}\delta\mathbf{p}_{u,f} = \boldsymbol{\Phi}_{pp}(t_f, t_0)^{-1}\mathbf{H}^T\boldsymbol{\lambda}$$

The state change due to active control at the final time t_f is

$$\delta\mathbf{x}_{u,f} = \boldsymbol{\Phi}_{xp}(t_f, t_0)\boldsymbol{\Phi}_{pp}(t_f, t_0)^{-1}\mathbf{H}^T\boldsymbol{\lambda}$$

Substituting $\delta\mathbf{x}_{u,f}$ into $\mathbf{g}_f(\delta\mathbf{x}_{u,f}, t_f)$ generates

$$\mathbf{H}\boldsymbol{\Phi}_{xp}(t_f, t_0)\boldsymbol{\Phi}_{pp}(t_f, t_0)^{-1}\mathbf{H}^T\boldsymbol{\lambda} + \mathbf{H}\boldsymbol{\Phi}_{xx}(t_f, t_0)\delta\mathbf{x}_{h,0} + \eta_m - \delta\mathbf{y} = \mathbf{0}$$

If $\text{rank}(\mathbf{H}) = s$, then $\mathbf{H}\boldsymbol{\Phi}_{xp}(t_f, t_0)\boldsymbol{\Phi}_{pp}(t_f, t_0)^{-1}\mathbf{H}^T$ is invertible (and the inverse is equivalent to the pseudoinverse). Solving for $\boldsymbol{\lambda}$:

$$\boldsymbol{\lambda} = \left(\mathbf{H}\boldsymbol{\Phi}_{xp}(t_f, t_0)\boldsymbol{\Phi}_{pp}(t_f, t_0)^{-1}\mathbf{H}^T\right)^{-1}\left[-\mathbf{H}\boldsymbol{\Phi}_{xx}(t_f, t_0)\delta\mathbf{x}_{h,0} - \eta_m + \delta\mathbf{y}\right]$$

yielding

$$\delta\mathbf{p}_{u,0} = \mathbf{\Phi}_{pp}(t_f,t_0)^{-1}\mathbf{H}^T\left(\mathbf{H}\mathbf{\Phi}_{xp}(t_f,t_0)\mathbf{\Phi}_{pp}(t_f,t_0)^{-1}\mathbf{H}^T\right)^{-1}\left[-\mathbf{H}\mathbf{\Phi}_{xx}(t_f,t_0)\delta\mathbf{x}_{h,0} - \eta_m + \delta\mathbf{y}\right]$$

The adjoint as a function of time may be written as

$$\delta\mathbf{p}_u(t) = \mathbf{\Lambda}_{0,\eta}(t,t_0)\delta\mathbf{w} + \mathbf{\Lambda}_y(t,t_0)\delta\mathbf{y}$$

where

$$\delta\mathbf{w}^T = \begin{bmatrix} \delta\mathbf{x}_{h,0}^T & \eta_m^T \end{bmatrix}$$

$$\mathbf{\Lambda}_{0,\eta}(t,t_0)$$

$$= \mathbf{\Phi}_{pp}(t,t_0)\mathbf{\Phi}_{pp}(t_f,t_0)^{-1}\mathbf{H}^T\left(\mathbf{H}\mathbf{\Phi}_{xp}(t_f,t_0)\mathbf{\Phi}_{pp}(t_f,t_0)^{-1}\mathbf{H}^T\right)^{-1}\begin{bmatrix} -\mathbf{H}\mathbf{\Phi}_{xx}(t_f,t_0) & -\mathbb{I}_{s\times s} \end{bmatrix}$$

$$\mathbf{\Lambda}_y(t,t_0) = \mathbf{\Phi}_{pp}(t,t_0)\mathbf{\Phi}_{pp}(t_f,t_0)^{-1}\mathbf{H}^T\left(\mathbf{H}\mathbf{\Phi}_{xp}(t_f,t_0)\mathbf{\Phi}_{pp}(t_f,t_0)^{-1}\mathbf{H}^T\right)^{-1}$$

The optimal control law $\mathbf{u}^*$ is approximated by $\mathbf{u}^* \approx \mathbf{u}_h + \delta\mathbf{u} = \delta\mathbf{u}$, yielding

$$\mathbf{u}^* \approx -\frac{\partial\mathbf{f}}{\partial\mathbf{u}}^T\mathbf{\Lambda}_{0,\eta}(t,t_0)\delta\mathbf{w} - \frac{\partial\mathbf{f}}{\partial\mathbf{u}}^T\mathbf{\Lambda}_y(t,t_0)\delta\mathbf{y}$$

Substituting this back into the control distance performance function (2.4) yields

$$\begin{aligned} P = \int_{t_0}^{t_f}\Bigg[&\frac{1}{2}\delta\mathbf{w}^T\mathbf{\Lambda}_{0,\eta}(\tau,0)^T\frac{\partial\mathbf{f}}{\partial\mathbf{u}}\frac{\partial\mathbf{f}}{\partial\mathbf{u}}^T\mathbf{\Lambda}_{0,\eta}(\tau,0)\delta\mathbf{w} \\ &+\delta\mathbf{y}^T\mathbf{\Lambda}_y(\tau,0)^T\frac{\partial\mathbf{f}}{\partial\mathbf{u}}\frac{\partial\mathbf{f}}{\partial\mathbf{u}}^T\mathbf{\Lambda}_{0,\eta}(\tau,0)\delta\mathbf{w} \\ &+\frac{1}{2}\delta\mathbf{y}^T\mathbf{\Lambda}_y(\tau,0)^T\frac{\partial\mathbf{f}}{\partial\mathbf{u}}\frac{\partial\mathbf{f}}{\partial\mathbf{u}}^T\mathbf{\Lambda}_y(\tau,0)\delta\mathbf{y}\Bigg]d\tau \end{aligned}$$

Realizing that neither $\delta\mathbf{w}$ nor $\delta\mathbf{y}$ depend on time, both vectors are factored out of the integration operation. To simplify notation, the following definitions are made:

$$\mathbf{G}_{ww} = \int_{t_0}^{t_f}\frac{1}{2}\mathbf{\Lambda}_{0,\eta}(\tau,0)^T\frac{\partial\mathbf{f}}{\partial\mathbf{u}}\frac{\partial\mathbf{f}}{\partial\mathbf{u}}^T\mathbf{\Lambda}_{0,\eta}(\tau,0)d\tau \tag{2.20}$$

$$\mathbf{G}_{yw} = \int_{t_0}^{t_f}\mathbf{\Lambda}_y(\tau,0)^T\frac{\partial\mathbf{f}}{\partial\mathbf{u}}\frac{\partial\mathbf{f}}{\partial\mathbf{u}}^T\mathbf{\Lambda}_{0,\eta}(\tau,0)d\tau \tag{2.21}$$

$$\mathbf{G}_{yy} = \int_{t_0}^{t_f}\frac{1}{2}\mathbf{\Lambda}_y(\tau,0)^T\frac{\partial\mathbf{f}}{\partial\mathbf{u}}\frac{\partial\mathbf{f}}{\partial\mathbf{u}}^T\mathbf{\Lambda}_y(\tau,0)d\tau \tag{2.22}$$

This allows the control distance performance function P to be written as

$$P = \delta\mathbf{y}^T\mathbf{G}_{yy}\delta\mathbf{y} + \delta\mathbf{y}^T\mathbf{G}_{yw}\delta\mathbf{w} + \delta\mathbf{w}^T\mathbf{G}_{ww}\delta\mathbf{w}$$

which is a quadratic form in two vector variables ($\delta\mathbf{w}$ and $\delta\mathbf{y}$). Note that the deterministic optimal control distance metric d_C for the MRBVP is $d_C = \delta\mathbf{y}^T\mathbf{G}_{yy}\delta\mathbf{y}$.

2.1.4.3 Uncertain Boundary Conditions and Measurements

As discussed in §2.1.4.1 and §2.1.4.2, $\delta\mathbf{x}_{h,0}$ and η_m are considered random variables $\delta\mathbf{X}_{h,0}$ and η_m, respectively. The random variables $\delta\mathbf{X}_{h,0}$ and η_m are now assumed to have the following statistical properties

$$\mathbb{E}\left[\delta\mathbf{X}_{h,0}\right] = \mathbf{0}$$

$$\mathbb{E}\left[\eta_m\right] = \mathbf{0}$$

and

$$\mathrm{Var}\left[\delta\mathbf{X}_{h,0}\right] = \mathbb{E}\left[\delta\mathbf{X}_{h,0}\delta\mathbf{X}_{h,0}^T - \mathbb{E}\left[\delta\mathbf{X}_{h,0}\right]\mathbb{E}\left[\delta\mathbf{X}_{h,0}\right]^T\right] = \mathbf{P}_0$$

$$\mathrm{Var}\left[\eta_m\right] = \mathbb{E}\left[\eta_m\eta_m^T - \mathbb{E}\left[\eta_m\right]\mathbb{E}\left[\eta_m\right]^T\right] = \mathbf{R}$$

The vector $\delta\mathbf{w}$ is now allowed to be a random variable $\delta\mathbf{W}$, which has the statistical properties

$$\mathbb{E}\left[\delta\mathbf{W}\right] = \mathbf{0}$$

$$\mathrm{Var}\left[\delta\mathbf{W}\right] = \begin{bmatrix} \mathbf{P}_0 & \mathbf{0} \\ \mathbf{0} & \mathbf{R} \end{bmatrix} = \mathbf{P}_W$$

Note that the initial state covariance matrix $\mathbf{P}_0$ and the measurement uncertainty matrix $\mathbf{R}$ are uncorrelated. The measurement residual at the time of measurement is deterministic, so the control distance performance function may be written as a random variable of the form

$$P = \delta\mathbf{y}^T\mathbf{G}_{yy}\delta\mathbf{y} + \delta\mathbf{y}^T\mathbf{G}_{yw}\delta\mathbf{W} + \delta\mathbf{W}^T\mathbf{G}_{ww}\delta\mathbf{W} \tag{2.23}$$

Which is a random variable with a quadratic form in $\delta\mathbf{W}$. Examining (2.23) it is clear that it has the same quadratic form as (2.16), allowing the same approach used in the UTPBVP case to be used to compute and/or approximate the control distance metric distribution. Leveraging the results in Appendix A.2, the MRBVP distribution has a mean and variance of

$$\mu_P = d_C + \mathrm{Tr}\left[\mathbf{G}_{ww}\mathbf{P}_W\right]$$

$$\sigma_P^2 = \delta\mathbf{y}^T\mathbf{G}_{yw}\mathbf{P}_W\mathbf{G}_{yw}^T\delta\mathbf{y} + 2\mathrm{Tr}\left[\mathbf{G}_{ww}\mathbf{P}_W\mathbf{G}_{ww}\mathbf{P}_W\right]$$

It is now illustrative to examine several boundary cases of (2.23).

- **Case 1: $\delta\mathbf{y} \to \mathbf{0}$.** In this situation there is precisely zero measurement residual between the predicted measurement and the actual measurement. The control distance random variable P reduces to

$$P = \delta\mathbf{W}^T\mathbf{G}_{ww}\delta\mathbf{W}$$

which is not identically zero, and has positive finite probability density over $[0, \infty)$. The mean and variance reduce to

$$\mu_P = \mathrm{Tr}\left[\mathbf{G}_{ww}\mathbf{P}_W\right]$$

$$\sigma_P^2 = 2\mathrm{Tr}\left[\mathbf{G}_{ww}\mathbf{P}_W\mathbf{G}_{ww}\mathbf{P}_W\right]$$

This is because even though the residual is identically zero, it is possible that the initial state uncertainty and measurement uncertainty may have exactly canceled the necessary control effort. The control distance distribution must be positive to account for systemic uncertainty. Note that the probability of this case occurring is $\mathbb{P}\left[\delta\mathbf{y} = \mathbf{0}\right] = 0$.

- **Case 2: $\mathbf{P}_W \to \mathbf{0}$.** This case corresponds to a situation with perfect state and measurement knowledge. The control distance P becomes

$$P = d_C = \delta\mathbf{y}^T\mathbf{G}_{yy}\delta\mathbf{y}$$

In this case the uncertainty has been completely removed from the problem and the apparent control distance $P = d_C$ is now a deterministic function of the projected state discrepancy onto the sensor measurement space.

- **Case 3: $\delta\mathbf{y} \to \mathbf{0}$ and $\mathbf{P}_W \to \mathbf{0}$.** In this scenario, both the measurement residual and the system uncertainty are identically zero. The control distance reduces to $P = 0$ as one would intuitively expect.

Because (2.16) has a quadratic form, existing theory involving quadratic forms of normal random variables may be applied. As with the UTPBVP, to apply existing results (see Appendix A.1) P must be transformed into a standard non-central quadratic form. Once in this form Pearson's Approximiation may be used.

2.1.5 Stochastic Dominance

The task of sensibly ranking probability distributions is confounded by the fact that many distributions have positive finite densities over their entire intervals, which often have significant overlap. Thus, there is a finite positive probability that a random variable X with a 'smaller' distribution with have a larger realized value x than a realized random variable y with a 'larger' distribution. Figure 2.3(a) illustrates such a situation

in which there is a nontrivial control distance distribution overlap between two different hypothetical UCT pairings. The concept of stochastic dominance gives a framework with which one may sensibly rank random variable distributions. The following definition and results are summarized from Meucci [32].

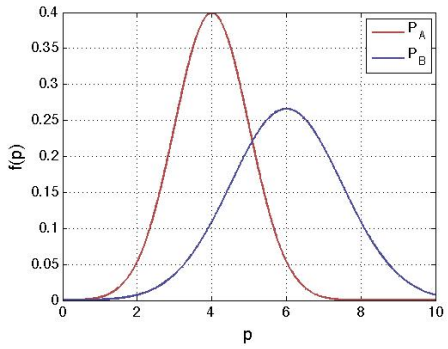

(a) Example of overlapping Control Distance PDFs. Note that there exists a finite and non-trivial probability that either UCT pairing may be correct.

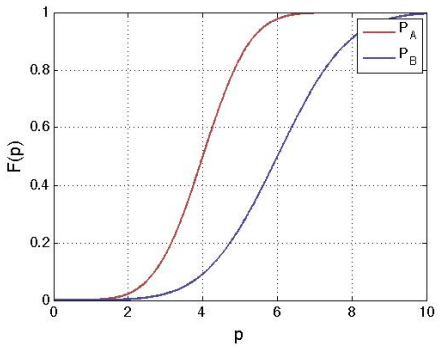

(b) CDF of overlapping Control Distances. Pairing A is clearly more sensible than pairing B

Figure 2.3: Illustrative PDF and CDF of two candidate UCT Pairings

The question now faced is how to rank UCT pairings sensibly. Figure 2.3(b) illustrates how a UCT pairing may rationally be made. Ideally, for every performance function value of $0 < p < \infty$, $F_A(p) > F_B(p)$. This is equivalent to choosing an arbitrary p and guaranteeing that $\mathbb{P}[P_A \leq p] \geq \mathbb{P}[P_B \leq p]$. In words, this means that it is more likely that UCT pairing A has a smaller control distance than UCT pairing B *for all possible control distances.* This is called stochastic dominance, formally defined below:

Definition 2.1.1. ***Order-q Stochastic Dominance:***

The distribution $f_A(p)$ is said to ***order-q dominate*** *the distribution $f_B(p)$ if, for all $p \in [0, \infty]$, the following inequality holds:*

$$\mathcal{I}^q[f_A(p)] \geq \mathcal{I}^q[f_B(p)] \tag{2.24}$$

where the operator $\mathcal{I}[\cdot]$ is the integration operator over $p \in [0, \infty)$. If $q = 1$ ($F_A(p) \geq F_B(p)$), distribution $f_A(p)$ is said to weakly dominate $f_B(p)$.

Brief inspection of (2.24) shows us that order q dominance implies order $q + 1$ dominance. Starting

with $q = 0$, this gives the following result

$$0\text{-dom} \Rightarrow 1\text{-dom} \Rightarrow \cdots \Rightarrow \text{q-dom}$$

Since 0-dom does not typically occur, the first order dominance that can reasonably be expected is $q = 1$. Order $q = 1$ dominance is equivalent to the Cumulative Distribution Function (CDF) of the distribution of N_a being strictly less that the CDF of the random variable N_b. Orders higher than $q = 1$ do not always have a clear, intuitive meaning. In general, there is no guarantee that there exists an order q such that any two distributions may be consistently ranked.

2.1.6 Maneuver Detection

A critical question to resolve when considering candidate UCT pairings in the UTPBVP or MRBVP problems is whether a maneuver has occurred or the computed control distance distribution is completely the consequence of systemic uncertainty. It is argued here that assigning a probability to whether a maneuver occurred or not may require additional non-quantitative information and is out of the scope of this analysis. It is however possible to assign a probability that the nominal deterministic control distance d_C (the control distance in the absence of system uncertainty) is not explained by the modeled dynamics and uncertainty. Said differently, given a distribution of control distances based purely on the uncertainty of the boundary conditions or measurements, it is possible to determine the probability that the nominal cost is greater than the system uncertainty. This is distinct from determining the probability that a maneuver has occurred, and is in many ways similar to the traditional Mahanobis distance approach. If the probability that d_C is larger than the systemic uncertainty, then it is quite likely that an un-modeled disturbance, possibly a maneuver, has occurred.

The approach outlined in the UTPBVP and MRBVP frameworks generates two important pieces of information that may be used to detect maneuvers. Both performance distance metrics may be written in the following form:

$$P = l + \mathbf{m}^T\mathbf{V} + \mathbf{V}^T\mathbf{N}\mathbf{V} \tag{2.25}$$

where $\mathbf{V} \in \mathbb{R}^r$ is a zero-mean ($\mathbb{E}[\mathbf{V}] = \mathbf{0}$) random variable with distribution $f_v(\mathbf{v})$, $l \geq 0$, $l \in \mathbb{R}$, $\mathbf{m} \in \mathbb{R}^r$, and

$\mathbf{N} \in \mathbb{S}^{+,r\times r}$. The nominal deterministic control distance is defined as $d_C = l$, and the systemic uncertainty is re-defined as a random variable $P_u = \mathbf{m}^T\mathbf{V} + \mathbf{V}^T\mathbf{N}\mathbf{V}$ with distribution $P_u \in f_u(p_u)$. The distance metric distribution may then be written as $P = d_C + P_u$. To address the issue of detecting a possible maneuver two assumptions are first made and then a null hypothesis H_0 is formed.

(1) The initial and final state/measurement estimate distributions are unbiased.

(2) In the absence of truth knowledge, it is assumed that $d_C \approx d_{C,true}$. The nominal control distance d_C is considered a working analog for the true distance $d_{C,true}$.

The null hypothesis H_0 is $P_u \geq d_C$. This is equivalent to stating that if a specific instantiation p_u of the systemic noise $P_u \in f_u(p)$ is greater than the deterministic control distance of the mean case d_C, then H_0 is true. The probability that H_0 is true is defined as

$$p_0 = \mathbb{P}\left[H_0 \text{ is true}\right] = \mathbb{P}\left[P_u \geq d_C\right]$$

Note that choosing d_C in the above equation is purely arbitrary, and other thresholds may be viewed as engineering design parameters. The converse hypothesis H_1 that $P_u \leq d_C$ - that d_C is larger than an instantiated value p_u of the systemic noise - may be written as

$$\begin{aligned} p_1 &= \mathbb{P}\left[H_1 \text{ is true }\right] = \mathbb{P}\left[H_0 \text{ is not true}\right] \\ &= 1 - \mathbb{P}\left[P_u \geq d_C\right] = \mathbb{P}\left[P_u \leq d_C\right] \end{aligned}$$

because $p_0 + p_1 = 1$. The probability p_1 that H_1 is true may be rewritten as

$$p_1 = \mathbb{P}\left[P_u \leq d_C\right] = \int_{-\infty}^{d_C} f_u(p_u)dp_u \tag{2.26}$$

To interpret what $p_1 \in [0, 1)$ means and what conditions lead to specific values of p_1, nominal and boundary cases are briefly examined.

- p_1 is small: This occurs when the nominal control distance is quite small in relation to the systemic uncertainty P_u. The probability that d_C is not explained by the system uncertainty is small. In other words, the nominal control distance d_C is not anomalous.

- p_1 is large: Conversely, this occurs when the nominal control distance d_C is large in relation to the systemic uncertainty distribution $f_u(p_u)$. The system uncertainty does not explain the deterministic control distance and the object in question may have executed a maneuver.

- $d_C \approx \mathbb{E}[P_u]$: When $d_C \approx \mathbb{E}[P_u]$ either H_0 or H_1 may be true with $p_0 \approx p_1$. In this situation, if a maneuver did occur, it may not be detectable, or at the very best, may be on the threshold of detectibility.

The probability p_1 that d_C is not explained by the distriubtion $f_u(p_u)$ is at this point completely general, subject to the linearization about the nominal optimal trajectory $(\mathbf{x}_n(t), \mathbf{p}_n(t))$ or $(\mathbf{x}_h(t), \mathbf{0})$. Operationally, for each UCT correlation and for each measurement residual computation using the UTPBVP or MRBVP framework, an anomalous probability threshold p_a may be defined. If $p_1 \geq p_a$, then the deterministic control distance for the problem is insufficiently explained by the homogeneous dynamics and uncertainty inherent in the boundary conditions / measurements. Such a case can be flagged for further analysis.

Computing the expected value $\mathbb{E}[P_u]$ can provide an intuitive lower limit on the detectible control distance. Below this value $p_0 > 0.5$, and it is more likely that the control distance from the inherent system uncertainty is larger than any maneuver that may have occurred. Note that, as with choosing how p_0 is constructed and the value of the anomaly probability threshold p_a, choosing $p_0 > 0.5$ is an engineering design parameter that must be chosen in the context of systems level design criterion.

2.1.6.1 Gaussian Uncertainty

If $\mathbf{V}$ has a zero-mean Gaussian distribution, then it may also be shown that

$$\mu_u = \mathbb{E}[P_u] = \mathrm{Tr}[\mathbf{N}\mathbf{P}_V]$$
$$\sigma_u^2 = \mathbb{E}\left[(P_u - \mathbb{E}[P_u])^2\right] = \mathbf{m}^T\mathbf{P}_V\mathbf{m} + 2\mathrm{Tr}[\mathbf{N}\mathbf{P}_V\mathbf{N}\mathbf{P}_V]$$

Thus, the minimum maneuver detectibility threshold $d_{C,d,min}$ is defined here as

$$d_{C,d,min} = \mathrm{Tr}[\mathbf{N}\mathbf{P}_V] \tag{2.27}$$

Using the Cauchy-Schwartz inequality (2.6), an upper bound on the minimum detectible $\Delta V_{d,min}$ can be computed:

$$\Delta V_{d,min} = \sqrt{2(t_f - t_0)\mathrm{Tr}\left[\mathbf{N}\mathbf{P}_V\right]} \tag{2.28}$$

Equations (2.27) and (2.28) are particularly useful as they capture the effects of the boundary condition uncertainties (whether full state uncertainties or measurements), local dynamics (about the linearized connecting trajectories), geometries, and observation gaps to give an operator an upper bound on the minimum detectible control cost (either $d_{C,d,min}$ or $\Delta V_{d,min}$). Calculating such a detection threshold can help operators make tasking decisions or guide engineering efforts during sensor system development and placement.

2.2 Simulation and Results

The computation of the control distance distribution is first validated for the UTPBVP problem, then the UTPBVP and MRBVP approaches are individually illustrated with examples in this section. Simulations were written in MATLAB and used un-perturbed Keplerian dynamics, but could be developed for general perturbed dynamics as well.

2.2.1 Validation: Single Object Control Distance Distribution

To verify that the theoretical results accurately represent the true distribution of the performance function a scenario with a single initial and final UCT is examined. The mean and covariance of UCT_0 and UCT_f are described in Table 2.1. A 400 km altitude circular orbit is used as the reference orbit for the Hill frame. The initial and final covariances $\mathbf{P}_0$ and $\mathbf{P}_f$ for each coordinate $\mathbf{x}_0$ and $\mathbf{x}_f$ are formed as a diagonal

Table 2.1: Verification Test Case Boundary Conditions and Associated Uncertainty

Coordinate	$\mathbf{x}_0$	σ_0	$\mathbf{x}_f$	σ_f
Radial - r (m)	0	1	0	1
Along-Track - s (m)	-100	1	100	1
Cross-Track - w (m)	0	1	50	1
Radial - $\dot{r}$ (m/s)	0	0.05	0	0.05
Along-Track - $\dot{s}$ (m/s)	0	0.05	0	0.05
Cross-Track - $\dot{w}$ (m/s)	0	0.05	0	0.05

covariance matrix of the form

$$\mathbf{P} = \text{diag}\left(\left[\begin{array}{cccccc} \sigma_r^2 & \sigma_s^2 & \sigma_w^2 & \sigma_{\dot{r}}^2 & \sigma_{\dot{w}}^2 & \sigma_{\dot{w}}^2 \end{array}\right]\right)$$

The time interval under consideration is $[t_0, t_f] = [0, 0.5]$ orbits. Four methods are used to verify the theory developed in this paper:

- *Monte Carlo Simulation ('Truth'):* Individual realizations of the distribution of $\mathbf{X}_0 \in N(\mathbf{x}_0, \mathbf{P}_0)$ and $\mathbf{X}_0 \in N(\mathbf{x}_0, \mathbf{P}_0)$ are randomly generated and simulated. 10,000 simulations are run, their control distance is determined, and the composite numerical PDF and CDF is computed.

- *Gaussian Approximation:* The Gaussian approximation (2.17) and (2.18) discussed in §2.1.3 is generated and the corresponding PDF and CDF are analytically determined.

- *Sampled Distribution:* The known boundary condition distribution of $\delta\mathbf{Z} \in N(\mathbf{0}, \mathbf{P}_z)$ is instantiated and the corresponding control distance realization computed according to (2.16). 100,000 realizations are generated and the corresponding PDF and CDF approximations are determined.

- *Pearson's Approximation:* Given computed values for $\boldsymbol{\omega}(t_f, t_0)$ and $\boldsymbol{\Omega}(t_f, t_0)$, Pearson's Approximation is used to generate the first three moments of the true distribution.

The Monte Carlo (method 1) results are considered 'Truth' for the purposes of this validation. Figures 2.5(a) and 2.5(b) show the verification results of the PDF and CDF using methods 1-4 outlined above.

The Gaussian approximation of the distribution agrees nicely with the Monte Carlo results. It is clear that not all of the PDF or CDF is captured, as the Monte Carlo PDF has a 'long tail' and absolutely zero probability for $P < 0$, where the Gaussian approximation has neither attribute. However, the Gaussian approximation CDF matches very nicely with all other validation curves. The sampled distribution found by directly generating $\delta\mathbf{Z} \in N(\mathbf{0}, \mathbf{P}_z)$ and computing each corresponding realization p matched the Monte Carlo results very closely. As expected, $\mathbb{P}[P < 0] = 0$, and the sampled distribution exhibited a 'long tail' very similar to the Monte Carlo simulations. Lastly, Pearson's Approximation appears to do an excellent job of approximating the Monte Carlo and sampled distributions of the control distance.

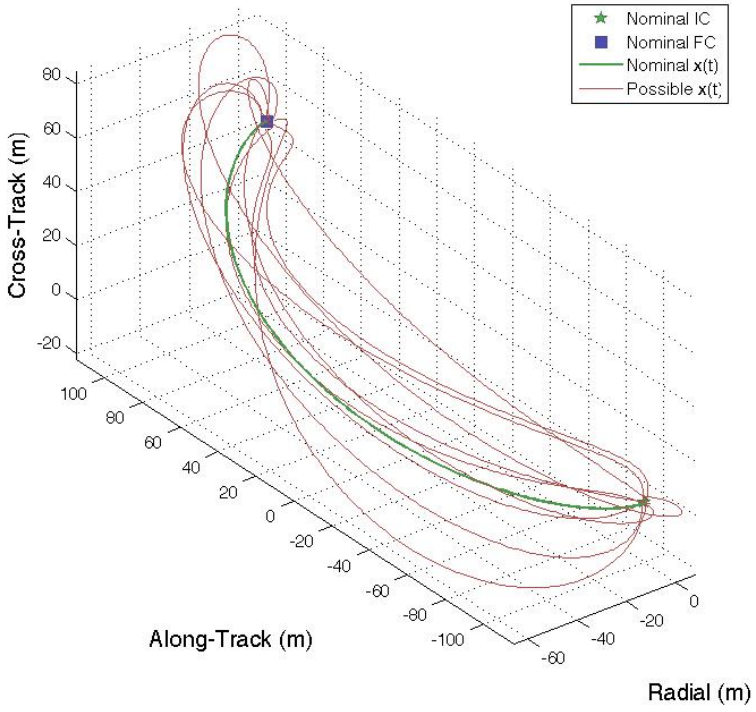

Figure 2.4: Nominal trajectory for the validation test case. 10 representative optimal trajectories from the Monte Carlo simulations are shown to demonstrate the variation in the optimal trajectory paths.

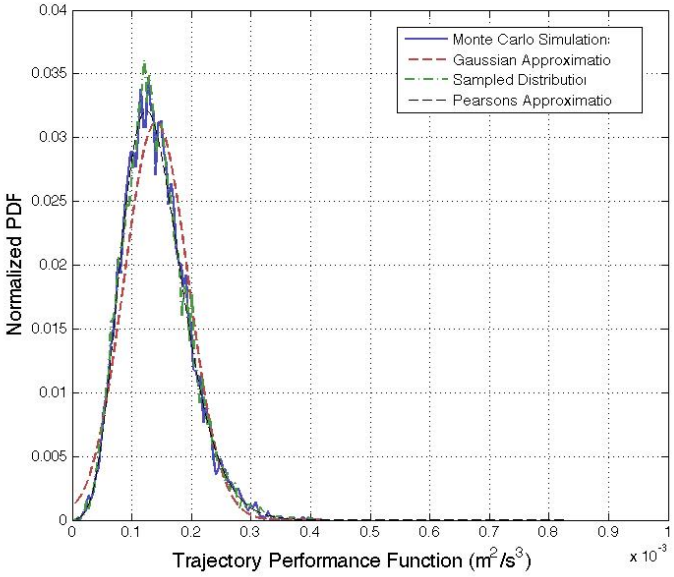

(a) Computed PDF

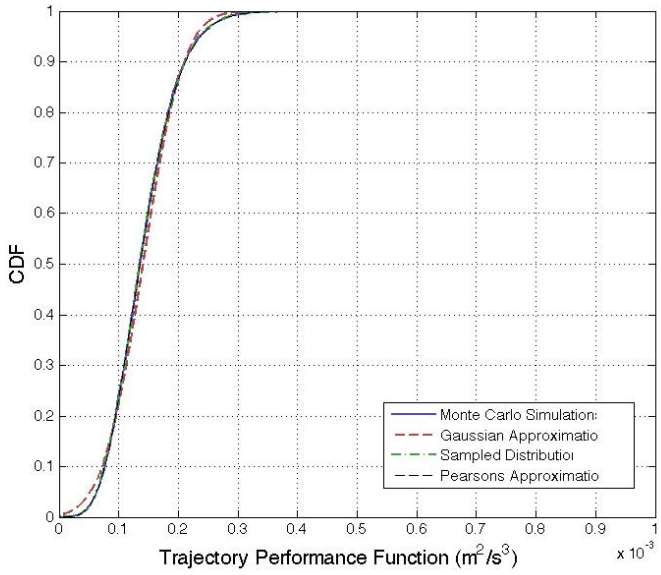

(b) Computed CDF

Figure 2.5: Validation of PDF and CDF Computation Methodologies.

2.2.2 Example 2.1: Geostationary Cluster Cross-Tagging

This example is inspired by Intelsat constellation TLE cross-tagging [33]. The scenario involves a two-spacecraft cluster in GEO in which the first spacecraft executes a small maneuver ($\text{UCT}_{0,1}$ executes a 5 m/s impulsive maneuver in the inertial z direction). It is assumed that each spacecraft has been tracked long enough before the maneuver so that they have nominal pre-maneuver ephemeris estimates. Because changes in observation angles may not be significant during or immediately after an orbit maintenance maneuver at GEO, this scenario assumes that the maneuver occurs immediately after observation ends. New observations are made starting the next available observation period, approximately 14 hours later and continue over the next several days. Collected observations are used to generate post-maneuver UCTs for both spacecraft. After both the initial and final UCTs are formed the objective is then to compute the control distance distributions for each individual association as well as the combined control distance distributions for mutually exclusive cases.

Table 2.2 shows the initial orbit elements, Table 2.3 shows the uncertainties for each UCT, and Table 2.4 describes the mutually exclusive association combinations to be examined. The nominal adjoints $\mathbf{p}_n(t)$ were found using a shooting-based Newton-method descent and the control distance distributions were computed using Pearson's Approximation. Figure 2.6 depicts the optimal connecting trajectories between each combination of initial and final UCTs. Table 2.5 enumerates the detectible maneuver threshold, the nominal connecting trajectory distance, and the probability that the nominal control distance is larger than the systemic uncertainty for each candidate correlation. Figure 2.7(a) shows the associated control distance metric distribution CDF for each combination and Figure 2.7(b) shows the combined control metric CDFs for each mutually exclusive case.

Table 2.2: Example 2.1 initial orbit elements for both satellites

$\mathbf{oe}$	$\mathbf{oe}_{0,1}$	$\mathbf{oe}_{0,2}$
a (km)	42,086	42,086
e ()	0.0005	0.0005
i (deg)	0.05	0.05
Ω (deg)	0	0
ω (deg)	0	0
f (deg)	0	-0.1

Table 2.3: Example 2.1 geostationary cluster Initial and final UCT Uncertainties

ECI Unc.	$\mathrm{UCT}_{0,1}$	$\mathrm{UCT}_{0,2}$	$\mathrm{UCT}_{f,1}$	$\mathrm{UCT}_{f,2}$
σ_x (m)	100	100	50	25
σ_y (m)	50	100	75	50
σ_z (m)	75	100	75	75
$\sigma_{\dot{x}}$ (m/s)	0.5	0.5	0.75	0.25
$\sigma_{\dot{y}}$ (m/s)	1.0	1.0	1.25	0.5
$\sigma_{\dot{z}}$ (m/s)	1.0	1.0	1.25	0.5

Table 2.4: Example 2.1 object association case descriptions

Case	**Pairing**	**Associations**
1	a	$\mathrm{UCT}_{0,1} \rightarrow \mathrm{UCT}_{f,1}$
	b	$\mathrm{UCT}_{0,2} \rightarrow \mathrm{UCT}_{f,2}$
2	a	$\mathrm{UCT}_{0,1} \rightarrow \mathrm{UCT}_{f,2}$
	b	$\mathrm{UCT}_{0,2} \rightarrow \mathrm{UCT}_{f,1}$

Table 2.5: Example 2.1 maneuver detection quantities

	$\Delta V_{d,min}$ (m/s)	ΔV_C (m/s)	p_1
1-a	4.416	6.697	0.819
1-b	3.167	0.068	0.000
2-a	3.168	3.961	0.732
2-b	4.416	7.818	0.883

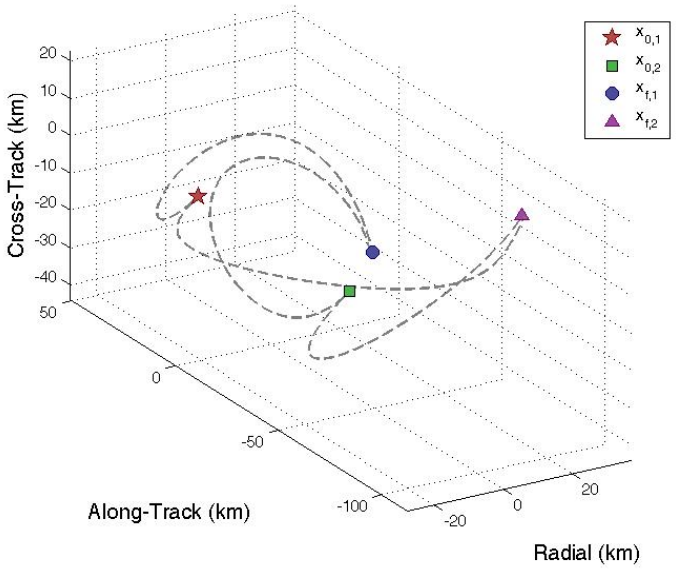

Figure 2.6: Example 2.1 candidate optimal connecting trajectories in a rotating Hill frame (circular reference orbit, a = 42,086 km, i = 0 deg)

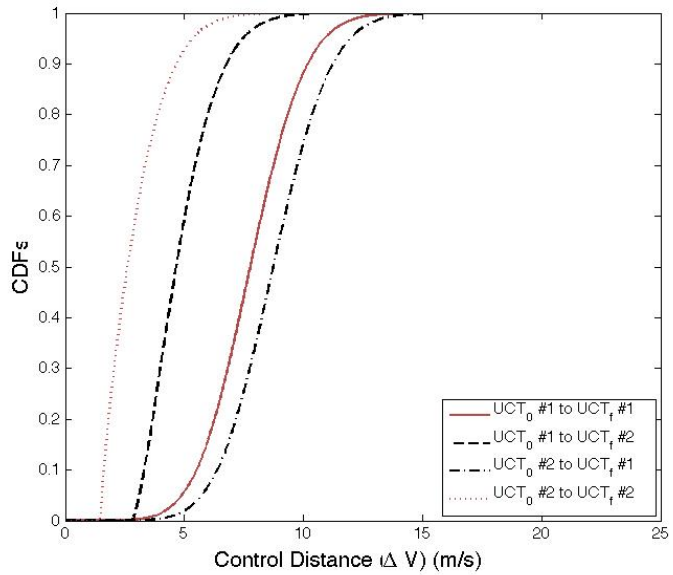

(a) Individual control distances in terms of ΔV

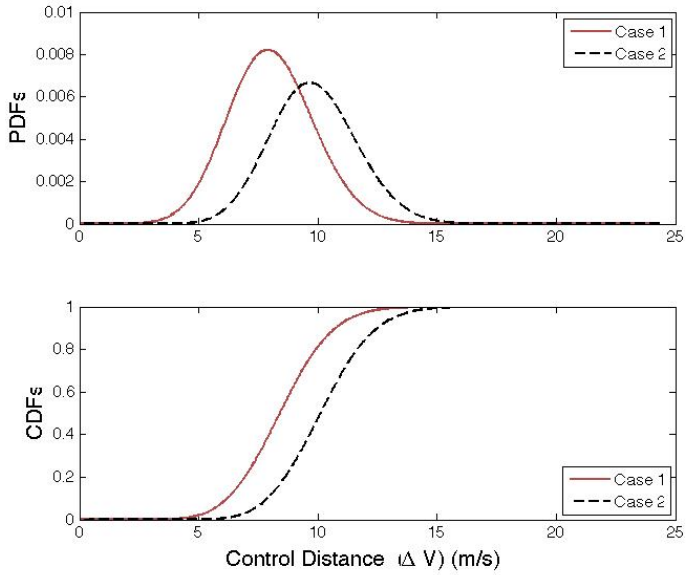

(b) Mutually exclusive control distances for cases 1 and 2 in terms of ΔV.

Figure 2.7: Example 2.1 control distance distributions for candidate connecting trajectories and mutually exclusive association cases

Examining Figure 2.7(a) it is clear that connecting either $\mathrm{UCT}_{0,1}$ or $\mathrm{UCT}_{0,2}$ to $\mathrm{UCT}_{f,1}$ (the final state following the 5 m/s ΔV inclination maneuver) pushes the control distance distributions right by at least 5 m/s, as well as further diffuses the distribution. This is as expected as $\mathrm{UCT}_{f,1}$ possesses larger uncertainties

in both position and velocity. There is no large difference due to changes in the along-track direction when compared to the rather large inclination maneuver. However, the control distance metric differential due to the combined along-track maneuver is large enough for Figure 2.7(b) to exhibit a lower cost for Case 1 (as found by applying Definition 2.1.1), which is known to be the truth. Examining the CDF shown in Figure 2.7(b) also indications that mean ΔV distance is slightly more than 8 m/s. While at first this seems large with respect to the known size of the impulse (5 m/s), it is important to realize that the mean control metric distance of 8 m/s is for all possible combinations of boundary conditions, each of which has a 1-σ magnitude of approximately 1 m/s. In this context the mean control metric distance of 8 m/s matches our intuition.

2.2.3 Example 2.2: Geostationary Maneuver Detection

Real-time maneuver detection is illustrated in this example by examining scenario in which a GEO spacecraft executes a small North-South maneuver to correct for an inclination error of 0.25 degrees. Before the maneuver an observer is assumed to be filtering optical measurements of the object and propagating an estimate and covariance in real-time. To correct the spacecraft inclination error an impulsive maneuver immediately after time t_0 of $\Delta V = 13.4$ m/s is executed, unknown to the observer. The maneuver occurs immediately after the observer's filter processes its last measurement. The time between the initial maneuver (which is also the time of the previous measurement and filter update) and the next measurement is $\Delta t = t_f - t_0 = 42$ hours. The satellite initial orbit elements are $\mathbf{oe}_0 = [a, e, i, \Omega, \omega, f] =$ [42086 km, 0, 0.25 deg, 0 deg, 0 deg, 0 deg]. The state uncertainty of the geostationary satellite at time t_0 is $\sigma_x = 40$ m, $\sigma_y = 20$ m, $\sigma_z = 20$ m, $\sigma_{\dot{x}} = 3.0$ m/s, $\sigma_{\dot{y}} = 1.5$ m/s, and $\sigma_{\dot{z}} = 1.5$ m/s. The optical measurement uncertainty at the final time t_f is $\sigma_m = 5$ arcseconds. The observing ground station is located where the inertial x axis intersects the surface of the Earth at time t_f. The measurement equation for the optical boresight azimuth β and elevation γ is then

$$\begin{bmatrix} \beta \\ \gamma \end{bmatrix} = \mathbf{y} = \mathbf{h}(\mathbf{x}) = \begin{bmatrix} \tan^{-1}\left(\frac{y}{\sqrt{(x-R_e)^2+y^2+z^2}}\right) \\ \tan^{-1}\left(\frac{z}{\sqrt{(x-R_e)^2+y^2+z^2}}\right) \end{bmatrix} \tag{2.29}$$

Because the measurement residual $\delta\mathbf{y} = \mathbf{y}_m - \mathbf{h}(\mathbf{x})$ is a random variable that is realized for each measurement (it is considered constant for each measurement and control metric distribution computation cycle), distributions corresponding to several residuals must be computed. The measurement residuals for the maneuvering case is enumerated in Table 2.6

Table 2.6: Example 2.2 measurement residuals at $t_f = 42$ hours

	nominal	σ-point 1	σ-point 2	σ-point 3	σ-point 4
$\delta\beta$ (rad)	2.46e-05	2.46e-05	2.46e-05	4.89e-05	3.86e-07
$\delta\gamma$ (rad)	4.33e-03	4.36e-03	4.31e-03	4.33e-03	4.33e-03

Figure 2.8 plots Pearson's Approximation of the control distance distribution. The traditional approach to maneuver detection would compute the Mahalanobis distance of the pre-update residual. In the

absence of process noise the covariance used to compute the Mahalanobis distance is

$$\text{Var}\left[\delta\mathbf{y}\right] = \mathbf{H}\mathbf{\Phi}_{xx}(t_f, t_0)\mathbf{P}_0\mathbf{\Phi}_{xx}(t_f, t_0)^T\mathbf{H}^T + \mathbf{R}$$

In the nominal case with the ΔV maneuver, the Mahalanobis distance is M-D = 8.92, well into the region in which Mahalanobis-based methods would detect the maneuver (though not characterize the maneuver).

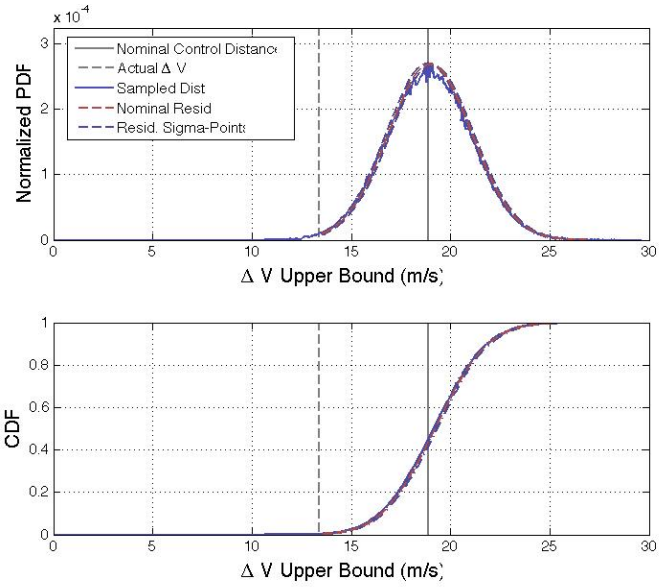

Figure 2.8: Example 2.2 control distance Probability Density Function (PDF) and Cumulative Distribution Functions (CDFs). The vertical black line is the true maneuver magnitude, The vertical dashed-grey line is the nominal control distance in ΔV space ΔV_C, the red and dashed-blue lines are the nominal and sigma-point control distance distributions found using Pearson's Approximation, and the green line is the sampled distribution with $N = 100,000$.

For illustrative purposes, if there were no maneuver and the measurement residual were precisely zero, the control distance distribution would be as shown in Figure 2.9.

The distribution of the systemic uncertainty is compared directly with the nominal control distance d_C in Figure 2.10. The probability that the deterministic control distance d_C is greater than the system uncertainty is $p_1 = \mathbb{P}\left[P_u \leq d_C\right] \approx 0.99981$. The nominal performance in ΔV-space is $\Delta V_C = 18.9$ m/s, the upper bound on the minimum detectible ΔV is $\Delta V_{d,min} = 3.6$ m/s, and the true maneuver size is $\Delta V = 13.4$ m/s. The mean ΔV distance including systemic uncertainty is $\mathbb{E}\left[\Delta V\right] = 19.2$ m/s. Examining this data, one can conclude that because p_1 is large, it is likely that the deterministic portion of the control distance

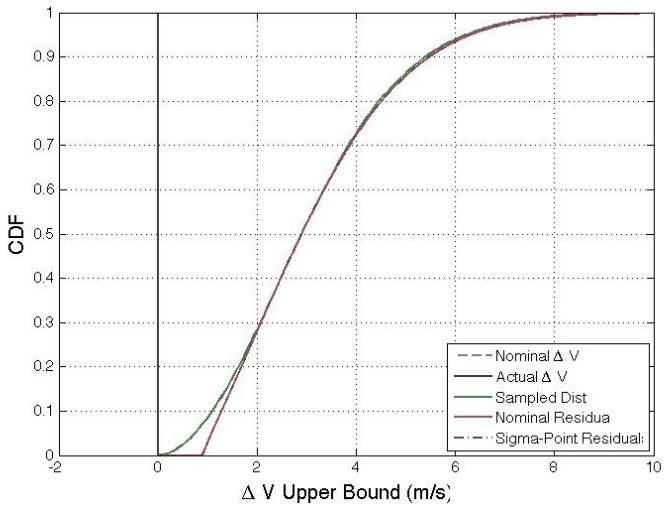

Figure 2.9: Example 2.2 control distance CDF for a non-maneuvering spacecraft. Both the true maneuver and nominal control distance are precisely zero.

is not an artifact of the systemic noise and that a maneuver may have occurred.

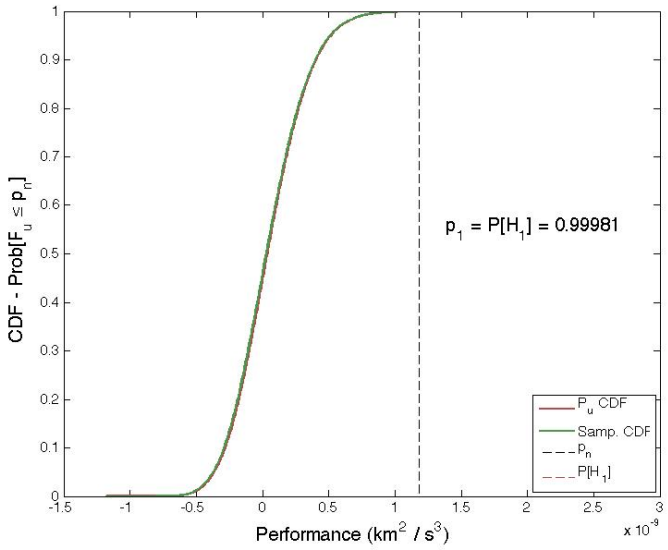

Figure 2.10: A direct comparison of the deterministic control distance d_C and the systemic uncertainty represented by the random variable P_u. The probability that H_1 is true is computed as p_1 = 0.95688, indicating that the d_C is very likely too large to be an artifact of systemic uncertainty; it is likely that either the object maneuvered or there are unmodeled perturbations at work.

As indicated by the discussion for this example, the approach used for the MRBVP generates a

control distance distribution that incorporates the inherent system uncertainty and has metric and optimality guarantees. It should however be emphasized that the method is only capable of detecting maneuvers that are observable (based on the observation geometry, dynamics, observation gap duration, etc.).

2.3 Chapter Summary

In this chapter performance indices are leveraged to use trajectory optimality itself to quantify the optimal control distance metric between a homogeneous trajectory and a given optimal trajectory connecting two boundary conditions. In general, a large class of performance functions are shown to have the same properties as distance metrics. Hamiltonian-based optimal control approaches are used to determine the optimal control policy given system dynamics. The Uncertain Two-Point Boundary Value Problem (UTPBVP) is defined and with uncertain boundary conditions shown to have a control distance metric distribution that is a quadratic form. The UTPBVP is further shown to be a potential approach to assist in Uncorrelated Track (UCT)-based object correlation. Real-time maneuver detection and characterization is shown to be supported by the Measurement Residual Boundary Value Problem (MRBVP), which measures the control metric distance distribution based on partial state boundary conditions generated by measurement residuals. The approach is found to generate control distance distributions based on observable state changes. Stochastic dominance is introduced and its utility in comparing control distance distributions is discussed. Hypothesis testing is invoked to generate probabilities that the deterministic control distance in the trajectory is too large to be explained by systemic uncertainty. In cases where this probability is high it is likely that a maneuver may have occurred. The general uncertain boundary condition approach and subsequent control distance distribution approximation is validated using Monte Carlo approaches and direct sampling of the random boundary conditions. A numerical example inspired by operational cross-tagging problems in geosynchronous orbit demonstrates how the UTPBVP approach may be leveraged to correlate objects correctly. A second example is given showing how real-time measurement residuals may be used to both detect and characterize maneuvers.

Chapter 3

Computing Reachability Set Subspaces

Intercept reachability sets, defined here as the position subspace of a full state reachability set, has tremendous utility in strategic and tactical SSA applications. As discussed briefly in the introduction, computation of the full reachability set, from which the intercept reachability set can be determined, is hampered by dimensionality-related computation issues. Position subpsace reachability sets can also support object search efforts. If the control authority of an object is known, the position set of the object must necessarily contain the object and can therefore be used to identify specific regions of space in which to search for the object. This chapter investigates alternate analytical formalisms to compute the intercept reachability subspace without computing the full state reachability set, thereby reducing or avoiding dimensionality-driven computational issues.

Reachability theory provides a robust framework in which controller synthesis may be evaluated for both capability and safety. Because a reachable set contains every possible trajectory of a system, it can account for a large class of control failure modes and is also an appropriate metric of control capability. In aerospace systems applications such as vehicle collision avoidance, operational safety planning, and capability demonstration are directly related to reachability set computation, and can benefit immensely from reductions in the computation requirements for computing such sets. In particular the problem of correlating orbiting objects executing un-observed maneuvers may benefit greatly by bounding search regions to within computed reachable sets

The theory supporting formalized reachability has been extensively developed in controls literature and may be directly derived from optimal control theory [34, 35, 36, 37, 38]. Computing the reachability set

for a given system involves satisfying the dynamic programming principle and/or solving the HamiltonJacobi Bellman partial differential equation (HJB PDE), which has direct analogs in solving general optimal control problems. Traditional applications of reachability theory have focused on continuous differential systems, and have since been further generalized to apply to a variety of additional problems. Several of these applications will be discussed, followed by a motivation for and summary of the contents of this paper.

Reachability theory has been successfully applied to differential game settings, specifically to aircraft mid-air collision avoidance where one aircraft is avoiding another [39] and to automated aerial refueling [40]. In both applications the controller attempts to accomplish goals whilst an adversarial control (either an adversary or worst-case disturbance) attempts to move the system towards an 'un-safe' configuration.

Hybrid system control applications have leveraged reachable set computation for control synthesis [41] and safety validation [42]. Reachability theory has also been applied to hybrid systems in a differential game setting [43], further widening its applicability.

Direct analytical computation of reachable sets is difficult and has motivated significant research aimed at determining which classes of systems may be analytically solved as well as various numerical techniques to reduce the computation burden and generate over/under-approximated reachability sets. Research into whether an analytical solution exists for a given reachability problem has demonstrated that some classes of dynamics may be analytically computed, specifically linear integrator or pure undamped oscillator systems [44]. Further, some problems have been found to be reducible to geometric problems based on insight into the propagation of the dynamics [45]. For systems with polynomial equations of motion it has been shown that reachability problems can be re-cast as a sum of squares formulation using barrier certificates and solved either directly or iteratively [46].

Over-approximations of reachable sets are desirable as they are typically performed in the context of system safety, where conservative reachability set computations are useful for risk reduction. For multi-affine systems it has been demonstrated that the state-space may be partitioned iteratively using rectangles to effeciently generate overapproximations of the reachable state-space [47]. Polytopic reachability sets, which have straightforward parameterization and computation, have been shown to provide accurate conservative outer bounds for linear and norm-bounded nonlinear systems [34, 48]. Vast improvement in over-approximated

reachability set computation efficiencies has been realized for linear systems using zonotopes [49] and support functions [50]. Similar work has computed reachability sets for nonlinear systems by linearizing at each propagation step and conservatively accounting for uncertainty, also generating conservative over-approximations expressed using zonotopes [51]. Ellipsoidal reachability set over- and under-approximations have been proposed for some time and have been applied to several problems [34, 52]. Similar to over-approximation approaches, ellipsoidal techniques have been used to incorporate uncertainty into reachability set computation [53, 54]. In these settings uncertainty is added as an adversarial input to the system, producing a worst-case open-loop reachable set.

In general, the computation of reachable sets is severely hampered by the dimensionality of the problem, with the required computation typically scaling as an exponential of the problem dimension ($\mathcal{O}(k^{n-1})$), with n being the dimension of the state-space and k being some discretization of the state-space. Exceptions to this dimensionality-driven computational limitation are many of the over/under-approximation methods discussed above, as well as some limited cases in which analytical computation is possible. For general non-linear systems, however, exact reach set computation retains exponential scaling.

Operationally, optimal estimation algorithms such as batch estimation (Least Squares, Nonlinear Least Squares, etc.) and minimum variance estimation (Kalman Filters, Extended Kalman Filters, Unscented Kalman Filters, etc.) are used to process observations and provide optimal state estimates [55]. This being the case, operational reachability analyses must leverage available information, specifically state estimates and associated covariance matrices. Previous work has generated directly applicable results to this problem in the context of differential games [56]. In this case it is assumed that the initial reachability set, the unsafe set, and the control input are all modeled as ellipsoids, and ellipsoidal over-approximations of the reachability set are derived for Linear Time-Invariant (LTI) systems.

The primary contributions of this chapter are a) necessary and sufficient conditions that may be used to find exact state maxima within state-space partitions for nonlinear reachability problems with ellipsoidal initial sets, b) application of state partition maxima to position and velocity subspaces, allowing for $\mathcal{O}(n)$ tests for nonlinear reachability necessary conditions, c) a method to add initial condition constraints to position- and velocity-subspace extrema calculations, providing a method to compute exact position- and

velocity reachability set subspaces in $\mathcal{O}(k^{n/2-1})$ calculations for systems with nonlinear dynamics, d) a means by which one may compute exact position reachability subspaces for nonlinear systems as seen by observing instrumentation, and e) the relationship of control singularities to position reachability maxima with nonlinear dynamics.

Background reachability theory and notation are introduced in §3.1 along with common reachability set computational methods and caveats. In §3.2.1 existing reachability and optimal control theory are applied to a large class of nonlinear systems and their behavior is examined in detail. Ellipsoidal initial reachability sets are considered in particular due to their direct relationship with covariance ellipsoids generated by industry-standard optimal estimation methodologies. The optimal control for the class of problems examined is generated. The contributions of the paper are derived in §3.2.2 by leveraging classical results from optimal controls to generate necessary and sufficient conditions with which optimal trajectories producing subspace extremals may be found. Several observations are made and a short discussion of the computational properties of the methods is given. A candidate solution procedure to compute the exact position reachability subspace is outlined based on Newton's method in §3.3. Examples illustrating the contributions of the paper and applicability to on-orbit object correlation and tracking are given in §4.3. Finally, §3.5 discusses conclusions and future work.

3.1 Reachability Theory

The Hamilton-Jacobi Bellman (HJB) PDE formulation for reachability is based on a general performance index similar to the *Problem of Bolza*. Because the aim is to find the maximum set of reachable states it is desirable to maximize the performance index. For completeness a common derivation [57, 58] using optimal controls is given here. The performance index $P \in \mathbb{R}$ for a differential system $\dot{\mathbf{x}} = \mathbf{f}(\mathbf{x}, \mathbf{u}, t)$, with $\mathbf{x} \in \mathbb{R}^n$, $\mathbf{u} \in \mathbb{R}^m$, and $t \in [t_0, t_f]$ is specified as

$$P = \int_{t_0}^{t_f} \mathcal{L}(\mathbf{x}(\tau), \mathbf{u}(\tau), \tau) d\tau + V(\mathbf{x}_f, t_f) \tag{3.1}$$

with $\mathcal{L}(\cdot,\cdot,\cdot) \in \mathbb{R}$ called the the trajectory performance and $V(\cdot,\cdot) \in \mathbb{R}$ called the final value function. The performance index can be restated using the Dynamic Programming Equation as

$$V(\mathbf{x}_0, t_0) = \underset{\mathbf{u}\in U}{\text{opt}} \left[\int_{t_0}^{t_f} \mathcal{L}(\mathbf{x}(\tau), \mathbf{u}(\tau), \tau) d\tau + V(\mathbf{x}_f, t_f) \right] \tag{3.2}$$

which relates the current cost to go ($V(\mathbf{x}_0, t_0)$ with the cost to go at a future time t_f ($V(\mathbf{x}_f, t_f)$) and where the 'opt' argument is understood to be 'min', 'max', 'inf', or 'sup,' depending on the application. If t_0 and t_f is chosen such that $t_0 = t$ and $t_f = t + \delta t$, then (3.2) is re-written as

$$V(\mathbf{x}, t) = \underset{\mathbf{u}\in U}{\text{opt}} \left[\int_{t}^{t+\delta t} \mathcal{L}(\mathbf{x}(\tau), \mathbf{u}(\tau), \tau) d\tau + V(\mathbf{x} + \delta\mathbf{x}, t + \delta t) \right]$$

Individually, each term is now expanded using a Taylor series. Starting with the integration term, along an optimal trajectory $(\mathbf{x}^*, \mathbf{u}^*)$,

$$\int_{t}^{t+\delta t} \mathcal{L}(\mathbf{x}^*(\tau), \mathbf{u}^*(\tau), \tau) d\tau = \mathcal{L}(\mathbf{x}^*, \mathbf{u}^*, t)\delta t + O(\|\delta t\|^2)$$

For the optimal value function at time $t + \delta t$,

$$\delta\mathbf{x} = \frac{d\mathbf{x}}{dt}\delta t + O(\|\delta t\|^2) = \mathbf{f}(\mathbf{x}, \mathbf{u}, t)\delta t + O(\|\delta t\|^2)$$

Making

$$V(\mathbf{x} + \delta\mathbf{x}, t + \delta t) = V(\mathbf{x}, t) + \frac{\partial V}{\partial \mathbf{x}}^T \mathbf{f}(\mathbf{x}, \mathbf{u}, t)\delta t + \frac{\partial V}{\partial t}\delta t + O(\|\delta t\|^2)$$

Substituting this back in to the expression for $V(\mathbf{x}, t)$ generates

$$V(\mathbf{x}, t) = \underset{\mathbf{u}\in U}{\text{opt}} \left[\mathcal{L}(\mathbf{x}, \mathbf{u}, t)\delta t + V(\mathbf{x}, t) + \frac{\partial V}{\partial \mathbf{x}}^T \mathbf{f}(\mathbf{x}, \mathbf{u}, t)\delta t + \frac{\partial V}{\partial t}\delta t + O(\|\delta t\|^2) \right]$$

Subtracting $V(\mathbf{x}, t)$ from both sides and observing that $(\partial V/\partial t)\delta t$ does not depend on $\mathbf{u}$ generates

$$\frac{\partial V}{\partial t}\delta t + \underset{\mathbf{u}\in U}{\text{opt}} \left[\mathcal{L}(\mathbf{x}, \mathbf{u}, t)\delta t + \frac{\partial V}{\partial \mathbf{x}}^T \mathbf{f}(\mathbf{x}, \mathbf{u}, t)\delta t + O(\|\delta t\|^2) \right] = 0$$

Ignoring terms that are $O(\|\delta t\|^2)$ and dividing by δt generates the traditional form of the HJB PDE.

$$\frac{\partial V}{\partial t} + \underset{\mathbf{u}\in U}{\text{opt}} \left[\mathcal{L}(\mathbf{x}, \mathbf{u}, t) + \frac{\partial V}{\partial \mathbf{x}}^T \mathbf{f}(\mathbf{x}, \mathbf{u}, t) \right] = 0 \tag{3.3}$$

The HJB PDE (3.3) is a necessary condition of optimality along all optimal trajectories. Note that the 'opt' argument has been retained, as no second-order assumptions have been made (no minimum/maximum

assumptions). As with individual optimal trajectories discussed in Chapter 2, the second term is often called the Optimal Control Hamiltonian, defined as

$$\mathcal{H}^*\left(\mathbf{x}, \frac{\partial V}{\partial \mathbf{x}}^T, \mathbf{u}, t\right) = \underset{\mathbf{u}\in U}{\text{opt}}\left[\mathcal{L}(\mathbf{x}, \mathbf{u}, t) + \frac{\partial V}{\partial \mathbf{x}}^T \mathbf{f}(\mathbf{x}, \mathbf{u}, t)\right]$$

As such, the state and adjoint dynamics along optimal trajectories are the same [58, 59]. The reachability Hamiltonian $\mathcal{H}^*$ state and adjoint dynamics along optimal trajectories with the input $\mathbf{u}^*$ are

$$\dot{\mathbf{x}} = \frac{\partial \mathcal{H}^*}{\partial \mathbf{p}} \tag{3.4}$$

$$\dot{\mathbf{p}} = -\frac{\partial \mathcal{H}^*}{\partial \mathbf{x}} \tag{3.5}$$

where, due to the Transversality Conditions (2.11), the adjoint $\mathbf{p}$ is equivalent to $(\partial \mathbf{V}/\partial \mathbf{x})^T$. To reduce the full HJB PDE to the minimum time reachability HJB PDE, the Lagrangian must be chosen such that the underlying performance index P represents time. In this case

$$P = \int_{t_0}^{t_f} \mathcal{L}(\mathbf{x}(\tau), \mathbf{u}(\tau), \tau) d\tau = \int_{t_0}^{t_f} 1 d\tau = t_f - t_0 = \Delta t$$

Substituting this into the HJB PDE produces

$$\frac{\partial V}{\partial t} + 1 + \underset{\mathbf{u}\in U}{\text{opt}}\left[\frac{\partial V}{\partial \mathbf{x}}^T \mathbf{f}(\mathbf{x}, \mathbf{u}, t)\right] = 0$$

It can be observed that the optimal control policy $\mathbf{u}$ that optimizes the Optimal Control Hamiltonian $\mathcal{H}^*$ is in no way influenced by the minimum time Lagrangian. Thus, the minimum time HJB PDE is typically written without the Lagrangian $\mathcal{L}(\mathbf{x}, \mathbf{u}, t) = 1$ as

$$\frac{\partial V}{\partial t} + \sup_{\mathbf{u}\in U}\left[\frac{\partial V}{\partial \mathbf{x}}^T \mathbf{f}(\mathbf{x}, \mathbf{u}, t)\right] = 0 \tag{3.6}$$

and the corresponding Hamiltonian for minimum time reachability problems is

$$\mathcal{H}^* = \sup_{\mathbf{u}\in U}\left[\mathbf{p}^T \mathbf{f}(\mathbf{x}, \mathbf{u}, t)\right] \tag{3.7}$$

To solve the HJ PDE, it is also required that the problem statement include an initial boundary condition $V(\mathbf{x}_0, t_0) \leq 0$ whose zero-level set defines the initial reachability set boundary [60, 61, 62]. From this definition of the initial reachable set and from the transversality conditions (2.11) the initial conditions for $\mathbf{p}$ may also

constructed:

$$\mathbf{p}_0 = \frac{\partial V(\mathbf{x}_0, t_0)}{\partial \mathbf{x}_0} \tag{3.8}$$

Formally, using the HJB PDE framework the reachability set is defined as

$$\mathcal{R}(t; V(\mathbf{x}_0, t_0)) = \{\mathbf{x} | V(\mathbf{x}, t) \leq 0\} \tag{3.9}$$

Where for present purposes $t \geq t_0$ and the final value function $V(\mathbf{x}, t)$ is the solution the the HJ PDE (3.6). This notation differs somewhat from the notation used in Chapter 2, where the reachability set was qualitatively defined using the feasible control set U, trajectory inequality constraints $\mathbf{h}(\mathbf{x}(t), t) \leq 0$, boundary condition constraints $\mathbf{g}(\mathbf{x}_0, t_0, \mathbf{x}_f, t_f) = \mathbf{0}$, and initial time t_0. A trajectory solution method samples a specific $\mathbf{x}_0$ and $\mathbf{p}_0$ that satisfies $V(\mathbf{x}_0, t_0) = 0$ and utilizes their respective differential equations (3.4) and (3.5) to numerically propagate a single point or region of the reachability set [66, 67]. Another alternative is to solve (3.6) for $V(\mathbf{x}, t)$ and use level-set methods to identify the reachability set. The solution for $V(\mathbf{x}, t)$ is typically difficult to obtain analytically and in general is not smooth. Viscosity solution numerical methods for solving 1^{st}-order PDEs such as (3.6) are often used to approximate $V(\mathbf{x}, t)$ [60, 61, 62, 63, 64]. In the majority of applications numerical methods are used to generate local solutions of $V(\mathbf{x}, t)$, whereas in this chapter the analytical forms are examined to provide additional insight.

3.2 A Method to Compute Reachability Set Subspaces

3.2.1 A Class of Nonlinear Dynamics

Before investigating methods to compute reachability set subspaces the class of dynamics for which the analysis is done must be reviewed. For general systems, an ellipsoid can be specified as the initial boundary of the reachability set:

$$V(\mathbf{x}_{0,c}, t_0) = [\mathbf{x}_c - \mathbf{x}_{0,c}]^T \mathbf{E} [\mathbf{x}_c - \mathbf{x}_{0,c}] - 1 = 0$$

Where $\mathbf{E}$ is a symmetric positive definite matrix ($\mathbf{E} \in \mathbb{S}_+^{n \times n}$), $\mathbf{x}_{0,c}$ is the initial absolute state, and $\mathbf{x}_c$ is the point about which the initial reachability set is centered. To ease notation, the coordinate system may be translated or referenced to a nominal trajectory such that $\mathbf{x}_c - \mathbf{x}_{0,c}$ can be replaced with a relative state $\mathbf{x}_0$,

yielding

$$V(\mathbf{x}_0, t_0) = \mathbf{x}_0^T \mathbf{E} \mathbf{x}_0 - 1 = 0 \tag{3.10}$$

An ellipsoidal initial reachability set such as (3.10) is chosen because it precisely represents the set of states that exist within a level set of a Gaussian probability density function as is readily available from typical estimation algorithms, such as batch filters or minimum variance estimators [55].

Definition 3.2.1. *Ellipsoidal Reachability Problem Statement (ERPS)*

A problem is an ERPS when there exists an initial reachability boundary condition ellipsoid $V(\boldsymbol{x}_0, t_0) = \boldsymbol{x}_0^T \boldsymbol{E} \boldsymbol{x}_0 - 1 \leq 0$, $\boldsymbol{E} \in \mathbb{S}_+^{n \times n}$, *dynamics* $\dot{\boldsymbol{x}} = \boldsymbol{f}(\boldsymbol{x}, \boldsymbol{u}, t)$, *and admissible control set* $\boldsymbol{u} \in U$, *where* U *is defined as*

$$U = \{ \boldsymbol{u} \mid \boldsymbol{u}^T \boldsymbol{u} \leq u_m^2 \} \tag{3.11}$$

where $u_m \in \mathbb{R}, u_m > 0$. *This definition of the admissible control set* U *is assumed for the remainder of this paper.*

Understanding that initial states on the outter-most boundary of the initial reachability set defined by $V(\mathbf{x}_0, t_0) = 0$ will ultimately form the surface of the maximal final reachability set surface, (3.10) may be considered to be an equality constraint of the form $\mathbf{x}_0^T \mathbf{E} \mathbf{x}_0 - 1 = 0$. From this condition, applying the Transversality conditions (2.11) [58, 59] produces the adjoint state initial condition

$$\mathbf{p}_0 = -2\lambda_0 \mathbf{E} \mathbf{x}_0 \tag{3.12}$$

where λ_0 is the Lagrange multiplier associated with the initial condition constraint. Note that (3.12) differs from slightly from the traditional definition given in (3.8) due to considering the surface of the ellipsoid an initial equality constraint rather than a zero-level set of $V(\mathbf{x}_0, t_0)$. The general nonlinear system dynamics are written as $\dot{\mathbf{x}} = \mathbf{f}(\mathbf{x}, \mathbf{u}, t)$, where $\mathbf{x} \in \mathbb{R}^n$ and $\mathbf{u} \in \mathbb{R}^m$. Using (3.7), the Hamiltonian $\mathcal{H}^*$ is then

$$\mathcal{H}^* = \sup_{\mathbf{u} \in U} \left[\mathbf{p}^T \mathbf{f}(\mathbf{x}, \mathbf{u}, t) \right]$$

where the feasible control set $U = \{ \mathbf{u} | \ \|\mathbf{u}\|_2 \leq u_m \}$. In general, there are two cases for the optimal feasible control:

(1) $\mathbf{u}^*$ lies on the surface of the feasible control set

(2) $\mathbf{u}^*$ lies strictly within the feasible control set

For dynamic systems that are affine in control, such as Keplerian motion (in cartesian coordinates) and Gauss' Variational Equations, the optimal control $\mathbf{u}^*$ generating the maximum reachability surface lies on the surface of the control constraint surface, so case 1 will be assumed for this analysis (this case also includes 'bang-bang' type optimal contol). To find the optimal control law $\mathbf{u}^*$ that maximizes the reachability set, the problem is reformulated as

$$\mathbf{u}^* = \arg\max_{\mathbf{u}\in U} \mathbf{p}^T \mathbf{f}(\mathbf{x}, \mathbf{u}, t)$$

with the equality constraint g_u:

$$g_u(\mathbf{u}) = 0 = \frac{1}{u_m^2}\mathbf{u}^T\mathbf{u} - 1$$

Using parametric optimization methods [58, 59], the parametric optimization Lagrangian L is formed (introducing the associated Lagrange multiplier λ_u) and the first and second derivatives with respect to $\mathbf{u}$ are taken:

$$L = \mathbf{p}^T \mathbf{f}(\mathbf{x}, \mathbf{u}, t) + \lambda_u g_u(\mathbf{u})$$

$$\frac{\partial L}{\partial \mathbf{u}} = \mathbf{p}^T \frac{\partial \mathbf{f}}{\partial \mathbf{u}} + \lambda_u \frac{\partial g_u}{\partial \mathbf{u}}$$

$$\frac{\partial^2 L}{\partial \mathbf{u}^2} = \mathbf{p}^T \frac{\partial^2 \mathbf{f}}{\partial \mathbf{u}^2} + \lambda_u \frac{\partial^2 g_u}{\partial \mathbf{u}^2}$$

The analytic forms of $\partial g_u/\partial \mathbf{u}$ and $\partial^2 g_u/\partial \mathbf{u}^2$ are

$$\frac{\partial g_u}{\partial \mathbf{u}} = \frac{2}{u_m^2}\mathbf{u}^T$$

$$\frac{\partial^2 g_u}{\partial \mathbf{u}^2} = \frac{2}{u_m^2}\mathbb{I}_{m\times m}$$

The first-order necessary condition becomes

$$\mathbf{p}^T \frac{\partial \mathbf{f}}{\partial \mathbf{u}} + \frac{2\lambda_u}{u_m^2}\mathbf{u}^T = \mathbf{0}$$

yielding

$$\mathbf{u}^* = -\frac{u_m^2}{2\lambda_u}\left[\frac{\partial \mathbf{f}}{\partial \mathbf{u}}^T \mathbf{p}\right]$$

The second-order necessary condition becomes

$$\mathbf{p}^T \frac{\partial^2 \mathbf{f}}{\partial \mathbf{u}^2} + \frac{2\lambda_u}{u_m^2}\mathbb{I} < 0$$

giving

$$\lambda_u \mathbb{I} < -\frac{u_m^2}{2}\left[\mathbf{p}^T \frac{\partial^2 \mathbf{f}}{\partial \mathbf{u}^2}\right] \tag{3.13}$$

Enforcing the equality constraint $g_u(\mathbf{u}^*) = 0$:

$$\frac{1}{u_m^2}\left(-\frac{u_m^2}{2\lambda_u}\right)^2 \left[\mathbf{p}^T \frac{\partial \mathbf{f}}{\partial \mathbf{u}} \frac{\partial \mathbf{f}}{\partial \mathbf{u}}^T \mathbf{p}\right] - 1 = 0$$

producing

$$\lambda_u = \pm \frac{u_m}{2} \left\| \frac{\partial \mathbf{f}}{\partial \mathbf{u}}^T \mathbf{p} \right\|_2$$

which, after substituting into the expression for $\mathbf{u}^*$, finally provides

$$\mathbf{u}^* = \pm u_m \frac{\frac{\partial \mathbf{f}}{\partial \mathbf{u}}^T \mathbf{p}}{\left\| \frac{\partial \mathbf{f}}{\partial \mathbf{u}}^T \mathbf{p} \right\|_2} \tag{3.14}$$

where the sign of the expression depends on the second-order inequality expression (3.13).

Remark 3.2.1. *Assumptions on the Class of Nonlinear Dynamics*

In the above optimal control solution it was assumed that the optimal control $\boldsymbol{u}^*$ reside on the boundary of the admissible control set U. This is always the case for system dynamics that are affine with control (for example if $\dot{\boldsymbol{x}} = \boldsymbol{f}(\boldsymbol{x}, t) + \boldsymbol{g}(\boldsymbol{x}, t)\boldsymbol{u}$). Such systems are representative of typical Newtonian equations of motion (Keplerian motion, N-body motion, Gauss' Variational Equations, etc.).

Definition 3.2.2. *Class of Nonlinear Systems*

If a nonlinear system under consideration has an optimal control $\boldsymbol{u}^*$ that resides on the boundary of the control set U defined in (3.11), it is termed a Restricted Nonlinear System (RNS).

Using the optimal control shown in (3.14) the Hamiltonian then becomes

$$\mathcal{H}^* = \mathbf{p}^T \mathbf{f}(\mathbf{x}, \mathbf{u}^*, t) \tag{3.15}$$

We may then write the state and adjoint dynamics along optimal trajectories as

$$\frac{\partial \mathcal{H}^*}{\partial \mathbf{p}} = \dot{\mathbf{x}} = \mathbf{f}(\mathbf{x}, \mathbf{u}^*, t) \tag{3.16}$$

and

$$-\frac{\partial \mathcal{H}^*}{\partial \mathbf{x}} = \dot{\mathbf{p}} = -\left(\frac{\partial \mathbf{f}}{\partial \mathbf{x}}^T\right)\mathbf{p} \tag{3.17}$$

where again, $\mathbf{u}^*$ is defined in (3.14). Recalling from (3.12) that $\mathbf{p}_0 = -2\lambda_0 \mathbf{E}\mathbf{x}_0$, It is now convenient to define the solutions to (3.16) and (3.17) as

$$\mathbf{x}(t) = \phi_x(t; \mathbf{x}_0, -2\lambda_0 \mathbf{E}\mathbf{x}_0, t_0) \tag{3.18}$$

and

$$\mathbf{p}(t) = \phi_p(t; \mathbf{x}_0, -2\lambda_0 \mathbf{E}\mathbf{x}_0, t_0) \tag{3.19}$$

In general, the solutions $\mathbf{x}(t) = \phi_x(t; \mathbf{x}_0, -2\lambda_0 \mathbf{E}\mathbf{x}_0, t_0)$ and $\mathbf{p}(t) = \phi_p(t; \mathbf{x}_0, -2\lambda_0 \mathbf{E}\mathbf{x}_0, t_0)$ do not have an analytical form and in many cases must be simultaneously numerically computed.

3.2.2 Analytical Results

With the background theory for reachability introduced and the class of nonlinear systems under consideration defined the analytical results are now derived. Combining the optimal control (3.14) with the optimal ajdoint trajectory (3.19) generates

$$\mathbf{u}^* = \pm u_m \frac{\frac{\partial \mathbf{f}}{\partial \mathbf{u}^*}^T \phi_p(t, \mathbf{x}_0, -2\lambda_0 \mathbf{E}\mathbf{x}_0, t_0)}{\| \frac{\partial \mathbf{f}}{\partial \mathbf{u}^*}^T \phi_p(t, \mathbf{x}_0, -2\lambda_0 \mathbf{E}\mathbf{x}_0, t_0) \|_2}, \tag{3.20}$$

there are two distinct cases that must be examined.

(1) $\frac{\partial \mathbf{f}}{\partial \mathbf{u}^*}^T \phi_p(t, \mathbf{x}_0, -2\lambda_0 \mathbf{E}\mathbf{x}_0, t_0) \neq \mathbf{0}$ at time t: In this case the optimal control (3.20) is well defined and continuous (observe that $\mathbf{p}(t) \in \mathcal{C}^0$ for all time t).

(2) $\frac{\partial \mathbf{f}}{\partial \mathbf{u}^*}^T \phi_p(t, \mathbf{x}_0, -2\lambda_0 \mathbf{E}\mathbf{x}_0, t_0) = \mathbf{0}$ at time t: This situation results in causing $\mathbf{u}^*$ to become singular exactly at time t. This case necessitates the definition

$$\mathbf{P}(t, \mathbf{x}_0, \lambda_0, \mathbf{E}, t_0) = \frac{\partial \mathbf{f}}{\partial \mathbf{u}^*}^T \phi_p(t, \mathbf{x}_0, -2\lambda_0 \mathbf{E}\mathbf{x}_0, t_0) \tag{3.21}$$

where $\mathbf{P}(t, \mathbf{x}_0, \lambda_0, \mathbf{E}, t_0) \in \mathbb{R}^m$. Note that $\mathbf{P}(t, \mathbf{x}_0, \lambda_0, \mathbf{E}, t_0) = \frac{\partial \mathbf{f}}{\partial \mathbf{u}^*}^T \phi_p(t, \mathbf{x}_0, t_0) = \mathbf{0}$ when $\mathbf{p}(t) = \mathbf{0}$ or when $\mathbf{p}(t)$ is in the nullspace $\mathcal{N}$ of $[\partial \mathbf{f}/\partial \mathbf{u}^*]^T$.

The possibility of a control singularity requires additional investigation. If the adjoint $\mathbf{p}(t)$ evolves such that $\mathbf{P}(t, \mathbf{x}_0, \lambda_0, \mathbf{E}, t_0) = \mathbf{0}$, then as limits are taken before and after the singularity it can be shown that the unit vector defined in (3.20) effectively 'switches' direction at some special time t. This motivates the following definition and theorem:

Definition 3.2.3. *Switching Time*

Given an initial state $\boldsymbol{x}_0$ belonging to an ERPS, the time t at which $\boldsymbol{P}(t, \boldsymbol{x}_0, \lambda_0, \boldsymbol{E}, t_0) = \boldsymbol{0}$, if such a t exists, is defined as the switching time T_s for that initial state.

Lemma 3.2.1. *Switching Time Existence*

An initial state $\boldsymbol{x}_0$ in an ERPS with dynamics $\dot{\boldsymbol{x}} = \boldsymbol{f}(\boldsymbol{x}, \boldsymbol{u}, t)$ and $m < n$ has a switching time T_s if and only if $\boldsymbol{P}(t, \boldsymbol{x}_0, \lambda_0, \boldsymbol{E}, t_0) = \boldsymbol{0}$, where $\boldsymbol{x}_0 \neq \boldsymbol{0}$.

Proof: This result follows directly from observing that, by definition, $\boldsymbol{E}$ is full rank and the Lagrange multiplier $\lambda_0 \neq 0$, yielding $\boldsymbol{p}_0 \neq \boldsymbol{0}$, and $Rank([\partial \boldsymbol{f}/\partial \boldsymbol{u}^*]^T) \leq m$. This being the case, the null-space dimensionality $Dim(\mathcal{N}([\partial \boldsymbol{f}/\partial \boldsymbol{u}^*]^T)) \geq n - m > 0$. Therefore, there exists a set of non-trivial initial conditions $\boldsymbol{x}_0$ that are currently switching at any time $t = T_s \in (-\infty, \infty)$ if and only if $\boldsymbol{P}(t, \boldsymbol{x}_0, \lambda_0, \boldsymbol{E}, t_0) = \boldsymbol{0}$, where $\boldsymbol{x}_0 \neq \boldsymbol{0}$. □

Lemma 3.2.1 will be used in the following sections to demonstrate switching times for specific optimal trajectories. To simplify notation and to emphasize the need to solve both $\mathbf{x}$ and $\mathbf{p}$ simultaneously, the state and adjoint dynamics are now concatenated into a larger state $\mathbf{z} \in \mathbb{R}^{2n}$ such that

$$\mathbf{z} = \begin{bmatrix} \mathbf{x} \\ \\ \mathbf{p} \end{bmatrix}$$

From which it follows that

$$\dot{\mathbf{z}} = \begin{bmatrix} \dot{\mathbf{x}} \\ \\ \dot{\mathbf{p}} \end{bmatrix} = \begin{bmatrix} \frac{\partial \mathcal{H}^*}{\partial \mathbf{p}} \\ \\ -\frac{\partial \mathcal{H}^*}{\partial \mathbf{x}} \end{bmatrix} = \mathbf{f}_z(\mathbf{x}, \mathbf{p}, t)$$

and

$$\mathbf{z}(t) = \phi_z(t; \mathbf{x}_0, \mathbf{E}\mathbf{p}_0, t_0) = \int_{t_0}^{t} \mathbf{f}_z(\mathbf{x}(\tau), \mathbf{p}(\tau), \tau) d\tau$$

With the initial conditions $\mathbf{x}(\tau = t_0) = \mathbf{x}_0$ and $\mathbf{p}(\tau = t_0) = -2\lambda_0 \mathbf{E}\mathbf{x}_0$. Using this notation the following general result is demonstrated:

Theorem 3.2.1. *State Partition Reachability Maximum*

Given an ERPS with RNS dynamics, a state and adjoint partition

$$\boldsymbol{x} = \begin{bmatrix} \boldsymbol{x}_r \\ \\ \boldsymbol{x}_s \end{bmatrix}, \ \boldsymbol{p} = \begin{bmatrix} \boldsymbol{p}_r \\ \\ \boldsymbol{p}_s \end{bmatrix}$$

with $\boldsymbol{x}_r$ *and* $\boldsymbol{p}_r \in \mathbb{R}^r$, $\boldsymbol{x}_s$ *and* $\boldsymbol{p}_s \in \mathbb{R}^s$, $r + s = n$, $r \geq 1$, *and with* $\boldsymbol{u}$ *in the norm-bounded set* U, *the absolute maximum partitioned state value* $\boldsymbol{x}_{r,f}$ *at the final time* t_f *as well as the corresponding initial conditions* $\boldsymbol{x}_0$ *satisfying (3.10) are found by solving*

$$\begin{bmatrix} \boldsymbol{x}_{r,f} \\ \\ \boldsymbol{x}_{r,f} \\ \\ \boldsymbol{0} \end{bmatrix} = \boldsymbol{T}\phi_z(t_f; \boldsymbol{x}_0, -2\lambda_0 \boldsymbol{E}\boldsymbol{x}_0, t_0) \tag{3.22}$$

and

$$\boldsymbol{x}_0^T \boldsymbol{E}\boldsymbol{x}_0 - 1 = 0 \tag{3.23}$$

for $\boldsymbol{x}_{r,f}$, $\boldsymbol{x}_0$, *and* λ_0, *with*

$$\boldsymbol{T} = \begin{bmatrix} \mathbb{I} & \boldsymbol{0} & \boldsymbol{0} & \boldsymbol{0} \\ \\ \boldsymbol{0} & \boldsymbol{0} & \mathbb{I} & \boldsymbol{0} \\ \\ \boldsymbol{0} & \boldsymbol{0} & \boldsymbol{0} & \mathbb{I} \end{bmatrix}$$

and λ_0 *defined as the Lagrange multiplier associated with the initial condition constraint (3.23).*

Proof: This result is obtained by choosing an appropriate final performance index to maximize and applying the Transversality conditions (2.11) [58] to impose conditions on (and eliminate) the adjoint states.

Choosing the performance index at the final time to be

$$K(\boldsymbol{x}_f, t_f) = \frac{1}{2}\boldsymbol{x}_{r,f}^T \boldsymbol{x}_{r,f} = \frac{1}{2}\boldsymbol{x}_f^T \begin{bmatrix} \mathbb{I}_{r\times r} & \boldsymbol{O}_{r\times s} \\ \boldsymbol{O}_{s\times r} & \boldsymbol{O}_{s\times s} \end{bmatrix} \boldsymbol{x}_f$$

then the Transversality conditions, which are necessary conditions of optimality relating initial and final boundary conditions of the states and adjoints, impose the following values for the initial and final adjoint states:

$$\boldsymbol{p}_0 = -\frac{\partial K}{\partial \boldsymbol{x}_0} - \lambda_0 \frac{\partial g}{\partial \boldsymbol{x}_0} = -2\lambda_0 \boldsymbol{E}\boldsymbol{x}_0 \tag{3.24}$$

$$\boldsymbol{p}_f = \frac{\partial K}{\partial \boldsymbol{x}_f} + \lambda_f \frac{\partial g}{\partial \boldsymbol{x}_f} = \begin{bmatrix} \mathbb{I}_{r\times r} & \boldsymbol{O}_{r\times s} \\ \boldsymbol{O}_{s\times r} & \boldsymbol{O}_{s\times s} \end{bmatrix} \boldsymbol{x}_f \tag{3.25}$$

The notation $\partial K/\partial \boldsymbol{x}_0$ and $\partial g/\partial \boldsymbol{x}_0$ is used to show that the partials are evaluated at $\boldsymbol{x} = \boldsymbol{x}_0$ (similarly $\partial V/\partial \boldsymbol{x}_f$ and $\partial g/\partial \boldsymbol{x}_f$ are evaluated at $\boldsymbol{x} = \boldsymbol{x}_f$). Examining (3.24) and (3.25), it can be seen that

$$\boldsymbol{p}_f = \begin{bmatrix} \boldsymbol{p}_{r,f} \\ \boldsymbol{p}_{s,f} \end{bmatrix} = \begin{bmatrix} \boldsymbol{x}_{r,f} \\ \boldsymbol{0} \end{bmatrix} = \phi_p(t_f; \boldsymbol{x}, -2\lambda_0 \boldsymbol{E}\boldsymbol{x}_0, t_0) \tag{3.26}$$

Further, $\boldsymbol{x}_{r,f}$ must be the result of an optimal state trajectory which may be written as

$$\boldsymbol{x}_{r,f} = \begin{bmatrix} \mathbb{I}_{r\times r} & \boldsymbol{O}_{r\times s} \end{bmatrix} \phi_x(t_f; \boldsymbol{x}_0, -2\lambda_0 \boldsymbol{E}\boldsymbol{x}_0, t_0) \tag{3.27}$$

Lastly, the initial condition constraint (3.23) must be satisfied. Together, these relations yield $n + r + 1$ equations with the corresponding $n + r + 1$ unknowns ($\boldsymbol{x}_{r,f}$, $\boldsymbol{x}_0$, and λ_0). Satisfying the necessary conditions of optimality reflected in (3.26), (3.27), and (3.23) then generates the maximum reachable $\boldsymbol{x}_{r,f}$ along with the corresponding initial conditions $\boldsymbol{x}_0$ and Lagrange multiplier λ_0. □

With the result demonstrated in Theorem 3.2.1 for general ERPS systems with RNS dynamics, the following results are generated for applications related to space object correlation. For such systems it is often convenient to form the state and adjoint dynamic equations such that the state partitions are in terms

of position and velocity:

$$\mathbf{x}^T = \begin{bmatrix} \mathbf{d}^T & \mathbf{v}^T \end{bmatrix}$$
$$\mathbf{p}^T = \begin{bmatrix} \mathbf{p}_d^T & \mathbf{p}_v^T \end{bmatrix}$$

where $\mathbf{d}, \mathbf{v}, \mathbf{p}_d, \mathbf{p}_v \in \mathbb{R}^{n/2}$, $r = s = n/2$. Position-/velocity-specific results are now derived.

Theorem 3.2.2. *Reachability Position Maximum*

Given an ERPS with RNS dynamics, where $\boldsymbol{u}$ is in the norm-bounded set U, the absolute maximum position $\boldsymbol{d}_f$ at time t_f as well as the corresponding initial conditions $\boldsymbol{x}_0^T = [\boldsymbol{d}_0^T \ \boldsymbol{v}_0^T]$ satisfying (3.10) are found by solving the following system of equations:

$$\begin{bmatrix} \boldsymbol{d}_f \\ \boldsymbol{d}_f \\ \boldsymbol{0} \end{bmatrix} = \boldsymbol{M}\phi_z(t_f; \boldsymbol{x}_0, -2\lambda_0 \boldsymbol{E}\boldsymbol{x}_0, t_0) \tag{3.28}$$

$$\begin{bmatrix} \boldsymbol{d}_0 \\ \boldsymbol{v}_0 \end{bmatrix}^T \boldsymbol{E} \begin{bmatrix} \boldsymbol{d}_0 \\ \boldsymbol{v}_0 \end{bmatrix} - 1 = 0 \tag{3.29}$$

for $\boldsymbol{d}_0$, $\boldsymbol{v}_0$, $\boldsymbol{d}_f$, and λ_0, where

$$\boldsymbol{M} = \begin{bmatrix} \mathbb{I} & \boldsymbol{0} & \boldsymbol{0} & \boldsymbol{0} \\ \boldsymbol{0} & \boldsymbol{0} & \mathbb{I} & \boldsymbol{0} \\ \boldsymbol{0} & \boldsymbol{0} & \boldsymbol{0} & \mathbb{I} \end{bmatrix}_{\frac{3}{2}n \times 2n}$$

and λ_0 is the Lagrange multiplier associated with the initial condition constraint (3.29).

Proof: This proof follows the same approach as Theorem 3.2.1, generating the equations

$$\begin{bmatrix} \boldsymbol{d}_f \\ \boldsymbol{0} \end{bmatrix} = \phi_p(t_f, \boldsymbol{x}_0, -2\lambda_0 \boldsymbol{E}\boldsymbol{x}_0, t_0) \tag{3.30}$$

and

$$\boldsymbol{d}_f = \begin{bmatrix} \mathbb{I} & \boldsymbol{0} \end{bmatrix} \phi_x(t_f, \boldsymbol{x}_0, -2\lambda_0 \boldsymbol{E}\boldsymbol{x}_0, t_0) \tag{3.31}$$

Equations (3.30) and (3.31) may be combined to form (3.28), and in conjuction with the constraint (3.29) provide $3n/2 + 1$ equations and $3n/2 + 1$ unknowns ($\boldsymbol{d}_0$, $\boldsymbol{v}_0$, $\boldsymbol{d}_f$, and λ_0). Thus, by solving (3.28) and (3.29)

one may determine not only the maximum distance $\boldsymbol{d}_f$, but also the associated initial conditions $\boldsymbol{d}_0$ and $\boldsymbol{v}_0$. □

Theorem 3.2.3. *Reachability Velocity Maxima*

Given an ERPS with RNS dynamics, where $\boldsymbol{u}$ is in the norm-bounded set U, the absolute maximum reachable velocity $\boldsymbol{v}_f$ at time t_f as well as the corresponding initial conditions $\boldsymbol{x}_0^T = [\,\boldsymbol{d}_0^T \;\; \boldsymbol{v}_0^T\,]$ satisfying (3.10) are found by solving the following equations:

$$\begin{bmatrix} \boldsymbol{v}_f \\ \boldsymbol{0} \\ \boldsymbol{v}_f \end{bmatrix} = \boldsymbol{N}\phi_z(t_f; \boldsymbol{x}_0, -2\lambda_0 \boldsymbol{E}\boldsymbol{x}_0, t_0) \tag{3.32}$$

$$\begin{bmatrix} \boldsymbol{d}_0 \\ \boldsymbol{v}_0 \end{bmatrix}^T \boldsymbol{E} \begin{bmatrix} \boldsymbol{d}_0 \\ \boldsymbol{v}_0 \end{bmatrix} - 1 = 0 \tag{3.33}$$

where

$$\boldsymbol{N} = \begin{bmatrix} \boldsymbol{0} & \mathbb{I} & \boldsymbol{0} & \boldsymbol{0} \\ \boldsymbol{0} & \boldsymbol{0} & \mathbb{I} & \boldsymbol{0} \\ \boldsymbol{0} & \boldsymbol{0} & \boldsymbol{0} & \mathbb{I} \end{bmatrix}_{\frac{3}{2}n \times 2n}$$

and λ_0 is the Lagrange multiplier associated with the initial condition constraint (3.33).

Proof: This argument is the same as for Theorem 3.2.1 with the following changes:

$$K(\boldsymbol{x}_f, t_f) = \frac{1}{2}\boldsymbol{x}_f^T \begin{bmatrix} \boldsymbol{0} & \boldsymbol{0} \\ \boldsymbol{0} & \mathbb{I} \end{bmatrix} \boldsymbol{x}_f \tag{3.34}$$

$$\boldsymbol{p}_f = \frac{\partial K}{\partial \boldsymbol{x}_f} + \lambda_f \frac{\partial g}{\partial \boldsymbol{x}_f} = \begin{bmatrix} \boldsymbol{0} & \boldsymbol{0} \\ \boldsymbol{0} & \mathbb{I} \end{bmatrix} \boldsymbol{x}_f = \boldsymbol{p}_f \tag{3.35}$$

providing the following $3n/2 + 1$ equations:

$$\begin{bmatrix} \boldsymbol{0} \\ \boldsymbol{v}_f \end{bmatrix} = \phi_p(t_f, \boldsymbol{x}_0, -2\lambda_0 \boldsymbol{E}\boldsymbol{x}_0, t_0) \tag{3.36}$$

$$\begin{bmatrix} \boldsymbol{d}_0 \\ \boldsymbol{v}_0 \end{bmatrix}^T \boldsymbol{E} \begin{bmatrix} \boldsymbol{d}_0 \\ \boldsymbol{v}_0 \end{bmatrix} - 1 = 0 \tag{3.37}$$

$$\boldsymbol{v}_f = \begin{bmatrix} \boldsymbol{0} & \mathbb{I} \end{bmatrix} \phi_x(t_f, \boldsymbol{x}_0, -2\lambda_0 \boldsymbol{E}\boldsymbol{x}_0, t_0) \tag{3.38}$$

Solving for ($\boldsymbol{d}_0$, $\boldsymbol{v}_0$, $\boldsymbol{v}_f$, and λ_0) using (3.32) and (3.33) is now possible. □

With Theorems 3.2.1, 3.2.2, and 3.2.3 established, reachability necessary conditions may now be formalized. Additionally, the results in Theorems 3.2.2 and 3.2.3 can be leveraged to derive results for a-priori position- or velocity-direction reachability extrema.

Corollary 3.2.1. *Reachability Necessary Conditions*

Given an ERPS with RNS dynamics, if an initial state $\boldsymbol{x}_0$ satisfies (3.10), and the state-space $\boldsymbol{x}$ is partitioned into $q \leq n$ disjoint subspaces $\boldsymbol{x}_{r_1}, \boldsymbol{x}_{r_2}, \ldots, \boldsymbol{x}_{r_{q-1}}, \boldsymbol{x}_{r_q}$ such that $r_1 + r_2 + \cdots + r_{q-1} + r_q = n$, then the resulting final state $\boldsymbol{x}_f$ using any admissible control law at time t_f must satisfy

$$\boldsymbol{x}_{r,f_i}^T \boldsymbol{x}_{r,f_i} \leq \boldsymbol{x}_{r,f,mx_i}^T \boldsymbol{x}_{r,f,mx_i}, \; i = 1, \ldots, q \tag{3.39}$$

where $\boldsymbol{x}_{r,f,mx_i}$ is the state maxima for the i^{th} partition found using Theorem 3.2.1.

Proof: For each partition $\boldsymbol{x}_{r_i}$, $i = 1, \ldots, q$, Theorem 3.2.1 may be applied to compute the maximum possible state partition final value $\boldsymbol{x}_{r,f,mx_i}$ at the final time t_f. Since the partitions are disjoint and jointly compose the state-space $\boldsymbol{x}$, any reachable final state $\boldsymbol{x}_f$ must satisfy (3.39). □

In the case that $q = n$ (each partition is one-dimensional), then using Corollary 3.2.1 a conservative outer bound may be generated for an ERPS with RNS dynamics in $\mathcal{O}(n)$ zero-finding operations in $n + r + 1$ variables.

Corollary 3.2.2. *Position and Velocity Reachability Necessary Conditions*

Given an ERPS with RNS dynamics, if an initial state ($\boldsymbol{d}_0$, $\boldsymbol{v}_0$) satisfies (3.10), then the resulting state ($\boldsymbol{d}_f$, $\boldsymbol{v}_f$) using any admissible control law at time t_f must satisfy

$$\boldsymbol{d}_f^T \boldsymbol{d}_f \leq \boldsymbol{d}_{f,mx}^T \boldsymbol{d}_{f,mx} \tag{3.40}$$

and

$$\boldsymbol{v}_f^T \boldsymbol{v}_f \leq \boldsymbol{v}_{f,mx}^T \boldsymbol{v}_{f,mx} \tag{3.41}$$

where $\boldsymbol{d}_{f,max}$ *and* $\boldsymbol{v}_{f,max}$ *are the disjoint position and velocity maxima found using Theorems 3.2.2 and 3.2.3 independently.*

Proof: Defining $\boldsymbol{d}_{f,mx}$ *as the maximum reachable distance vector found by using Theorem 3.2.2, and* $\boldsymbol{v}_{f,mx}$ *as the maximum reachable velocity vector found by using Theorem 3.2.3, it is clear that both* $\boldsymbol{d}_{f,mx}$ *and* $\boldsymbol{d}_{f,mx}$ *are extremal solutions that maximize the performance indicies*

$$P_d = \boldsymbol{d}_f^T \boldsymbol{d}_f$$

and

$$P_v = \boldsymbol{v}_f^T \boldsymbol{v}_f$$

respectively. Thus, any non-extremal solution $(\boldsymbol{d}_f, \boldsymbol{v}_f)$ *of* $\dot{\boldsymbol{x}} = \boldsymbol{f}(\boldsymbol{x}, \boldsymbol{u}, t)$ *with* $\boldsymbol{u} \in U$ *subject to the restrictions discussed in Definition 3.2.2 and with* $(\boldsymbol{d}_0, \boldsymbol{v}_0)$ *satisfying (3.10) must be inclusively bounded by* $(\boldsymbol{d}_{f,mx}, \boldsymbol{v}_{f,mx})$. □

Corollary 3.2.3. *A-Priori Position-Direction Reachability*

Given an ERPS with RNS dynamics, where $\boldsymbol{u}$ *is in the norm-bounded set* U*, and an initial position direction* $\hat{\boldsymbol{d}}_0$ *is specified, the absolute maximum reachable position* $\boldsymbol{d}_f$ *at time* t_f *as well as the corresponding initial direction magnitude* d *and velocity* $\boldsymbol{v}_0$ *satisfying (3.10) are found by solving the equations given in Theorem 3.2.2 with the substitution* $\boldsymbol{d}_0 = d\hat{\boldsymbol{d}}_0$.

Proof: With the substitution $\boldsymbol{d}_0 = d\hat{\boldsymbol{d}}_0$*, equations (3.28) and (3.29) form a set of* $n+2$ *equations with the* $n+2$ *unknowns* $\boldsymbol{d}_f$*,* λ_0*,* d*, and* $\boldsymbol{v}_0$*.* □

Corollary 3.2.4. *A-Priori Velocity-Direction Reachability*

Given an ERPS with RNS dynamics, where $\boldsymbol{u}$ *is in the norm-bounded set* U*, and an initial velocity direction* $\hat{\boldsymbol{v}}_0$ *is specified, the absolute maximum reachable velocity* $\boldsymbol{v}_f$ *at time* t_f *as well as the corresponding initial direction* $\boldsymbol{d}_0$ *and velocity magnitude* v *satisfying (3.10) are found by solving the equations given in Theorem 3.2.3 with the substitution* $\boldsymbol{v}_0 = v\hat{\boldsymbol{v}}_0$*.*

Proof: With the substitution $\boldsymbol{v}_0 = v\hat{\boldsymbol{v}}_0$*, equations (3.32) and (3.33) form a set of* $n+2$ *equations with the* $n+2$ *unknowns* $\boldsymbol{v}_f$*,* λ_0*,* $\boldsymbol{d}_0$*, and* v*.* □

Figure 3.1 visualizes the concepts proven in Theorem 3.2.2 and Corollary 3.2.3, but applies equally well to Theorem 3.2.3 and Corollary 3.2.4.

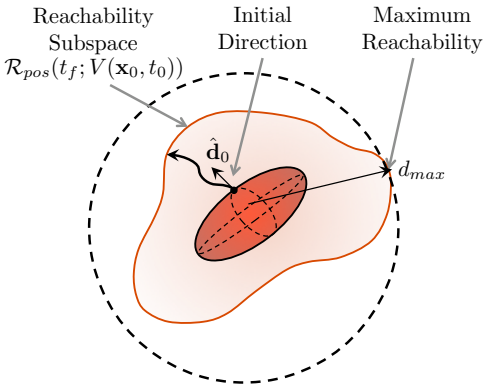

Figure 3.1: Visualization of Theorem 3.2.2 and Corollary 3.2.3 with initial arbitrary ellipsoid surface described by $V(\mathbf{x}_0, t_0) = 0$. The absolute maximum position is $\mathbf{d}_{f,max}$, which can be used to construct a maximum bound (dashed circle). The maximum directional position surface is represented by $\mathcal{R}_{pos}(t_f; V(\mathbf{x}_0, t_0))$.

Remark 3.2.2. *Final Position / Velocity Reachability Surface Computation Reduction*

The results discussed in Corollaries 3.2.3 and 3.2.4 enable a discretized sampling of the true maximum position or velocity reachability surfaces (respectively) using a sample-space of the initial reachability set in $n/2-1$ *dimensions (*$\mathcal{O}(k^{n/2-1})$ *operations), rather than* $n-1$ *dimensions (*$\mathcal{O}(k^{n-1})$ *operations), where* $\boldsymbol{x} \in \mathbb{R}^n$*. This reduction in problem dimensionality can significantly decreases computation requirements for generating either maximum position or velocity reachability sets. Thus, for a 3-DOF problem (*$n = 6$*), only a 2-dimensional set of initial position (velocity) directions parameterized by* $\hat{\boldsymbol{d}}_0$ *(*$\hat{\boldsymbol{v}}_0$*) must be used*

to compute a set of corresponding final positions $\boldsymbol{d}_f$ (velocities $\boldsymbol{v}_f$) representing a sampling of the exact reachability surface at time t_f. The position reachability set and velocity reachability sets are represented by $\mathcal{R}_{pos}(t_f; V(\boldsymbol{x}_0, t_0))$ and $\mathcal{R}_{vel}(t_f; V(\boldsymbol{x}_0, t_0))$, respectively. Note also that $\mathcal{R}_{pos}(t_f; V(\boldsymbol{x}_0, t_0)) \subset \mathcal{R}(t_f; V(\boldsymbol{x}_0, t_0))$ and $\mathcal{R}_{vel}(t_f; V(\boldsymbol{x}_0, t_0)) \subset \mathcal{R}(t_f; V(\boldsymbol{x}_0, t_0))$

Corollary 3.2.5. *Projected Position Reachability Maxima*

Given a 3-DOF ERPS with RNS dynamics, $\boldsymbol{u}$ in the norm-bounded set U, and an orthonormal transformation $\boldsymbol{H}$ from the inertial frame $\mathcal{I}$ (the frame in which the dynamics are based) to an observer frame $\mathcal{O}$, the projected maximum position $\boldsymbol{h}_f \in \mathbb{R}^2$ at time t_f with initial direction $\hat{\boldsymbol{d}}_0$ as well as the corresponding initial direction magnitude d and velocity $\boldsymbol{v}_0$ satisfying (3.29) are found by solving

$$\begin{bmatrix} \boldsymbol{d}_f \\ \tilde{\mathbf{H}}^T \tilde{\boldsymbol{H}} \boldsymbol{d}_f \\ \boldsymbol{0} \end{bmatrix} = \boldsymbol{M} \phi_z(t_f; \boldsymbol{x}_0, -2\lambda_0 \boldsymbol{E} \boldsymbol{x}_0, t) \tag{3.42}$$

and

$$\begin{bmatrix} d\hat{\boldsymbol{d}}_0 \\ \boldsymbol{v}_0 \end{bmatrix}^T \boldsymbol{E} \begin{bmatrix} d\hat{\boldsymbol{d}}_0 \\ \boldsymbol{v}_0 \end{bmatrix} - 1 = 0 \tag{3.43}$$

for d, $\boldsymbol{v}_0$, $\boldsymbol{d}_f$, and λ_0, where

$$\tilde{\boldsymbol{H}}^T = \begin{bmatrix} \hat{\boldsymbol{h}}_1 & \hat{\boldsymbol{h}}_2 & \boldsymbol{0} \end{bmatrix}$$

and

$$\boldsymbol{H}^T = \begin{bmatrix} \hat{\boldsymbol{h}}_1 & \hat{\boldsymbol{h}}_2 & \hat{\boldsymbol{h}}_1 \end{bmatrix}$$

with $\hat{\boldsymbol{h}}_1$ and $\hat{\boldsymbol{h}}_2$ being the two basis vectors of $\mathcal{O}$ that are orthogonal to the observer line-of-sight unit vector $\hat{\boldsymbol{h}}_3$, and the projected distance $\boldsymbol{h}_f$ defined by $\boldsymbol{h}_f = \tilde{\boldsymbol{H}} \boldsymbol{d}_f$.

Proof: This proof progresses along similar lines to the proof in Corollary 3.2.3, with the exception that the final value function is constructed to maximize $\boldsymbol{h}_f^T \boldsymbol{h}_f$, and is defined as

$$V(\boldsymbol{x}_f, t_f) = \frac{1}{2} \begin{bmatrix} \boldsymbol{d}_f \\ \boldsymbol{v}_f \end{bmatrix}^T \begin{bmatrix} \tilde{\boldsymbol{H}}^T \tilde{\boldsymbol{H}} & \boldsymbol{0} \\ \boldsymbol{0} & \boldsymbol{0} \end{bmatrix} \begin{bmatrix} \boldsymbol{d}_f \\ \boldsymbol{v}_f \end{bmatrix} \tag{3.44}$$

Using the transversality condition for $\boldsymbol{p}_f$ *and following the steps outlined in Theorem 3.2.2,*

$$\begin{bmatrix} \tilde{\boldsymbol{H}}^T \tilde{\boldsymbol{H}} \boldsymbol{d}_f \\ \boldsymbol{0} \end{bmatrix} = \phi_p(t_f; \boldsymbol{x}_0, -2\lambda_0 \boldsymbol{E}\boldsymbol{x}_0, t) \tag{3.45}$$

which, when combined with the state dynamics

$$\boldsymbol{d}_f = \begin{bmatrix} \mathbb{I} & \boldsymbol{0} \end{bmatrix} \phi_x(t_f; \boldsymbol{x}_0, -2\lambda_0 \boldsymbol{E}\boldsymbol{x}_0, t)$$

provides 8 equations to solve 8 unkowns ($\boldsymbol{d}_f$*,* d*,* $\boldsymbol{v}_0$*, and* λ_0*), from which* $\boldsymbol{h}_f = \tilde{\boldsymbol{H}}\boldsymbol{d}_f$ *may be computed.* □

Remark 3.2.3. *Projected Position Reachability Surface Utility*

The result from Corollary 3.2.5 benefits from Remark 3.2.2 in addition to the following: For cases in which an observer is searching for where the final state could be, it may be very convenient to define an projected position reachability set in terms of azimuth and elevation coordinates. After the position reachability set at time t_f *has been projected to a plane perpendicular to the observer's line-of-sight vector* $\hat{\boldsymbol{h}}_3$ *this becomes a straightforward process and can significantly aid search strategies. Put another way, a search space in azimuth-elevation space in an observer frame* $\mathcal{O}$ *can be constructed with a sampling of* k^2 *points spanning feasible initial directions* $\hat{\boldsymbol{d}}_0$*.*

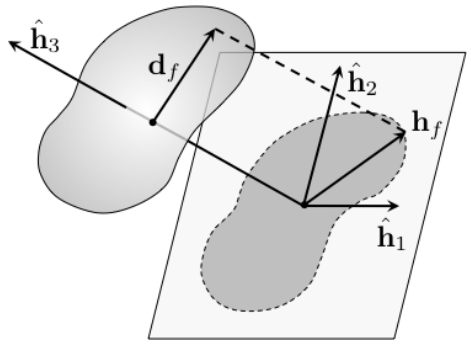

Figure 3.2: Visualization of 3D position reachability set planar projection orthogonal to an observer line-of-sight vector $\hat{\mathbf{h}}_3$

Remark 3.2.4. *Hamiltonian Value*

For both Theorems 3.2.2 and 3.2.3 and Corollaries 3.2.3, 3.2.4, and 3.2.5, the transversality conditions

require that

$$\mathcal{H}_0^* = \frac{\partial V}{\partial t_0} + \lambda \frac{\partial g}{\partial t_0}$$

and

$$\mathcal{H}_f^* = -\frac{\partial V}{\partial t_f} - \lambda \frac{\partial g}{\partial t_f}$$

Then if the optimal Hamiltonian $\mathcal{H}^*$ does not have any explicit dependence on time, i.e.

$$\frac{d\mathcal{H}^*}{dt} = \frac{\partial \mathcal{H}^*}{\partial t} = 0$$

then $\mathcal{H}^* = 0$ over $t \in [t_0, t_f]$. This property is useful for monitoring the health of numerical integration methods.

Finally, we are now able to relate position maxima with the optimal control switching time as well as generalize the applicability of the transversality condition results.

Theorem 3.2.4. *Partition Maxima and Switching Time*

Given an ERPS with RND dynamics, $\boldsymbol{u} \in U$, $n > m$, a state partition such that $\boldsymbol{x}^T = [\boldsymbol{x}_r^T \ \boldsymbol{x}_s^T]$ with $\boldsymbol{x}_r \in \mathbb{R}^{n-m}$ and $\boldsymbol{x}_s \in \mathbb{R}^m$, initial state ($\boldsymbol{x}_0$) satisfying (3.10), and control gradient $\partial \boldsymbol{f}/\partial \boldsymbol{u}$ such that

$$\frac{\partial \boldsymbol{f}}{\partial \boldsymbol{u}}_{n\times m} = \begin{bmatrix} \boldsymbol{0}_{n-m\times m} \\ \frac{\partial \boldsymbol{f}_v}{\partial \boldsymbol{u}}_{m\times m} \end{bmatrix} \tag{3.46}$$

and $Rank(\partial \boldsymbol{f}_v/\partial \boldsymbol{u}) = m < n$, the partiation state $\boldsymbol{x}_{r,f}$ at time t_f is a maxima if and only if the control is switching and $t_f = T_s$.

Proof: First, proving $(\boldsymbol{p}_{m,f} = \boldsymbol{0}) \Rightarrow (t_f = T_s)$. From (3.25) it is clear that $\boldsymbol{p}_f^T = [\ \boldsymbol{p}_{r,f}^T \quad \boldsymbol{0}^T\ ]^T$, requiring $\boldsymbol{p}_{m,f} = \boldsymbol{0}$ and causing $\boldsymbol{p}_f$ to be within the nullspace of $\partial \boldsymbol{f}/\partial \boldsymbol{u}$, forcing $\boldsymbol{P}(t, \boldsymbol{x}_0, \lambda_0, \boldsymbol{E}, t_0) = \boldsymbol{0}$, forcing t to be a switching time T_s.

For $(t_f = T_s) \Rightarrow (\boldsymbol{p}_{m,f} = \boldsymbol{0})$. If $t = T_s$ then by Lemma 3.2.1 the control is currently switching and $\boldsymbol{P}(t, \boldsymbol{x}_0, \lambda_0, \boldsymbol{E}, t_0) = \boldsymbol{0}$. Due to the form of $\partial \boldsymbol{f}/\partial \boldsymbol{u}$ and since $Rank(\partial \boldsymbol{f}_v/\partial \boldsymbol{u}) = m < n$, we may conclude that the only $\boldsymbol{p}_f$ that satisfies $[\partial \boldsymbol{f}_v/\partial \boldsymbol{u}]^T \boldsymbol{p}_{m,f} = \boldsymbol{0}$ is the trivial solution $\boldsymbol{p}_{m,f} = \boldsymbol{0}$. □

This is an interesting result, as for position/velocity state partitions Theorem 3.2.4 implies that if all of the velocity states have explicit control in their dynamics, then position extrema are guaranteed to have switching controls at time $T_s = t_f$.

3.3 Solution Procedure

In this section, a solution procedure for Theorem 3.2.2 is examined in detail. With minor modifications, the same procedure can be adapted to Theorem 3.2.3 and Corollaries 3.2.3 and 3.2.4, and 3.2.5. The method shown here is by no means the only solution approach; it is simply the approach used to generate the results discussed in §4.3. The form of the equations to be solved from Theorem 3.2.2 presents the problem of actually computing $\mathbf{d}_0$, $\mathbf{v}_0$, $\mathbf{d}_f$, and λ_0. Fortunately, the form of equations (3.28) and (3.29), lends itself to adaptation to a Newton's method solving schema. Defining the unknown variables as

$$\zeta^T = \begin{bmatrix} \mathbf{d}_0^T & \mathbf{v}_0^T & \mathbf{d}_f^T & \lambda_0 \end{bmatrix} \tag{3.47}$$

The constraints (3.28) and (3.29) are re-written as

$$\mathbf{g}_1(\zeta)_{9\times 1} = \mathbf{M}\phi_z(t; \begin{bmatrix} \mathbf{d}_0 \\ \mathbf{v}_0 \end{bmatrix}, -2\lambda_0 \mathbf{E} \begin{bmatrix} \mathbf{d}_0 \\ \mathbf{v}_0 \end{bmatrix}, t) - \begin{bmatrix} \mathbf{d}_f \\ \mathbf{d}_f \\ \mathbf{0} \end{bmatrix}$$

$$\mathbf{g}_2(\zeta)_{1\times 1} = \begin{bmatrix} \mathbf{d}_0 \\ \mathbf{v}_0 \end{bmatrix}^T \mathbf{E} \begin{bmatrix} \mathbf{d}_0 \\ \mathbf{v}_0 \end{bmatrix} - 1 = 0$$

and are then combined into a composite function $\mathbf{g}(\zeta)$

$$\mathbf{g}(\zeta)^T = \begin{bmatrix} \mathbf{g}_1(\zeta)^T & \mathbf{g}_2(\zeta) \end{bmatrix}$$

whose zeros we are interested in computing (thereby satisfying the equations in Theorem 3.2.2). Using a Taylor expansion, $\mathbf{g}(\zeta)$ is written as

$$\mathbf{g}(\zeta_0 + \delta\zeta) = \mathbf{g}(\zeta_0) + \frac{\partial \mathbf{g}}{\partial \zeta_0}\delta\zeta + O(\|\delta\zeta\|^2)$$

where ζ_0 is the value about which the Taylor expansion is computed. Dropping second-order terms and higher, introducing an iteration based notation, and requiring that $\mathbf{g}(\zeta_0 + \delta\zeta) = \mathbf{0}$, we obtain

$$\delta\zeta_k = -\left[\frac{\partial \mathbf{g}}{\partial \zeta_k}\right]^{-1} \mathbf{g}(\zeta_k)$$

which provides the iteration formula:

$$\zeta_{k+1} = \zeta_k - \left[\frac{\partial \mathbf{g}}{\partial \zeta_k}\right]^{-1} \mathbf{g}(\zeta_k) \tag{3.48}$$

This formulation motivates the computation of $\partial\mathbf{g}/\partial\zeta$

$$\frac{\partial \mathbf{g}}{\partial \zeta} = \begin{bmatrix} \frac{\partial \mathbf{g}_1}{\partial \zeta} \\ \\ \frac{\partial \mathbf{g}_2}{\partial \zeta} \end{bmatrix} = \begin{bmatrix} \frac{\partial \mathbf{g}_1}{\partial \mathbf{d}_0} & \frac{\partial \mathbf{g}_1}{\partial \mathbf{v}_0} & \frac{\partial \mathbf{g}_1}{\partial \mathbf{d}_f} & \frac{\partial \mathbf{g}_1}{\partial \lambda_0} \\ \\ \frac{\partial \mathbf{g}_2}{\partial \mathbf{d}_0} & \frac{\partial \mathbf{g}_2}{\partial \mathbf{v}_0} & \frac{\partial \mathbf{g}_2}{\partial \mathbf{d}_f} & \frac{\partial \mathbf{g}_1}{\partial \lambda_0} \end{bmatrix} \tag{3.49}$$

which is a $(3n/2+1) \times (3n/2+1)$ matrix. Examining the partial derivatives of $\mathbf{g}_1(\zeta)$:

$$\frac{\partial \mathbf{g}_1}{\partial \mathbf{d}_0}_{9\times 3} = \mathbf{M}\frac{\partial \phi_z}{\partial \mathbf{d}_0} \tag{3.50}$$

$$\frac{\partial \mathbf{g}_1}{\partial \mathbf{v}_0}_{9\times 3} = \mathbf{M}\frac{\partial \phi_z}{\partial \mathbf{v}_0} \tag{3.51}$$

$$\frac{\partial \mathbf{g}_1}{\partial \mathbf{d}_f}_{9\times 3} = -\begin{bmatrix} \mathbb{I} \\ \\ \mathbb{I} \\ \\ \mathbf{0} \end{bmatrix} \tag{3.52}$$

$$\frac{\partial \mathbf{g}_1}{\partial \lambda_0}_{9\times 1} = \frac{\partial \phi_z}{\partial \lambda_0} \tag{3.53}$$

Similarly, for $\mathbf{g}_2(\zeta)$:

$$\frac{\partial \mathbf{g}_2}{\partial \mathbf{d}_0}_{1\times 3} = 2\begin{bmatrix} \mathbf{d}_0 \\ \\ \mathbf{v}_0 \end{bmatrix}^T \mathbf{E} \begin{bmatrix} \mathbb{I} \\ \\ \mathbf{0} \end{bmatrix}$$

$$\frac{\partial \mathbf{g}_2}{\partial \mathbf{v}_0}_{1\times 3} = 2\begin{bmatrix} \mathbf{d}_0 \\ \\ \mathbf{v}_0 \end{bmatrix}^T \mathbf{E} \begin{bmatrix} \mathbf{0} \\ \\ \mathbb{I} \end{bmatrix}$$

$$\frac{\partial \mathbf{g}_2}{\partial \mathbf{d}_f}_{1\times 3} = \mathbf{0}$$

$$\frac{\partial \mathbf{g}_2}{\partial \lambda_0}_{1\times 1} = 0$$

By definition, the trajectory solution $\phi_z(\cdot)$ is one-to-one and onto with respect to $\mathbf{d}_0$, $\mathbf{v}_0$, $\mathbf{p}_{d,0}$, and $\mathbf{p}_{v,0}$. Also by definition, $\mathbf{E}$ is full rank. Since $(\mathbf{d}_0, \mathbf{v}_0)$ is on the surface of (3.10), it may never be the trivial

solution ($\mathbf{x}_0 = \mathbf{0}$).

There is now both a set of equations given by Theorem 3.2.2 that determine the maximum distance reachability given an ellipsoidal initial reachability set and all the necessary equations to apply Newton's method in solving those equations.

3.3.1 Linear Time-Varying Dynamics

In the case that an ERPS has dynamics of the form $\dot{\mathbf{x}} = \mathbf{A}(t)\mathbf{x} + \mathbf{B}(t)\mathbf{u}$, many simplifications of the results in Section 3.2.1 can be made.

The co-state dynamics may be written as

$$\dot{\mathbf{p}} = -\mathbf{A}(t)^T\mathbf{p}$$

Giving the time-parametric solution:

$$\mathbf{p}(t) = \mathbf{\Phi}_p(t, t_0)\mathbf{p}_0$$

Because $\mathbf{p}_0 = -2\lambda_0\mathbf{E}\mathbf{x}_0$, this further simplifies to

$$\mathbf{p}(t) = 2\mathbf{\Phi}_p(t, t_0)\mathbf{E}\mathbf{x}_0 \tag{3.54}$$

The time-parametric optimal control $\mathbf{u}^*(t)$ becomes

$$\mathbf{u}^*(t) = u_m \frac{\mathbf{B}(t)^T\mathbf{\Phi}_p(t, t_0)\mathbf{E}\mathbf{x}_0}{\|\mathbf{B}(t)^T\mathbf{\Phi}_p(t, t_0)\mathbf{E}\mathbf{x}_0\|_2} \tag{3.55}$$

The state equation of motion then becomes

$$\dot{\mathbf{x}} = \mathbf{A}(t)\mathbf{x} + u_m\mathbf{B}(t)\frac{\mathbf{B}(t)^T\mathbf{\Phi}_p(t, t_0)\mathbf{E}\mathbf{x}_0}{\|\mathbf{B}(t)^T\mathbf{\Phi}_p(t, t_0)\mathbf{E}\mathbf{x}_0\|_2}$$

providing the state time-parametric solution:

$$\begin{aligned}\mathbf{x}(t) = \mathbf{\Phi}_\mathbf{x}(t, t_0)\mathbf{x}_0 + \\ u_m\int_{t_0}^{t}\mathbf{\Phi}_x(\tau, t_0)\mathbf{B}(\tau)\frac{\mathbf{B}(\tau)^T\mathbf{\Phi}_p(\tau, t_0)\mathbf{E}\mathbf{x}_0}{\|\mathbf{B}(\tau)^T\mathbf{\Phi}_p(\tau, t_0)\mathbf{E}\mathbf{x}_0\|_2}d\tau\end{aligned} \tag{3.56}$$

This realization is similar to previously derived equations of motion for LTV systems with ellipsoidal feasible control sets U [56]. The switching time criterion $\mathbf{P}(t, \mathbf{x}_0, \lambda_0, \mathbf{E}, t_0)$ reduces to

$$\mathbf{P}(t, \mathbf{x}_0, \lambda_0, \mathbf{E}, t_0) = 2\mathbf{B}(t)^T \mathbf{\Phi}_p(t, t_0)\mathbf{x}_0$$

and is only dependent on t and $\mathbf{x}_0$. The reachability results from Section 3.2.1 may now be applied to the time-parametric solutions for $\mathbf{x}(t)$ and $\mathbf{p}(t)$, which now have forms that are much easier to compute than in the general nonlinear case. Note also that if a state transition matrix for $\mathbf{z}(t)$, $\mathbf{\Phi}_z(t, t_0)$ is available, then

$$\frac{\partial \phi_z}{\partial \mathbf{z}_0} = \mathbf{\Phi}_z(t, t_0) \tag{3.57}$$

yielding

$$\frac{\partial \phi_z}{\partial \mathbf{d}_0}_{2n\times n/2} = \mathbf{\Phi}_z(t, t_0)_{2n\times 2n} \begin{bmatrix} \mathbb{I} \\ \mathbf{0} \\ -2\lambda_0 \mathbf{E}_{dd} \\ -2\lambda_0 \mathbf{E}_{dv}^T \end{bmatrix}_{2n\times n/2}$$

and

$$\frac{\partial \phi_z}{\partial \mathbf{v}_0}_{2n\times n/2} = \mathbf{\Phi}_z(t, t_0)_{2n\times 2n} \begin{bmatrix} \mathbf{0} \\ \mathbb{I} \\ -2\lambda_0 \mathbf{E}_{dv} \\ -2\lambda_0 \mathbf{E}_{vv} \end{bmatrix}_{2n\times n/2}$$

with $\mathbf{E}_{dd}$, $\mathbf{E}_{dv}$, and $\mathbf{E}_{vv}$ being the appropriate sub-matrices of the ellipsoid matrix $\mathbf{E}$.

3.3.2 Linear Time-Invariant Dynamics

If the dynamics of an ERPS happen to be of the form $\dot{\mathbf{x}} = \mathbf{A}\mathbf{x} + \mathbf{B}\mathbf{u}$, the the results from §3.3.1 may be further simplified, as the state-transition matrix $\mathbf{\Phi}_p(t, t_0)$ for the adjoint state may be computed analytically as

$$\mathbf{\Phi}_p(t, t_0) = e^{-\mathbf{A}^T(t-t_0)} \tag{3.58}$$

yielding an analytical solution for the adjoint as a function of time. Note that this also produces an analytic function of $\mathbf{u}^*(t)$, for which potential switching times may be algebraically computed. This result will be demonstrated in several following examples.

3.4 Examples

This section contains examples illustrating the Theorems, Corollaries, and Remarks discussed above. Examples 3.1, 3.2, and 3.3 are all analytically solvable as mentioned in the Introduction and shown by [44]. Example 3.4 applies the results of this paper to a 4-dimensional nonlinear relative orbit motion problem.

3.4.1 Example 3.1: Single DOF Free Motion

A single DOF free motion example is very instructive in emphasizing the results in Theorems 3.2.2, 3.2.3, and 3.2.4, as well as Corollary 3.2.2. To begin with, the boundary condition $V(\mathbf{x}_0, t_0)$, $\mathbf{x} \in \mathbb{R}^2$, $t_0 = 0$, is chosen to be

$$V(\mathbf{x}_0, t_0) = \begin{bmatrix} d_0 \\ v_0 \end{bmatrix}^T \begin{bmatrix} \frac{1}{2} & 0 \\ 0 & \frac{1}{2} \end{bmatrix} \begin{bmatrix} d_0 \\ v_0 \end{bmatrix} - 1 \leq 0$$

For free motion, the dynamic equations are

$$\begin{bmatrix} \dot{d} \\ \dot{v} \end{bmatrix} = \begin{bmatrix} 0 & 1 \\ 0 & 0 \end{bmatrix} \begin{bmatrix} d \\ v \end{bmatrix} + \begin{bmatrix} 0 \\ 1 \end{bmatrix} u \tag{3.59}$$

From equations (3.12), (3.18), (3.19), (3.20), and dynamics (3.59), the following results and closed-loop optimal dynamics are obtained:

$$p_v(t) = -d_0 t + v_0 \tag{3.60}$$

$$\mathbf{P}(t, \mathbf{x}_0, \lambda_0, \mathbf{E}, t_0) = \begin{bmatrix} -t & 1 \end{bmatrix} \begin{bmatrix} d \\ v \end{bmatrix} \tag{3.61}$$

$$u(t) = u_m \frac{p_v(t)}{\|p_v(t)\|} = u_m \frac{-d_0 t + v_0}{\| - d_0 t + v_0 \|} \tag{3.62}$$

$$-d_0 T_s + v_0 = 0 \tag{3.63}$$

The piece-wise continuous time-parametric dynamics for $0 \leq t \leq T_s$ are:

$$d(t) = d_0 + v_0 t + u_m \frac{1}{2} \frac{v_0}{|v_0|} t^2 \tag{3.64}$$

$$v(t) = v_0 + u_m \frac{v_0}{|v_0|} t \tag{3.65}$$

and for $t > T_s$ (after the switching time):

$$d(t) = d_{T_s} + v_{T_s}(t - T_s) - u_m \frac{1}{2} \frac{v_0}{|v_0|} (t - T_s)^2 \tag{3.66}$$

$$v(t) = v_{T_s} - u_m \frac{v_0}{|v_0|} (t - T_s) \tag{3.67}$$

The switching time T_s can be negative, however since $t_0 = 0 \leq t$, then any initial condition (d_0, v_0) such that $v_0/d_0 < 0$ will not result in a switching trajectory (it will have in a sense already switched). For the purposes of this example, the maximum control is chosen to be $u_m = 1$ and the reachability surface in both position (d) and velocity (v) will be examined at times $t_f = 0$, $t_f = 0.5$, $t_f = 1$, $t_f = 1.5$, and $t_f = 2$. Figure 3.3 shows a sampling of points located on the initial reachability set propagated according to (3.64) and (3.65). Table 3.1 demonstrates the principles in Theorem 3.2.2 by solving (3.28) and (3.29) for this problem. Similarly, Table 3.2 does the same for Theorem 3.2.3 by solving (3.32) and (3.33).

Table 3.1: Position maxima, associated initial condtions, Lagrange multiplier, and computed switching time for Example 1

	$t_f = 0$	$t_f = 0.5$	$t_f = 1$	$t_f = 1.5$	$t_f = 2$
$d_{f,mx}$	1.414	1.706	2.500	3.675	5.162
d_0	1.414	1.265	1.000	0.784	0.632
v_0	0.000	0.632	1.000	1.177	1.265
λ_0	-1.000	-1.349	-2.500	-4.684	-8.162
T_s	0	0.500	1.000	1.500	2.000

Table 3.2: Velocity maxima, associated initial condtions, and Lagrange multiplier for Example 1

	$t_f = 0$	$t_f = 0.5$	$t_f = 1$	$t_f = 1.5$	$t_f = 2$
$v_{f,mx}$	1.414	1.914	2.414	2.914	3.414
d_0	0.000	0.000	0.000	0.000	0.000
v_0	1.414	1.414	1.414	1.414	1.414
λ_0	-1.000	-1.354	-1.707	-2.061	-2.414

Note in Figure 3.3 that the necessary conditions for a given final state pair to have originated in

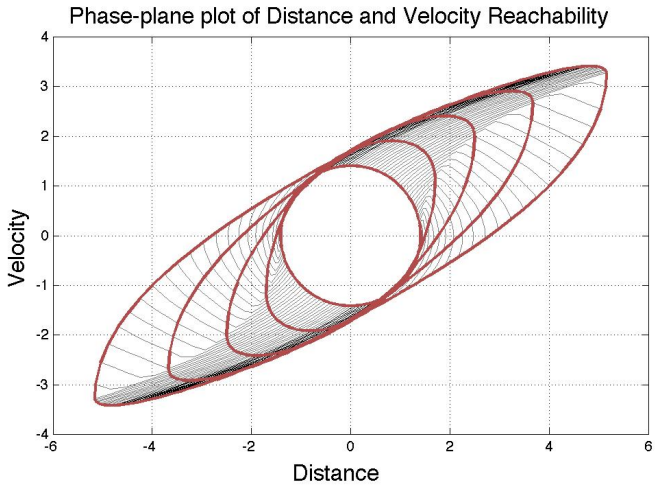

Figure 3.3: 1-DOF free motion reachability phase-space at times $t_f = 0$, $t_f = 0.5$, $t_f = 1$, $t_f = 1.5$, and $t_f = 2$ (red lines). Note that the distance (position) maxima occur exactly when the control $u(t)$ is switching, demonstrating Theorem 3.2.4.

the initial reachability set are that (d_f, v_f) be strictly bounded by the d_f and v_f values shown in Tables 3.1 and 3.2, just as required in Corollary 3.2.2. The numerically generated results in Tables 3.1 and 3.2 match the analytical trajectories and switching times given above to within the stopping criteria of the zero-finding procedure. Further, As shown by Theorem 3.2.4 and Table 3.1, the position maxima occur exactly when $t_f = T_s$, which for this example is $t_f = v_0/d_0$. It is also important to observe that the surface of the reachability set is not guaranteed to be smooth at any time $t > t_0$, as can be seen on the $t_f = 2$ surface in Figure 3.3 where the optimal position trajectory is currently switching.

3.4.2 Example 3.2: Single DOF Oscillator

A single DOF oscillator is instructive in emphasizing the results in Theorems 3.2.2, 3.2.3, and 3.2.4, as well as Corollary 3.2.2. To begin with, the boundary condition $V(\mathbf{x}_0, t_0)$, $\mathbf{x} \in \mathbb{R}^2$, $t_0 = 0$, is chosen to be

$$V(\mathbf{x}_0, t_0) = \begin{bmatrix} d_0 \\ v_0 \end{bmatrix}^T \begin{bmatrix} \frac{1}{2} & 0 \\ 0 & \frac{1}{2} \end{bmatrix} \begin{bmatrix} d_0 \\ v_0 \end{bmatrix} - 1 \leq 0$$

For an oscillator, the dynamic equations are

$$\begin{bmatrix} \dot{d} \\ \dot{v} \end{bmatrix} = \begin{bmatrix} 0 & 1 \\ -\omega^2 & 0 \end{bmatrix} \begin{bmatrix} d \\ v \end{bmatrix} + \begin{bmatrix} 0 \\ 1 \end{bmatrix} u \tag{3.68}$$

where ω is the natural frequency of the oscillator. From equations (3.12), (3.18), (3.19), (3.20), and dynamics (3.68), the following results and closed-loop optimal dynamics are obtained:

$$p_v(t) = -\frac{1}{\omega}\sin(\omega t)d_0 + \cos(\omega t)v_0 \tag{3.69}$$

$$\mathbf{P}(t, \mathbf{x}_0, \lambda_0, \mathbf{E}, t_0) = \begin{bmatrix} -\frac{1}{\omega}\sin(\omega t) & \cos(\omega t) \end{bmatrix} \begin{bmatrix} d \\ v \end{bmatrix} \tag{3.70}$$

$$u(t) = u_m \frac{-\frac{1}{\omega}\sin(\omega t)d_0 + \cos(\omega t)v_0}{\| -\frac{1}{\omega}\sin(\omega t)d_0 + \cos(\omega t)v_0 d_0 \|} \tag{3.71}$$

$$T_s = \frac{1}{\omega}\tan^{-1}\left(\omega \frac{v_0}{d_0}\right) \tag{3.72}$$

Note that since $p_v(t)$ is periodic, the switching time T_s is periodic as well ($T_s' = T_s + k2\pi,\ k \in \mathbb{Z}$). The pre-switching time-parametric dynamics are:

$$\begin{aligned} d(t) = \cos(\omega t)d_0 + \sin(\omega t)v_0 + \\ u_m \tfrac{2}{\omega^2}\sin\left(\tfrac{1}{2}\omega t\right)^2 u(t) \end{aligned} \tag{3.73}$$

$$v(t) = -\omega\sin(\omega t)d_0 + \cos(\omega t)v_0 + \frac{1}{\omega}\sin(\omega t)u(t) \tag{3.74}$$

The post-switch time-parametric equations are easily computed. For this example, $u_m = 1$ and $\omega = 1$. The reachability set at times $t_f = 0$, $t_f = \pi/4$, $t_f = \pi/2$, $t_f = 3\pi/2$, and $t_f = \pi$ are computed and shown along with sample trajectories on Figure 3.4. As with Example 3.1, Theorems 3.2.2 and 3.2.3 are applied and the results are shown in Tables 3.3 and 3.4. Figure 3.6 visualizes Corollary 3.2.2 by plotting $d_{f,mx}$ and $v_{f,mx}$ for $t_f = \pi/2$ directly on the reachability phase-plane. Inspection of Figure 3.6 emphasizes that if a trajectory starts within the initial reachability set it will be strictly contained within the bounds computed using Theorems 3.2.2 and 3.2.3.

Figure 3.6 demonstrates the computation gain to be realized if only necessary conditions for reachability are desired. Parameterizing the 1-DOF problem and discretizing the surface of the original reachability

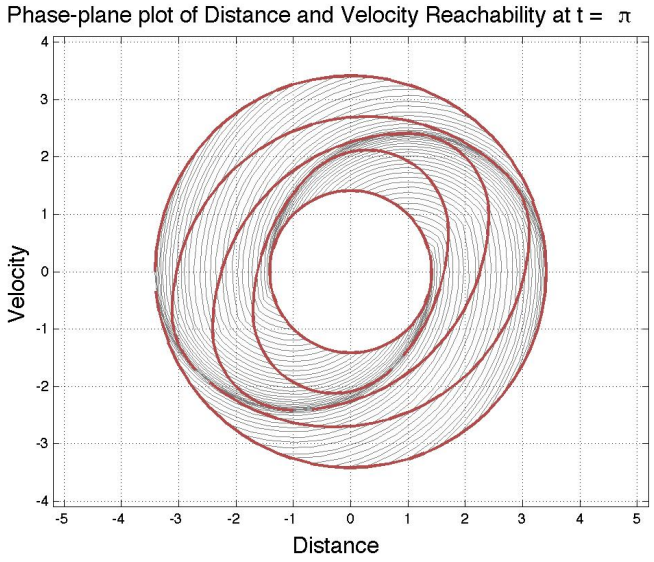

Figure 3.4: 1-DOF oscillator reachability phase-space at times $t_f = 0$, $t_f = \frac{\pi}{4}$, $t_f = \frac{\pi}{2}$, $t_f = \frac{3\pi}{4}$, and $t_f = \pi$ (red lines)

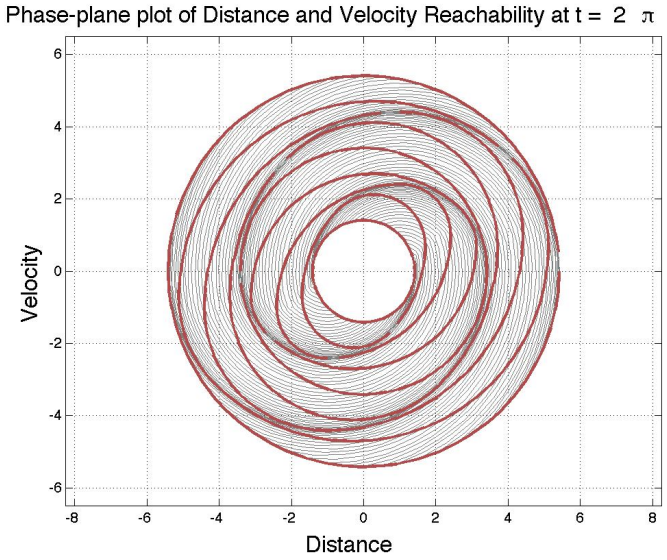

Figure 3.5: 1-DOF oscillator reachability phase-space at times $t_f = 0$ to $t_f = 2\pi$ (red lines) to emphasize periodicity of reachability sets.

surface requires k points, each of which must be propagated (using methods discussed in Section 3.1) from t_0 to t_f. Conversely, applying Theorems 3.2.2 and 3.2.3 requires only two zero-finding computations. Extending this to a 3-DOF system, the discretization of the initial reachability surface (a hyper-ellipsoid of dimension 5)

Table 3.3: Position maxima, associated initial condtions, Lagrange multiplier, and computed switching time for Example 3.2

	$t_f = 0$	$t_f = \frac{\pi}{4}$	$t_f = \frac{\pi}{2}$	$t_f = \frac{3\pi}{4}$	$t_f = \pi$
$d_{f,mx}$	1.414	1.707	2.414	3.121	3.414
d_0	1.414	1.000	0.000	-1.000	-1.414
v_0	0.000	1.000	1.414	1.000	0.000
λ_0	-0.500	-0.604	-0.854	-1.104	-1.207
T_s	0.000	0.785	1.571	2.356	3.142

Table 3.4: Velicty maxima, associated initial condtions, and Lagrange multiplier for Example 3.2

	$t_f = 0$	$t_f = \frac{\pi}{4}$	$t_f = \frac{\pi}{2}$	$t_f = \frac{3\pi}{4}$	$t_f = \pi$
$v_{f,mx}$	1.414	2.121	2.414	2.707	3.414
d_0	0.000	-1.000	-1.414	-1.000	0.000
v_0	1.414	1.000	0.000	-1.000	-1.414
λ_0	-1.000	-1.500	-1.707	-1.914	-2.414

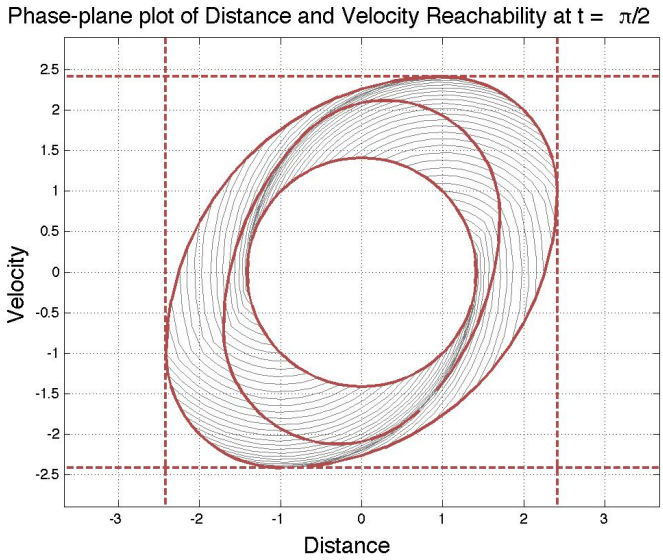

Figure 3.6: 1-DOF oscillator reachability at time $t_f = \pi/2$ (solid red) is bounded by $d_{f,mx} = 2.414$ and $v_{f,mx} = 2.414$ (dashed red)

contains k^5 points which must be propagated, after which the reachability hyper-surface must be projected down to position and velocity space. However, determining the necessary conditions for reachability using Theorems 3.2.2 and 3.2.3 still only requires two zero-finding computations (albeit in higher dimensions). As with the free motion example, the numerically generated results in Tables 3.3 and 3.4 match the analytical trajectories and switching times given above to within the stopping criteria of the zero-finding procedure.

3.4.3 Example 3.3: Two DOF Free Motion

The purpose of this example is to apply the developed theory to the same system as in Example 3.1 in a higher-dimensional problem, allowing for some deeper insight into Corollaries 3.2.3 and 3.2.4. The initial reachability set is represented by $V(\mathbf{x}_0, t_0)$, with $\mathbf{x}_0 \in \mathbb{R}^4$ and $t_0 = 0$:

$$V(\mathbf{x}_0, t_0) = \begin{bmatrix} \mathbf{d}_0 \\ \mathbf{v}_0 \end{bmatrix}^T \begin{bmatrix} \frac{1}{2}\mathbb{I} & \mathbf{0} \\ \mathbf{0} & \frac{1}{2}\mathbb{I} \end{bmatrix} \begin{bmatrix} \mathbf{d}_0 \\ \mathbf{v}_0 \end{bmatrix} - 1 \leq 0$$

For 2-DOF Free Motion, the dynamics are

$$\begin{bmatrix} \dot{\mathbf{d}}_0 \\ \dot{\mathbf{v}}_0 \end{bmatrix} = \begin{bmatrix} \mathbf{0} & \mathbb{I} \\ \mathbf{0} & \mathbf{0} \end{bmatrix} \begin{bmatrix} \mathbf{d}_0 \\ \mathbf{v}_0 \end{bmatrix} + \begin{bmatrix} \mathbf{0} \\ \mathbb{I} \end{bmatrix} \mathbf{u} \tag{3.75}$$

Again, from equations (3.12), (3.18), (3.19), (3.20), and dynamics (3.75), the following results and closed-loop optimal dynamics are obtained:

$$\mathbf{p}_v(t) = -\mathbf{d}_0 t + \mathbf{v}_0 \tag{3.76}$$

$$\mathbf{P}(t, \mathbf{x}_0, \lambda_0, \mathbf{E}, t_0) = \begin{bmatrix} -t\mathbb{I} & \mathbb{I} \end{bmatrix} \mathbf{x}_0 \tag{3.77}$$

$$\mathbf{u}(t) = u_m \frac{\mathbf{p}_v(t)}{\|\mathbf{p}_v(t)\|} = u_m \frac{-\mathbf{d}_0 t + \mathbf{v}_0}{\| -\mathbf{d}_0 t + \mathbf{v}_0 \|} \tag{3.78}$$

$$T_s = \{t | \mathbf{P}(t, \mathbf{x}_0, \lambda_0, \mathbf{E}, t_0) = \mathbf{0}\} \tag{3.79}$$

For this example there is only a switching time T_s for a trajectory starting at $(\mathbf{d}_0, \mathbf{v}_0)$ if $\mathbf{d}_0$ and $\mathbf{v}_0$ are parallel. As Lemma 3.2.1 shows, problems of dimension n only have m switching dimensions at any time t, meaning that many initial states satisfying $V(\mathbf{x}_0, t_0) = 0$ will not switch (and thus, according to Theorem 3.2.4, will never be position maxima). The time-parametric state dynamics are:

$$\mathbf{d}(t) = \mathbf{d}_0 + \mathbf{v}_0 t + u_m \int_0^t \tau \frac{-\mathbf{d}_0 \tau + \mathbf{v}_0}{\| -\mathbf{d}_0 \tau + \mathbf{v}_0 \|} d\tau \tag{3.80}$$

$$\mathbf{v}(t) = \mathbf{v}_0 + u_m \int_0^t \frac{-\mathbf{d}_0 \tau + \mathbf{v}_0}{\| -\mathbf{d}_0 \tau + \mathbf{v}_0 \|} d\tau \tag{3.81}$$

Because of the higher-dimensionality of this example and in the interest of brevity, only the maximum position reachability set illustrating Corollary 3.2.3 is computed. For this example, the maximum control input is chosen to be $u_m = 1$. Figure 3.7 depicts a discretization of the exact position reachability set found by choosing initial directions $\hat{\mathbf{d}}_0$ and applying equations (3.28) and (3.29) with the substitution $\mathbf{d}_0 = d\hat{\mathbf{d}}_0$, as shown in Corollary 3.2.3.

Because this is a 2-DOF example, initial directions are parameterizable in terms of a single angle θ, which is varied from $\theta = 0$ to $\theta = 2\pi$ in $\pi/64$ increments. This being the case, the entire maximum position reachability set at time $t_f = 1$ is determined with $k = 129$ zero-finding operations, rather than exploring the entire feasible space of $k^{n-1} = k^3 = 2,146,689$ initial conditions, integrating, and searching for position maxima.

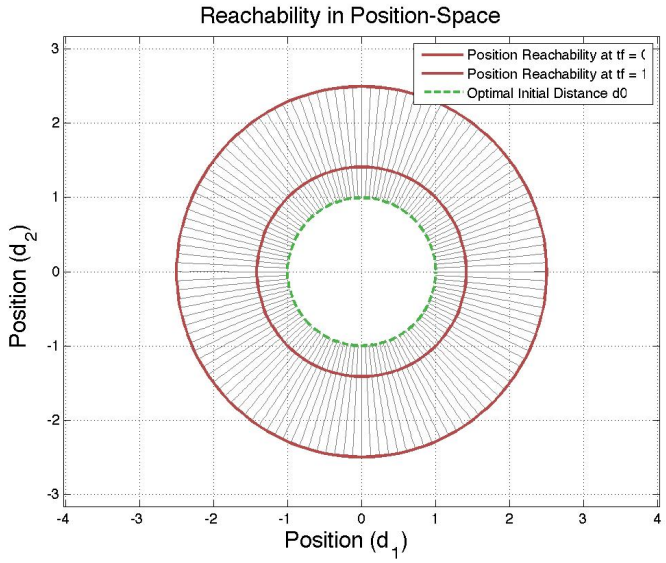

Figure 3.7: 2-DOF free motion reachability illustration of Corollary 3.2.3. Note that all of the optimal trajectories satisfy Theorem 3.2.4 and are currently switching at time $t_f = T_s = 1$.

To gain additional insight into Theorem 3.2.4, Figure 3.8 shows a single trajectory that touches the maximum position reachability surface at $t = 1$ compared with neighboring trajectories. All of the trajectories shown in Figure 3.8 have the same initial position vector $\mathbf{d}_0^T = \left[\sqrt{2}, \sqrt{2}\right]^T$, but are allowed to vary $\mathbf{v}_0$ while satisfying the ellipsoid constraint (3.29). The optimal trajectory is indeed switching, as evaluting $\mathbf{p}_v(t)$ yields

$$\mathbf{p}_v(t) = -\mathbf{d}_0 t + \mathbf{v}_0 = -\begin{bmatrix} \sqrt{2} \\ \sqrt{2} \end{bmatrix} t + \begin{bmatrix} \sqrt{2} \\ \sqrt{2} \end{bmatrix} = 0$$

which implies that $t = T_s = 1$.

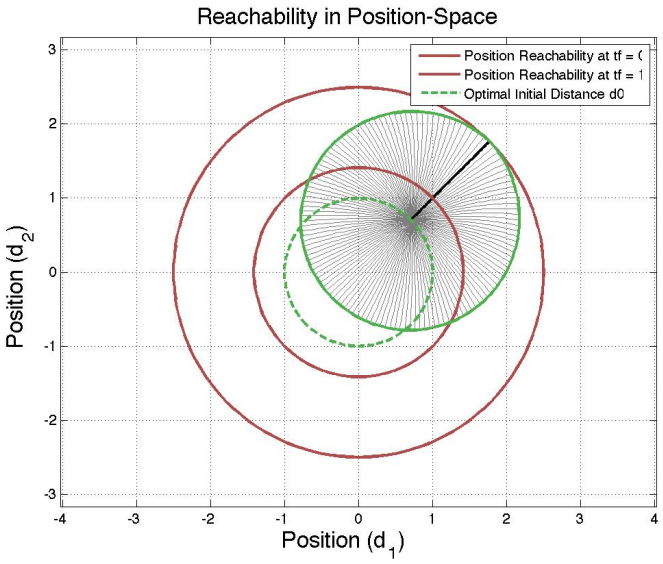

Figure 3.8: Visualization of optimal position extrema trajectory (solid black) and neighboring suboptimal trajectories (thin grey). Observe that the sub-optimal trajectories are slowly curving away from the optimal trajectory.

As with Example 3.2, Theorem 3.2.2 may be applied to this problem, and a bounding circle with radius $\mathbf{d}_{f,mx}$ can be found with a single zero-finding computation. Because of the ellipsoid $\mathbf{E}$ choice in this example, such a circle would exactly overlap the maximum position reachability set boundaries found using Corollary 3.2.3.

3.4.4 Example 3.4: 2-DOF Nonlinear Relative Orbital Motion

Given an arbitrary reference orbit solution $\mathbf{x}_r(t)$, the reference radius (r_r), radius time derivative ($\dot{r}_r$), and true anomaly rate ($\dot{f}_r$) can be directly computed. In this case, the relative equations of motion can be

written in the form $\dot{\mathbf{x}} = \mathbf{f}(\mathbf{x}, t) + \mathbf{B}\mathbf{u}$ [65]:

$$\dot{\mathbf{x}} = \begin{bmatrix} \dot{x} \\ \dot{y} \\ \ddot{x} \\ \ddot{y} \end{bmatrix} = \begin{bmatrix} \dot{x} \\ \dot{y} \\ 2\dot{f}_r\left(\dot{y} - y\frac{\dot{r}_r}{r_r}\right) + x\dot{f}_r^2 + \frac{\mu}{r_r^2} - \frac{\mu}{r^3}\left(r_r + x\right) \\ -2\dot{f}_r\left(\dot{x} - x\frac{\dot{r}_r}{r_r}\right) + y\dot{f}_r^2 - \frac{\mu}{r^3}y \end{bmatrix} + \mathbf{B}\mathbf{u} \tag{3.82}$$

where

$$\mathbf{B} = \begin{bmatrix} \mathbf{0}_{2\times 2} \\ \mathbb{I}_{2\times 2} \end{bmatrix}$$

and the inertial radius of the spacecraft is r, defined as

$$r = \sqrt{\left(r_r + x\right)^2 + y^2}$$

$\partial\mathbf{f}/\partial\mathbf{x}$ can now be computed. These equations of motion are in a rotating Hill frame, meaning that the radial axis (x) always points along the radius vector from the Earth, and the along-track axis (y) is defined as orthogonal to the radial vector and positive in the direction of the reference orbit velocity. In this frame, the negative (x) axis always points towards Earth. The partial with respect to the control input, $\partial\mathbf{f}/\partial\mathbf{u}$, is simply

$$\frac{\partial \mathbf{f}}{\partial \mathbf{u}} = \mathbf{B} \tag{3.83}$$

To compute $\partial\phi_z/\partial\mathbf{d}_0$ and $\partial\phi_z/\partial\mathbf{v}_0$, $\mathbf{\Phi}_z(t, t_0)$ must be integrated over the interval $s \in [t_0, t]$ with the initial condition $\mathbf{\Phi}_z(t_0, t_0) = \mathbb{I}$. The equation to integrate is

$$\dot{\mathbf{\Phi}}_z(s, t_0) = \mathbf{A}_z\mathbf{\Phi}_z(s, t_0)$$

where $\mathbf{A}_z = \partial\mathbf{f}_z/\partial\mathbf{z}$ evaluated at $\mathbf{z} = \mathbf{z}(s)$, $s \in [t_0, t]$ (note that $\mathbf{z}(s)$ must be integrated simultaneously with $\mathbf{\Phi}_z(s, t_0)$). For this example, $\mathbf{A}_z$ becomes

$$\mathbf{A}_z = \begin{bmatrix} \frac{\partial \mathbf{f}}{\partial \mathbf{x}} & u_m\mathbf{B}\left(\frac{\mathbb{I}}{\|\mathbf{B}^T\mathbf{p}\|} - \frac{\mathbf{B}^T\mathbf{p}\mathbf{p}^T\mathbf{B}}{\|\mathbf{B}^T\mathbf{p}\|^3}\right)\mathbf{B}^T \\ \frac{\partial}{\partial \mathbf{x}}\left(-\frac{\partial \mathbf{f}}{\partial \mathbf{x}}^T\mathbf{p}\right) & -\frac{\partial \mathbf{f}}{\partial \mathbf{x}}^T \end{bmatrix} \tag{3.84}$$

As with previous examples, the initial reachability set represented by $V(\mathbf{x}_0, t_0)$ is chosen to be

$$V(\mathbf{x}_0, t_0) = \begin{bmatrix} \mathbf{d}_0 \\ \mathbf{v}_0 \end{bmatrix}^T \begin{bmatrix} \frac{1}{r_d^2}\mathbb{I} & 0 \\ 0 & \frac{1}{r_v^2}\mathbb{I} \end{bmatrix} \begin{bmatrix} \mathbf{d}_0 \\ \mathbf{v}_0 \end{bmatrix} - 1 \leq 0$$

with r_d set to 1m and r_v set to 0.1 m/s. Because motion in the z direction is only weakly coupled with x and y motion, and because two-dimensional figures have a more straightforward interpretation, the problem is restricted to motion in x and y, causing $\mathbf{x}_0 \in \mathbb{R}^4$.

The chosen reference orbit is in a equatorial circular Low Earth Orbit (LEO) with an altitude of 400km. The argument of perigee is 0 degrees, and the initial true anomaly is 0 degrees (the object starts at perigee). This is integrated over the time interval $[0, P]$, where P is the orbit period ($P = 5556s$), to produce $\mathbf{r}_r(t)$ and $\mathbf{v}_r(t)$, from which $r_r(t)$, $\dot{r}_r(t)$, and $\dot{f}_r(t)$ are determined. The available control authority is chosen to be $u_m = 2e^{-5}m/s^2$, equivalent to a 500kg spacecraft with a 0.01N thruster. In using Corollary 3.2.3, $\hat{\mathbf{d}}_0$ is varied within the x-y plane over $[0, 2\pi]$ at samplings sufficient to generate detailed surfaces. Figure 3.9 shows the maximum position reachability set and associated trajectories in the rotating Hill frame (in which the coordinates are set) at $t_f = \frac{3}{4}P$, and Figure 3.10 shows the same set with $t_f = [\frac{1}{4}P, \frac{1}{2}P, \frac{3}{4}P, P]$.

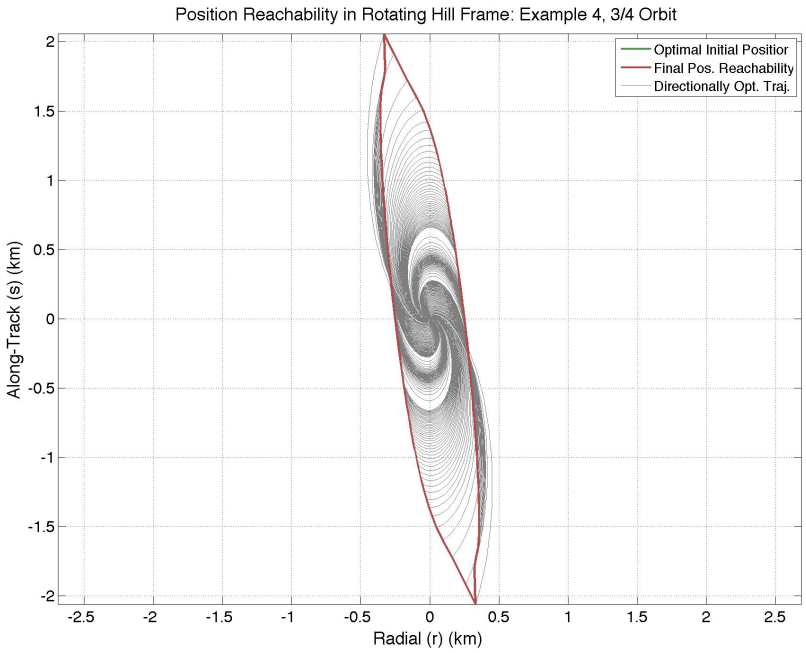

Figure 3.9: Position-Reachability Set for 2-DOF Nonlinear Relative Keplerian motion in a rotating Hill frame.

As seen in Figures 3.9 and 3.10, despite evenly distributed initial directions, the dynamics cause significant distortion in the distribution of the final positions, with the vast majority of final positions $\mathbf{d}_f$

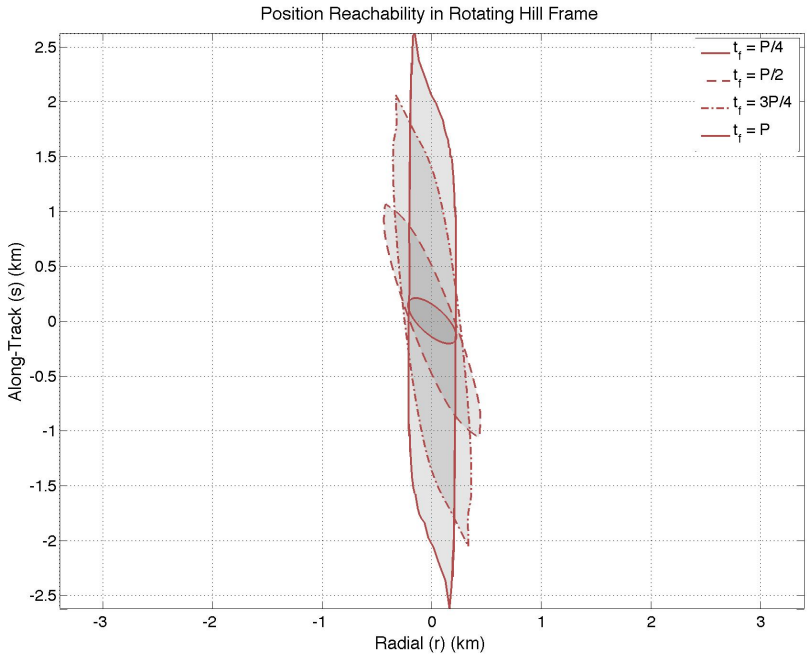

Figure 3.10: Position-Reachability Set for 2-DOF Nonlinear Relative Keplerian motion at times $t_f = [\frac{1}{4}P, \frac{1}{2}P, \frac{3}{4}P, P]$ in a rotating Hill frame

being clustered as time progresses. Also, because the control authority u_m is relatively weak compared to the local dynamics, the reachability set expands and contracts over time, implying that relative points reachable at one time may not be reachable at subsequent times. It should be noted that, as the final time t_f increased, the solutions for each directional reachability trajectory exhibited increasingly larger residuals when trying to satisfying the equations shown in Corollary 3.2.3. At this time it is suspected this is due to a skewing of the integrated state-transition matrix $\mathbf{\Phi}_z(t_f, t_0)$, as a straightforward Runga-Kutta $4^{th}/5^{th}$ integration algorithm was used. In concordance with Remark 3.2.4, $\dot{\mathcal{H}} = 0$ for these dynamics, suggesting that the structure of the Hamiltonian would best be preserved using Symplectic integration methods.

3.5 Chapter Summary

Previous related work and theory development is discussed, along with several examples of applied reachability in existing literature. Connections between optimal control, the Hamilton Jacobi Bellman PDE, and minimum time reachability set computation are examined. The Hamilton Jacobi Bellman PDE

reachability formalism is applied to Restricted Nonlinear Systems (RNSs) with ellipsoidal initial reachability sets, making derived results consistent with and directly applicable to industry-standard optimal estimation schema. For RNSs with ellipsoidal initial reachability sets, the optimal control is developed and switching conditions examined.

The concept of switching times in the context of reachability is formalized, and control switching is proven to occur for RNSs with ellipsoidal initial reachability sets and where $n > m$. Maximal position and velocity cases in optimal control were examined to prove that maximum bound calculations for both position- and velocity-space can be directly computed by solving two sets of $3n/2+1$ equations $O(k)$, rather than exhaustively searching the entire feasible set of initial conditions in $n-1$ dimensions ($O(k^{n-1})$). Taken together, the position and velocity extrema provide two necessary conditions for reachability from an initial ellipsoidal reachability set, offering a quick test for reachability. A further constrained application of optimal control yield a methodology to compute the exact maximum position- or velocity-reachable set by solving a set of $n+2$ equations over $n/2-1$ dimensions ($O(k^{n/2-1})$), rather than searching the feasible set of initial conditions in $n-1$ dimensions ($O(k^{n-1})$). However, the computational complexity is difficult to compare in the general case as the operation types are very different.

For RNSs in which input acts as an acceleration, it is shown that as a special case of Theorem 3.2.4 position extrema trajectories (global or directional) are always experiencing optimal control is switching precisely at the time in question.

Several examples are used to illustrate the theorems and corollaries developed in this chapter. Global position- and velocity-extrema are computed using the described methods, and the computational advantages are emphasized. A 1-DOF double-integrator and 1-DOF harmonic oscillator are analyzed in detail to emphasize extrema computation, reachability necessary conditions, and switching times. A 2-DOF free-motion example is examined to provide insight into the computation benefits of exact position reachability surface calculation. Lastly, a nonlinear 2-DOF Keplerian orbit relative motion example is given, highlighting the main thrust of nonlinear applicability derived in this paper.

Chapter 4

Generalized Metric Range Sets and Orbit Range

As discussed extensively in Chapter 1, computation of orbital range sets can provide significant tactical and strategic benefits to SSA activities. As a necessary pre-condition to computing orbit range sets, a rigorous framework supporting optimal generalized range theory must be developed. Two basic requirements on such a generalized range set are that all manner of range sets can be described by the new framework, and that the ranges be computed represent distance metrics (in the general sense). Building on results discussed in Chapter 2 regarding Optimal Control Problem (OCP) distance metrics, this chapter demonstrates how general independent parameter mapping functions may be constructed, examines cases in which generalized independent parameters also represent metrics, and rigorously defines Generalized Metric Range Sets. Orbit range is addressed first as a motivational problem with a resulting Lemma describing how singularities caused by coasting arcs may be avoided. Orbit range is addressed directly as an extended, detailed example, demonstrating how orbit range may be computed.

Range, whether for automobiles or aircraft, is typically defined as the time-independent maximum distance a vehicle can travel given a specified quantity of fuel. Such range sets are often used in strategic and tactical settings to determine where assets should be located. Range is also a useful mission planning tool; once generated it is very easy and intuitive to determine which objects are within or outside of the range set. Strategic, tactical, and mission planning tools such as range would be very useful for on-orbit spacecraft operations, however objects in orbit present two complications: 1) they are always moving along their potential fields, and 2) they may experience long periods of quiescence between maneuvers.

When endeavoring to compute an optimal reachability set with arbitrary integral constraints it is

convenient to use a framework that leverages proven results for traditional time-constrained reachability. A particularly useful example of such an optimal reachability set is the range set, often used in the context of aircraft, defined here as the set of reachable states in the state-space given an integral constraint that is also a metric. Integration constraints that possess distance metric properties are desirable as they are natural and intuitive measures of range.

Background literature in optimal reachability sets given time integral constraints (specifically integrating over $t \in [t_0, t_f]$) is extensive. If the optimal value function in the Dynamic Programing Equation (DPE) is not discontinuous it can be shown that the Hamilton Jacobi Bellman Partial Differential Equation (HJB PDE) must be satisfied along all optimal trajectories generating an optimal reachability set [34, 35, 37, 38, 57]. A short derivation of optimal reachability set theory given time integral constraints is given in §3.1.

Analytical solutions to the HJB PDE are rarely found, however many methods may be used to approximately generate optimal reachability sets given an initial or final set. Two methods briefly discussed here are viscosity solution methods and trajectory based methods. In general, viscosity solution methods directly integrate the HJB PDE given an initial condition (set) over time, either forwards or backwards, and compute the zero-level sets of the resulting value function [60, 61, 62, 63, 64]. Alternately, rather than treating the reachability set as a viscosity solution to the HJB PDE, individual optimal trajectories or expansions about these trajectories may be used to sample and represent the reachability set surface [66, 67, 24].

Alternative integration constraints of interest may include performance function costs, capital allocation limits, fuel mass, or control effort. High fidelity computations of fuel limited aircraft and/or launch vehicle range, electric motor angle/angle-rate reachability given total energy constraints may be useful.

The problem of computing optimal reachability sets for space applications has received considerable attention. There are two important sub-problems of reachability set computation: those of rendezvous, where the object's position and velocity is controlled, and those of interception, where only the position subspace must be controlled. Spacecraft rendezvous is particularly well studied, though typically in a fixed-time framework with individual trajectories. An example of an approach combining sequences of impulsive maneuvers and intermediate parking orbits is given by Marec [25] and more recently in Lou, et al [73]. Intercept trajectories or intercept rechability sets for space objects have been largely investigated in the

context of missile defense [74, 75]. Past studies first posed and solved free-time, fuel constrained reachability in the vicinity of initial orbits [25], as well as more general free-time, fuel constrained reachability sets for co-aligned, co-planar elliptical orbits [77]. More recently, direct parametric optimization of impulse timing and direction has begun to re-address the fuel-optimal, time-free orbit reachability problem [78] using only a single impulse outside of the purview of classical orbit transfer results [71, 80].

Motivated specifically by minimum-fuel orbital reachability but with other forms of integral constraint reachability sets in mind, the goal of this paper is to adapt the typical optimal reachability framework using general alternate independent parameters and constraints, as well as identify and address problematic mappings. Because under specific conditions optimal control performance indices have the same properties as metrics (Theorem 2.1.1), a rigorous definition of Generalized Metric Range Sets is given and several common instances discussed.

The extended example at the end of this chapter endeavors to demonstrate how ΔV-constrained range sets in orbit element space may be computed using the General Independent Parameter (GIP) HJB PDE, optimal control policies, and existing numerical reachability set tools. §4.4.1 discusses the chosen coordinates and equations of motion, assumptions, the mapping from time- to ΔV-integration space, the optimal control policy derivation, and the optimal state and adjoint equations of motion. In §4.4.2 three detailed examples are given. The first verifies the numerical results using classical ellipse-to-ellipse optimal trajectory maneuvers, the second demonstrates relative control authority in various orbit-element regions, and the third example examines some of the advantages of using implicitly defined surfaces to represent the surface of the range set. An extended discussion is given, followed by a Chapter Summary.

The specific contributions of this chapter are a) the introduction of a general alternate independent parameter and its mapping function with time, b) the derivation of the Hamilton-Jacobi-Bellman (HJB) PDE using an General Independent Parameter, c) the necessary conditions on the independent parameter mapping function for a mapping to be invertible, d) the definition and discussion of Generalized Metric Range Sets, e) an approach to transform a class of problems with discontinuous value functions to problems with continuous value functions, f) the use of ΔV as an independent parameter to compute orbit range sets, g) derivation of the resulting optimal control policy that recovers classical astrodynamics maneuvers

from the necessary conditions for optimal control, h) validation of the propagated orbit element range set using analogous classical maneuvers, and e) the demonstration of potential strategic, tactical, and mission planning applications of range sets.

A motivating problem is briefly outlined and some fundamental problems in computing a maximum range set (fuel-limited reachability) are discussed in §4.1. In §4.2 the independent parameter mapping function is introduced, followed by the detailed derivation of a General Independent Parameter (GIP) HJB PDE. Necessary conditions on the independent parameter mapping function integrand are developed and a discussion is given. A short verification of the adjoint state dynamics in the new integration space and several illustrations of interest are given and discussed. §4.2 closes with a Lemma detailing how ΔV integration space discontinuities may be circumvented through intelligent choice of state-space coordinates. Worked examples of the utility of the approach are given in §4.3, including a detailed worked example demonstrating how the central results of the paper may be used to compute free-time, fuel-constrained range sets using orbital elements. An extended example is given in §4.4 in which orbit range is computed for semi-major axis, eccentricity, and inclination. Finally, a chapter summary is given in in §4.5.

4.1 Approach Motivation

To properly motivate the theoretical contributions the classical primer vector problem in astrodynamics [29] is first stated, then an attempt to transform it to a fuel-limited, minimum-fuel, free-time reachability problem involving the HJB PDE is made. As mentioned in the Introduction, several past efforts have addressed similar problems [79] or resticted versions of this problem[77, 78]. For central-body motion, minimizing fuel usage is equivalent to minimizing the characteristic velocity, ΔV. For a single trajectory (of

which reachability sets are composed) the TPBVP may be written as a problem statement of the form

$$\inf_{\mathbf{u}\in U} \Delta V = \inf_{\mathbf{u}\in U} \|\mathbf{u}(t)\|_{L_1} = \inf_{\mathbf{u}\in U} \int_{t_0}^{t_f} \|\mathbf{u}(\tau)\|_2 d\tau$$

$$\text{s.t. } \dot{\mathbf{x}} = \mathbf{f}(\mathbf{x},\mathbf{u}) = \begin{bmatrix} \dot{\mathbf{r}} \\ \\ \dot{\mathbf{v}} \end{bmatrix} = \begin{bmatrix} \mathbf{v} \\ \\ -\frac{\mu}{\|\mathbf{r}\|_2^3}\mathbf{r} + \mathbf{u} \end{bmatrix}$$

$$U = \{\mathbf{u}(t) \mid \|\mathbf{u}(t)\|_2 \le u_m\}$$

$$\mathbf{x}(t_0) = \mathbf{x}_0,\ \mathbf{x}(t_f) = \mathbf{x}_f$$

where $\mathbf{r},\mathbf{v},\mathbf{u} \in \mathbb{R}^3$, the final time $t_f > t_0$ is the final time, $u_m > 0$ is the maximum deliverable acceleration, and $\mu > 0$ is a gravitational constant. The optimal control policy found using the Pontryagin Maximum Principle is

$$\mathbf{u}(t) = \begin{cases} -u_m \frac{\mathbf{p}_v(t)}{\|\mathbf{p}_v(t)\|_2} & \text{if } \|\mathbf{p}_v(t)\|_2 > 1 \\ \\ \mathbf{0} & \text{if } \|\mathbf{p}_v(t)\|_2 \le 1 \end{cases} \tag{4.1}$$

with $\mathbf{p}_v$ being the adjoint state associated with velocity $\mathbf{v}$. To write the problem above using ΔV constraints in a manner similar to the minimum-time reachability HJB PDE formulation, the dynamics must first be written with ΔV as the independent parameter. The relationship between ΔV and time t is expressed in the performance function above, generating

$$\frac{d\mathbf{x}}{d\Delta V} = \frac{d\mathbf{x}}{dt}\frac{dt}{d\Delta V} = \frac{\mathbf{f}(\mathbf{x},\mathbf{u})}{\|\mathbf{u}\|_2}$$

It is here that the motivation for this paper is encountered. The optimal control policy (4.1) specifically states that in the time domain there may be large periods where the spacecraft drifts along a homogeneous trajectory ($\mathbf{u}^* = \mathbf{0}$). In this case the state dynamics with respect to ΔV become undefined, causing the optimal control Hamiltonian and the HJB PDE itself to become undefined. Intuitively this happens because when the problem is integrated forward in the ΔV domain, dynamics occuring during homogeneous drift periods are not captured, generating discontinuities in the state, Hamiltonian, and HJB PDE.

To circumvent this poorly defined mapping constants of motion for integrable systems that are affine in control ($\dot{\mathbf{x}} = \mathbf{f}(\mathbf{x},t) + \mathbf{B}\mathbf{u}$) are now briefly examined and used to motivate the organization of the Theory section (§4.2). Given that there is an invertible mapping between the state-space $\mathbf{x}$ and constants of motion $\mathbf{k}$ such that $\mathbf{k} = \mathbf{c}(\mathbf{x},t)$ and $\mathbf{x} = \mathbf{c}^{-1}(\mathbf{k},t)$, and observing that for homogeneous trajectories ($\mathbf{u} = \mathbf{0}$) the total

time derivative of $\mathbf{c}(\mathbf{x},t)$ is

$$\begin{aligned}\frac{d}{dt}\mathbf{c}(\mathbf{x},t) &= \frac{\partial \mathbf{c}}{\partial \mathbf{x}}\dot{\mathbf{x}} + \frac{\partial \mathbf{c}}{\partial t} \equiv 0 \\ &= \frac{\partial \mathbf{c}}{\partial \mathbf{x}}\mathbf{f}(\mathbf{x},t) + \frac{\partial \mathbf{c}}{\partial t} \equiv 0\end{aligned}$$

If the control $\mathbf{u}$ is now allowed to be non-zero, then the total time derivative of $\mathbf{k} = \mathbf{c}(\mathbf{x},t)$ may be written as

$$\begin{aligned}\dot{\mathbf{k}} = \frac{d}{dt}\mathbf{c}(\mathbf{x},t) &= \frac{\partial \mathbf{c}}{\partial \mathbf{x}}\dot{\mathbf{x}} + \frac{\partial \mathbf{c}}{\partial t} = 0 \\ &= \frac{\partial \mathbf{c}}{\partial \mathbf{x}}\mathbf{f}(\mathbf{x},t) + \frac{\partial \mathbf{c}}{\partial \mathbf{x}}\mathbf{B}\mathbf{u} + \frac{\partial \mathbf{c}}{\partial t} \\ &\Rightarrow \dot{\mathbf{k}} = \frac{\partial \mathbf{c}}{\partial \mathbf{x}}\mathbf{B}\mathbf{u}\end{aligned}$$

meaning that the total time derivative of the constants of motion $\mathbf{k}$ is linear with respect to the control $\mathbf{u}$. Changing the independent parameter from time t to ΔV now produces

$$\frac{d\mathbf{k}}{d\Delta V} = \frac{d\mathbf{k}}{dt}\frac{dt}{d\Delta V} = \frac{\partial \mathbf{c}}{\partial \mathbf{x}}\mathbf{B}\hat{\mathbf{u}},$$

avoiding the singularity associated with the original problem when $\mathbf{u}^* \to \mathbf{0}$, as the constants of motion by definition do not change during homogeneous motion.

To fully address this motivating problem and approach, the following section derives the GIP HJB PDE using a general independent parameter. Cases where the mapping function is poorly defined are identified and discussed. It is then demonstrated that this motivating problem, as well as the proposed solution to avoid the singularity, is an example of a Generalized Metric Range Set. At the end of the Theory section the method outlined above to transform cases such as the motivating problem into solvable problems is formally proposed. Combined, these developments facilitate reachability set computation using existing methods for problems with general independent parameters.

4.2 Generalized Independent Parameter Theory

Theorem 2.1.1 in the Appendix demonstrates that Optimal Control Problem (OCP) performance indices are metrics over the domain of admissible and reachable boundary values when the index Lagrangian $\mathcal{L}(\mathbf{x},\mathbf{u},t) \geq 0$ along the entire trajectory. When solving problems such as the one introduced in §4.1 it is very convenient if the new independent parameter is also a metric. Metrics have excellent intuitive meaning, as

they are always positive or zero, symmetric, and satisfy the triangle inequality. In this section the GIP HJG PDE is first derived using a general free parameter mapping function. A definition for Generalized Range (GR) is given, and several illustrations are then discussed.

4.2.1 Mapping Function

To derive the GIP HJB PDE, a function $l(\mathbf{x}, \mathbf{u}, t)$ is defined such that

$$s = S(\mathbf{x}(\cdot), \mathbf{u}(\cdot), t) = \int_{t_0}^{t} l(\mathbf{x}(\tau), \mathbf{u}(\tau), \tau) d\tau + s_0 \tag{4.2}$$

where s is a new general independent parameter, $\mathbf{x} \in \mathbb{R}^n$ is the state, and $\mathbf{u} \in \mathbb{R}^m$ is the control input. The notation $\mathbf{x}(\cdot)$ and $\mathbf{u}(\cdot)$ refers to the state and control along trajectories using either time (t) or the general independent parameter (s) as the independent parameter. For now, it is required that $S(\mathbf{x}(\cdot), \mathbf{u}(\cdot), t) \in \mathbb{R}$ be invertible with respect to t over the interval $[t_0, t_f]$. Figure 4.1 depicts what such a function may look like and emphasizes the mapping from time t to the independent parameter s. Assuming then that the inverse

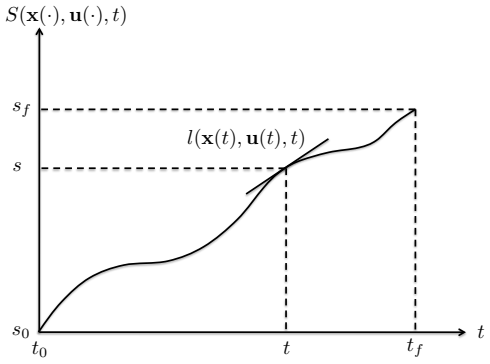

Figure 4.1: Visualization of the fully invertible independent parameter mapping function $s = S(\mathbf{x}(\cdot), \mathbf{u}(\cdot), t)$

$S^{-1} \equiv R$ exists, the following definitions are made

$$s_0 = S(\mathbf{x}(\cdot), \mathbf{u}(\cdot), t_0)$$

$$s_f = S(\mathbf{x}(\cdot), \mathbf{u}(\cdot), t_f)$$

$$t_0 = S^{-1}(\mathbf{x}(\cdot), \mathbf{u}(\cdot), s_0) = R(\mathbf{x}(\cdot), \mathbf{u}(\cdot), s_0)$$

$$t_f = S^{-1}(\mathbf{x}(\cdot), \mathbf{u}(\cdot), s_f) = R(\mathbf{x}(\cdot), \mathbf{u}(\cdot), s_f)$$

It is said then that the function S and its inverse R are both one-to-one and onto between the intervals $[t_0, t_f]$ and $[s_0, s_f]$. Computing the total time derivative of s:

$$\frac{ds}{dt} = \frac{d}{dt} S(\mathbf{x}(\cdot), \mathbf{u}(\cdot), t) = l(\mathbf{x}(t), \mathbf{u}(t), t)$$

Similarly, the total derivative of time with respect to the general independent parameter is

$$\frac{dt}{ds} = \frac{d}{dt} R(\mathbf{x}(\cdot), \mathbf{u}(\cdot), s) = \frac{1}{l(\mathbf{x}(s), \mathbf{u}(s), s)}$$

The state variable $\mathbf{x}$ may be written in terms of the new independent parameter s as $\mathbf{x}(t(s)) = \mathbf{x}(R(\mathbf{x}(\cdot), \mathbf{x}(\cdot), s))$. The system dynamics may then be rewritten with respect to the new independent parameter $s \in [s_0, s_f]$:

$$\mathbf{x}' = \frac{d\mathbf{x}}{ds} = \frac{d\mathbf{x}}{dt}\frac{dt}{ds} = \frac{\mathbf{f}(\mathbf{x}(t), \mathbf{u}(t), t)}{l(\mathbf{x}(s), \mathbf{u}(s), s)}$$

Since $\mathbf{x}'$ still contains references to t, these must be replaced using the function $t = R(\mathbf{x}(\cdot), \mathbf{u}(\cdot), s) + t_0$:

$$\mathbf{x}' = \frac{d\mathbf{x}}{ds} = \frac{\mathbf{f}(\mathbf{x}(t), \mathbf{u}(t), t)}{l(\mathbf{x}(s), \mathbf{u}(s), s)} = \frac{\tilde{\mathbf{f}}(\mathbf{x}, \mathbf{u}, s)}{\tilde{l}(\mathbf{x}, \mathbf{u}, s)}$$

where the $\tilde{\cdot}$ notation indicates that a function $\cdot$ is written in terms of the new independent parameter s (for example the state equations of motion $\tilde{\mathbf{f}}(\cdot,\cdot,\cdot)$ are understood to be in terms of s, while $\mathbf{f}(\cdot,\cdot,\cdot)$ are in terms of t). The $\tilde{\cdot}$ notation is used through the remainder of the paper in the interest of brevity.

4.2.2 Generalized Independent Parameter Hamilton Jacobi PDE

Now that the dynamics have been entirely rewritten in terms of the independent parameter s, the relationship with the Hamilton Jacobi Bellman PDE may now be determined. Recall the Dynamic Programming Equation (DPE)

$$V(\mathbf{x}_0, t_0) = \underset{\mathbf{u} \in U}{\text{opt}} \left[\int_{t_0}^{t_f} \mathcal{L}(\mathbf{x}, \mathbf{u}, \tau) d\tau + V(\mathbf{x}_f, t_f) \right] \tag{4.3}$$

where the 'opt' operation may be either an infimum or supremum. The pair $(\mathbf{x}^*, \mathbf{u}^*)$ denote the optimum trajectory found using either the infimum or supremum on the DPE shown in (4.3). Under the assumption that $V(\mathbf{x}, t)$ is sufficiently smooth, along an optimal trajectory it can be shown that

$$\frac{dV}{dt} = -\mathcal{L}(\mathbf{x}^*, \mathbf{u}^*, t)$$

Thus, to change the independent parameter in the DPE (4.3), the rate of change of the Lagrangian must first be determined:

$$\frac{dV}{ds} = \frac{dV}{dt}\frac{dt}{ds} = -\frac{\mathcal{L}(\mathbf{x}^*(t), \mathbf{u}^*(t), t)}{l(\mathbf{x}^*(s), \mathbf{u}^*(s), s)} = -\frac{\tilde{\mathcal{L}}(\mathbf{x}^*, \mathbf{u}^*, s)}{\tilde{l}(\mathbf{x}^*, \mathbf{u}^*, s)}$$

Now, the DPE using the new independent parameter s is written as

$$\tilde{V}(\mathbf{x}_0, s_0) = \underset{\mathbf{u}\in U}{\text{opt}}\left[\int_{s_0}^{s_f}\left(\frac{\tilde{\mathcal{L}}(\mathbf{x}, \mathbf{u}, v)}{\tilde{l}(\mathbf{x}, \mathbf{u}, v)}\right)dv + \tilde{V}(\mathbf{x}_f, s_f)\right] \tag{4.4}$$

Following a standard HJB PDE derivation [57], the initial boundary conditions are chosen as $\mathbf{x}_0 = \mathbf{x}$ and $s_0 = s$ and the final boundary conditions $\mathbf{x}_f$ and s_f are chosen such that $\mathbf{x}_f = \mathbf{x} + \delta\mathbf{x}$ and $s_f = s + \delta s$. The modifiend DPE (4.4) is then written as

$$\tilde{V}(\mathbf{x}, s) = \underset{\mathbf{u}\in U}{\text{opt}}\left[\int_{s}^{s+\delta s}\left(\frac{\tilde{\mathcal{L}}(\mathbf{x}, \mathbf{u}, v)}{\tilde{l}(\mathbf{x}, \mathbf{u}, v)}\right)dv + \tilde{V}(\mathbf{x} + \delta\mathbf{x}, s + \delta s)\right]$$

The incremental state change $\delta\mathbf{x}$ from an incremental independent parameter change δs may be written as

$$\delta\mathbf{x} = \frac{d\mathbf{x}}{ds}\delta s + O(\|\delta s\|^2) = \frac{\tilde{\mathbf{f}}(\mathbf{x}, \mathbf{u}, s)}{\tilde{l}(\mathbf{x}, \mathbf{u}, s)}\delta s + O(\|\delta s\|^2)$$

The Taylor series expansion of the value function at $s_f = s + \delta s$ becomes

$$\begin{aligned}
&\tilde{V}(\mathbf{x} + \delta\mathbf{x}, s + \delta s) \\
&= \tilde{V}\left(\mathbf{x} + \frac{\tilde{\mathbf{f}}(\mathbf{x}, \mathbf{u}, s)}{\tilde{l}(\mathbf{x}, \mathbf{u}, s)}\delta s + O(\|\delta s\|^2), s + \delta s\right) \\
&= \tilde{V}(\mathbf{x}, s) + \frac{\partial\tilde{V}}{\partial\mathbf{x}}^T\frac{\tilde{\mathbf{f}}(\mathbf{x}, \mathbf{u}, s)}{\tilde{l}(\mathbf{x}, \mathbf{u}, s)}\delta s + \frac{\partial\tilde{V}}{\partial s}\delta s + O(\|\delta s\|^2)
\end{aligned}$$

Similarly, the Lagrangian may be written as

$$\int_{s}^{s+\delta s}\left(\frac{\tilde{\mathcal{L}}(\mathbf{x}, \mathbf{u}, v)}{\tilde{l}(\mathbf{x}, \mathbf{u}, v)}\right)dv = \frac{\tilde{\mathcal{L}}(\mathbf{x}, \mathbf{u}, s)}{\tilde{l}(\mathbf{x}, \mathbf{u}, s)}\delta s + O(\|\delta s\|^2)$$

Substituting these relationships into the modified DPE produces

$$\tilde{V}(\mathbf{x}, s) = \underset{\mathbf{u}\in U}{\text{opt}}\left[\frac{\tilde{\mathcal{L}}(\mathbf{x}, \mathbf{u}, s)}{\tilde{l}(\mathbf{x}, \mathbf{u}, s)}\delta s + \tilde{V}(\mathbf{x}, s) + \frac{\partial\tilde{V}}{\partial\mathbf{x}}^T\frac{\tilde{\mathbf{f}}(\mathbf{x}, \mathbf{u}, s)}{\tilde{l}(\mathbf{x}, \mathbf{u}, s)}\delta s + \frac{\partial\tilde{V}}{\partial s}\delta s + O(\|\delta s\|^2)\right]$$

Subtracting $\tilde{V}(\mathbf{x}, s)$ from both sides, ignoring terms of $O(\|\delta s\|^2)$ or higher, and dividing both sides by δs generates the GIP HJB PDE:

$$\frac{\partial\tilde{V}}{\partial s} + \underset{\mathbf{u}\in U}{\text{opt}}\left[\frac{\tilde{\mathcal{L}}(\mathbf{x}, \mathbf{u}, s)}{\tilde{l}(\mathbf{x}, \mathbf{u}, s)} + \frac{\partial\tilde{V}}{\partial\mathbf{x}}^T\frac{\tilde{\mathbf{f}}(\mathbf{x}, \mathbf{u}, s)}{\tilde{l}(\mathbf{x}, \mathbf{u}, s)}\right] = 0 \tag{4.5}$$

It can be shown that the second term in (4.5) has many of the special properties of Hamiltonians in classical mechanics [28]. Further, Pontryagin's Maximum Principle requires that the gradient $\partial V/\partial \mathbf{x}$ satisfies all of the properties of an adjoint variable $\mathbf{p}$ in a Hamiltonian system [57]. The Optimal Control Hamiltonian (OCH) may then be written as

$$\tilde{\mathcal{H}}(\mathbf{x},\mathbf{p},\mathbf{u},s) = \underset{\mathbf{u}\in U}{\text{opt}}\left[\frac{\tilde{\mathcal{L}}(\mathbf{x},\mathbf{u},s)}{\tilde{l}(\mathbf{x},\mathbf{u},s)} + \mathbf{p}^T\frac{\tilde{\mathbf{f}}(\mathbf{x},\mathbf{u},s)}{\tilde{l}(\mathbf{x},\mathbf{u},s)}\right] \tag{4.6}$$

where the adjoint variable $\mathbf{p} = \partial\tilde{V}/\partial\mathbf{x}$. Note that none of the steps make any second-order optimality assumptions, so the 'opt' argument may be replaced with an optimization argument as desired (e. g. 'min,' 'max,' 'infimum', 'supremum'). To derive the equations of motion of the adjoint in the s-domain, an approach similar to that in classical mechanics [29, 28, 68] is used. Variations in the trajectory performance index

$$\tilde{P} = \int_{s_0}^{s_f}\frac{\tilde{\mathcal{L}}(\mathbf{x},\mathbf{u},v)}{\tilde{l}(\mathbf{x},\mathbf{u},v)}dv$$

are examined as a starting point. Recalling the definition of the Hamiltonian using the new independent parameter (4.6), the performance index $\tilde{P}$ may be re-written as

$$\tilde{P} = \int_{s_0}^{s_f}\left[\tilde{\mathcal{H}}(\mathbf{x},\mathbf{p},\mathbf{u},v) - \mathbf{p}^T\mathbf{x}'\right]dv$$

Taking the first variation of $\tilde{P}$ about optimal trajectories (and thereby assuming that $\partial\tilde{\mathcal{H}}/\partial\mathbf{u} = \mathbf{0}$) generates

$$\delta\tilde{P} = \int_{s_0}^{s_f}\left[\frac{\partial\tilde{\mathcal{H}}}{\partial\mathbf{x}}\delta\mathbf{x} + \frac{\partial\tilde{\mathcal{H}}}{\partial\mathbf{p}}\delta\mathbf{p} - \mathbf{p}^T\delta\mathbf{x}' - \mathbf{x}'^T\delta\mathbf{p}\right]ds$$

Using integration by parts the second to last term in the integrand may be re-written:

$$\int_{s_0}^{s_f}\mathbf{p}^T\delta\mathbf{x}'dv = \mathbf{p}^T\delta\mathbf{x}'\Big|_{s_0}^{s_f} - \int_{s_0}^{s_f}\mathbf{p}'^T\delta\mathbf{x}dv$$

Substituting this relation, observing that the problem is essentially a Two-Point Boundary Value Problem ($\delta\mathbf{x}(s_0) = \delta\mathbf{x}(s_f) = \mathbf{0}$), and simplifying yields

$$\delta\tilde{P} = \int_{s_0}^{s_f}\left[\left(\frac{\partial\tilde{\mathcal{H}}}{\partial\mathbf{x}} + \mathbf{p}'\right)\delta\mathbf{x} + \left(\frac{\partial\tilde{\mathcal{H}}}{\partial\mathbf{p}} - \mathbf{x}'\right)\delta\mathbf{p}\right]dv$$

Requiring stationarity ($\delta\tilde{P} = 0$) for arbitrary variations $\delta\mathbf{x}$ and $\delta\mathbf{p}$ necessitates that

$$\mathbf{x}' = \frac{d\mathbf{x}}{ds} = \frac{\partial\tilde{\mathcal{H}}}{\partial\mathbf{p}} \tag{4.7}$$

and

$$\mathbf{p}' = \frac{d\mathbf{p}}{ds} = -\frac{\partial \tilde{\mathcal{H}}}{\partial \mathbf{x}} \tag{4.8}$$

Equations (4.7) and (4.8) precisely mirror the classical results for time-based trajectory optimization.

Remark 4.2.1. ***Initial Conditions on the GIP HJB PDE***

The assumptions of the HJB PDE derivation involved supposing an initial condition $V(\boldsymbol{x}_0, t_0)$ or $\tilde{V}(\boldsymbol{x}_0, s_0)$ in the modified Dynamic Programing Equation (4.4). By convention, the zero-level sets of $V(\boldsymbol{x}_0, s_0)$ are used to define the boundary of the reachable set, as when $V(\boldsymbol{x}, s) = 0$, it may equivalently be said that the Performance-to-go $V(\boldsymbol{x}, s)$ is zero.

4.2.3 Mapping Function Invertibility

Thus far it has been required that the integration mapping parameter function $s = S(\mathbf{x}(\cdot), \mathbf{u}(\cdot), t)$ be invertible, and that $t = R(\mathbf{x}(\cdot), \mathbf{u}(\cdot), s)$ is its inverse (S and R satisfy the identity relation $t = R(\mathbf{x}(\cdot), \mathbf{u}(\cdot), S(\mathbf{x}(\cdot), \mathbf{u}(\cdot), t))$ for the domain $t \in [t_0, t_f]$ and range $s \in [s_0, s_f]$) [23]. Several pertinent cases for the value of $l(\mathbf{x}, \mathbf{u}, t)$ are now investigated with the aim of identifying invertibility requirements on the parameter mapping function $S(\mathbf{x}(\cdot), \mathbf{u}(\cdot), t)$. More cases exist, but are not exhaustively enumerated here.

(1) $l(\mathbf{x}(\cdot), \mathbf{u}(\cdot), t) = \pm\infty$ (but not $= 0$) over $t \in [t_0, t_f]$. The slope l has become vertical, meaning that an infinitesimal change in time t will cause a finite (or even infinite) change in the independent parameter s. The function S is said to be *left-invertible*, and there exists a unique onto mapping R from $s \in [s_0, s_f]$ to $t \in [t_0, t_f]$, but the reverse mapping is not one-to-one. Figure 4.2 illustrates this case. Note that when this occurs, the GIP HJB PDE (4.5) reduces to $\partial \tilde{V}/\partial s = 0$, implying that the value function is constant and the reach set does not progress in such regions. Similarly, $\mathbf{x}' \to \mathbf{0}$ and $\mathbf{p}' \to \mathbf{0}$, meaning that the dynamics cease to propagate while $l(\mathbf{x}, \mathbf{u}, t) = \pm\infty$.

(2) $l(\mathbf{x}(\cdot), \mathbf{u}(\cdot), t) = 0$ (but not $= \pm\infty$) over $t \in [t_0, t_f]$. The slope of l is completely horizontal, requiring a finite change in time t to induce an infinitesimal change in the independent parameter s. The function S is said to be *right-invertible*, and there exists a unique onto mapping S from $t \in [t_0, t_f]$ to $s \in [s_0, s_f]$, but the reverse mapping R is not one-to-one. Figure 4.3 illustrates this case. When this

situation occurs the HJB PDE (4.5), the Hamiltonian (4.6), and the state/adjoint dynamics (4.7) and (4.8) become undefined and the value function $\tilde{V}(\mathbf{x}, s)$ experiences a discontinuity, violating one of the assumptions of the HJB PDE derivation. This is the case the motivating problem in §4.1 emphasizes.

(3) $l(\mathbf{x}(\cdot), \mathbf{u}(\cdot), t) = \pm\infty$ and $l(\mathbf{x}(\cdot), \mathbf{u}(\cdot), t) = 0$ over $t \in [t_0, t_f]$. The function experiences discontinuities on both the domain $t \in [t_0, t_f]$ and the range $s \in [s_0, s_f]$, and is neither left- nor right-invertible. Figure 4.4 illustrates this case.

(4) $-\infty < l(\mathbf{x}(\cdot), \mathbf{u}(\cdot), t) < \infty$ over $t \in [t_0, t_f]$. The S has both a positive and negative slope over its domain $t \in [t_0, t_f]$. The function S is right-invertible, as the mapping from $t \in [t_0, t_f]$ is onto, though the reverse mapping is not onto. Figure 4.5 illustrates this case.

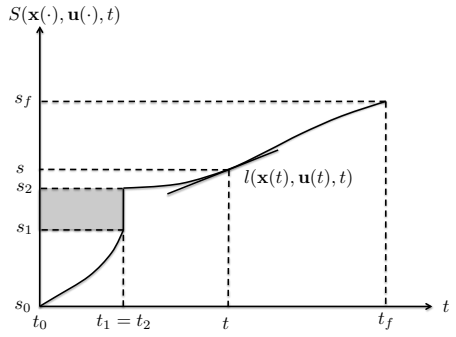

Figure 4.2: Case 1: $l(\mathbf{x}, \mathbf{u}, t) = \pm\infty$

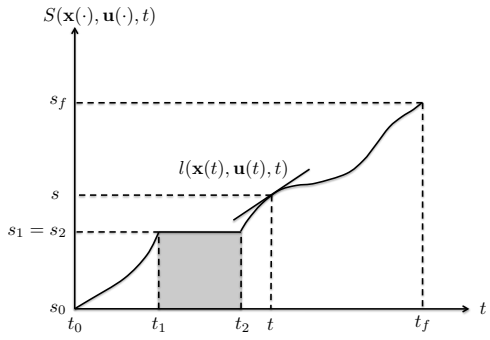

Figure 4.3: Case 2: $l(\mathbf{x}, \mathbf{u}, t) = 0$

These cases motivate the following remarks

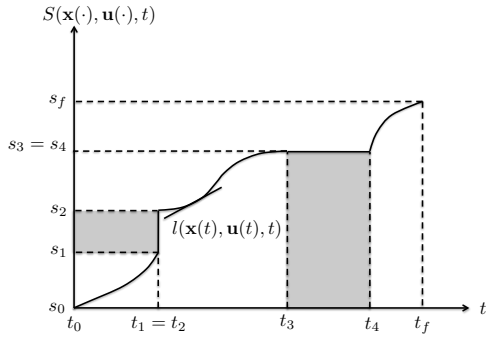

Figure 4.4: Case 3: $l(\mathbf{x},\mathbf{u},t) = \pm\infty$ and $l(\mathbf{x},\mathbf{u},t) = 0$

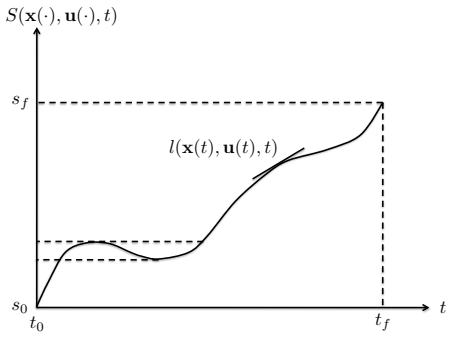

Figure 4.5: Case 4: $-\infty < l(\mathbf{x},\mathbf{u},t) < \infty$

Remark 4.2.2. ***Parameter Mapping Function Integrand Constraints***

For the mapping $S(\boldsymbol{x}(\cdot),\boldsymbol{u}(\cdot),t)$ to be invertible, the parameter mapping function integrand $l(\boldsymbol{x},\boldsymbol{u},t)$ must satisfy either

$$0 < l(\boldsymbol{x}(\cdot),\boldsymbol{u}(\cdot),t) < \infty,\ \forall t \in [t_0,t_f] \tag{4.9}$$

or

$$-\infty < l(\boldsymbol{x}(\cdot),\boldsymbol{u}(\cdot),t) < 0,\ \forall t \in [t_0,t_f] \tag{4.10}$$

Requiring either (4.9) or (4.10) ensures that the mapping $s = S(\boldsymbol{x}(\cdot),\boldsymbol{u}(\cdot),t)$ is one-to-one and onto.

Remark 4.2.3. ***Ideal Integration Domain***

If the independent parameter mapping function S is both left- and right-invertible, then both the GIP HJB PDE (4.5) in s and the classical HJB PDE in t are suitable settings in which to solve optimal control problems. If S is only right-invertible, then the traditional HJB PDE propagated in t may be a more convenient domain for solving optimal control problems. If S is only left-invertible, then the GIP HJB PDE (4.5) in s may be

the most convenient domain in which to solve optimal control problems. A change in coordinates and/or control variables may significantly alter the invertibility of the independent parameter mapping function.

4.2.4 Generalized Range and Related Results

Having developed the GIP HJB PDE and examined several special cases for independent parameter mapping functions, the main theoretical results are now presented and discussed.

Remark 4.2.4. ***Reachability with Integration Equality Constraints***

Given a reachability problem with an integration constraint of the form

$$\int_{t_0}^{t_f} c(\boldsymbol{x}, \boldsymbol{u}, \tau) d\tau + c_0 - c_f = 0$$

where $t_f > t_0$ is unspecified, the constraint integrand $c(\boldsymbol{x}, \boldsymbol{u}, t)$ may be used as the parameter mapping integrand $l(\boldsymbol{x}, \boldsymbol{u}, t)$, and the corresponding value function $\tilde{V}(\boldsymbol{x}, s)$ computing using the GIP HJB PDE

$$\frac{\partial \tilde{V}}{\partial s} + \underset{\boldsymbol{u} \in U}{opt} \left[\frac{\tilde{\mathcal{L}}(\boldsymbol{x}, \boldsymbol{u}, s)}{\tilde{c}(\boldsymbol{x}, \boldsymbol{u}, s)} + \frac{\partial \tilde{V}}{\partial \boldsymbol{x}}^T \frac{\tilde{\boldsymbol{f}}(\boldsymbol{x}, \boldsymbol{u}, s)}{\tilde{c}(\boldsymbol{x}, \boldsymbol{u}, s)} \right] = 0$$

by integrating over the parameter constraints $s \in [s_0, s_f] = [c_0, c_f]$.

Remark 4.2.4 briefly discusses the primary means by which free-time reachability problems with an integral constraint may be approached using the GIP HJB PDE framework. The situation mentioned in Remark 4.2.4 and associated illustrations is now elaborated upon. The definition of a Generalized Metric Range Set (GMRS) is given and its implications and utility are discussed.

Definition 4.2.1. ***Generalized Metric Range Set***

An optimal reachability set found using a Generalized Independent Parameter (possibly by propagating the GIP HJB PDE) where the mapping function integrand is the performance index Lagrangian ($l(\boldsymbol{x}(t), \boldsymbol{u}(t), t) = \mathcal{L}(\boldsymbol{x}(t), \boldsymbol{u}(t), t)$), $s_0 = 0$, and $l(\boldsymbol{x}(t), \boldsymbol{u}(t), t) \geq 0$ at all points along all optimal trajectories is called a Generalized Metric Range Set (GRS).

If a GIP is defined such that $\tilde{l}(\mathbf{x}(s), \mathbf{u}(s), s) \geq 0$ and $\tilde{l}(\mathbf{x}(s), \mathbf{u}(s), s) = \tilde{\mathcal{L}}(\mathbf{x}(s), \mathbf{u}(s), s)$, the equivalent performance function

$$P = s_f = \int_{t_0}^{t_f} \mathcal{L}(\mathbf{x}(\tau), \mathbf{u}(\tau), \tau) d\tau$$

is a metric over the reachable state space and the independent parameter is equivalent to the metric 'distance' between the initial and final reachability sets. This scenario corresponds to both the nominal, fully invertible independent parameter mapping case, as well as the right-invertible independent parameter mapping (case 2). The GIP HJB PDE (4.5) is reduced to

$$\frac{\partial \tilde{V}}{\partial s} + 1 + \underset{\mathbf{u}\in U}{\text{opt}}\left[\frac{\partial \tilde{V}}{\partial \mathbf{x}}^T \frac{\tilde{\mathbf{f}}(\mathbf{x},\mathbf{u},s)}{\tilde{\mathcal{L}}(\mathbf{x},\mathbf{u},s)}\right] = 0 \tag{4.11}$$

Note that if the GIP Hamiltonian Lagrangian is chosen to be identically zero but the original mapping function $l(\mathbf{x},\mathbf{u},t) = \mathcal{L}(\mathbf{x},\mathbf{u},t)$ is kept, then the 1 is eliminated and (4.11) appears exactly as a traditional minimum-time optimal reachability formulation (which uses time as the independent parameter). However in this instance it is with respect to the performance function *metric* P that the HJB PDE is integrated. This situation is precisely the one found in the motivation problem introduced in §4.1. Note that whether the Lagrangian is kept or not, the optimal control policy, state dynamics, adjoint dynamics, and the initial condition remain the same, generating equivalent reachability sets. Importantly, this implies that when using the GIP HJB PDE to solve a Generalized Metric Range Set problem, one may equivalently use

$$\frac{\partial \tilde{V}}{\partial s} + \underset{\mathbf{u}\in U}{\text{opt}}\left[\frac{\partial \tilde{V}}{\partial \mathbf{x}}^T \frac{\tilde{\mathbf{f}}(\mathbf{x},\mathbf{u},s)}{\tilde{\mathcal{L}}(\mathbf{x},\mathbf{u},s)}\right] = 0 \tag{4.12}$$

rather than (4.11). A reachability problem satisfying Definition 4.2.1 is called a Generaliezd Metric Range Set because it is an optimal reachability set using an arbitrary general independent parameter that also represents a metric distance. Definition 4.2.1, while at first seeming arbitrary, has deep and intuitive interpretations. Firstly, by choosing to scale the dynamics with respect to the new independent parameter metric, zero level sets of $\tilde{V}(\mathbf{x},P)$, $P \in [P_0 \ P_f]$ define sets in the state space $\mathbf{x}$ at fixed metric distances from the set $\tilde{V}(\mathbf{x}_0,P_0)$. Such sets are intuitively the most fundamental definition of 'range.' Second, because the new independent parameter $s \to P$ is a metric, and the only requirement on P from Theorem 2.1.1 is that $\mathcal{L}(\mathbf{x},\mathbf{u},t) \geq 0$. This makes a large variety of common performance indices both viable metrics and independent parameters for Generalized Metric Range Set computation. Some common performance indices and applications are briefly discussed.

Illustration 4.2.1. *Minimum Time Reachability*

For minimum time reachability, $l(\boldsymbol{x}(t),\boldsymbol{u}(t),t) = \mathcal{L}(\boldsymbol{x}(t),\boldsymbol{u}(t),t) = 1 \geq 0$. *If* $s_0 = t_0 = 0$, *then* $P = t_f$. *As*

noted, because $\mathcal{L}(\boldsymbol{x}(t), \boldsymbol{u}(t), t) = 1 \geq 0$, $P = t_f$ *is also a metric. Thus, the minimum time reachability problem is an example of a Generalized Metric Range Set. Under this schema* $ds \equiv dt$. *Substituting into (4.5) yields*

$$\frac{\partial V}{\partial t} + \underset{\boldsymbol{u}\in U}{opt}\left[\frac{\partial V}{\partial \boldsymbol{x}}^T \boldsymbol{f}(\boldsymbol{x}, \boldsymbol{u}, t)\right] = 0$$

which is the traditional minimum time reachability HJB realization. This independent parameter mapping is similar to that shown in Figure 4.1.

Illustration 4.2.2. *Minimum Fuel Reachability*

Minimum fuel reachability problem performance indices are often expressed as an L_1 *norm of the control trajectory* $\boldsymbol{u}(t)$. *These performance indices have Lagrangians of the form* $\|\boldsymbol{u}(t)\|_2$. *Choosing* $l(\boldsymbol{x}(t), \boldsymbol{u}(t), t) = \mathcal{L}(\boldsymbol{x}(t), \boldsymbol{u}(t), t) = \|\boldsymbol{u}(t)\|_2 \geq 0$, *satisfies Definition 4.2.1. It can therefore be said that such problems are also examples of Generalized Metric Range Sets. The GIP HJB PDE for this system is*

$$\frac{\partial \tilde{V}}{\partial \Delta V} + \underset{\boldsymbol{u}\in U}{opt}\left[\frac{\partial \tilde{V}}{\partial \boldsymbol{x}}^T \frac{\tilde{\boldsymbol{f}}(\boldsymbol{x}, \boldsymbol{u}, \Delta V)}{\|\boldsymbol{u}\|_2}\right] = 0$$

This is precisely the situation encountered in the motivating problem in §4.1.

Illustration 4.2.3. *Quadratic Cost Functional Reachability*

If $l(\boldsymbol{x}(t), \boldsymbol{u}(t), t) = \mathcal{L}(\boldsymbol{x}(t), \boldsymbol{u}(t), t) = \boldsymbol{x}^T(t)\boldsymbol{Q}\boldsymbol{x}(t) + 2\boldsymbol{x}^T(t)\boldsymbol{N}\boldsymbol{u}(t) + \boldsymbol{u}^T(t)\boldsymbol{Q}\boldsymbol{u}(t) \geq 0$, *with* $\boldsymbol{Q} \in \mathbb{R}^{n\times n}$ *being positive semi-definite and* $\boldsymbol{R} \in \mathbb{R}^{m\times m}$ *being positive definite, then given a fixed final quadratic cost the problem may be computed as a Generalized Metric Range Set. Equation (4.5) then becomes*

$$\frac{\partial \tilde{V}}{\partial P} + \underset{\boldsymbol{u}\in U}{opt}\left[\frac{\partial \tilde{V}}{\partial \boldsymbol{x}}^T \frac{\tilde{\boldsymbol{f}}(\boldsymbol{x}, \boldsymbol{u}, P)}{\boldsymbol{x}^T\boldsymbol{Q}\boldsymbol{x} + 2\boldsymbol{x}^T\boldsymbol{N}\boldsymbol{u} + \boldsymbol{u}^T\boldsymbol{Q}\boldsymbol{u}}\right] = 0$$

Solving $\|\boldsymbol{u}(t)\|_{L_2}$ *fuel cost analogs is a special case of this scenario.*

Now that sufficient discussion and illustration has been given to the GIP HJB PDE and a definition for Generalized Metric Range Sets has ben reviewed, a method by which a sublcass of problems with independent parameter mapping functions shown in Case 2 ($l(\mathbf{x}(t), \mathbf{u}(t), t) = 0$) may be solved is introduced. Importantly this approach applies to the motivating minimum fuel primer vector problem.

Lemma 4.2.1. ***Solving Optimal Reachability Problems with*** ΔV ***Mapping Functions*** *Given an optimal reachability problem with control appearing as an acceleration and an independent parameter mapping*

function integrand $l(\boldsymbol{u}(t)) = \|\boldsymbol{u}(t)\|_2$ *over* $t \in [t_0, t_f]$ *where* t_f *is unspecified, the optimal reachability problem may instead by solved by writing the dynamics in terms of the* $n-1$ *constants of motion* $\boldsymbol{k} = \boldsymbol{c}(\boldsymbol{x}, t) \in \mathbb{R}^{n-1}$*, considering the original control acceleration* $\boldsymbol{u}$ *to be un-bounded, and using the* n^{th} *time-varying integral of motion* $K(\boldsymbol{x}, t) \in \mathbb{R}$ *as an additional control parameter.*

Proof: *The time-dynamics of the* $n-1$ *constants of motion may be written as*

$$\dot{\boldsymbol{k}} = \boldsymbol{g}(\boldsymbol{k}, K(\boldsymbol{k}, t), t)\boldsymbol{u}$$

The corresponding GIP HJB PDE (4.5) is:

$$\frac{\partial \tilde{V}}{\partial \Delta V} + \underset{K,\, \boldsymbol{u} \in U}{opt} \left[\frac{\partial \tilde{V}}{\partial \boldsymbol{k}}^T \tilde{g}(\boldsymbol{k}, K, \Delta V) \frac{\boldsymbol{u}}{\|\boldsymbol{u}\|_2} \right] = 0$$

The HJB PDE is well defined over $s \in [s_0, s_f]$*, as when* $\|\boldsymbol{u}(t)\|_2 = 0$ *the constants of motion* $\boldsymbol{k}$ *have absolutely no dynamics (*$d\boldsymbol{k}/dt = \boldsymbol{0}$*). Conversely, as the optimal trajectory is propagated in the* s*-domain the constants of motion are never stationary (*$d\boldsymbol{k}/ds \neq \boldsymbol{0}$*).* □

Lemma 4.2.1 provides a method by which the impulsive variant of the fuel-constrained, minimum fuel, free time optimal reachability problem may be solved. It is important to note that because constants of motion are required to use this approach, the system must be integrable. For systems that are affine in control acceleration $\mathbf{u}(t)$ (such as Newtonian systems), minimum fuel problems require coasting arcs ($\mathbf{u}(t) = \mathbf{0}$), and if they are integrable Lemma 4.2.1 provides a means by which to compute their minimum fuel reachability sets. Said differently, using Lemma 4.2.1, the motivating problem may still be posed in an analytically tractable form. This solution approach benefits greatly from the fact that it also satisfies the definition of a Generalized Metric Range Set (Definition 4.2.1). A detailed application of this Lemma 4.2.1 to on-orbit range may be found in [69] and two simpler worked examples are given in the next section.

4.3 Range Examples

Two straightforward analytical examples are given, followed by a more complex third example. The first generates the aircraft range equation result using the GIP HJB PDE, while the second applies Lemma 4.2.1 to the linear 2^{nd}-order oscillator. The final example also applies Lemma 4.2.1 to the orbit range problem posed in §4.1.

4.3.1 Example 4.1: Aircraft Range

The aircraft range equation developed by Louis Breguet is a classic formula that generates a nominal aircraft range based on a specified final mass m_f (dry mass) and initial mass m_0 (wet mass) such that $m_0 = m_f + \Delta m$. The problem statement given below is unique as there is no control input to optimize. Regardless, the GIP HJB PDE framework may still be applied to compute range sets.

$$\text{find } r_{max} = \sup_{u \in U} r$$

$$\text{s.t. } \dot{r} = f(r, m)$$

$$\Delta m = \int_{t_0}^{t_f} \dot{m}(\tau) d\tau$$

$$r(t_0) = 0,\ m(t_0) = m_0$$

$$t_0 \text{ and } t_f \text{ are unspecified, } U \in \{\varnothing\}$$

For steady-state level flight, the one-dimensional equation of motion $\dot{r} = f(r, m)$ is

$$\dot{r} = f(r, m) = \sqrt{\frac{2mg}{\rho C_L S}} \tag{4.13}$$

where r is distance, m is the current mass at time $t \in [t_0, t_f]$, C_L is the coefficient of lift, and S is the nominal surface area of the lifting surface. To apply the GIP HJB PDE approach to computing the range of an aircraft as a reachability problem, an independent parameter mapping is first found, then the resulting GIP HJB PDE is simplified and solved. Aircraft are limited in the mass of fuel they carry, making mass an ideal alternate integration variable. The mass integration mapping function is chosen to be

$$\Delta m = m_f - m_0 = \int_{t_0}^{t_f} \frac{dm}{d\tau} d\tau$$

For most aircraft systems, $\dot{m}$ may be modeled as proportional to the propulsion system thrust, $\dot{m} = -kF_t$. Substituting the steady-state thrust $F_t = (C_D/C_L)mg$ generates $\dot{m} = -k(C_D/C_L)mg$. The independent parameter mapping function then becomes

$$m(t) = \int_{t_0}^{t} \left(-k \frac{C_D}{C_L} m(\tau) g\right) d\tau + m_0$$

This function is a one-to-one and onto mapping from $[t_0, t_f]$ to $[m_0, m_f]$ as long as $m > 0\ \forall t \in [t_0, t_f]$, making the optimal trajectory in mass recoverable in terms of time (and back to mass as well). Further, note that

while the sign of the mapping function integrand is negative, this is purely a result of the direction in which mass flow is defined to occur; an opposite sign can be obtained by defining the mass flow rate differently or by using negative time dynamics. The solution to this example may still be considered a Generalized Metric Range Set as described in Definition 4.2.1. The equations of motion defined in (4.13) are scalar and do not involve control. Thus without loss of generality $\tilde{\mathcal{L}}(\mathbf{x}, \mathbf{u}, s) = 0$ and the range set is dependent only on propagation of the system dynamics. The GIP HJB for the steady-state, constant altitude aircraft case is written after some simplification as

$$\frac{\partial \tilde{V}}{\partial m} + \frac{\partial \tilde{V}}{\partial r}\left(-\frac{1}{kmg}\sqrt{\frac{2C_L mg}{\rho C_D^2 S}}\right) = 0 \tag{4.14}$$

The objective in solving this PDE is to compute $\tilde{V}(r, m)$ over $[m_0, m_f]$. The values of r where $\tilde{V}(r, m) = 0$ over $[m_0, m_f]$ are the ranges for those aircraft masses. Equation (4.14) may be solved by separation, producing

$$\tilde{V}(r, m) = r - \frac{2}{k}\sqrt{\frac{2}{\rho g S}\frac{C_L}{C_D^2}}\left(\sqrt{m_0} - \sqrt{m}\right) \tag{4.15}$$

for $r \in [0, \infty)$ and $m \in [m_0, m_f]$. Similarly, directly integrating (4.14) with respect to m over $[m_0, m_f]$ yields the classical Breguet equation

$$r_{max} = r = \frac{2}{k}\sqrt{\frac{2}{\rho g S}\frac{C_L}{C_D^2}}\left(\sqrt{m_0} - \sqrt{m_f}\right)$$

with the boundary condition $r_0 = 0$ and integration over m_0 to m_f. Using the HJB PDE with an alternate independent parameter (mass rather than time) produces the same result as the more straightforward change of integration variables in the original derivation by Breguet.

4.3.2 Example 4.2: Amplitude Range

In this example the maximum free-time, control-limited range (reachability) of the classic 2^{nd}-order undamped oscillator amplitude will be solved using the approach outlined in Lemma 4.2.1. A 2^{nd}-order linear oscillator $\ddot{x} = -\omega_n^2 x + u$ may be written in terms of integrals of motion A and θ:

$$\dot{A} = f_A(A, \theta, u) = \frac{\cos\theta}{\omega_n} u \tag{4.16}$$

$$\dot{\theta} = f_\theta(A, \theta, u) = \omega_n - \frac{\sin\theta}{A} u \tag{4.17}$$

where A is the amplitude of the oscillation in position coordinates, θ is the angle between x and $\dot{x}$ in the phase space, ω_n is the natural frequency, and u is an acceleration input. The ΔV constrained, free time, maximum amplitude problem is written formally as

$$\begin{aligned} \text{find } A_{max} &= \sup_{u \in U} A \\ \text{s.t. } \dot{A} &= f_A(A, \theta, u) = \frac{\cos\theta}{\omega_n} u \\ \dot{\theta} &= f_\theta(A, \theta, u) = \omega_n - \frac{\sin\theta}{A} u \\ \Delta V &= \int_{t_0}^{t_f} |u(\tau)| d\tau \\ A(t_0) &= A_0,\ \theta(t_0) = \theta_0 \end{aligned}$$

$$t_0 \text{ and } t_f \text{ are unspecified, } U = \{u \mid u \in \mathbb{R}\}$$

Choosing the alternate integration metric to be ΔV requires the independent parameter mapping function integrand $l(A, \theta, u, t)$ to be defined such that

$$\Delta V = V_f - V_0 = \int_{t_0}^{t_f} |u(\tau)| d\tau$$

In this case, if the traditional coordinates x and $\dot{x}$ are used the mapping function becomes problematic if $u(\tau) = 0$ (see Case 2 in §4.2). Because A is constant in the absence of control there is no discontinuity when $u(\tau) = 0$. The phase angle θ however is not constant in the absence of control. Fortunately θ appears in terms of sin and cos operations in the dynamics for A and θ; If the input $u(\tau)$ is allowed to be unconstrained and the total time is unconstrained θ may be treated as a control parameter. This range set may be considered an example of a Generalized Metric Range Set, described in Definition 4.2.1. Thus, to compute the free-time, ΔV constrained range of the amplitude A, the goal is now to find the optimal policy for θ and u using the GIP HJB PDE. For this example the GIP HJB PDE becomes

$$\frac{\partial \tilde{V}}{\partial \Delta V} + \sup_{\theta \in [0, 2\pi), u} \left[\frac{\partial \tilde{V}}{\partial A} \frac{f_A(A, \theta, u)}{|u|} \right] = 0$$

The Hamiltonian is then written as

$$\mathcal{H} = \sup_{\theta \in [0, 2\pi), u} \left[p_A \frac{\cos\theta}{\omega_n} \operatorname{sgn}(u) \right] \tag{4.18}$$

Upon inspection, the optimal control policy $(\theta^*, \text{sgn}(u^*))$ is

$$(\theta^*, \text{sgn}(u^*)) = \begin{cases} (0,1) \text{ or } (\pi,-1) \text{ if } p_A \geq 0 \\ (\pi,1) \text{ or } (0,-1) \text{ if } p_A < 0 \end{cases} \tag{4.19}$$

The result in (4.19) is very intuitive. If $p_A \geq 0$, $(\theta^*, \text{sgn}(u^*))$ will increase A $(\dot{A} > 0)$. Conversely, if $p_A < 0$, $(\theta^*, \text{sgn}(u^*))$ will decrease A $(\dot{A} < 0)$. The dynamics of p_A with respect to $d\Delta V$ are

$$\frac{dp_A}{d\Delta V} = -\frac{d\mathcal{H}}{dA} = -\frac{d}{dA}\left(p_A \frac{\cos\theta}{\omega_n}\text{sgn}(u)\right) = 0$$

Since the objective is to maximize the range of A it is now assumed that $p_A > 0$ (the minimum case can be found by choosing $p_A < 0$). Note that once p_A is specified, because $dA/d\Delta V = 0$, p_A is constant as ΔV changes. The GIP HJB PDE with the optimal control input becomes

$$\frac{\partial \tilde{V}}{d\Delta V} + \frac{\partial \tilde{V}}{dA}\frac{1}{\omega_n} = 0$$

This PDE is separable and can be re-written as

$$dA = -\frac{1}{\omega_n} d\Delta V \Rightarrow \int_{A_0}^{A} dA = \frac{1}{\omega_n}\int_0^{\Delta V} d\Delta V$$

yielding the value function $\tilde{V}(A, \Delta V)$:

$$\tilde{V}(A, \Delta V) = A - A_0 - \frac{1}{\omega_n}\Delta V \tag{4.20}$$

Recalling that reachability sets may be defined as level sets of $\tilde{V}(A, \Delta V) = 0$ generates

$$A_{max} = A = A_0 + \frac{1}{w}\Delta V$$

which is the maximum time-independent amplitude range given an integral constraint on the control effort u (ΔV). To verify this solution partials of $\tilde{V}(A, \Delta V)$ are evaluated and compared with the GIP HJB PDE:

$$\frac{\partial \tilde{V}}{\partial \Delta V} + \frac{\partial \tilde{V}}{\partial A}\frac{\cos(0)}{\omega_n}\text{sgn}(1) = \frac{1}{\omega_n} - \frac{1}{\omega_n} = 0$$

which satisfies the GIP HJB PDE.

4.3.3 Example 4.3: Motivating Problem for Planar, Co-aligned Orbits

Using a Variation of Parameters approach the time rate of change of arbitrary constants of motion under non-homogeneous motion may be found. For this worked problem Gauss' Variational Equations

(GVEs) for the classical orbit elements are used [70, 65]. This example demonstrates how Lemma 4.2.1 may be applied to GVEs to determine the semi-major axis and eccentricity range using ΔV as the independent parameter. This is a subproblem of the motivating problem in §4.1. Orbit element range computation using this coordinate pair is an excellent example because the results may be validated using classically derived optimal co-aligned ellipse-to-ellipse impulsive transfers [71]. As previously mentioned, a similar, significantly more complicated derivation of the orbit element range set for a, e, and i is the subject of a separate paper [69]. Again, as the desired independent parameter is ΔV (a common mass-independent fuel metric in spacecraft operations), the independent parameter mapping function is

$$\Delta V = V_f - V_0 = \int_{t_0}^{t_f} \|\mathbf{u}(\tau)\| d\tau$$

yielding $l(\mathbf{x}(t), \mathbf{u}(t), t) = \|\mathbf{u}(t)\|$. As discussed in Illustration 4.2.2, using this mapping function integrand makes the solution to this problem a Generalized Metric Range Set. Gauss' Variational Equations for semi-major axis (a) and eccentricity (e) are written as [70, 65]

$$\frac{da}{dt} = \frac{2a^{\frac{3}{2}} e \sin f}{\mu^{\frac{1}{2}}(1-e^2)^{\frac{1}{2}}} u_r + \frac{a^{\frac{3}{2}}(1+e\cos f)}{\mu^{\frac{1}{2}}(1-e^2)^{\frac{1}{2}}} u_\theta \tag{4.21}$$

$$\frac{de}{dt} = \frac{a^{\frac{1}{2}}(1-e^2)^{\frac{1}{2}} \sin f}{\mu^{\frac{1}{2}}} u_r + \frac{a^{\frac{1}{2}}(1-e^2)^{\frac{1}{2}}}{\mu^{\frac{1}{2}}} \left[\frac{e\cos^2 f + 2\cos f + e}{1+e\cos f} \right] u_\theta \tag{4.22}$$

where μ is the gravitational parameter of the central body in question, and f is the true anomaly. As with the Amplitude Range example, the phasing argument f (true anomaly) is considered a control parameter. The control acceleration is defined as $\mathbf{u}(t) = [u_r,\ u_\theta]^T$, where u_r is the acceleration in the radial direction and u_θ is the control in the along-track direction. The geometry of the problem is shown in Figure 4.6. Writing the state as $\mathbf{x}^T = [a,\ e]^T$ and the dynamics as $\dot{\mathbf{x}} = \mathbf{f}(\mathbf{x}, f)\mathbf{u}$, the GIP HJB PDE (4.5) becomes

$$\frac{\partial \tilde{V}}{\partial s} + \sup_{u\epsilon U, f\epsilon[0,2\pi)} \left[\frac{\partial \tilde{V}}{\partial \mathbf{x}}^T \mathbf{f}(\mathbf{x}, f) \frac{\mathbf{u}}{\|\mathbf{u}\|_2} \right] = \mathbf{0}$$

Noting that the control now appears as a unit vector, it is re-parameterized such that

$$\frac{\mathbf{u}}{\|\mathbf{u}\|_2} = \begin{bmatrix} \sin\beta \\ \cos\beta \end{bmatrix} = \hat{\mathbf{u}}(\beta)$$

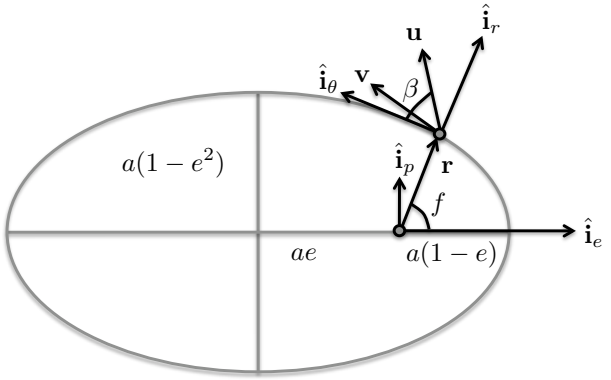

Figure 4.6: Planar orbit geometry

The optimal control Hamiltonian associated with the new GIP HJB PDE is

$$\begin{aligned}\mathcal{H} = \left(\frac{a^{\frac{1}{2}}}{\mu^{\frac{1}{2}}(1-e^2)^{\frac{1}{2}}}\right) \sup_{\beta, f\in[0,2\pi)} \Big[& p_a \left(2ae\sin f \sin\beta + 2a(1+e\cos f)\cos\beta\right) \\ & + p_e \left((1-e^2)\sin f\sin\beta + \frac{1-e^2}{1+e\cos f}\left(e\cos^2 f + 2\cos f + e\right)\cos\beta\right)\Big]\end{aligned} \tag{4.23}$$

Note that explicit instances of $\mathbf{u}$ have disappeared and are replaced with β. To find the optimal control policy (f^*, β^*) the first-order necessary conditions $\partial\mathcal{H}/\partial f = 0$ and $\partial\mathcal{H}/\partial\beta = 0$ are examined and the common factor is ignored. Collecting terms of $\sin f\cos\beta$ and $\cos f\sin\beta$ in $\partial\mathcal{H}/\partial f$ produces

$$\begin{aligned}\frac{\partial\mathcal{H}}{\partial f} &= \left(2p_a ae + p_e\left(1-e^2\right)\right)\cos f\sin\beta \\ &+ \left[-2p_a ae + p_e\left(-\left(1-e^2\right) + \frac{e\left(1-e^2\right)\left(e\cos f^2 + 2\cos f + e\right)}{\left(e\cos f + 1\right)^2}\right)\right]\sin f\cos\beta = 0\end{aligned}$$

and collecting terms in $\sin\beta$ and $\sin f\cos\beta$ for $\partial\mathcal{H}/\partial\beta$ generates

$$\begin{aligned}\frac{\partial\mathcal{H}}{\partial\beta} = -\left(2p_a\left(1+e\cos f\right) + p_e\frac{\left(1-e^2\right)\left(e\cos f^2 + 2\cos f + e\right)}{e\cos f + 1}\right)\sin\beta \\ + \left(2p_a ae + p_e(1-e^2)\right)\sin f\cos\beta = 0\end{aligned}$$

Unfortunately a frontal assault to solve for (f^*, b^*) does not yield extrema. Careful inspection of the first-order necessary conditions, however, reveals the following candidate optimal control policies:

$$\begin{aligned}(f_1, \beta_1) &= (0, 0) \\ (f_2, \beta_2) &= (\pi, 0) \\ (f_3, \beta_3) &= (0, \pi) \\ (f_4, \beta_4) &= (\pi, \pi)\end{aligned}$$

Detailed examination of the Hamiltonian values and second-order necessary conditions using each of the candidate control policies generates the following optimal control policy:

$$(f^*, \beta^*) = \begin{cases} f = 0, \beta = 0 \text{ if } p_a \geq 0 \text{ and } p_a \geq \frac{-ae}{1-e^2} p_e \\ f = \pi, \beta = 0 \text{ if } p_a < 0 \text{ and } p_a \leq \frac{-ae}{1-e^2} p_e \\ f = 0, \beta = \pi \text{ if } p_a \geq 0 \text{ and } p_a < \frac{-ae}{1-e^2} p_e \\ f = \pi, \beta = \pi \text{ if } p_a < 0 \text{ and } p_a > \frac{-ae}{1-e^2} p_e \\ f \in [0, 2\pi), \beta \in [0, 2\pi) \text{ if } p_a = 0, p_e = 0 \end{cases} \tag{4.24}$$

Each of the optimal control policies corresponds directly to a classically derived optimal orbit raising / lowering maneuver [71], as shown in Table 4.1. To compute the value function using the GIP HJB PDE,

Table 4.1: Example 4.3 Optimal Control Policy Equivalence

(f^*, β^*)	**Classical Maneuver**	**Description**
$(0, 0)$	Raise Apoapsis	Impulse at periapsis along the velocity vector
$(\pi, 0)$	Raise Periapsis	Impulse at apoapsis along the velocity vector
$(0, \pi)$	Lower Apoapsis	Impulse at periapsis opposite the velocity vector
(π, π)	Lower Periapsis	Impulse at apoapsis opposite the velocity vector

the Level Set Toolbox [64] is used. The initial value function $\tilde{V}(a, e, \Delta V_0 = 0) = 0$ is constructed such that the initial level set is an ellipse centered at $a_c = 24,393$ km and $e_c = 0.7253$ with radii $r_a = 693$ km and $r_e = 0.0068$. The value function domain is discretized with 101 grid points in both the semi-major axis and eccentricity directions. The value function is propagated using the GIP HJB PDE (4.5) in fixed ΔV steps of 7.43 m/s, with the optimal control Hamiltonian (4.23) and optimal control policy (4.24). To verify that the zero-level sets correctly compute the orbit element range set, the range contours are compared with analytically available solutions from classical orbit mechanics [71]. The orbit element range sets found using the GIP HJB PDE as well as the classical results are shown in Figures 4.7 and 4.8.

As Figures 4.7 and 4.8 demonstrate, computing the orbit element range set using the GIP HJB PDE and the approach outlined in Lemma 4.2.1 agrees nicely with the classical results. There is a slight discrepancy on the lower right-hand side because the initial level set is an ellipsoid, while the analytical case requires the initial set to be a point in the state space.

It is important to understand that because the independent parameter is now fuel rather than time,

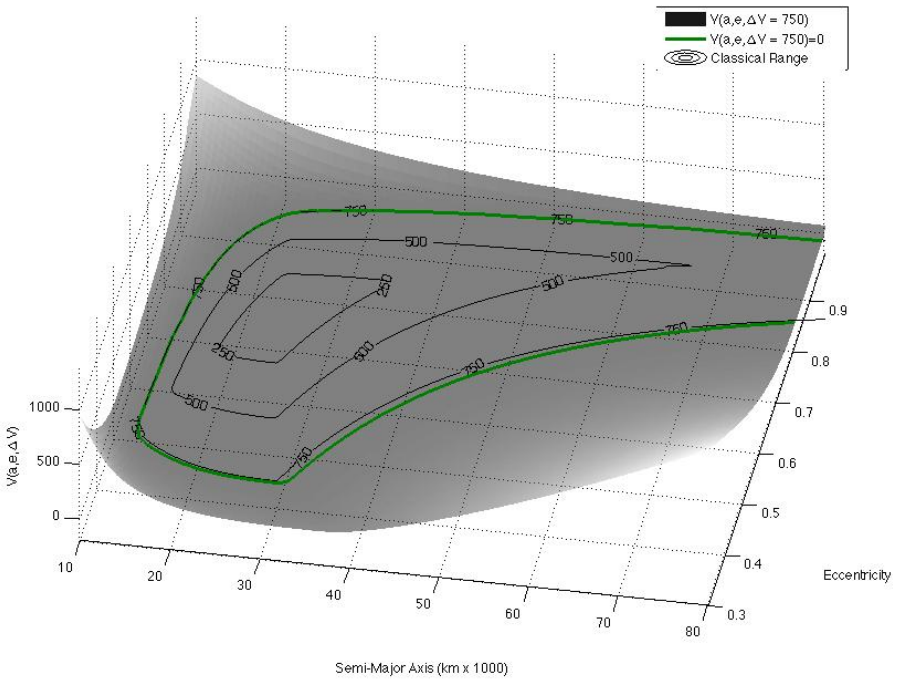

Figure 4.7: Example 4.3 planar orbit element range using ΔV as an independent parameter. Contour lines (and values) indicate a specific quantity of ΔV (m/s) is required to reach a particular semi-major axis / eccentricity coordinate.

and there are no longer any direct references to time, the range plots shown are free-time. Using this formulation, along any optimal trajectory using ΔV as the independent parameter, one can 'pause' the trajectory at any arbitrary value of $\Delta V \in [\Delta V_0, \Delta V_f]$ and keep the object in a parking orbit for arbitrarily large periods of time, then resume the optimal impulse profile. The overall approach using the GIP HJB PDE along with the method outlined in Lemma 4.2.1 can be used with other orbit element sets (such as the equinoctial orbit element set), or even the full orbit element set.

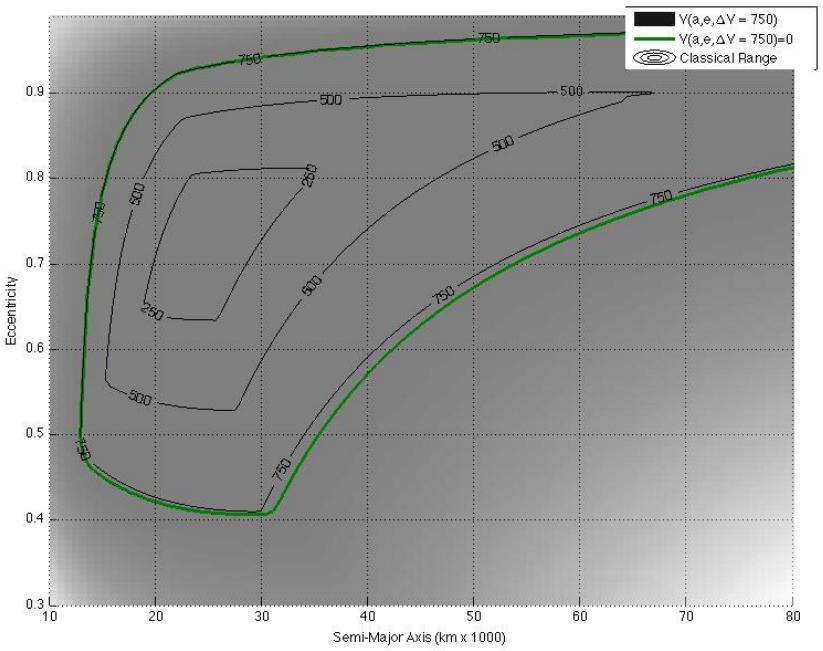

Figure 4.8: Example 4.3 planar orbit element range using ΔV as an independent parameter. Same as plot in Figure 4.7, but viewing only the $a - e$ plane.

4.4 Extended Example: Orbit Range

This section endeavors to demonstrate how ΔV-constrained range sets in orbit element space may be computed using the General Independent Parameter (GIP) HJB PDE, optimal control policies, and existing numerical reachability set tools. §4.4.1 discusses the chosen coordinates and equations of motion, assumptions, the mapping from time- to ΔV-integration space, the optimal control policy derivation, and the optimal state and adjoint equations of motion. In §4.4.2 three examples are given. The first verifies the numerical results using classical ellipse-to-ellipse optimal trajectory maneuvers, the second demonstrates relative control authority in various orbit-element regions, and the third example examines some of the advantages of using implicitly defined surfaces to represent the surface of the range set.

4.4.1 Application of the General Independent Parameter Theory

To apply the framework outlined in Chapter 4 for the General Independent Parameter HJB PDE and the results from Lemma 4.2.1, Gauss' Variational Equations for the classical orbit elements with arbitrary disturbance accelerations are now introduced. Several critical assumptions are then made before scaling the dynamics into the ΔV integration space and determining the optimal control policy.

4.4.1.1 Equations of Motion

Gauss' Variational Equations (GVEs) for the classical orbit elements $\mathbf{oe}^T = [a, e, i, \Omega, \omega, f]$ (visualized in Figure 4.9) with arbitrary accelerations $\mathbf{a}^T = [a_r, a_\theta, a_h]^T$ (expressed in a rotating Hill frame) may be written as [70, 82, 65]

$$\frac{d\mathbf{oe}}{dt} = \mathbf{f}(\mathbf{oe})\mathbf{a} \tag{4.25}$$

where a is the semi-major axis, e is the eccentricity, i is the inclination, Ω is the ascending node, ω is the argument of periapsis, and f is the true anomaly. The problem is now reduced in scope by making the following assumptions:

[A1] The user is unconcerned with the duration of an optimal maneuver from an initial orbit element set

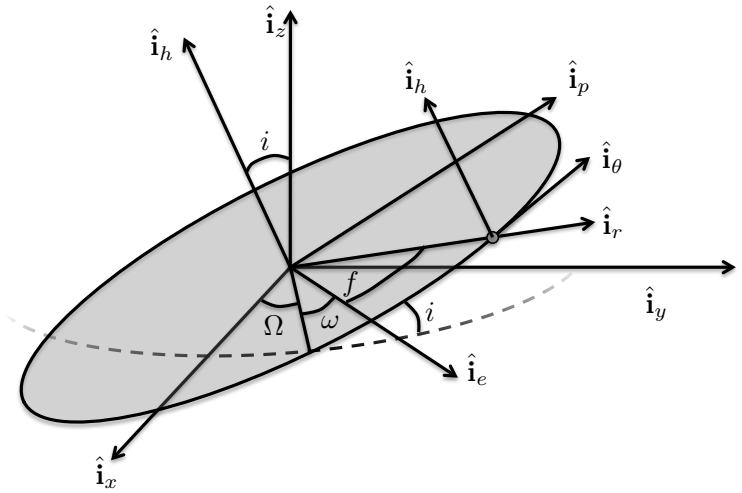

Figure 4.9: Orbit geometry using classical orbit elements relative to the inertial cartesian frame $\mathcal{N}: \hat{\mathbf{i}}_x, \hat{\mathbf{i}}_y, \hat{\mathbf{i}}_z$, the orbit frame $\mathcal{E}: \hat{\mathbf{i}}_e, \hat{\mathbf{i}}_p, \hat{\mathbf{i}}_h$, and the rotating Hill frame $\mathcal{H}: \hat{\mathbf{i}}_r, \hat{\mathbf{i}}_\theta, \hat{\mathbf{i}}_h$.

$\mathbf{oe}_0$ to a final orbit element set $\mathbf{oe}_f$. The problem is considered a 'free-time' optimal control problem.

[A2] The general accelerations a_r, a_θ, and a_h in the rotating Hill frame are the result of corresponding control accelerations u_r, u_θ, and u_h.

[A3] For the first part of this analysis dynamics in the ascending node Ω are ignored (but are discussed in §4.4.1.6).

[A4] Similar to the ascending node Ω, the argument of periapsis (ω) dynamics are ignored for the first portion of this analysis (but are discussed in §4.4.1.6).

Starting from the classical GVE form [70, 82, 65], with algebraic manipulation the time dynamics for a, e, and i are written in terms of only a, e, i, ω, and f, generating the following equations of motion:

$$\frac{da}{dt} = \frac{2a^{\frac{3}{2}} e \sin f}{\mu^{\frac{1}{2}}(1-e^2)^{\frac{1}{2}}} u_r + \frac{a^{\frac{3}{2}}(1+e\cos f)}{\mu^{\frac{1}{2}}(1-e^2)^{\frac{1}{2}}} u_\theta \tag{4.26}$$

$$\frac{de}{dt} = \frac{a^{\frac{1}{2}}(1-e^2)^{\frac{1}{2}} \sin f}{\mu^{\frac{1}{2}}} u_r + \frac{a^{\frac{1}{2}}(1-e^2)^{\frac{1}{2}}}{\mu^{\frac{1}{2}}} \left[\frac{e\cos^2 f + 2\cos f + e}{1+e\cos f}\right] u_\theta \tag{4.27}$$

$$\frac{di}{dt} = \frac{a^{\frac{1}{2}}}{\mu^{\frac{1}{2}}(1-e^2)^{\frac{1}{2}}} \left[\frac{(1-e^2)\cos(\omega+f)}{1+e\cos f}\right] u_h \tag{4.28}$$

Equations (4.26), (4.27), and (4.28) are the general equations of orbit element motion excluding dynamics for Ω, ω, and f.

4.4.1.2 Alternate Independent Parameter Mapping

To transform the integration variable in (4.26), (4.27), and (4.28) from time to ΔV, an independent parameter mapping function is used. The general independent parameter mapping function [81] is written as

$$s = S(\mathbf{x}(\cdot), \mathbf{u}(\cdot), t) = \int_{t_0}^{t} l(\mathbf{x}(\tau), \mathbf{u}(\tau), \tau) d\tau + s_0$$

where it is required that $l(\mathbf{x}, \mathbf{u}, t) \geq 0$ along an optimal trajectory $\mathbf{x}^*(\cdot), \mathbf{u}^*(\cdot)$, $t \in [t_0, t_f]$. A standard metric for orbital fuel usage is the characteristic velocity[83] $s = \Delta V$, which may be written as

$$\Delta V = \int_{t_0}^{t} \|\mathbf{u}(\tau)\|_2 d\tau$$

with $s_0 = \Delta V_0 = 0$ and $\mathbf{u}(t)$ is defined to be

$$\mathbf{u}^T = \begin{bmatrix} u_r & u_\theta & u_h \end{bmatrix}$$

Choosing ΔV to be the alternate independent parameter suggests that

$$l(\mathbf{x}, \mathbf{u}, t) = \|\mathbf{u}(t)\|_2 \tag{4.29}$$

With this choice it is important to realize that if $\mathbf{u}(t) = \mathbf{0}$ at any time $t \in [t_0, t_f]$, then there is no unique map back from the ΔV independent parameter back to time, though a minimum time mapping may exist (there happen to be infinite mappings back to time due to the singularity). Note that, as discussed in Lemma III.1 in Holzinger, et al.[81], when $\mathbf{u}(t) = \mathbf{0}$, the dyamics of the semi-major axis, eccentricity, and inclination are well defined and identically zero. It is now necessary to further limit the scope of this effort by making two more assumptions:

[A5] The control inputs $\mathbf{u}$ are impulsive. Because of mapping ambiguities between time and ΔV, and because under control accelerations the true anomaly f changes, it is expedient to consider impulsive control inputs.

[A6] When integrating in the ΔV independent parameter space, it is very convenient use the true anomaly f and the argument of periapsis ω as a control variables. This is perfectly sensible, as a spacecraft

operator can use both f and ω (as it drifts due to J_2 perturbations) as timing/phasing control variables. The parameters f and ω are considered control parameters with $f, \omega \in [0, 2\pi)$.

Combined, all of these assumptions allow the general time dynamics of the orbit elements (4.25) to be written in the form

$$\frac{d\mathbf{oe}_{tr}}{dt} = \mathbf{f}_{tr}(\mathbf{oe}_{tr}, f, \omega)\mathbf{u}$$

with the $\cdot_{tr}$ subscript indicating the truncated orbit element set

$$\mathbf{oe}_{tr}^T = \begin{bmatrix} a & e & i \end{bmatrix}^T \tag{4.30}$$

The control variables are the control acceleration $\mathbf{u}$, true anomaly f, and argument of periapsis ω.

4.4.1.3 Hamilton Jacobi Bellman Formulation

To compute a range set the GIP HJB PDE must first be formulated in terms of the chosen state coordinates and independent parameter. The general form of the GIP HJB PDE derived in §4.2.2 is

$$\frac{\partial \tilde{V}}{\partial s} + \underset{\mathbf{u}\in U}{\text{opt}} \left[\frac{\tilde{\mathcal{L}}(\mathbf{x}, \mathbf{u}, s)}{\tilde{l}(\mathbf{x}, \mathbf{u}, s)} + \frac{\partial \tilde{V}}{\partial \mathbf{x}}^T \frac{\tilde{\mathbf{f}}(\mathbf{x}, \mathbf{u}, s)}{\tilde{l}(\mathbf{x}, \mathbf{u}, s)} \right] = \mathbf{0} \tag{4.31}$$

where the 'opt' argument may be either 'inf' or 'sup.', U is the set of permissible controls, $\tilde{\mathcal{L}}$ is the trajectory cost, and $\tilde{l}$ is the mapping function integrand. For a general reachability problem, the optimization operation is a supremum, and the Lagrangian $\tilde{\mathcal{L}}(\mathbf{x}, \mathbf{u}, s) = 0$. With the choice of the independent parameter mapping function slope in (4.29) and the truncated dynamics (4.30), the HJB PDE for this problem is

$$\frac{\partial \tilde{V}}{\partial \Delta V} + \sup_{u\in U, f, \omega \in [0,2\pi)} \left[\frac{\partial \tilde{V}}{\partial \mathbf{oe}_{tr}}^T \mathbf{f}_{tr}(\mathbf{oe}_{tr}, f, \omega) \frac{\mathbf{u}}{\|\mathbf{u}\|_2} \right] = \mathbf{0}$$

Noting that the optimal control now appears as a unit vector, it is convenient to reparameterize $\hat{\mathbf{u}}$ such that

$$\hat{\mathbf{u}} = \frac{\mathbf{u}}{\|\mathbf{u}\|_2} = \begin{bmatrix} \sin\beta\cos\gamma \\ \cos\beta\cos\gamma \\ \sin\gamma \end{bmatrix} = \hat{\mathbf{u}}(\beta, \gamma)$$

where $\beta \in [0, 2\pi)$ is the angle of the impulse from $\hat{\mathbf{i}}_\theta$ in the r-θ orbit plane and $\gamma \in [-\pi/2, \pi/2]$ is the angle $\hat{\mathbf{u}}$ forms with the orbit plane (both illustrated in Figure 4.10). The final form of the HJB PDE for computing

range using a subset of the orbit elements $\mathbf{oe}_{tr}$ is then

$$\frac{\partial \tilde{V}}{\partial \Delta V} + \sup_{f,\omega,\beta\in[0,2\pi),\gamma\in[-\frac{\pi}{2},\frac{\pi}{2}]} \left[\frac{\partial \tilde{V}}{\partial \mathbf{oe}_{tr}}^{T} \mathbf{f}_{tr}(\mathbf{oe}_{tr}, f, \omega)\hat{\mathbf{u}}(\beta,\gamma) \right] = \mathbf{0}$$

Note that the transformation from time to ΔV as the independent parameter and the re-parameterization of the control unit vector $\hat{\mathbf{u}}$ has eliminated any singularity associated with $\mathbf{u}(t) = \mathbf{0}$; the dynamics with respect to ΔV using the new control variables f, ω, β, and γ are well defined for all control variable parameters. The dynamics in terms of the new independent parameter ΔV may be written in their final form as

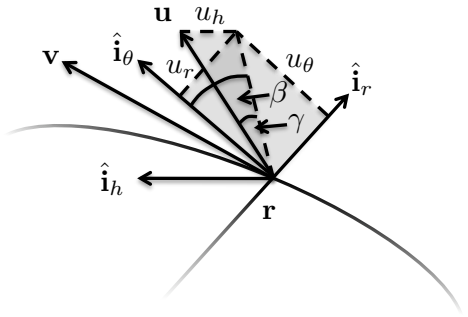

Figure 4.10: Control acceleration $\mathbf{u}$ decomposition and parameterization in the rotating Hill frame

$$\frac{da}{d\Delta V} = \left(\frac{a^{\frac{1}{2}}}{\mu^{\frac{1}{2}}(1-e^2)^{\frac{1}{2}}} \right) (2ae\sin f \sin\beta\cos\gamma + 2a(1+e\cos f)\cos\beta\cos\gamma) \tag{4.32}$$

$$\frac{de}{d\Delta V} = \left(\frac{a^{\frac{1}{2}}}{\mu^{\frac{1}{2}}(1-e^2)^{\frac{1}{2}}} \right) \left((1-e^2)\sin f \sin\beta\cos\gamma + \frac{1-e^2}{1+e\cos f}\left(e\cos^2 f + 2\cos f + e\right)\cos\beta\cos\gamma \right) \tag{4.33}$$

$$\frac{di}{d\Delta V} = \left(\frac{a^{\frac{1}{2}}}{\mu^{\frac{1}{2}}(1-e^2)^{\frac{1}{2}}} \right) \left(\frac{(1-e^2)\cos(\omega+f)}{1+e\cos f}\sin\gamma \right) \tag{4.34}$$

The transformation from the classical Gauss Variational Equations (GVEs) for orbit elements to (4.32), (4.33), and (4.34) essentially examines the incremental change in semi-major axis, eccentricity, and inclination as incremental amounts of ΔV are expended on the orbiting object. A brief examination of (4.32), (4.33), and (4.34) (and recalling the orbit property identities used in its formulation) show us that it is valid for all elliptical orbits, specifically for $a > 0$, $e \in [0, 1)$, and $i \in \mathbb{R}$. Though out of scope for the present effort, the approach thus far can also be applied to other non-singular orbit elements (such as equinoctial orbit elements). The Optimal Control Hamiltonian is now

$$\mathcal{H} = \sup_{f,\omega,\beta\in[0,2\pi),\gamma\in[-\frac{\pi}{2},\frac{\pi}{2}]} \left[\mathbf{p}^T \mathbf{f}_{tr}(\mathbf{oe}_{tr}, f, \omega)\hat{\mathbf{u}}(\beta,\gamma) \right]$$

with the understanding that the adjoint state $\mathbf{p}$ is equivalent to the gradient of the value function $\tilde{V}$ with respect to the state space ($\mathbf{p} = \partial\tilde{V}/\partial\mathbf{œ}_{tr}$). All of the terms $p_j(d\text{œ}_{tr,j}/d\Delta V)$, $j = 1, 2, 3$, have a common factor of $a^{\frac{1}{2}}/\mu^{\frac{1}{2}}(1-e^2)^{\frac{1}{2}}$, allowing the Hamiltonian to be written in expanded form as

$$\begin{aligned}\mathcal{H} = \left(\frac{a^{\frac{1}{2}}}{\mu^{\frac{1}{2}}(1-e^2)^{\frac{1}{2}}}\right) \sup_{f,\omega,\beta\epsilon[0,2\pi),\gamma\epsilon[-\frac{\pi}{2},\frac{\pi}{2}]} \Bigg[& p_a\Big(2ae\sin f\sin\beta\cos\gamma + 2a(1+e\cos f)\cos\beta\cos\gamma\Big) \\ & + p_e\left((1-e^2)\sin f\sin\beta\cos\gamma + \frac{1-e^2}{1+e\cos f}\left(e\cos^2 f + 2\cos f + e\right)\cos\beta\cos\gamma\right) \\ & + p_i\left(\frac{(1-e^2)\cos(\omega+f)}{1+e\cos f}\sin\gamma\right)\Bigg]\end{aligned} \tag{4.35}$$

The Hamiltonian in (4.35) is examined in the next subsection to determine the optimal control policy using standard optimal control approaches [27, 29, 28].

4.4.1.4 Optimal Control Policy

To determine the optimal control policy $(f^*, \omega^*, \beta^*, \gamma^*)$ that minimizes the Optimal Control Hamiltonian, the first-order necessary conditions must be satisfied:

$$\frac{\partial\mathcal{H}}{\partial\mathbf{u}} = \begin{bmatrix} \frac{\partial\mathcal{H}}{\partial f} & \frac{\partial\mathcal{H}}{\partial\omega} & \frac{\partial\mathcal{H}}{\partial\beta} & \frac{\partial\mathcal{H}}{\partial\gamma} \end{bmatrix} = \mathbf{0}_{4\times1}$$

Solving for $(f, \omega, \beta, \gamma)$ that satisfy the four equations generated by the first-order necessary condition will yield the control laws that generate maxima, minima, and saddle points. The common factor outside of the 'sup' arguement may be ignored, as it contains none of the control variables. Each of the four equations generated by the first-order necessary condition are now computed. For $\partial\mathcal{H}/\partial f = 0$:

$$\begin{aligned}\frac{\partial\mathcal{H}}{\partial f} = {} & p_a\Big(2ae\cos f\sin\beta - 2ae\cos\beta\sin f\Big) \\ & - p_e\Bigg(\cos f\sin\beta\left(e^2-1\right) - \frac{\cos\beta\left(e^2-1\right)\left(2\sin f + 2e\cos f\sin f\right)}{e\cos f+1} \\ & + \frac{e\cos\beta\sin f\left(e^2-1\right)\left(e\cos f^2 + 2\cos f + e\right)}{\left(e\cos f+1\right)^2}\Bigg) \\ & + p_i\left(-\frac{(1-e^2)\sin(\omega+f)}{1+e\cos f}\sin\gamma + \frac{(1-e^2)\cos(\omega+f)}{(1+e\cos f)^2}\sin f\sin\gamma\right) = 0\end{aligned}$$

For $\partial\mathcal{H}/\partial\omega = 0$:

$$\frac{\partial\mathcal{H}}{\partial\omega} = -p_i\left(\frac{(1-e^2)\sin(\omega+f)}{1+e\cos f}\sin\gamma\right) = 0$$

For $\partial\mathcal{H}/\partial\beta = 0$:

$$\frac{\partial\mathcal{H}}{\partial\beta} = -p_a\left(2a\sin\beta\,(e\cos f+1)\cos\gamma - 2ae\cos\beta\cos\gamma\sin f\right)$$
$$-p_e\left(\left(e^2-1\right)\cos\beta\sin f\cos\gamma - \frac{\left(e^2-1\right)\left(e\cos f^2+2\cos f+e\right)}{e\cos f+1}\sin\beta\cos\gamma\right) = 0$$

and for $\partial\mathcal{H}/\partial\gamma = 0$:

$$\frac{\partial\mathcal{H}}{\partial\gamma} = -p_a\left(2ae\sin f\sin\beta\sin\gamma + 2a(1+e\cos f)\cos\beta\sin\gamma\right)$$
$$-p_e\left((1-e^2)\sin f\sin\beta\sin\gamma + \frac{1-e^2}{1+e\cos f}\left(e\cos^2 f+2\cos f+e\right)\cos\beta\sin\gamma\right)$$
$$+p_i\left(\frac{(1-e^2)\cos(\omega+f)}{1+e\cos f}\cos\gamma\right)$$

While at first these expressions appear quite complicated, after examination there are several common terms in each partial derivative. Re-organizing and simplifying produces

$$\frac{\partial\mathcal{H}}{\partial f} = \left(2p_a ae + p_e\left(1-e^2\right)\right)\cos f\sin\beta\cos\gamma$$
$$+\left[-2p_a ae + p_e\left(-\left(1-e^2\right) + \frac{e\left(1-e^2\right)\left(e\cos f^2+2\cos f+e\right)}{\left(e\cos f+1\right)^2}\right)\right]\sin f\cos\beta\cos\gamma \tag{4.36}$$
$$+\left(p_i\frac{1-e^2}{1+e\cos f}\left(\sin(\omega+f)+e\sin\omega\right)\right)\sin\gamma = 0$$

$$\frac{\partial\mathcal{H}}{\partial\omega} = \left(-p_i\frac{(1-e^2)}{1+e\cos f}\right)\sin(\omega+f)\sin\gamma = 0 \tag{4.37}$$

$$\frac{\partial\mathcal{H}}{\partial\beta} = -\left(2p_a\left(1+e\cos f\right) + p_e\frac{\left(1-e^2\right)\left(e\cos f^2+2\cos f+e\right)}{e\cos f+1}\right)\sin\beta\cos\gamma$$
$$+\left(2p_a ae + p_e(1-e^2)\right)\sin f\cos\beta\cos\gamma = 0 \tag{4.38}$$

$$\frac{\partial\mathcal{H}}{\partial\gamma} = \left(-2p_a ae - p_e(1-e^2)\right)\sin f\sin\beta\sin\gamma$$
$$+\left(-2p_a a(1+e\cos f) - p_e\frac{\left(1-e^2\right)\left(e\cos f^2+2\cos f+e\right)}{e\cos f+1}\right)\cos\beta\sin\gamma \tag{4.39}$$
$$+\left(-p_i\frac{1-e^2}{1+e\cos f}\right)\cos(\omega+f)\cos\gamma = 0$$

To simplify this analysis, (4.36) - (4.39) are examined in a sinusoidal form by considering the more complicated terms as coefficients:

$$\frac{\partial\mathcal{H}}{\partial f} = k_{f,1}\cos f\sin\beta\cos\gamma + k_{f,2}\sin f\cos\beta\cos\gamma + k_{f,3}\left(\sin(\omega+f)+e\sin\omega\right)\sin\gamma = 0$$

$$\frac{\partial\mathcal{H}}{\partial\omega} = k_{\omega,1}\sin(\omega+f)\sin\gamma = 0$$

$$\frac{\partial \mathcal{H}}{\partial \beta} = k_{\beta,1} \sin\beta\cos\gamma + k_{\beta,2} \sin f \cos\beta\cos\gamma = 0$$

$$\frac{\partial \mathcal{H}}{\partial \gamma} = k_{\gamma,1} \sin f \sin\beta\sin\gamma + k_{\gamma,2} \cos\beta\sin\gamma + k_{\gamma,3} \cos(\omega + f)\cos\gamma = 0$$

Note that the coefficients $k_{\cdot,\cdot}$ depend only on a, e, i, p_a, p_e, p_i, and f. By inspection the coefficients $k_{\cdot,\cdot}$ are typically non-zero except in transient cases (i.e. $p_a, p_e, p_i = 0$) or degenerate cases ($e = 1$). Rather, examining the factorization above it is clear that careful selection of optimal control values $f^*, \omega^*, \beta^*, \gamma^*$ will satisfy the first-order necessary condition of optimality. The sinusoidal solutions are enumerated below in Table 4.2. Despite significant effort no extremal solutions besides those in Table 4.2 have been found. For some very specific orbit regimes, critical points $f^*, \omega^*, \beta^*, \gamma^*$ not represented in Table 4.2 have been found. However, these numerically generated critical points do not satisfy the second order necessary conditions and are saddle points in the Hamiltonian. Interestingly, there is no proof here that other extremal solutions do not exist; a full exploration of the admissible critical points is an excellent topic for further work. Despite the possible existence of additional extremal solutions, it remains that Table 4.2 enumerates all of the maneuvers suggested by free-time, fuel-optimal transfers in astrodynamics literature.

Table 4.2: Candidate pre-reduction optimal control policies

Case	$f^*, \omega^*, \beta^*, \gamma^*$	**Description**
1'	$0, \frac{\pi}{2}, 0, 0$	Raise ap. w/o change in Ω
2'	$0, \frac{3\pi}{2}, 0, 0$	Raise ap. w/o change in Ω
3'	$\pi, \frac{\pi}{2} 0, 0$	Raise per. w/o change in Ω
4'	$\pi, \frac{3\pi}{2} 0, 0$	Raise per. w/o change in Ω
5'	$0, \frac{\pi}{2}, \pi, 0$	Lower ap. w/o change in Ω
6'	$0, \frac{3\pi}{2}, \pi, 0$	Lower ap. w/o change in Ω
7'	$\pi, \frac{\pi}{2}, \pi, 0$	Lower per. w/o change in Ω
8'	$\pi, \frac{3\pi}{2}, \pi, 0$	Lower per. w/o change in Ω
9'	$0, 0, 0, -\frac{\pi}{2}$	Dec. i at per., per. at Ω
10'	$0, 0, 0, \frac{\pi}{2}$	Inc. i at per., per. at Ω
11'	$\pi, 0, 0, -\frac{\pi}{2}$	Inc. i at ap., per. at Ω
12'	$\pi, 0, 0, \frac{\pi}{2}$	Dec. i at ap., per. at Ω
13'	$0, \pi, 0, -\frac{\pi}{2}$	Dec. i at per., ω opposite Ω
14'	$0, \pi, 0, \frac{\pi}{2}$	Inc. i at per., ω opposite Ω
15'	$\pi, \pi, 0, -\frac{\pi}{2}$	Inc. i at ap., ω opposite Ω
16'	$\pi, \pi, 0, \frac{\pi}{2}$	Dec. i at ap., ω opposite Ω

There are 16 candidate optimal control policies generated by the first-order necessary conditions and

enumerated in Table 4.2. As mentioned, the ascending node dynamics[70, 82, **?**]

$$\frac{d\Omega}{dt} = \frac{a^{\frac{1}{2}}(1-e^2)^{\frac{1}{2}}}{\mu^{\frac{1}{2}}(1+e\cos f)}\frac{\sin(\omega+f)}{\sin i}\sin\gamma$$

are identically zero for cases 1 through 8. Due to previous assumptions several options may be eliminated. For cases 1-8, changes in Ω are ignorable [A3], and choosing $\omega = 0$ has no impact on the magnitude of the Hamiltonian. This allows $\omega = 0$ rather than $\pi/2$ or $3\pi/2$, collapsing the first 8 cases to 4 individual cases. For cases 9-16, since the actual value of ω is ignorable so long as the necessary conditions are satisfied [A4], the set of maneuvers that occur opposite the ascending node are eliminated, leaving cases 9-12. Further, computing the Hamiltonians for cases 9-12, despite the fact that they all satisfy the second order neceesary conditions of optimality ($\partial^2\mathcal{H}/\partial(f,\omega,\beta,\gamma)^2 < 0$) the inclination maneuvers that occur at periapsis generate universally smaller Hamiltonian values than those at apoapsis, allowing cases 9 and 10 to be disregarded. After eliminating these cases the minimal set of remaining optimal control policy candidates are shown in Table 4.3.

Table 4.3: Candidate post-reduction optimal control policies

Case	$f^*, \omega^*, \beta^*, \gamma^*$	**Description**
1	$0, 0, 0, 0$	Raise apoapsis
2	$\pi, 0, 0, 0$	Raise periapsis
3	$0, 0, \pi, 0$	Lower apoapsis
4	$\pi, 0, \pi, 0$	Lower periapsis
5	$\pi, 0, 0, -\frac{\pi}{2}$	Increase i at apoapsis
6	$\pi, 0, 0, \frac{\pi}{2}$	Decrease i at apoapsis

If ascending node or argument of periapsis had been retained as state variables with corresponding adjoints, then neither [A3] nor [A4] apply and additional optimal control policies would be generated. The critical points must now be examined to determine which solutions are maxima, minima, and saddle points of the Hamiltonian $\mathcal{H}$ given the states a, e, i, and the adjoint states p_a, p_e, and p_i. Because there are six discrete optimal control policies, the values of the Hamiltonian at the critical points $(f_i^*, \omega_i^*, \beta_i^*, \gamma_i^*)$ must each be computed and compared to one another, determining over which regions of adjoint space each are optimal. In continuous control policies the second derivative of the Hamiltonian with respect to the control parameters would be examined, but since there are discrete control candidates they must be examined individually. The values of the Hamiltonian at each critical point are evaluated and denoted by $\mathcal{H}_i$, where i

denotes the optimal control policy case in Table 4.3:

$$\mathcal{H}_1 = 2\,(e+1)\,(ap_a + (1-e)p_e)$$

$$\mathcal{H}_2 = 2\,(e-1)\,(-ap_a + (1+e)p_e)$$

$$\mathcal{H}_3 = -2\,(e+1)\,(ap_a + (1-e)p_e)$$

$$\mathcal{H}_4 = -2\,(e-1)\,(-ap_a + (1+e)p_e)$$

$$\mathcal{H}_5 = p_i(1+e)$$

$$\mathcal{H}_6 = -p_i(1+e)$$

As a matter of analytical convenience the adjoint is now parameterized as

$$\mathbf{p} = \begin{bmatrix} p_a \\ p_e \\ p_i \end{bmatrix} = \|\mathbf{p}\|_2 \begin{bmatrix} \hat{p}_a \\ \hat{p}_e \\ \hat{p}_i \end{bmatrix} = \|\mathbf{p}\|_2 \begin{bmatrix} \cos\theta\cos\phi \\ \sin\theta\cos\phi \\ \sin\phi \end{bmatrix}$$

where θ and ϕ are used to parameterize the direction of the adjoint (in a manner very similar to the control unit vector parameterization in terms of β and γ). The reverse mapping from $\hat{p}_a$, $\hat{p}_e$, and $\hat{p}_i$ to θ and ϕ may be written as

$$\tan\theta = \frac{\hat{p}_e}{\hat{p}_a}$$

and

$$\tan\phi = \frac{\hat{p}_i}{\sqrt{\hat{p}_a^2 + \hat{p}_e^2}}$$

Because the adjoint appears linearly in the Hamiltonian, the optimal control policy $(f^*, \omega^*, \beta^*, \gamma^*)$ may be found by viewing $\mathcal{H}_i$ as a function of the adjoint variable direction parameterized by θ and ϕ. By inspection $\mathcal{H}_i$ are sinusoids with respect to θ and ϕ, and have precisely one minima and one maxima. The values of $\hat{p}_a$, $\hat{p}_e$, and $\hat{p}_i$ for which $\mathcal{H}_i$ vanish, are minimized, and maximized are shown in Table 4.4. Upon examination, starting at $\theta = 0$ and increasing to $\theta = 2\pi$ while keeping $\phi = 0$, the maximum Hamiltonian transitions from $\mathcal{H}_1 \to \mathcal{H}_4 \to \mathcal{H}_3 \to \mathcal{H}_2 \to \mathcal{H}_1$. The points at which they are equal in terms of p_a and p_e (note that p_i does not impact these boundaries) are

$$\mathcal{H}_1 = \mathcal{H}_4 \to \frac{p_e}{p_a} = +\infty \to p_a = 0, p_e > 0$$

Table 4.4: Values of $\hat{p}_a$, $\hat{p}_e$, and $\hat{p}_i$, for which $\mathcal{H}_i$ vanishes, is minimized, or is maximized

	$\mathcal{H}_i = 0$	**Minimum**	**Maximum**
$\mathcal{H}_1$	$\frac{\hat{p}_e}{\hat{p}_a} = \frac{\pm a}{\mp(1-e)}$	$\frac{\hat{p}_e}{\hat{p}_a} = \frac{-(1-e)}{-a}$	$\frac{\hat{p}_e}{\hat{p}_a} = \frac{(1-e)}{a}$
$\mathcal{H}_2$	$\frac{\hat{p}_e}{\hat{p}_a} = \frac{\pm a}{\pm(1+e)}$	$\frac{\hat{p}_e}{\hat{p}_a} = \frac{(1+e)}{-a}$	$\frac{\hat{p}_e}{\hat{p}_a} = \frac{-(1+e)}{a}$
$\mathcal{H}_3$	$\frac{\hat{p}_e}{\hat{p}_a} = \frac{\pm a}{\mp(1-e)}$	$\frac{\hat{p}_e}{\hat{p}_a} = \frac{(1-e)}{a}$	$\frac{\hat{p}_e}{\hat{p}_a} = \frac{-(1-e)}{-a}$
$\mathcal{H}_4$	$\frac{\hat{p}_e}{\hat{p}_a} = \frac{\pm a}{\pm(1+e)}$	$\frac{\hat{p}_e}{\hat{p}_a} = \frac{-(1+e)}{a}$	$\frac{\hat{p}_e}{\hat{p}_a} = \frac{(1+e)}{-a}$
$\mathcal{H}_5$	$\hat{p}_i = 0$	$\hat{p}_i = -1$	$\hat{p}_i = 1$
$\mathcal{H}_6$	$\hat{p}_i = 0$	$\hat{p}_i = 1$	$\hat{p}_i = -1$

$$\mathcal{H}_4 = \mathcal{H}_3 \rightarrow \frac{p_e}{p_a} = \frac{ae}{-(1-e^2)}$$

$$\mathcal{H}_3 = \mathcal{H}_2 \rightarrow \frac{p_e}{p_a} = -\infty \rightarrow p_a = 0, p_e < 0$$

$$\mathcal{H}_2 = \mathcal{H}_1 \rightarrow \frac{p_e}{p_a} = \frac{-ae}{(1-e^2)}$$

Similarly, when $\phi = \pi/2$ or $\phi = -\pi/2$ the Hamiltonians $\mathcal{H}_5$ and $\mathcal{H}_6$ respectively are also maxima. Because the switching boundaries between $\mathcal{H}_1$ through $\mathcal{H}_4$ do not depend on ϕ, the boundaries where each of these regions switches to $\mathcal{H}_5$ or $\mathcal{H}_6$ must be found.

$$\mathcal{H}_1 = \mathcal{H}_5 \rightarrow \tan\phi = 2\left(a\cos\theta + (1-e)\sin\theta\right)$$

$$\mathcal{H}_2 = \mathcal{H}_5 \rightarrow \tan\phi = -2\frac{1-e}{1+e}\left(-a\cos\theta + (1+e)\sin\theta\right)$$

$$\mathcal{H}_3 = \mathcal{H}_5 \rightarrow \tan\phi = -2\left(a\cos\theta + (1-e)\sin\theta\right)$$

$$\mathcal{H}_4 = \mathcal{H}_5 \rightarrow \tan\phi = 2\frac{1-e}{1+e}\left(-a\cos\theta + (1+e)\sin\theta\right)$$

For $\mathcal{H}_6$ the analogous equations are

$$\mathcal{H}_1 = \mathcal{H}_6 \rightarrow \tan\phi = -2\left(a\cos\theta + (1-e)\sin\theta\right)$$

$$\mathcal{H}_2 = \mathcal{H}_6 \rightarrow \tan\phi = 2\frac{1-e}{1+e}\left(-a\cos\theta + (1+e)\sin\theta\right)$$

$$\mathcal{H}_3 = \mathcal{H}_6 \rightarrow \tan\phi = 2\left(a\cos\theta + (1-e)\sin\theta\right)$$

$$\mathcal{H}_4 = \mathcal{H}_6 \rightarrow \tan\phi = -2\frac{1-e}{1+e}\left(-a\cos\theta + (1+e)\sin\theta\right)$$

Examining the Hessians for eac $\mathcal{H}_i$ verifies that the second-order necessary condition is met. Using the switching lines found above and observing that $\tan\phi = p_i/\sqrt{p_a^2 + p_e^2}$, $\cos\theta = p_a$, and $\sin\theta = p_e$, the final optimal control policy is shown in (4.40).

$$
(f^*,\omega^*,\beta^*,\gamma^*) = \begin{cases}
\underline{(0,0,0,0)} \text{ if } p_a \geq 0, p_a \geq \frac{-ae}{1-e^2}p_e, \\
\text{and } -2(ap_a+(1-e)p_e)(p_a^2+p_e^2)^{\frac{1}{2}} \leq p_i \leq 2(ap_a+(1-e)p_e)(p_a^2+p_e^2)^{\frac{1}{2}} \\
\\
\underline{(\pi,0,0,0)} \text{ if } p_a < 0,\ p_a \leq \frac{-ae}{1-e^2}p_e \\
\text{and } 2\frac{1-e}{1+e}\left(-ap_a+(1+e)p_e\right)\left(p_a^2+p_e^2\right)^{\frac{1}{2}} \leq p_i \leq -2\frac{1-e}{1+e}\left(-ap_a+(1+e)p_e\right)\left(p_a^2+p_e^2\right)^{\frac{1}{2}} \\
\\
\underline{(0,0,\pi,0)} \text{ if } p_a \geq 0,\ p_a < \frac{-ae}{1-e^2}p_e \\
\text{and } 2(ap_a+(1-e)p_e)(p_a^2+p_e^2)^{\frac{1}{2}} \leq p_i \leq -2(ap_a+(1-e)p_e)(p_a^2+p_e^2)^{\frac{1}{2}} \\
\\
\underline{(\pi,0,\pi,0)} \text{ if } p_a < 0,\ p_a > \frac{-ae}{1-e^2}p_e \\
\text{and } -2\frac{1-e}{1+e}\left(-ap_a+(1+e)p_e\right)\left(p_a^2+p_e^2\right)^{\frac{1}{2}} \leq p_i \leq 2\frac{1-e}{1+e}\left(-ap_a+(1+e)p_e\right)\left(p_a^2+p_e^2\right)^{\frac{1}{2}} \\
\\
\underline{(\pi,0,0,-\frac{\pi}{2})} \text{ if } p_i > 2(ap_a+(1-e)p_e)(p_a^2+p_e^2)^{\frac{1}{2}}, p_i > -2\frac{1-e}{1+e}\left(-ap_a+(1+e)p_e\right)\left(p_a^2+p_e^2\right)^{\frac{1}{2}} \\
p_i > -2(ap_a+(1-e)p_e)(p_a^2+p_e^2)^{\frac{1}{2}}, \text{ and } p_i > 2\frac{1-e}{1+e}\left(-ap_a+(1+e)p_e\right)\left(p_a^2+p_e^2\right)^{\frac{1}{2}} \\
\\
\underline{(\pi,0,0,\frac{\pi}{2})} \text{ if } p_i > -2(ap_a+(1-e)p_e)(p_a^2+p_e^2)^{\frac{1}{2}}, p_i > 2\frac{1-e}{1+e}\left(-ap_a+(1+e)p_e\right)\left(p_a^2+p_e^2\right)^{\frac{1}{2}} \\
p_i > 2(ap_a+(1-e)p_e)(p_a^2+p_e^2)^{\frac{1}{2}}, \text{ and } p_i > -2\frac{1-e}{1+e}\left(-ap_a+(1+e)p_e\right)\left(p_a^2+p_e^2\right)^{\frac{1}{2}}
\end{cases} \tag{4.40}
$$

A visualization of the optimal control policy regions for a reference orbit ($a = 24{,}393$ km, $e = 0.7253$, and $i = 0$ deg) is shown in Figure 4.11. In practice it is computationally easier to simply compute $\mathcal{H}_1$ through $\mathcal{H}_6$, find largest value, and choose the corresponding control policy. A cursory examination of the computational burden involved in computing (4.40) indicates that simply computing $\mathcal{H}_i$ may in fact be the fastest option computationally.

The optimal control policy derived using the alternate independent parameter framework agrees with classical orbit dynamics nicely. In the case that $(f^*,\omega^*,\beta^*,\gamma^*) = (0,0,0,0)$, the adjoints are 'pointed' in the direction of larger semi-major axis and eccentricity, which a periapsis burn along the velocity vector will accomplish. Conversely, if $(f^*,\omega^*,\beta^*,\gamma^*) = (\pi,0,\pi,0)$, the adjoints are 'pointed' in the direction of positive eccentricity and slightly negative semi-major axis, which corresponds directly to an apoapsis maneuver that lowers periapsis (thus increasing eccentricity while decreasing semi-major axis). Similar arguments may be made for $(f^*,\omega^*,\beta^*,\gamma^*) = (0,0,\pi,0)$ and $(f^*,\omega^*,\beta^*,\gamma^**) = (\pi,0,0,0)$. The maneuvers to increase $((f^*,\omega^*,\beta^*,\gamma^*) = (\pi,0,0,-\pi/2))$ and decrease $((f^*,\omega^*,\beta^*,\gamma^*) = (\pi,0,0,\pi/2))$ inclination are also classical orbital maneuvers; the maneuver to change inclination should occur at the largest radius in the orbit, which corresponds to apoapsis ($f^* = \pi$).

Examining Table 4.3 it is clear that all maneuvers to modify only semi-major axis, eccentricity or

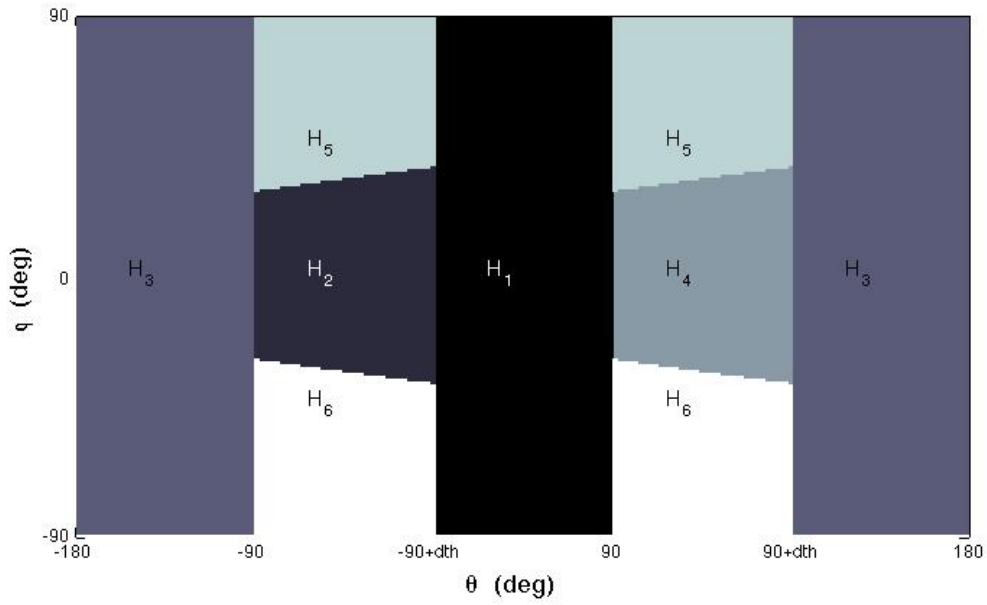

Figure 4.11: Regions of optimal control policy as a function of (θ, ϕ) for a reference orbit (a = 24,393 km, e = 0.7253). In this case 'dth' = $\tan^{-1}\left(-ae/(1-e^2)\right) + \pi/2$

inclination are present, and that with these optimal control policies as 'basis maneuvers', any fuel-optimal co-aligned ellipse-to-ellipse or escape maneuver with inclination change may be reconstructed. Further, in the presence of a central body with a non-zero J_2 term, assumptions [A3] and [A4] suggest the use of intermediate 'parking orbits' while ascending node and argument of periapsis phasing occurs. Thus, with the basis maneuvers contained in Table 4.3 and parking orbits, any free-time, fuel optimal arbitrary orbit to orbit transfer may be found using the results generated here. As a final note, for any of the optimal control policies outlined in (4.40), produce $d\omega/d\Delta V \to 0$. This can be seen by examining the argument of periapsis dynamics with respect to ΔV given by

$$\frac{d\omega}{d\Delta V} = \frac{1}{he}\left(-p\cos f \sin\beta\cos\gamma + (p+r)\sin f\cos\beta\sin\gamma\right) - \frac{r\sin(\omega+f)\cos i\sin\gamma}{h\sin i}$$

and substituting the optimal control policies. Figure 4.12 visualizes the optimal basis maneuvers as nodes in a graph, defined here as the Optimal Maneuver Graph (OMG). Using this representation it is easy to identify classical optimal maneuvers as paths starting and ending at the nodes in the OMG. The Hohman transfer, the bi-elliptic transfer, and bi-elliptic transfer with plane change maneuvers are illustrated.

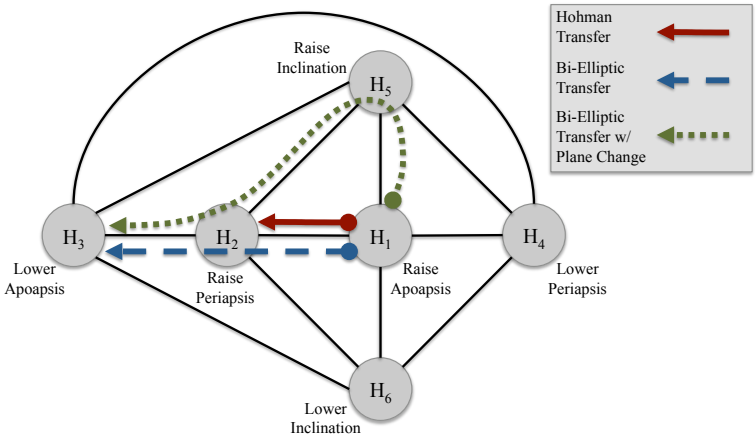

Figure 4.12: Optimal basis maneuvers visualized as nodes on a connected graph. Classical maneuver combinations are emphasized.

Examining this visualization, it is straightforward to understand that given a two-point boundary value problem and sufficient ΔV, finding the optimal initial adjoint will generate an optimal trajectory in ΔV-space that will exactly correspond to the classical maneuver combinations shown in Figure 4.12. It is also insightful to note that the graph in Figure 4.12 is not fully connected. Specifically, there are no connections between $\mathcal{H}_1$ and $\mathcal{H}_3$, $\mathcal{H}_2$ and $\mathcal{H}_4$, or $\mathcal{H}_5$ and $\mathcal{H}_6$. This matches intuition perfectly, as one would for example expect that after raising apoapsis it is sub-optimal to then immediately lower the orbit apoapsis.

Directionality of the edges on the OMG in Figure 4.12 is not clear and is beyond the scope of this effort. The authors feel a detailed analysis of the OMG, particularly the directionality of the edges given certain orbit regimes (a, e, and i), can provide deep insight into optimal combinations of maneuvers in general.

4.4.1.5 State and Adjoint Dynamics With Respect to The Alternate Independent Parameter

Now that an optimal control policy that generates $(f^*, \omega^*, \beta^*, \gamma^*)$ has been determined, the equations of motion for the state and adjoint variables a, e, i, p_a, p_e, and p_i with respect to ΔV for specific optimal trajectories must now be determined. The equations of motion may be simplified by observing that for

$f = 0, \pi$ and $\beta = 0, \pi$, $\sin f^* = \sin \beta^* = 0$ for all optimal control policies $(f^*, \omega^*, \beta^*, \gamma^*)$, producing

$$\frac{da}{d\Delta V} = \frac{a^{\frac{1}{2}}}{\mu^{\frac{1}{2}}(1-e^2)^{\frac{1}{2}}}\left[a(1+e\cos f^*)\right]\cos\beta^*\cos\gamma^* \tag{4.41}$$

$$\begin{aligned}\frac{de}{d\Delta V} &= \frac{a^{\frac{1}{2}}}{\mu^{\frac{1}{2}}(1-e^2)^{\frac{1}{2}}} \\ &\left[\frac{2(1-e^2)(e+\cos f^*)}{1+e\cos f^*}\right]\cos\beta^*\cos\gamma^*\end{aligned} \tag{4.42}$$

$$\frac{di}{d\Delta V} = \frac{a^{\frac{1}{2}}}{\mu^{\frac{1}{2}}(1-e^2)^{\frac{1}{2}}}\left[\frac{(1-e^2)\cos(\omega^*+f^*)}{1+e\cos f^*}\right]\sin\gamma^* \tag{4.43}$$

Along optimal trajectories, the necessary condition for optimality on the adjoint variables is that $d\mathbf{p}/d\Delta V = -\partial\mathcal{H}/\partial\mathbf{x}$. Observing that for $f = 0, \pi$ and $\beta = 0, \pi$, $\sin f^* = \sin\beta^* = 0$, $\cos^2 f^* = 1$, and $\cos^3 f^* = \cos f^*$, and carrying out significant simplifications generates

$$\begin{aligned}\frac{dp_a}{d\Delta V} = \frac{a^{\frac{1}{2}}}{\mu^{\frac{1}{2}}(1-e^2)^{\frac{1}{2}}}\Bigg[&-3(1+e\cos f^*)\cos\beta^*\cos\gamma^* p_a \\ &-\frac{(1-e^2)(e+\cos f^*)}{a(1+e\cos f^*)}\cos\beta^*\cos\gamma^* p_e \\ &-\frac{1-e^2}{a(e+\cos f^*)}\cos(\omega^*+f^*)\cos f^*\sin\gamma^* p_i\Bigg]\end{aligned} \tag{4.44}$$

$$\begin{aligned}\frac{dp_e}{d\Delta V} = \frac{a^{\frac{1}{2}}}{\mu^{\frac{1}{2}}(1-e^2)^{\frac{1}{2}}}\Bigg[&-\frac{2a\,(e+\cos f^*)}{(1-e^2)}\cos\beta^*\cos\gamma^* p_a \\ &+\frac{2e(e+\cos f^*)}{(1+e\cos f^*)}\cos\beta^*\cos\gamma^* p_e \\ &+\frac{1+e\cos f^*}{\cos f^*(e+\cos f^*)^2}\cos(\omega^*+f^*)\sin\gamma^* p_i\Bigg]\end{aligned} \tag{4.45}$$

$$\frac{dp_i}{d\Delta V} = 0 \tag{4.46}$$

Taken together, (4.44), (4.45), and (4.46) define the dynamics of the adjoint variables p_a, p_e, and p_i in the ΔV integration space along free-time, ΔV-optimal trajectories.

4.4.1.6 Applicability to Orbit Range with J_2 Perturbations

The the analysis thus far derived the required equations to compute optimal orbit range sets in a, e, and i using the classical GVE equations of motion. If J_2 perturbations are also considered, the time dynamics of the mean semi-major axis $\bar{a}$, mean eccentricity $\bar{e}$, and mean inclination $\bar{i}$ have the same form

as the un-perturbed orbit elements a, e, and i, while in general (with the exception of particular critical regions) the mean ascending node $\bar{\Omega}$ and mean argument of periapsis $\bar{\omega}$ drift at different rates over time. This property, that $(\bar{a}, \bar{e}, \bar{i})$ still behave as constants of motion while the orientation coordinates $\bar{\Omega}$ and $\bar{\omega}$ drift over time, can be exploited to realize significant ΔV savings in the general Two-Point Boundary Value Problem (TPBVP). Using these properties, trajectories in regions where J_2-induced drift rates in $\bar{\Omega}$ and $\bar{\omega}$ are non-zero (and different from one another) can place themselves in intermediate orbits and allow J_2 perturbations to perturb them until a desired instantaneous value of Ω and ω is reached. Because in [A1] it is assumed that the user is unconcerned with the total time of the orbit transfer, this effectively allows the user to transfer from any initial instantaneous orbit element set $\mathbf{oe}_0$ to any final instantaneous orbit element set $\mathbf{oe}_f$ incurring only the ΔV cost associated with transitioning from (a_0, e_0, i_0) to (a_f, e_f, i_f). Thus, the orbit element range set computation method developed in this paper provides the general minimum-fuel, free-time optimal transfer set from an initial orbit to any final orbit under J_2 perturbations.

4.4.1.7 Initial Conditions and Set Propagation

The boundary condition for the HJB PDE is typically given as an initial or final value function $\tilde{V}(\mathbf{x}, s)$. For the orbit range problem the range set is propagated forward, so an initial boundary condition $\tilde{V}(\bar{\mathbf{oe}}_{tr}, \Delta V_0) = 0$ is required for the problem to be well posed. The range set defined by $\tilde{V}(\bar{\mathbf{oe}}_{tr,f}, \Delta V_f) = 0$ as a function of ΔV may be computed using several methods. Two methods briefly introduced in the introduction and discussed here are a) trajectory-based and b) level-set based. Trajectory methods take an initial state, compute the initial adjoint state using $\mathbf{p}_0 = \partial \tilde{V}_0 / \partial \mathbf{x}_0$, and propagate the optimal trajectory according to (4.41), (4.42), (4.43), (4.44), (4.45), and (4.46). Level-set methods use PDE integration routines similar to those in computational fluid dynamics to propagate the initial condition according to the dynamics of the problem [60, 61, 62, 63]. Software to propagate the HJB PDE has been graciously made available online [64] and is used to compute range sets in this paper. Some of the intermediate computations to compute range set solutions using the Level Set Toolbox are given in Appendix B.2.

4.4.2 Simulation and Results

To demonstrate the analytical results in the previous sections and demonstrate the utility of the approach four examples are given. The first example validates the computed range set by comparing it to the analytical results for co-aligned, ellipse-to-ellipse transfers with inclination changes. The second example demonstrates some of the flexiblity of the approach by choosing $\tilde{V}_0$ such that there are several initial, unconnected regions where an object may exist. The third example demonstrates the benefits of being able to choose arbitrary initial conditions $\tilde{V}_0$ for computing final range sets.

4.4.2.1 Example 4.4: Range Set Verification

The initial condition for the range set verification example is defined by the ellipsoid expressed as

$$\tilde{V}(\mathbf{oe}_{tr,0}, 0) = \frac{(a - a_0)^2}{r_{a,0}^2} + \frac{(e - e_0)^2}{r_{e,0}^2} + \frac{(i - i_0)^2}{r_{i,0}^2} - 1 = 0$$

where $a_0 = 24{,}393$ km, $e_0 = 0.7253$, $i_0 = 0$ deg, $r_{a,0} = 1{,}250$ km, $r_{e,0} = 0.02440$, and $r_{i,0} = 3.0488$ deg. This orbit is known as a Geostationary Transfer Orbit (GTO), and is employed as an intermediate trajectory in a Hohman transfer from Low Earth Orbit (LEO) to Geostationary Earth Orbit (GEO). The independent parameter ΔV is integrated over the domain $\Delta V \in [0, 1000]$ m/s. To validate the computed range set at the final $\Delta V_f = 1000$ m/s, existing analytical ΔV requirements for co-aligned ellipse-to-ellipse transfers with inclination changes are generated and their level sets at $\Delta V_f = 1000$ m/s are computed (see Appendix B.1 for details). The two sets are shown superimposed in isometric, semi-major axis vs. eccentricity, semi-major axis vs. inclination, and eccentricity vs. inclination views in Figure 4.13.

The plots shown in Figure 4.13 demonstrate that the numerically propagated range set matches quite nicely with the analytically predicted range set. There are three types of discrepancies that can be observed. The first is due to the fact that the initial range set in the numerically propagated range set is not a single point but rather an ellipsoid of finite size. The second discrepancy is seen at larger semi-major axes (> 40,000 km) and eccentricities (> 0.9), and is likely due to a combination of numerical propagation step size and grid sizing. The final discrepancy compounds with the second discrepancy in that the dynamics are singular as $e \to 1$, exacerbating the numerical issues already discussed. At lower eccentricities and semi-major axes the

range is less sensitive to these effects and the discrepancies are much less pronounced.

Figure 4.13 illustrates several properties of optimal maneuvers in orbital regimes. Specifically, the range set expands 'fastest' (and forms corners) when propagating along lines of constant apoapsis or periapsis (raising/lower apoapsis/periapsis). Also, one can see that to maximally change inclination, it is sometimes desirable to also increase apoapsis first, then execute an inclination maneuver.

4.4.2.2 Example 4.5: Initial Sets in LEO, GTO, and GEO

This example demonstrates the relative impact of incremental quantities of ΔV have in different orbit regimes as well as how the initial condition may be chosen to simultaneously propagate multiple unconnected initial range sets. The initial range sets are chosen to be ellipsoids described in Table 4.5.

Table 4.5: Example 4.4 initial range sets

Parameter	**LEO**	**GTO**	**GEO**
a_0 (km)	6,700	24,393	42,086
e_0 ()	0	0.7253	0
i_0 (deg)	31	31	0
$r_{a,0}$ (km)	1,250	1,250	1,250
$r_{e,0}$ ()	0.0244	0.0244	0.0244
$r_{i,0}$ (deg)	3.0488	3.0488	3.0488

Each range set was propagated over a ΔV interval of $[0, 1000]$ m/s. The resulting range sets are shown in Figure 4.14. The various subplots in Figure 4.14 show all three range sets (which are all zero-level sets of the same solution $\tilde{V}(\bar{\mathbf{oe}}_{tr}, \Delta V_f = 1000 \text{ m/s}) = 0$) in isometric and planar views to aid in visualization. The effective utility of incremental amounts of ΔV starting at the three initial range sets is aptly demonstrated. As the dynamics of an inverse r^2 force model would suggest, orbits with low semi-major axes and eccentricities must expend larger amounts of ΔV to change their orbit elements than orbits with larger semi-major axes or eccentricities. Qualitatively, the LEO initial orbit achieves the least amount of range for 1000 m/s of ΔV, followed by the GEO initial orbit, with the best range obtained with an initial GTO range set.

4.4.2.3 Example 4.6: Arbitrary Initial Range Sets

To demonstrate the advantages of using zero-level sets to implicitly define initial sets, a non-convex, non-smooth initial range set is constructed using separating hyperplanes as an initial range set and its corresponding final range set (with $\Delta V = 500$ m/s) is computed. Figure 4.15 depicts the initial range set and Figure 4.16 shows the final range set. Because zero-level sets of the value function $\tilde{V}(\bar{\mathbf{oe}}_{tr}, \Delta V)$ implicitly define the surface of the range set, the union of initially separate range regions as they expand is directly handled. As a general note, the initial condition $\tilde{V}(\bar{\mathbf{oe}}_{tr,0}, \Delta V = 0) = 0$ may be any arbitrary function (allowing arbitrary initial range sets), though heuristically best numerical results are found when $\tilde{V}$ is at least $\mathcal{C}^0$.

4.4.2.4 Discussion of Results

The results presented in Examples 4.4 through 4.6 demonstrate the verification of the analytical results, relative control authorities for different starting orbits, and the ability to define arbitrary initial range sets. There are three overarching topics that bear additional discussion: analytical results, numerical issues, and geometric interpretations.

An excellent analytical result of the application of optimal controls to the time-independent range set computation problem is the generation of the standard classical maneuvers (outlined in Table 4.3) by applying the first- and second-order necessary conditions of optimality. In other words, the classical maneuvers were found using optimal control theory, and were not assumed based on prior knowledge of optimal maneuvers in Keplerian dynamics (such as the Hohman transfer). Also stemming from the analytical treatment of the problem using optimal controls is that the computed range set and optimal control policy has optimality guarantees. This is contrasted with combinatorial testing of maneuver sequences and sizes in ad-hoc or heuristic settings. Further, the basis maneuvers generated under this framework are also theoretically capable of reproducing more general classical orbit maneuvers such as the bi-elliptic orbit transfer and the bi-elliptic inclination change transfer. Lastly, though the classical orbit elements (and implicitly, the mean classical orbit elements) were used in this effort, it is clear that any set of constants of motion may be used as the coordinates in which to compute range.

Because the analytic solution of the range set given an initial condition is not known, the use of numerical methods[64] introduce several additional issues that must be considered. The first is grid sizing. In the numerical propagation the state space of interest is discretized into a grid. To be well posed numerically, the initial set must be at least one grid cell length in each dimension. Unfortunately because this problem suffers from the curse of dimensionality it is generally not possible to compute range sets for grids using arbitrarily small grid cell dimensions. This imposes lower limits on how small the initial range set may be, which operationally is usually much larger than the estimate covariance ellipsoid associated with the object in question. This can artificially increase the computed range set and must be accounted for given a particular application. Grid sizing also limits the resolution to which the range set may be computed. Care must be taken to use appropriately small grid sizings in regions of interest or sensitivity if high fidelity range set boundary computation is paramount.

The propagation of the range set is an initial value problem and is subject to many of the same problems that traditional differential equation initial valued problems suffer from. Most importantly this includes compounded integration error (as seen in Example 4.4). Coordinate singularities are also a numerical issue that is tightly coupled with integration step size. Example 4.4 illustrates that as the range set boundary approaches unit eccentricity the propagated range set disagrees with the analytical range set. The orbit element equations of motion become singular as $e \to 1$, and taking inappropriately large step sizes in such a region will generate poor results.

In terms of geometric interpretations of the range sets, it is useful to note that the required amount of ΔV to change inclination does not depend on the current inclination. This means that all else kept equal, an inclination range computed at the equator is the same as the inclination range computed in a polar orbit given a constant ΔV. This conveniently allows a computed range set to be translated along the inclination axis to a new starting inclination without the need to recompute the range set.

Also highlighted in the results (particularly Example 4.5) is the varying levels of control authority that are afforded to objects starting in different initial orbits. LEO objects are significantly hampered when compared to GTO or GEO objects given a constant ΔV. The geometric confirmation of this fact afforded by examining range sets is quite intuitive.

Once computed for various initial orbits and multiple quantities of ΔV, the orbit element range sets provide an excellent tool for strategic, tactical, or mission planning. Regions of orbital space that afford particularly large ranges are easily found and may be superimposed with space object catalogs to quickly (and geometrically) identify and examine possible spacecraft / object interactions. Similarly entire groups of spacecraft with varying initial orbits and quantities of ΔV may have their range sets computed and be superimposed into the same visualization, allowing for strategic interpretations analogous to those currently done with aircraft. Lastly, since the range sets are integrated with respect to ΔV, the range sets for varying levels of ΔV are easily computed to support sensitivity studies.

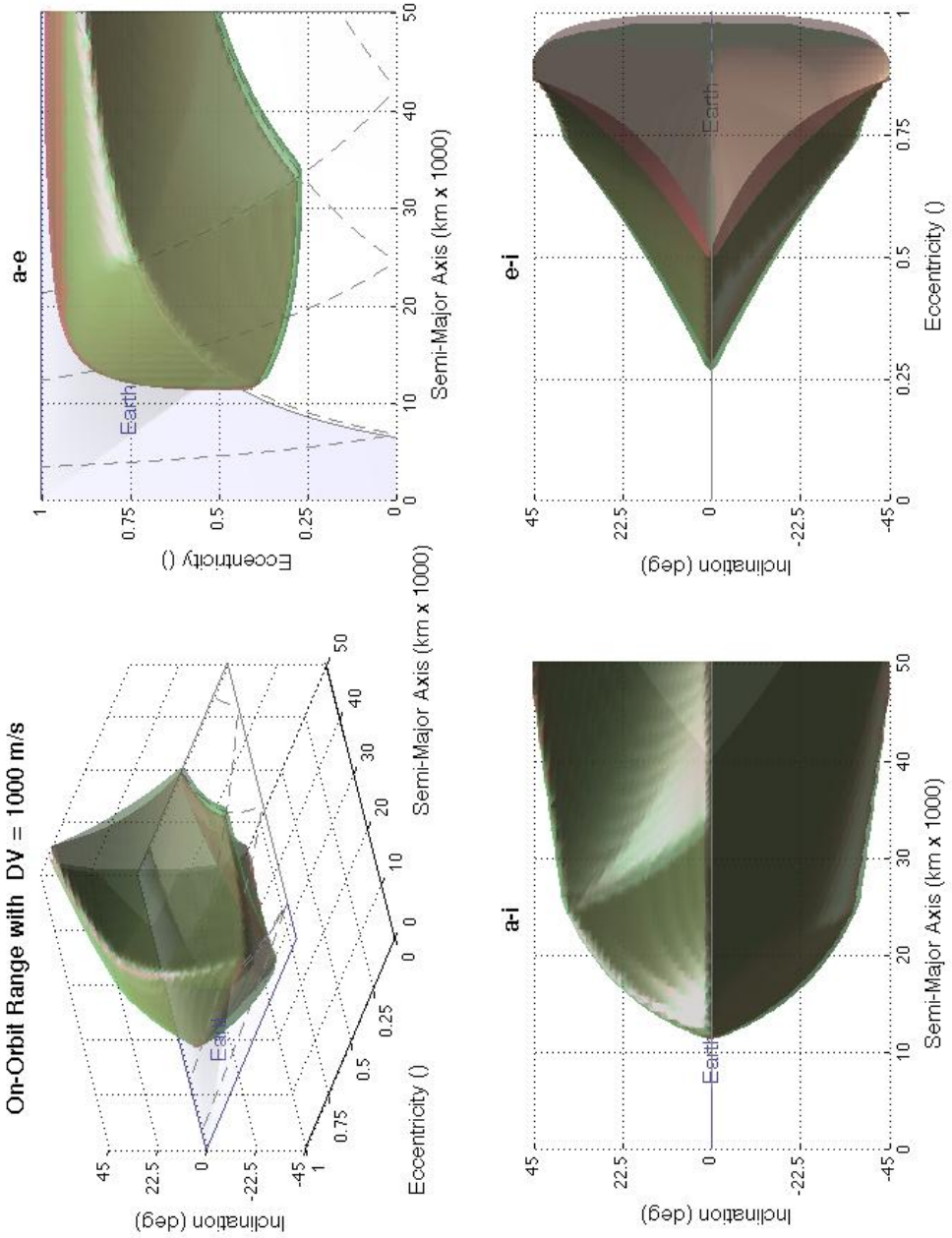

Figure 4.13: Example 4.4: Numerically propagated (green) and analytic (red) range sets for an initial GTO orbit with $\Delta V \in [0, 1000]$ m/s

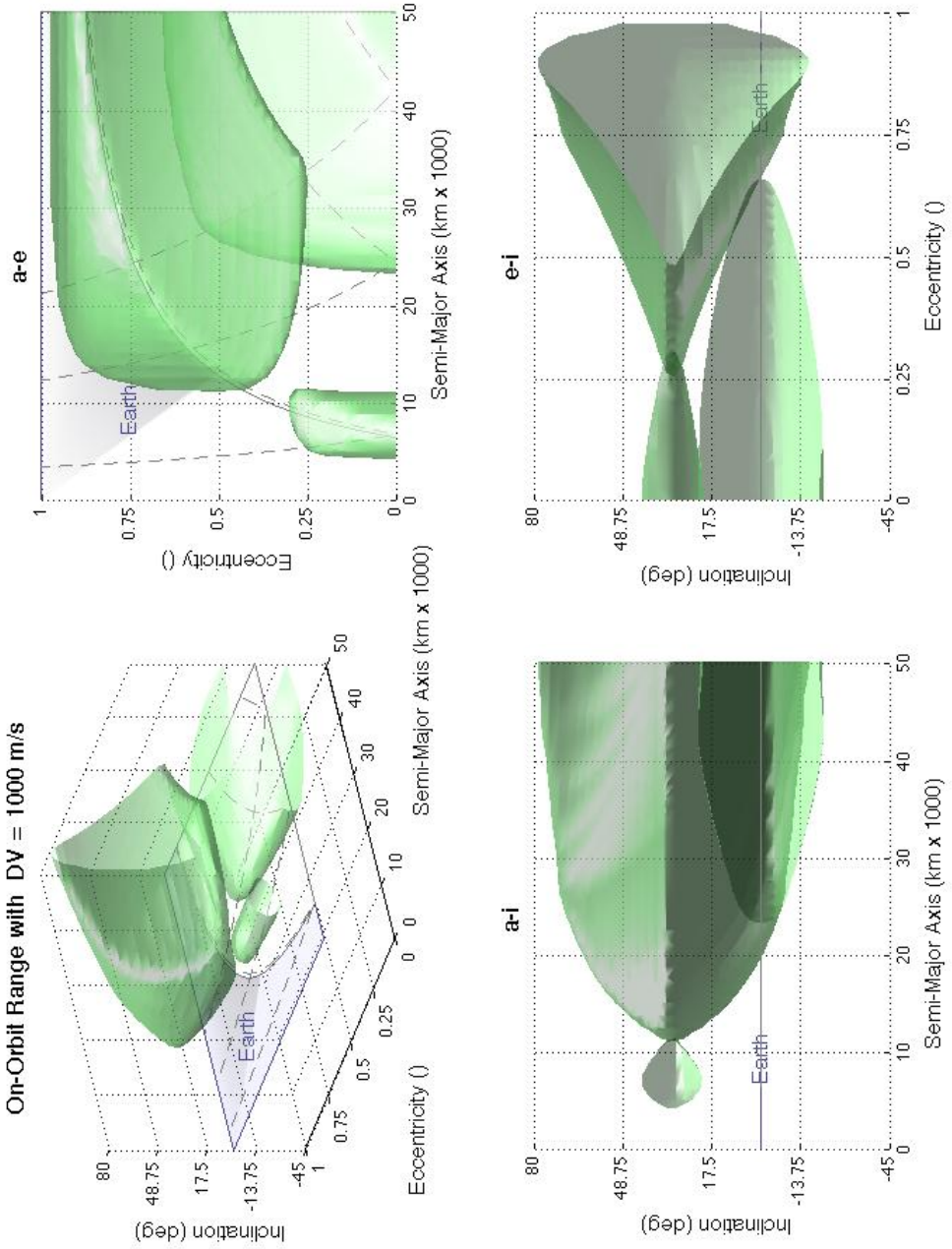

Figure 4.14: Example 4.5: Numerically propagated range sets for an initial LEO orbit (bottom left in a-e plane), GTO orbit (top middle in a-e plane), and GEO orbit (bottom right in a-e plane) with $\Delta V \in [0, 1000]$ m/s

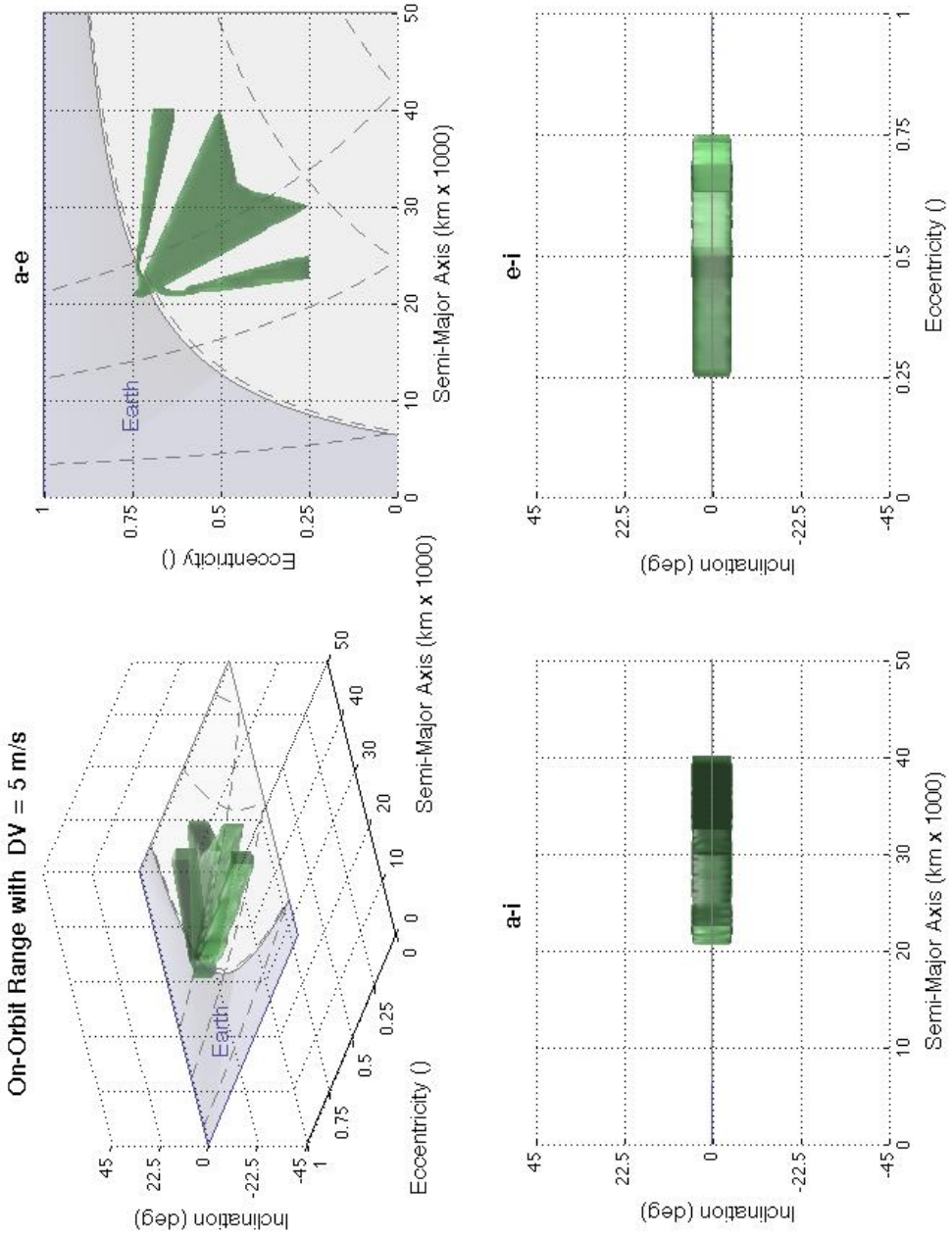

Figure 4.15: Example 4.6: Initial range set for the non-convex, non-smooth initial range set with $\Delta V \in [0, 500]$ m/s

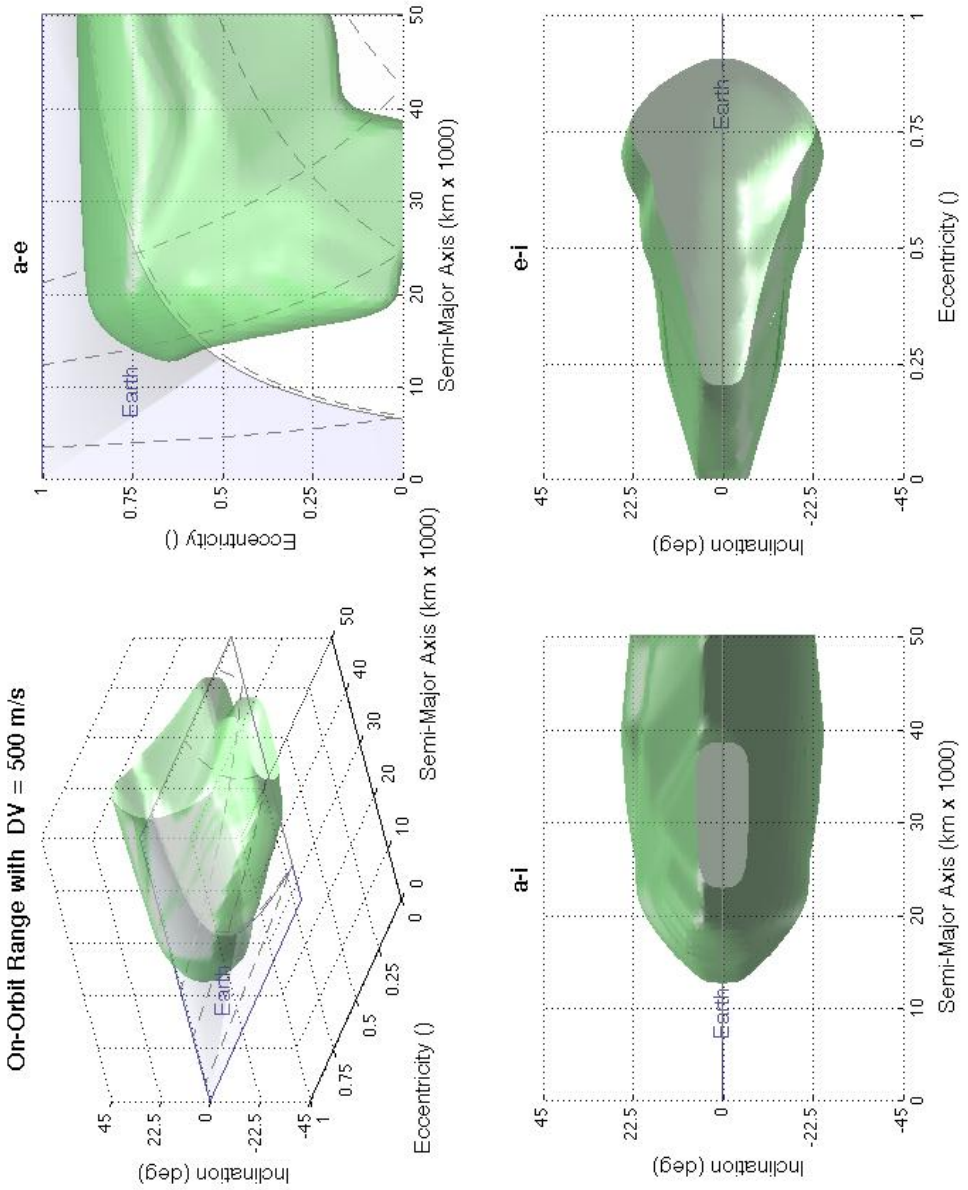

Figure 4.16: Example 4.6: Numerically propagated range sets for the non-convex, non-smooth initial range set with $\Delta V \in [0, 500]$ m/s

4.5 Chapter Summary

Fuel-optimal control for systems affine in control, specifically spacecraft, is used to motivate a rigorous examination of how optimal reachability sets using alternate independent parameters may be generated and how specific singular mappings may be circumvented. The mapping function between time and an arbitrary independent parameter is defined and the transformation of the time-dynamics into the dynamics with respect to a new independent parameter is given. Starting with the Dynamic Programming Equation the necessary conditions of optimality along optimal trajectories are combined with the independent parameter mapping function definition to derive the General Independent Parameter Hamilton Jacobi Bellman PDE. Necessary conditions for left, right, and full intervtibility of the independent parameter mapping function are reviewed and a discussion of convenient independent parameters is given. The dynamics of the adjoint state using the new integration parameter is shown to mirror those of the time-based adjoint dynamics. A definition for Generalized Metric Range Sets is given and several illustrations are introduced and discussed. A method is introduced by which the mapping singularity in the primer vector problem may be circumvented using constants of integration and impulsive assumptions. The classical Breugot aircraft range equation and the 2^{nd}-order oscillator amplitude range equation are developed as simple analytical examples of the modified Hamilton Jacobi Bellman PDE reachability applications. A more complex numerical example is given in which the orbit element range for co-planar, co-aligned orbits is derived, propagated, and validated against known classical results.

For the extended orbit range example, orbit element dynamics under arbitrary control accelerations and J_2 perturbations are used as basis coordinates for orbital range set computation. The range set computation is chosen to be time independent, allowing for the ascending node, argument of periapsis, and true anomaly to be viewed as ignorable coordinates or as control parameters. Control accelerations are also assumed to be impulsive, which is consistent with traditional optimal ΔV trajectory maneuvers. The independent parameter is chosen to be ΔV and the dynamics are transformed from time to ΔV space. The Hamilton Jacobi Bellman PDE using ΔV as an independent parameter is used as the basis for propagating the optimal time-independent range sets as a function of ΔV. The first- and second-order necessary

conditions of optimality are applied and the resulting optimal control policy as a function of the states and adjoints is found. The optimal control policy analytically reproduces the same basis maneuvers used in classical astrodynamics. Existing numerical toolboxes are used to propagate initial range sets allowing for the computation of final range sets as a function of ΔV. Numerically propagated results are validated against classical results for the co-aligned ellipse-to-ellipse transfer with inclination change case. Examples are given that demonstrate relative control authority of different initial orbits, and the ability to specify arbitrary initial range sets. Optimality guarantees of the solution and numerical issues related to the propagation are discussed. Utility in the strategic, tactical, and mission planning sense is shown to be similar to aircraft analogs.

Chapter 5

Conclusions and Future Work

SSA is a critical and persistent need for entities depending on access to space. Object attribute determination, an important facet of successful SSA, is supported by a number of activities that can benefit greatly from careful application of optimal control approaches. As claimed in the thesis statement in §1.1, activities that can benefit from optimal control methods are object and track correlation, maneuver detection, fuel usage estimation, operator priority inference, efficient intecept set computation, range set theory, and orbit range set generation. The relationships between each of the activites cited in the thesis statement and SSA-related ojbect attributes is given in Table 1.1 in §1.2.4. The summarization of past research in Table 1.3 demonstrates the interest in such object attribute determination activities as well as identifying where the contributions of this dissertation fit relative to existing results.

Fundamental to optimal control based object correlation is the concept of optimal control problem distance metrics, defined and discussed in Chapter 2. Along with control distance metrics, the Uncertain Two Point Boundary Value Problem (UTPBVP) and Measurement Residual Boundary Value Problem (MRBVP) approaches directly support object and track correlation, maneuver detection, fuel usage estimation, and operator priority inference. Control distance distributions combined with stochastic dominance provide a sensible method to rank candidate object correlations using a first-principles approach. Detecting maneuvers by examining the relative sizes of the deterministic and uncertain components of the control distance allows both the estimation of minimum detectible maneuver size, as well as a probability that the deterministic control distance is explained by the inherent system uncertainty. Because the control distance metric is naturally expressed in terms of ΔV, fuel usage estimation is automatically supported. Lastly, by determining

whether an object is maneuvering in a fuel optimal manner, it is possible to infer additional operator priorities.

For correlation, maneuver detection, and object characterization, future efforts include demonstrating utility with non-Gaussian boundary condition distributions, estimating control authority and distributions, and investigating true ΔV distance metrics for adaptation into this framework, decreasing the conservatism of the current approach. These improvements naturally improve both fuel usage estimation and operator priority inference efforts.

Efficient computation of minimum time position reachability sets, equivalent to intercept sets in some cases, is addressed in Chapter 3. In particular, for an n dimensional state space, the transversality conditions are leveraged to provide a set of $3n/2 + 1$ equations that may be used to compute the maximum possible reachable distance in a subspace of $\mathbb{R}^n$. Also, using trajectory methods, exact subspaces of reachability sets, for example intercept sets, may be computed. Though the methods discussed in Chpater 3 are applied to minimum time reachability sets, because they leverage the transversality conditions they may be applied to reachability sets using other performance functions.

Specific directions for future work may include trajectory density / sparsity attenuation, improved extrema computation methods, residual reduction for long-duration reachability computation, symplectic integration benefits, computational studies / comparisons, and applied reachability theory to specific dynamical systems of interest. Generalizations such as adding further initial, trajectory, or final constraints, leveraging existing work on generating functions, or methods to reduce reach-tube computation requirements may be pursued. Lastly, the methods developed in this chapter may be applied to reachability sets using alternate parameters and/or reachability sets using alternate independent parameters.

Chapter 4 derived the general independent parameter reachability framework, explored some of its properties, and examined an extensive example in which the full orbit range problem for semi-major axis, eccentricity, and inclination was solved. This effort motivated the another application of optimal control distance metrics, defining the Generalized Metric Range Set, of which nearly all existing reachability sets are instances (e.g. minimum time reachability, Breugot aircraft range equation, orbit range). The successful treatment of range set theory and a detailed derivation of orbit range optimal control policies and resulting

sets in Chapter 4 directly supports the SSA activities outlined in Table 1.3.

For future work, other instances of Generalized Metric Range Sets will be identified and solved in the new framework. Also, methods to convert currently intractable problems (such as those suffering from infinite mapping function slopes) to tractable problems will be pursued. Also, development of a mission planning tool emphasizing ease-of-use and range set visualization is planned. Further analytical efforts will investigate the constrained time, constrained fuel range problem that often encountered in operational settings, and quantification / characterization of error sources related to the numerical scheme used.

Bibliography

[1] L. James, "On Keeping the Space Environment Safe for Civil and Commercial Users," Statement of Lieutenant General Larry James, Commander, Joint Functional Component Command for Space, Before the Subcommittee on Space and Aeronautics, House Committee on Science and Technology, April 28, 2009.

[2] C. M. Cox, E. J. Degraaf, R. J. Wood, T. H. Crocker, "Intelligent Data Fusion for Improved Space Situational Awareness," AIAA Space 2005 Conference, September 2005.

[3] G. E. Payton, "Military Space Programs in Review of the Defense Authorization Request for Fiscal Year 2011 and Future Years Defense Program," Statement of Mr. Gary E. Payton, Deputy Under Secretary of the Air Force for Space Programs, Presentation to the House Armed Services Committee, Strategic Forces Subcommittee, United States House of Representatives, April 21, 2010, pg. 11.

[4] Joint Publication 3-14, Space Operations, 6 January 2009, p II-7, §15.

[5] J. Shoemaker, "Space Situational Awareness and Mission Protection," DARPATech 2005, August 9-11 2005.

[6] N. B. Shah, M. G. Richards, D. A. Broniatowski, J. R. Laracy, P. N. Springmann, D. E. Hastings, "System of Systems Architecture: The Case of Space Situational Awareness," AIAA Space 2007 Conference, September, 2007.

[7] S. Kullback, "Information Theory and Statistics," John Wiley & Sons, Inc., New York, 1959.

[8] T. Kailath, "The Divergence and Bhattacharyya Distance Measures in Signal Selection," IEEE Transactions on Communication Technology, Vol. Com-15, No. 1., February 1967.

[9] Air Force Instruction 14-124, Predictive Batlespace Awareness (PBA), 25 November, 2008.

[10] D. Oltrogge, S. Alfana, R. Gist, "Satellite Mission Operations Improvements Through Covariance Based Methods," AIAA 2002-1814, SatMax 2002: Satellite Performance Workshop, 22-24 April 2002, Laurel, MD.

[11] T. S. Kelso, "Analysis of the Iridium 33-Cosmos 2251 Collision," Advanced Maui Optical and Space Surveillance Technologies Conference, September, 2009.

[12] K. Hill, K. T. Alfriend, C. Sabol, "Covariance-based Uncorrelated Track Association," AIAA/AAS Astrodynamics Specialist Conference and Exhibit 18 - 21 August 2008, Honolulu, Hawaii, AIAA 2008-7211.

[13] A. B. Poore, "Multidimensional Asignment Formulation of Data Association Problems Arising from Multitarget and Multisensor Tracking," Computational Optimization and Applications, 3, pp. 27-57, Kluwer Academic Publishers, Netherlands, 1994.

[14] P. Willet, Y. Ruan, R. Streit, "Making the Probabilistic Multi-Hypothesis Tracker the Tracker of Choice," 1999 IEEE Aerospace Conference, Page(s):387 - 399 vol.4, 1999.

[15] J. D. Wolfe, J. L. Speyer, "Target Association Using Detection Methods," Journal of Guidance, Control, and Dynamics, Vol. 25, No. 6, NovemberDecember, 2002.

[16] Y. Ruan, P. Willet, "Multiple Model PMHT and its Application to the Second Benchmark Radar Tracking Problem," IEEE Transactions on Aerospace and Electronic Systems, Vol. 40, No. 4, October, 2004

[17] B. D. Tapley, B. E. Schutz, G. H. Born, "Statistical Orbit Determination," Elsevier Academic Press, Inc, Amsterdam, 2004.

[18] Z. J. Folcik, "Orbit determination using modern filters/smoothers and continuous thrust modeling," Thesis (S.M.), Massachusetts Institute of Technology, Dept. of Aeronautics and Astronautics, 2008.

[19] R. P. Patera, "Space Event Detection Method," Journal of Spacecraft and Rockets, Vol. 45, No. 3, MayJune 2008, pp. 554-559.

[20] B. S. Aaron, "Geosynchronous satellite maneuver detection and orbit recovery using ground based optical tracking," Thesis (S.M.), Massachusetts Institute of Technology, Dept. of Aeronautics and Astronautics, 2006.

[21] R. I. Abbot, T. P. Wallace, "Decision Support in Space Situational Awareness," Lincoln Laboratory Journal, Vol. 16, No. 2, 2007. pp. 297-335.

[22] H. Chen, G. Chen, D. Shen, E. P. Blasch, and K. Pham, "Orbital Evasive Target Tracking and Sensor Management," Dynamics of Information Systems, Chapter 12, pp. 233-255.

[23] A. W. Naylor, G. R. Sell, "Linear Operator Theory in Engineering and Science," Applied Mathematical Sciences 40, Springer-Verlag, New York, NY, 2000.

[24] M. J. Holzinger and D. J. Scheeres, "Reachability Results for Nonlinear Systems with Ellipsoidal Initial Sets," IEEE Transactions on Aerospace and Electronic Systems, In Press.

[25] J. Marec, "Optimal Space Trajectories," Studies in Astronautics 1, Elsevier Scientific Publishing Company, Amsterdam, 1979.

[26] E. D. Gustafson, D. J. Scheeres, "Optimal Timing of Control-Law Updates for Unstable Systems with Continuous Control," Journal of Guidance, Control, and Dynamics, Vol. 32, No. 3, MayJune, 2009.

[27] D. F. Lawden, "Optimal Trajectories for Space Navigation," Butterworths Mathematical Texts, Butterworths, London, 1963.

[28] R. F. Stengel, "Optimal Control and Estimation," Dover Publications, Mineola, 1994.

[29] D. F. Lawden, "Analytical Methods of Optimization," Dover Publications Inc., Mineola, NY, 2003.

[30] H. Yan, F. Fahroo, I. M. Ross, "Real-Time Computation of Neighboring Optimal Control Laws," AIAA Conference on Guidance, Navigation, and Control, 2002.

[31] A. M. Mathai, S. B. Provost, "Quadratic Forms in Random Variables: Theory and Applications," Marcel Dekker, Inc., New York, NY, 1992.

[32] A. Meucci, "Risk and Asset Allocation," 3rd Printing, Springer-Verlag, New York, NY, 2007.

[33] T. S. Kelso, "Two Years of International Cooperation on Conjunction Mitigation," 8^{th} US/Russian Space Surveillance Workshop, April, 2010.

[34] P. Varaiya, "Reach set computation using optimal control," Proceedings of the KIT Workshop on Verification of Hybrid Systems, pages 377-383, Grenoble, France, 1998.

[35] A. B. Kurzhanski, P. Varaiya, "Dynamic Optimization for Reachability Problems", Journal of Optimization Theory and Applications, Vol. 108, No. 2, pp 227-251, February 2001.

[36] J. Lygeros, "On the Relation of Reachability to Minimum Cost Optimal Control," IEEE Conference on Decision and Control, Las Vegas, December 2002.

[37] J. Lygeros, "On Reachability and Minimum Cost Optimal Control," Automatica 40, 2004.

[38] A. B. Kurzhanski, I. M. Mitchell, P. Varaiya, "Optimization Techniques for State-Constraineed Control and Obstacle Problems," Communicated by G. Leitmann, 2006.

[39] I. M. Mitchell, A. M. Bayen, and C. J. Tomlin, "A Time-Dependent Hamilton-Jacobi Formulation of Reachable Sets for Continuous Dynamic Games," IEEE Transactions on Automatic Control, Vol. 50, No. 7, July 2005

[40] J. Ding, J. Sprinkle, S. S. Sastry, and C. J. Tomlin, "Reachability Calculations for Automated Aerial Refueling," IEEE Conference on Decision and Control, Cancun, 2008.

[41] J. Lygeros, C. J. Tomlin, S. S. Sastry, "Controllers for reachability specifications for hybrid systems," Automatica 35 (1999) 349-370.

[42] I. Mitchell, A. M. Bayen, and C. J. Tomlin, "Validating a Hamilton-Jacobi Approximation to Hybrid System Reachable Sets," HSCC 2001, LNCS 2034, pp 418-432, 2001.

[43] C. J. Tomlin, J. Lygeros, S. S. Sastry, "A Game Theoretic Approach to Controller Design for Hybrid Systems," Proceedings of the IEEE, Vol 88, No. 7, July 2000.

[44] Lafferriere, G.; Pappas, G. J., and Yovine, S., "A new Class of decidable Hybrid Systems," Hybrid Systems: Computation and Control, Springer, 1999, 137-151

[45] Schmidt, C.; Oechsle, F., and Branz, W., "Research on trajectory planning in emergency situations with multiple objects," Proc. of the IEEE Intelligent Transportation Systems Conference, 2006, 988-992.

[46] Prajna, S. and Jadbabaie, "A. Safety Verification of Hybrid Systems Using Barrier Certificates," Hybrid Systems: Computation and Control, Springer, 2004, 477-492.

[47] Kloetzer, M., and Belta, C., "Reachability Analysis of Multi-affine Systems," Hybrid Systems: Computation and Control, Springer, 2006, 348-362

[48] I. Hwang, D. M. Stipanovic, and C. J. Tomlin, "Applications of Polytopic Approximations of Reachable Sets to Linear Dynamic Games and a Class of Nonlinear Systems," Proceedings of the American Control Conference, Denver, Colorado, 2003.

[49] Girard, A.; Guernic, C. L., and Maler, O., "Efficient Computation of Reachable Sets of Linear Time-Invariant Systems with Inputs," Hybrid Systems: Computation and Control, Springer, 2006, 257-271

[50] Girard, A., and Guernic, C. L., "Efficient Reachability Analysis for Linear Systems using Support Functions," Proc. of the 17th IFAC World Congress, 2008, 8966-8971.

[51] Althoff, M.; Stursberg, O., and Buss, M., "Reachability Analysis of Nonlinear Systems with Uncertain Parameters using Conservative Linearization," Proc. of the 47th IEEE Conference on Decision and Control, 2008, 4042-4048

[52] A. B. Kurzhanski, P. Varaiya, "Ellipsoidal Techniques for Reachability Analysis," Hybrid Systems: Computation and Control, Springer, 2000, 202-214.

[53] A. B. Kurzhanski and P. Varaiya, "On reachability under uncertainty," SIAM Journal on Control and Optimization, 41(1):181-216, 2002.

[54] A. N. Daryin, A. B. Kurzhanski and I. V. Vostrikov, "Reachability Approaches and Ellipsoidal Techniques for Closed-Loop Control of Oscillating Systems under Uncertainty," IEEE Conference on Decision and Control, 2006.

[55] "Applied Optimal Estimation," Edited by A. Gelb, The M.I.T. Press, Cambridge, 1974.

[56] N. Shishido, C. J. Tomlin, "Ellipsoidal Approximations of Reachabile Sets for Linear Games," IEEE Conference on Decision and Control, Syndey, December 2000.

[57] W. H. Fleming, H. M. Soner, "Controlled Markov Processes and Viscosity Solutions, 2^{nd} Ed." New York, Springer, 2006

[58] D. F. Lawden, "Analytical Methods of Optimization," Mineola, NY, Dover Publications, 2003.

[59] H. J. Sussmann, "Geometry and Optimal Control," Mathematical Control Theory, Springer-Verlag, 1998, 140-198.

[60] M. G. Crandall, L. C. Evans, and P. L. Lions, "Some properties of viscosity solutions of Hamilton-Jacobi equations," Transactions of the American Mathematical Society, Vol. 282, No. 2, April 1984.

[61] S. Osher, J. Sethian, "Fronts propagating with curvature-dependent speed:Algorithms based on Hamilton-Jacobi formulations," Journal of Computational Physics, 79, 12-49, 1988.

[62] J. A. Sethian, "Level set methods: Evolving interfaces in geometry, fluid mechanics, computer vision, and materials science." New York: Cambridge University Press, 1996.

[63] A. M. Bayen, C. J. Tomlin, "A construction procedure using characteristics for viscosity solutions of the Hamilton-Jacobi equation," IEEE Conference on Decision and Control, Orlando, 2001.

[64] I. M. Mitchell, "A Toolbox of Level Set Methods," UBC Department of Computer Science Technical Report TR-2007-11, June 2007.

[65] H. Schaub, J. L. Junkins, "Analytical Mechanics of Space Systems," Reston, VA, AIAA Educational Series, 2003.

[66] C. L. Navasca, A. J. Krener, "Solution of Hamilton Jacobi Bellman Equations," IEEE Conference on Decision and Control, Sydney, 2000.

[67] C. Navasca, A. J. Krener, "Patchy Solutions of Hamilton Jacobi Bellman Partial Differential Equations," In A. Chiuso, A. Ferrante and S. Pinzoni, eds, "Modeling, Estimation and Control, Lecture Notes in Control and Information Sciences," 364, pp. 251-270, 2007.

[68] D. T. Greenwood, "Classical Dynamics," Dover Publications Inc., Mineola, 1977.

[69] M. J. Holzinger, D. J. Scheeres, R. S. Erwin, "On-Orbit Range Computation Using Gauss' Variational Equations for Mean Orbit Elements with J_2 Perturbations," 21^{st} AAS/AIAA Space Flight Mechanics Meeting, New Orleans, Louisiana, February 2011.

[70] R. H. Battin, "An Introduction to the Mathematics and Methods of Astrodynamics, Revised Edition," AIAA Educational Series, AIAA Inc., Reston, VA, 1999.

[71] W. T. Thomson, "Introduction to Space Dynamics," Dover Publications Inc., Mineola, NY, 1986.

[72] G. J. J. Ruijgrok, "Elements of Airplane Performance," Delft University Press, 1990.

[73] Y. Luo, G. Tang, Y. Lei, H. Li, "Optimization of Multiple-Impulse, Multiple-Revolution Rendezvous Phasing Maneuvers," Journal of Guidance, Control, and Dynamics, Vol. 30, No. 4, July August 2007.

[74] N. X. Vinh, P. Lu, R. M. Howe, and E. G. Gilbert, "Optimal Interception with Time Constraint," Journal of Optimization Theory and Applications, Vol. 66, No. 3, September 1990.

[75] N. X. Vinh, E. G. Gilbert, R. M. Howe, R. Sheu, and P. Lu, "Reachable Domain for Interception at Hyperbolic Speeds," Acta Astronautica, Vol. 35, No. 1, pp. 1-8, 1995.

[76] J. P. Marec, "Optimal transfers between close elliptical orbits," NASA T. T. F. 554, 1969.

[77] J. V. Breakwell and W. Heine, "Minimum-impulse time-free transfer between neighboring non-coplanar elliptical orbits with major axes perpendicular to the line of nodes," AAS/AIAA Astrodynamics Specialist Conference, 1968.

[78] D. Xue, J. Li, H. Baoyin, F. Jiang, "Reachable Domain for Spacecraft with a Single Impulse," Journal of Guidance, Control, and Dynamics, Vol. 33, No. 3, May June 2010.

[79] P. Kats, "Reachable sets and singular arcs for minimum fuel problems based on norm-invariant systems," IEEE Transactions on Automatic Control, Vol. 17, No. 4, pp. 557-559, August 1972.

[80] R. R. Bate, D. D. Mueller, J. E. White, "Fundamentals of Astrodynamics," Dover Publications Inc., Mineola, NY, 1971.

[81] [Submitted] M. J. Holzinger, D. J. Scheeres, J. Hauser, "Optimal Free-Time Reachability Sets Using Alternate Integration Parameters," American Control Conference, San Francisco, June 2011.

[82] V. A. Chobotov, "Orbital Mechanics, 2nd Ed." AIAA Education Series, AIAA Inc., Reston, VA, 2002.

[83] I. M. Ross, "Space Trajectory Optimization and L1-Optimal Control Problems," in P. Gurfil (ed.), Modern Astrodynamics, pp. 155-188, Elsevier, Amsterdam, 2006.

Appendix A

Control Distance Appendices

A.1 Statistical Properties of Quadratic Forms with Gaussian Vectors

This section parallels a similar derivation in Mathai[31] with notation modified to apply to the problem presented in this paper. Starting with a random variable P with the quadratic form

$$P = l + \mathbf{m}^T\mathbf{V} + \mathbf{V}^T\mathbf{N}\mathbf{V} \tag{A.1}$$

where $\mathbf{V} \in N(\mathbf{0}, \mathbf{P}_V)$, $l \in \mathbb{R}$, $\mathbf{m} \in \mathbb{R}^r$, and $\mathbf{N} \in \mathbb{S}^{+,r\times r}$. The first task is to factor (A.1) into the form $P = p_{min} + \mathbf{X}^T\mathbf{N}\mathbf{X}$. To accomplish this, first define

$$\mathbf{X} = \mu_X + \mathbf{V}$$

giving $\mathbf{X} \in N(\mu_x, \mathbf{P}_V)$. Substituting into (A.1),

$$\begin{aligned} P &= l + \mathbf{m}^T(\mathbf{X} - \mu_X) + (\mathbf{X} - \mu_X)^T\mathbf{N}(\mathbf{X} - \mu_X) \\ &= l + \mathbf{m}^T\mathbf{X} - \mathbf{m}^T\mu_X + \mathbf{X}^T\mathbf{N}\mathbf{X} - 2\mu_X^T\mathbf{N}\mathbf{X} + \mu_X^T\mathbf{N}\mu_X \\ &= \left(l - \mathbf{m}^T\mu_X + \mu_X^T\mathbf{N}\mu_X\right) \\ &\quad + \left(\mathbf{m}^T - 2\mu_X^T\mathbf{N}\right)\mathbf{X} + \mathbf{X}^T\mathbf{N}\mathbf{X} \end{aligned}$$

Now μ_X must be chosen such that $\mathbf{m} - 2\mathbf{N}\mu_X = \mathbf{0}$, yielding

$$\mu_X = \frac{1}{2}\mathbf{N}^\dagger\mathbf{m}$$

The random variable P then reduces to

$$\begin{aligned} P &= \left(l - \mathbf{m}^T\mu_X + \mu_X^T\mathbf{N}\mu_X\right) + \mathbf{X}^T\mathbf{N}\mathbf{X} \\ &= \left(l - \frac{1}{2}\mathbf{m}^T\mathbf{N}^\dagger\mathbf{m} + \frac{1}{4}\mathbf{m}^T\mathbf{N}^\dagger\mathbf{N}\mathbf{N}^\dagger\mathbf{m}\right) + \mathbf{X}^T\mathbf{N}\mathbf{X} \\ &= \left(l - \frac{1}{4}\mathbf{m}^T\mathbf{N}^\dagger\mathbf{m}\right) + \mathbf{X}^T\mathbf{N}\mathbf{X} \end{aligned}$$

Defining

$$p_{min} = l - \frac{1}{4}\mathbf{m}^T\mathbf{N}^\dagger\mathbf{m},$$

the random variable P is now of the form $P = p_{min} + \mathbf{X}^T\mathbf{N}\mathbf{X}$. Now, with a random vector $\mathbf{X} \in N(\mu_x, \mathbf{P}_V)$, we are faced with determining the distribution of

$$Q = P - p_{min} = \mathbf{X}^T\mathbf{N}\mathbf{X}$$

The first step is to transform this problem to a unitary normal distribution. Define

$$\mathbf{Y} = \mathbf{P}_V^{-\frac{1}{2}}\mathbf{X}$$

where $\mathbf{P}_V^{\frac{1}{2}}$ is the matrix square root of $\mathbf{P}_V$ (more generally, any decomposition of $\mathbf{P}_V$ such that $\mathbf{P}_V = \mathbf{B}\mathbf{B}^T$ is sufficient). The new random vector $\mathbf{Y}$ has an expected value of

$$\mathbb{E}[\mathbf{Y}] = \mathbb{E}\left[\mathbf{P}_V^{-\frac{1}{2}}\mathbf{X}\right] = \mathbf{P}_V^{-\frac{1}{2}}\mathbb{E}[\mathbf{X}] = \mathbf{P}_V^{-\frac{1}{2}}\mu_X$$

The covariance is

$$\mathbb{E}\left[\mathbf{Y}\mathbf{Y}^T\right] = \mathbb{E}\left[\mathbf{P}_V^{-\frac{1}{2}}\mathbf{X}\mathbf{X}^T\mathbf{P}_V^{-\frac{1}{2}}\right]$$

$$= \mathbf{P}_V^{-\frac{1}{2}}\mathbb{E}\left[\mathbf{X}\mathbf{X}^T\right]\mathbf{P}_V^{-\frac{1}{2}} = \mathbf{P}_V^{-\frac{1}{2}}\mathbf{P}_V\mathbf{P}_V^{-\frac{1}{2}} = \mathbb{I}$$

Next, a second random vector $\mathbf{Z}$ is defined as

$$\mathbf{Z} = \mathbf{Y} - \mathbf{P}_V^{-\frac{1}{2}}\mu_X$$

The random vector $\mathbf{Z}$ has a mean of

$$\mathbb{E}[\mathbf{Z}] = \mathbb{E}\left[\mathbf{Y} - \mathbf{P}_V^{-\frac{1}{2}}\mu_X\right] = \mathbf{0}$$

and a covariance of

$$\mathbb{E}\left[\mathbf{Z}\mathbf{Z}^T\right] = \mathbb{E}\left[\left(\mathbf{Y} - \mathbf{P}_V^{-\frac{1}{2}}\mu_X\right)\left(\mathbf{Y} - \mathbf{P}_V^{-\frac{1}{2}}\mu_X\right)^T\right] = \mathbb{I}$$

Such a random vector $\mathbf{Z} \in N(\mathbf{0}, \mathbb{I})$ is said to be a Standard Gaussian Random Variable. The random variable $P - p_{min}$ may now be rewritten as

$$P - p_{min} = \frac{1}{2}\mathbf{X}^T\mathbf{N}\mathbf{X}$$

$$= \frac{1}{2}\mathbf{Y}^T\mathbf{P}_V^{-\frac{1}{2}}\mathbf{N}\mathbf{P}_V^{-\frac{1}{2}}\mathbf{Y}$$

$$= \frac{1}{2}\left(\mathbf{Z} + \mathbf{P}_V^{-\frac{1}{2}}\mu_X\right)^T\mathbf{P}_V^{-\frac{1}{2}}\mathbf{N}\mathbf{P}_V^{-\frac{1}{2}}\left(\mathbf{Z} + \mathbf{P}_V^{-\frac{1}{2}}\mu_X\right)$$

Now, choose an orthonormal transformation matrix $\mathbf{T}$ that diagonalizes $\mathbf{P}_V^{-\frac{1}{2}}\mathbf{N}\mathbf{P}_V^{-\frac{1}{2}}$, so

$$\mathbf{T}\mathbf{P}_V^{-\frac{1}{2}}\mathbf{N}\mathbf{P}_V^{-\frac{1}{2}}\mathbf{T}^T = \begin{bmatrix} \lambda_1 & \cdots & 0 \\ \vdots & \ddots & \vdots \\ 0 & \cdots & \lambda_l \end{bmatrix}$$

Note that for orthonormal transformations, $\mathbf{T}^{-1} = \mathbf{T}^T$. With this transformation, we now define a random vector $\mathbf{U}$ such that

$$\mathbf{U} = \mathbf{T}^T\mathbf{Z}$$

The mean of $\mathbf{U}$ is

$$\mathbb{E}[\mathbf{U}] = \mathbb{E}\left[\mathbf{T}^T\mathbf{Z}\right] = \mathbf{T}^T\mathbb{E}[\mathbf{Z}] = \mathbf{0}$$

and the covariance is

$$\mathbb{E}\left[\mathbf{U}\mathbf{U}^T\right] = \mathbb{E}\left[\mathbf{T}^T\mathbf{Z}\mathbf{Z}^T\mathbf{T}\right] = \mathbf{T}^T\mathbb{I}\mathbf{T} = \mathbb{I}$$

Again, $\mathbf{U}$ is a Standard Gaussian Random Vector. The random variable $P - p_{min}$ becomes

$$\begin{aligned} & P - p_{min} \\ = & \frac{1}{2}\left(\mathbf{U} + \mathbf{T}^T\mathbf{P}_V^{-\frac{1}{2}}\mu_X\right)^T \mathbf{T}^T\mathbf{P}_V^{-\frac{1}{2}}\mathbf{N}\mathbf{P}_V^{-\frac{1}{2}}\mathbf{T} \\ & \left(\mathbf{U} + \mathbf{T}^T\mathbf{P}_V^{-\frac{1}{2}}\mu_X\right) \\ = & \frac{1}{2}\left(\mathbf{U} + \mathbf{T}^T\mathbf{P}_V^{-\frac{1}{2}}\mu_X\right)^T \begin{bmatrix} \lambda_1 & \cdots & 0 \\ \vdots & \ddots & \vdots \\ 0 & \cdots & \lambda_l \end{bmatrix} \\ & \left(\mathbf{U} + \mathbf{T}^T\mathbf{P}_V^{-\frac{1}{2}}\mu_X\right) \end{aligned}$$

If the definition

$$\mathbf{b} = \mathbf{T}^T\mathbf{P}_V^{-\frac{1}{2}}\mu_X = \frac{1}{2}\mathbf{T}^T\mathbf{P}_V^{-\frac{1}{2}}\mathbf{N}^\dagger\mathbf{m}$$

is made, then we arrive at the simplified form

$$P - p_{min} = \frac{1}{2}(\mathbf{U} + \mathbf{b})^T \begin{bmatrix} \lambda_1 & \cdots & 0 \\ \vdots & \ddots & \vdots \\ 0 & \cdots & \lambda_l \end{bmatrix} (\mathbf{U} + \mathbf{b})$$

which can also be re-written as

$$P - p_{min} = \frac{1}{2}\sum_{i=1}^{r} \lambda_i (U_i + b_i) \tag{A.2}$$

where r is the size of $\mathbf{V}$. There are several special cases in which the distribution of $P - p_{min}$ is analytic (for example, when all λ_i are 0 or 1 the distribution is a chi-squared distribution), however for the application

in this paper this is not generally the case. Thus, an approximation of the distribution must be found. Several expansions which approximate (A.2) are known[31] (power series, Laguerre series, hyper-geometric functions, and zonal polynomals). Of particular interest is Pearson's Approximation which matches the first three moments of the true distribution and models the random variable as a non-central χ^2 variable. The approximation is

$$P \approx \frac{\theta_3}{\theta_2}\chi^2_v - \frac{\theta_2^2}{\theta_3} + \theta_1 + p_{min} \tag{A.3}$$

where

$$\theta_s = \sum_{j=1}^{2n} \lambda_j^s (1 + s b_j^2), \;\; s = 1, 2, 3$$

and the degree of freedom v is

$$v = \frac{\theta_2^3}{\theta_3^2}$$

A.2 Derivation of The Control Distance Distribution Mean and Variance

This appendix derives analytical first and second moments of the random variable introduced in Appendix A. The random variable P is written as

$$P = l + \mathbf{m}^T\mathbf{V} + \mathbf{V}^T\mathbf{N}\mathbf{V}$$

where $\mathbf{V} \in N(\mathbf{0}, \mathbf{P}_V)$, $l \in \mathbb{R}$, $\mathbf{m} \in \mathbb{R}^r$, and $\mathbf{N} \in \mathbb{S}^{+,r\times r}$. The first moment is

$$\mu_P = \mathbb{E}[P] = \mathbb{E}\left[l + \mathbf{m}^T\mathbf{V} + \mathbf{V}^T\mathbf{N}\mathbf{V}\right] = l + \mathbb{E}\left[\mathbf{V}^T\mathbf{N}\mathbf{V}\right]$$

Examining the last term using index notation,

$$\begin{aligned}
\mathbb{E}\left[\mathbf{V}^T\mathbf{N}\mathbf{V}\right] &= \mathbb{E}[V_i N_{ij} V_j] \\
&= N_{ij}\mathbb{E}[V_j V_i] \\
&= N_{ij} P_{ji} \\
&= \mathrm{Tr}[\mathbf{N}\mathbf{P}_V]
\end{aligned}$$

Generating

$$\mu_P = l + \mathrm{Tr}[\mathbf{N}\mathbf{P}_V] \tag{A.4}$$

The second moment of P is defined as

$$\sigma_P^2 = \mathbb{E}\left[P^2 - \mathbb{E}\left[P\right]^2\right]$$

After simplification, this may be written as

$$\sigma_P^2 = \mathbb{E}\left[2(\mathbf{m}^T\mathbf{V})(\mathbf{V}^T\mathbf{N}\mathbf{V}) + (\mathbf{m}^T\mathbf{V})^2 + (\mathbf{V}^T\mathbf{N}\mathbf{V})^2 - \mathrm{Tr}\left[\mathbf{N}\mathbf{P}_V\right]^2\right]$$

Examining each term individually:

$$\begin{aligned}
\mathbb{E}\left[2(\mathbf{m}^T\mathbf{V})(\mathbf{V}^T\mathbf{N}\mathbf{V})\right] &= 2\mathbb{E}\left[(m_iV_i)(V_jN_{jk}V_k)\right] \\
&= 2\mathbb{E}\left[(m_iV_i)(N_{jk}V_kV_j)\right] \\
&= 2m_iN_{jk}\mathbb{E}\left[V_kV_jV_i\right] \\
&= 0
\end{aligned}$$

$$\begin{aligned}
\mathbb{E}\left[(\mathbf{m}^T\mathbf{V})^2\right] &= \mathbb{E}\left[m_iV_im_jV_j\right] \\
&= \mathbb{E}\left[m_iV_iV_jm_j\right] \\
&= m_i\mathbb{E}\left[V_iV_j\right]m_j \\
&= m_iP_{ij}m_j \\
&= \mathbf{m}^T\mathbf{P}_V\mathbf{m}
\end{aligned}$$

$$\begin{aligned}
\mathbb{E}\left[(\mathbf{V}^T\mathbf{N}\mathbf{V})^2\right] &= \mathbb{E}\left[V_iN_{ij}V_jV_kN_{kl}V_l\right] \\
&= N_{ij}N_{kl}\mathbb{E}\left[V_iV_jV_kV_l\right] \\
&= N_{ij}N_{kl}\left(P_{ij}P_{kl} + P_{ik}P_{jl} + P_{il}P_{kj}\right) \\
&= N_{ij}N_{kl}P_{ij}P_{kl} + N_{ij}N_{kl}P_{ik}P_{jl} + N_{ij}N_{kl}P_{il}P_{kj} \\
&= N_{ij}P_{ji}N_{kl}P_{lk} + N_{ij}P_{jl}N_{lk}P_{ki} + N_{ij}P_{jk}N_{kl}P_{li} \\
&= \mathrm{Tr}\left[\mathbf{N}\mathbf{P}_V\right]^2 + \mathrm{Tr}\left[\mathbf{N}\mathbf{P}_V\mathbf{N}\mathbf{P}_V\right] + \mathrm{Tr}\left[\mathbf{N}\mathbf{P}_V\mathbf{N}\mathbf{P}_V\right]
\end{aligned}$$

Note that in the last term both $\mathbf{N}$ and $\mathbf{P}_V$ are symmetric. The second moment in the performance index is finally written as

$$\sigma_P^2 = \mathbf{m}^T\mathbf{P}_V\mathbf{m} + 2\mathrm{Tr}\left[\mathbf{N}\mathbf{P}_V\mathbf{N}\mathbf{P}_V\right] \tag{A.5}$$

Equations (A.4) and (A.5) exactly capture the first and second moments of the random variable P, as described in Appendix A.

Appendix B

Orbit Range Appendices

B.1 Analytical Ellipse-to-Ellipse ΔV Calculations

These derivations closely parallel a similar derivation in traditional literature[71, 80]. Given an initial semi-major axis, eccentricity, and inclination (a_1, e_1, i_1), our goal is to compute the minimum ΔV transfer to (a_2, e_2, i_2). First the planar portion of the transfer is considered, then the optimal inclination change is examined.

There are two cases in the planar transfer to consider: A) Initial impulse at periapsis and final impulse at new apoapsis, and B) Initial impulse at apoapsis and final impulse at new periapsis. Case A is associated with 'raising' orbits, and Case B is associated with 'lowering' orbits. The following identities are used:

$$r_a = a(1+e)$$

$$r_p = a(1-e)$$

$$\frac{r_a}{r_p} = \frac{1+e}{1-e}$$

$$v_a = \sqrt{\frac{\mu}{r_a}(1-e)} = \sqrt{\frac{\mu}{a}\frac{1-e}{1+e}}$$

$$v_p = \sqrt{\frac{\mu}{r_p}(1+e)} = \sqrt{\frac{\mu}{a}\frac{1+e}{1-e}}$$

For case A the periapsis of orbit 1 is the same as the periapsis of the transfer orbit, and the apoapsis of the transfer orbit is the same as orbit 2 ($r_{p_1} = r_{p_t}$ and $r_{a_t} = r_{a_2}$). The transfer orbit semi-major axis is defined as

$$a_t = \frac{1}{2}(r_{a_2} + r_{p_1})$$

and

$$\frac{r_{a_2}}{r_{p_1}} = \frac{r_{a_t}}{r_{p_t}} = \frac{1+e_t}{1-e_t}$$

The initial ΔV_{1A} may be written as

$$\Delta V_{1A} = v_{p_t} - v_{p_1} = \sqrt{\frac{2\mu}{r_{p_1}+r_{a_2}}\frac{r_{a_2}}{r_{p_1}}} - \sqrt{\frac{\mu}{r_{p_1}}(1+e_1)}$$

which may be written as

$$\Delta V_{1A} = \sqrt{\frac{\mu}{r_{p_1}}}\left(\sqrt{\frac{2r_{a_2}}{r_{p_1}+r_{a_2}}} - \sqrt{1+e_1}\right)$$

Similarly, the second impulse ΔV_{2A} at apoapsis may be written as

$$\Delta V_{2A} = v_{a_2} - v_{a_t} = \sqrt{\frac{\mu}{r_{a_2}}(1-e_2)} - \sqrt{\frac{2\mu}{r_{p_1}+r_{a_2}}\frac{r_{p_1}}{r_{a_2}}}$$

Simplifying produces

$$\Delta V_{2A} = \sqrt{\frac{\mu}{r_{a_2}}}\left(\sqrt{1-e_2} - \sqrt{\frac{2r_{p_1}}{r_{p_1}+r_{a_2}}}\right)$$

The total ΔV_A for Case A is then written as

$$\Delta V_A = |\Delta V_{1A}| + |\Delta V_{2A}| \tag{B.1}$$

Examining Case B the apoapsis of orbit 1 is also the apoapsis of the transfer orbit, and the periapsis of orbit 2 is the periapsis of the transfer orbit ($r_{a_1} = r_{a_t}$ and $r_{p_t} = r_{p_2}$). The transfer orbit characteristics a_t and e_t are defined as

$$a_t = \frac{1}{2}(r_{a_1} + r_{p_2})$$

and

$$\frac{r_{a_1}}{r_{p_2}} = \frac{r_{a_t}}{r_{p_t}} = \frac{1+e_t}{1-e_t}$$

The first impulse occurs at the apoapsis of orbit 1 and may be written as

$$\Delta V_{1B} = v_{a_1} - v_{a_t} = \sqrt{\frac{\mu}{r_{a_1}}(1-e_1)} - \sqrt{\frac{2\mu}{r_{p_2}+r_{a_1}}\frac{r_{p_2}}{r_{a_1}}}$$

This reduces to

$$\Delta V_{1B} = \sqrt{\frac{\mu}{r_{a_1}}}\left(\sqrt{1-e_1} - \sqrt{\frac{2r_{p_2}}{r_{p_2}+r_{a_1}}}\right)$$

The second impulse ΔV_{2B} at periapsis is written as

$$\Delta V_{2B} = v_{p_t} - v_{p_2} = \sqrt{\frac{2\mu}{r_{p_2}+r_{a_1}}\frac{r_{a_1}}{r_{p_2}}} - \sqrt{\frac{\mu}{r_{p_2}}(1+e_2)}$$

Which is further reduced to

$$\Delta V_{2B} = \sqrt{\frac{\mu}{r_{p_2}}}\left(\sqrt{\frac{2r_{a_1}}{r_{p_2}+r_{a_1}}} - \sqrt{1+e_2}\right)$$

The total ΔV_B for Case B is then

$$\Delta V_B = |\Delta V_{1B}| + |\Delta V_{2B}| \tag{B.2}$$

Lastly, to effect a plane change maneuver it must be determined whether it is optimal to maneuver at the apoapsis of the initial orbit or the apoapsis of the final orbit. If the maneuver at the first orbit apoapsis is optimal (if $r_{a,1} \geq r_{a,2}$) then the optimal ΔV_i due to inclination change will be

$$\Delta V_i = \left| 2 \sin\left(\frac{i_2 - i_1}{2}\right) \sqrt{\frac{\mu}{a_1} \frac{1 - e_1}{1 + e_1}} \right| \tag{B.3}$$

Alternatily, if it is optimal to change inclination and the final orbit apoapsis (if $r_{a,1} < r_{a,2}$), the optimal ΔV_i due to inclination change is

$$\Delta V_i = \left| 2 \sin\left(\frac{i_2 - i_1}{2}\right) \sqrt{\frac{\mu}{a_2} \frac{1 - e_2}{1 + e_2}} \right| \tag{B.4}$$

The total ΔV cost is the combined cost of either Case A or B in addition to the cost of the optimal ΔV_i. Combined, Case A and Case B with the optimal inclination change maneuver may be used to verify transfers from initial orbits defined by (a_1, e_1, i_1) to final orbits defined by (a_2, e_2, i_2).

B.2 Hamilton Jacobi Bellman PDE Viscosity Solution and Level Set Toolbox

To leverage existing software [64] that propagates initial valued range/reachability sets using the HJB PDE and apply them to the orbit range problem, the following intermediate results and software inputs are shown. See [64] for further theoretical references regarding the purpose behind these calculations. In the numerical scheme, the Hamiltonian $\mathcal{H}$ is approximated by

$$\hat{\mathcal{H}} = \mathcal{H}(\mathbf{x}, \frac{\mathbf{p}^+ + \mathbf{p}^-}{2}) - \bar{\alpha}(\mathbf{x}) \left[\frac{\mathbf{p}^+ - \mathbf{p}^-}{2} \right]$$

The second term numerically compensates for regions where the adjoint $\mathbf{p}$ is not continuous. The adjoint derivative approximation is given as

$$\alpha_j(\mathbf{x}) = \max_{\mathbf{p} \in P} \left| \frac{\partial \mathcal{H}}{\partial p_j} \right|$$

for all $j = 1, \ldots, n$. Recall from (4.35) that the optimal Hamiltonian with the optimal control policy $(f^*, \omega^*, \beta^*, \gamma^*)$ applied to this problem is written as

$$\begin{aligned} \mathcal{H} = \left(\frac{a^{\frac{1}{2}}}{\mu^{\frac{1}{2}} (1 - e^2)^{\frac{1}{2}}} \right) \Bigg[& p_a \left(2a(1 + e \cos f) \cos\beta \cos\gamma \right) \\ & + p_e \left(\frac{1 - e^2}{1 + e \cos f} \left(e \cos^2 f + 2 \cos f + e \right) \cos\beta \cos\gamma \right) \\ & + p_i \left(\frac{(1 - e^2) \cos(\omega + f)}{1 + e \cos f} \sin\gamma \right) \Bigg] \end{aligned}$$

Computing $\alpha_a(\mathbf{x})$ using $\mathcal{H}$ generates

$$\begin{aligned}
&\alpha_a(\bar{\mathbf{oe}}_{tr}) = \\
&\max_{\mathbf{p}\epsilon P}\left|\left(\frac{a^{\frac{1}{2}}}{\mu^{\frac{1}{2}}(1-e^2)^{\frac{1}{2}}}\right)[2a(1+e\cos f^*)]\cos\beta^*\cos\gamma^*\right| \\
&= \max_{\mathbf{p}\epsilon P}\left(\frac{a^{\frac{1}{2}}}{\mu^{\frac{1}{2}}(1-e^2)^{\frac{1}{2}}}\right)[2a(1+e\cos f^*)]\left|\cos\beta^*\cos\gamma^*\right| \\
&= \max_{\mathbf{p}\epsilon P}\left(\frac{a^{\frac{1}{2}}}{\mu^{\frac{1}{2}}(1-e^2)^{\frac{1}{2}}}\right)[2a(1+e\cos f^*)]
\end{aligned}$$

Taking P to be the unit sphere, by inspection $\alpha_a(\bar{\mathbf{oe}}_{tr})$ is maximized with respect to the adjoints when $(f^*,\omega^*,\beta^*,\gamma^*) = (0,0,0,0)$. Then $\alpha_a(\bar{\mathbf{oe}}_{tr})$ becomes

$$\alpha_a(\bar{\mathbf{oe}}_{tr})) = \left(\frac{a^{\frac{1}{2}}}{\mu^{\frac{1}{2}}(1-e^2)^{\frac{1}{2}}}\right)2a(1+e) \tag{B.5}$$

For $\alpha_e(\bar{\mathbf{oe}}_{tr})$:

$$\begin{aligned}
&\alpha_e(\bar{\mathbf{oe}}_{tr}) = \\
&\max_{\mathbf{p}\epsilon P}\left|\left(\frac{a^{\frac{1}{2}}}{\mu^{\frac{1}{2}}(1-e^2)^{\frac{1}{2}}}\right)\right. \\
&\left.\left(\frac{2(1-e^2)(e+\cos f^*)}{1+e\cos f*}\right)\cos\beta^*\cos\gamma^*\right|
\end{aligned}$$

By inspection $\alpha_e(\bar{\mathbf{oe}}_{tr})$ is maximized when $(f^*,\omega^*,\beta^*,\gamma^*) = (0,0,0,0)$, so $\alpha_e(\bar{\mathbf{oe}}_{tr})$ reduces to

$$\alpha_e(\bar{\mathbf{oe}}_{tr}) = \left(\frac{a^{\frac{1}{2}}}{\mu^{\frac{1}{2}}(1-e^2)^{\frac{1}{2}}}\right)2(1-e^2) \tag{B.6}$$

For $\alpha_i(\bar{\mathbf{oe}}_{tr})$:

$$\begin{aligned}
&\alpha_i(\bar{\mathbf{oe}}_{tr}) = \\
&\max_{\mathbf{p}\epsilon P}\left|\left(\frac{a^{\frac{1}{2}}}{\mu^{\frac{1}{2}}(1-e^2)^{\frac{1}{2}}}\right)\frac{(1-e^2)\cos(\omega^*+f^*)}{1+e\cos f^*}\sin\gamma^*\right| \\
&= \max_{\mathbf{p}\epsilon P}\left(\frac{a^{\frac{1}{2}}}{\mu^{\frac{1}{2}}(1-e^2)^{\frac{1}{2}}}\right)\left|\frac{(1-e^2)\cos(\omega^*+f^*)}{1+e\cos f^*}\sin\gamma^*\right|
\end{aligned}$$

Determining that γ^* should be $\pm\pi/2$:

$$\begin{aligned}
&\alpha_i(\bar{\mathbf{oe}}_{tr}) = \\
&\max_{\mathbf{p}\epsilon P}\left(\frac{a^{\frac{1}{2}}}{\mu^{\frac{1}{2}}(1-e^2)^{\frac{1}{2}}}\right)\frac{1-e^2}{1+e\cos f^*}\left|\cos(\omega^*+f^*)\right|
\end{aligned}$$

choosing $f^* = \pi$ and $\omega^* = 0$ maximizes $\alpha_i(\bar{\mathbf{oe}}_{tr})$, yielding

$$\alpha_i(\bar{\mathbf{oe}}_{tr}) = \left(\frac{a^{\frac{1}{2}}}{\mu^{\frac{1}{2}}(1-e^2)^{\frac{1}{2}}}\right)(1+e) \tag{B.7}$$

Taken together, (B.5), (B.6), and (B.7) are the optimal α_j, $j = 1, 2, 3$ for this problem.